Computer Simulation of Diagnostic and Therapeutic Applications of Ultrasound Propagation in Biological Tissues

by

Behzad Vafaeian

A thesis submitted in partial fulfillment of the requirements for the degree of

Doctor of Philosophy
in
Structural Engineering

Department of Civil and Environmental Engineering
University of Alberta

Abstract

Ultrasound has been widely utilized in diagnostic and therapeutic clinical practices. Further development of the application of ultrasound in the clinical practices requires comprehensive understanding of the physics of ultrasound propagation in biological tissues. In this research, computer simulation was used as a means for investigating the physics of ultrasound propagation in two particular diagnostic and therapeutic applications of ultrasound.

In the field of diagnostic ultrasound, quantitative ultrasound (QUS) for bone assessment was considered. Accurate diagnosis and monitoring osteoporosis based on measuring velocity and attenuation of ultrasonic waves transmitted into cancellous bone are the eventual aims of QUS. In this regards, the interaction between the micro-structure of cancellous bone and ultrasonic waves should be fully understood. Although many researches have been dedicated towards this goal, the physics of ultrasound propagation in cancellous bone has not yet been fully revealed. One of the approaches towards investigating the physics of the propagation is using computer simulation. QUS has been conventionally simulated using the finite difference time-domain (FDTD) method. However, large discrepancy (up to 75%) has been reported in the results of simulated QUS experiments when the FDTD method was employed. Some part of the discrepancy is logically believed to originate from the FDTD scheme for resolving the micro-structure of cancellous bone, and implicit formulations of the material discontinuity at the solid-fluid (bone-fluid) interface in the heterogeneous medium of cancellous bone. To mitigate the effect of these discrepancy sources, the standard Galerkin finite element method (FEM) in time domain was used as an alternative to the FDTD method. To demonstrate the capability of the FEM for simulating ultrasound propagation in cancellous bone, three-dimensional finite element models of six water-saturated cancellous bone samples were created and analyzed. The obtained

relations between the simulated ultrasonic parameters (velocity and attenuation of the ultrasound) and the bone density of the samples showed that different degree of osteoporosis presented by the sample could be clearly distinguished by the simulations. Moreover, comparing the results with other experimental and simulation studies indicated that the finite element simulations were in agreement with them; therefore, the FEM was demonstrated to be capable of simulating ultrasound propagation in water-saturated cancellous bone. To further investigate the accuracy of the method, finite element simulations and QUS experiments of ultrasound propagation in cancellous bone-mimicking phantoms, i.e. aluminum foams, were performed. The simulations and the experimental results had an average relative error of 10% when the simulated and experimental ultrasonic attenuation values were compared with each other. Assumed to be mainly caused by disregarding energy-absorbing mechanisms in the simulations, the observed discrepancy (10% on average) indicated that the FEM could effectively simulate QUS as along as the energy-absorbing mechanisms had relatively small contribution in total ultrasonic attenuation. Furthermore, the results strongly suggested that wave scattering and mode conversion might be the dominant attenuation mechanisms of ultrasound propagating in trabecular structures, particularly aluminum foams.

The therapeutic effect of low intensity pulsed ultrasound (LIPUS) on orthodontically induced inflammatory root resorption (OIIRR) was the second application of ultrasound considered in this thesis. The ultrasound has been observed to have stimulatory effect on new cementum regeneration that may lead to the prevention or the treatment of OIIRR. It is hypothesized that the stimulatory effect of LIPUS on new cementum regeneration is through LIPUS-induced mechanical signals. However, the stimulatory mechanical mechanism triggering new cementum regeneration has not been clearly understood yet. The aim of this study was to

evaluate the hypothesis on the stimulatory mechanical mechanism by seeking possible relations between the amounts of new cementum regeneration and ultrasonic parameters such as pressure amplitude and time-averaged energy density. To this end, the FEM was utilized to simulate the previously published experiment of ultrasonic wave propagation in the dentoalveolar structure of beagle dogs. The results demonstrated qualitative relations and quantitative positive correlations between the thickness of the regenerated cementum observed in the experiment and the magnitudes of the ultrasonic parameters.

Preface

This thesis is an original work by Behzad Vafaeian. Some parts of this thesis have been already published or submitted for publication as follows:

Chapter 4 of this thesis has been published as B. Vafaeian, M. El-Rich, T. El-Bialy, S. Adeeb, "The finite element method for micro-scale modeling of ultrasound propagation in cancellous bone", Ultrasonics, 54 (2014) 1663–1676. I was responsible for analyses and manuscript composition. M. El-Rich provided technical support and licence for the finite element meshing software package used in this work. T. EL-Bialy was involved in manuscript edits. S. Adeeb was the supervisory author and was involved with concept formation and manuscript composition.

The contents of Chapter 5 have been submitted for publication as B. Vafaeian, L. H. Le, T. N.H.T. Tran, M. El-Rich, T. El-Bialy, S. Adeeb, "The Finite Element Method for Micro-scale Modeling of Ultrasound Propagation in Trabecular Structures: A Comparison between the Simulated and Experimental Ultrasonic Attenuation in Aluminum Foams", Ultrasonics, submitted in July 2015. I was responsible for experiment design, analyses and manuscript composition. L. H. Le provided the apparatus and support required for the experiments and data acquisition in this work. T. N.H.T. Tran was responsible for performing the experiments and data acquisition. M. El-Rich provided technical support and licence for the finite element meshing software package used in this work. T. EL-Bialy was involved in manuscript edits. S. Adeeb was the supervisory author and was involved with concept formation and manuscript composition.

Chapter 6 of the present thesis has been published as B. Vafaeian, S. Al-Daghreer, M. El-Rich, S. Adeeb, T. El-Bialy, "Simulation of Low Intensity Ultrasound Propagating in a Beagle

Dog Dentoalveolar Structure to Investigate the Relations between Ultrasonic Parameters and Cementum Regeneration", Ultrasound in Medicine & Biology, Vol. 41, No. 8, pp. 2173–2190, 2015. I was responsible for the analyses and manuscript composition. S. Al-Daghreer provided the experimental data and micro computed tomography scan image data employed in this work. M. El-Rich provided technical support and licence for the finite element meshing software package utilized in the analyses. S. Adeeb was involved with concept formation and manuscript composition. T. EL-Bialy was the supervisory author and was involved with concept formation and manuscript composition.

Dedication

In dedication to my parents and wife *Maedeh*.

Acknowledgements

First, I would like to express my sincerest gratitude to Dr. Samer Adeeb, my supervisor, for his warm greetings, nice attitude, excellent and accurate guidance, encouragement, and for providing me with an absolutely stress-free atmosphere for doing research. I also need to thank him for encouraging me to study some pure mathematics which helped me to modify my logical thinking and argumentation.

Next, my gratitude goes out to my co-supervisors Dr. Marwan El-Rich and Dr. Tarek El-Bialy for guiding me through some parts of my research, providing me with constructive comments and patiently answering my questions.

The precious experimental part of this research would not have been possible without the laboratory facilities provided by Dr. Lawrence Le. I am indebted to him for his kind supports.

I would like to thank Dr. Saleh Al-Daghreer for commenting on parts of this thesis and providing me with guidelines, data and references needed for some parts of my research.

Special thanks must also be made to Dr. Amir Alizad for patiently answering my questions regarding signal-processing concepts partially used in this research.

I take this opportunity to express gratitude to all of my friends, especially our neighbor Majid Raghami, with whom I have spent hours of joy and happiness. I am also profoundly thankful to my Judo instructors Mr. Kelly Palmer and Mr. Gordon Okamura for their friendly greetings and dedication of time to teach me Judo.

I gratefully acknowledge the financial support I received from my supervisor and co-supervisors, Faculty of Graduate Study and Research (FGSR), and Graduate Student Association (GSA). Additionally, the Natural Sciences and Engineering Research Council of Canada (NSERC) provided partial funding for this project.

Table of Contents

List of Tables

List of Figures

Chapter 1

Introduction

1.1 Scope of dissertation

Ultrasonic waves are sound waves with frequencies beyond the limit of human hearing. These waves have shown to be useful in many diagnostic and therapeutic medical field applications. Ultrasonic waves and biological tissues have mutual effect on each other when ultrasonic waves propagate inside the tissues. The effects of biological tissues on ultrasonic waves are useful in the field of diagnostic ultrasound as these effects can be correlated with the structural properties of the tissue. In contrast, therapeutic ultrasound utilizes some therapeutic effects caused by the ultrasonic waves propagating in biological tissues. In both applications, it is vital to study the physics of ultrasonic propagation in the tissues. In the present dissertation, one particular case from each of the diagnostic and therapeutic applications of ultrasound was studied. Quantitative ultrasound (QUS) for bone assessment and the application of low intensity pulsed ultrasound (LIPUS) for the treatment of orthodontically induced inflammatory root resorption (OIIRR) were the cases from the diagnostic and therapeutic ultrasound respectively.

1.1.1 QUS for bone assessment

Quantitative ultrasound (QUS) for bone assessment is the application of ultrasonic waves by which osteoporosis is intended to be diagnosed and monitored. Since osteoporosis mainly occurs in the sites of cancellous bone, the health status of cancellous bone at different locations of the human body can be investigated by QUS. The status of cancellous bone depends on the physical (bulk density, porosity), mechanical (modulus of elasticity, ultimate strength) and micro-architectural (trabecular structures) properties of the bone. Based on the QUS methods, these properties can be potentially estimated through correlation with QUS parameters such as the speed of sound and ultrasonic attenuation in cancellous bone.

Although QUS for bone assessment has extensively attained its clinical applications, it still has more potential capabilities towards diagnosing and monitoring osteoporosis. So far, the clinical applications of QUS is only concerned with calculating the amount of cancellous bone (physical properties) revealed by QUS; however, it is experimentally demonstrated that QUS parameters also contain significant information about microarchitecture and material (tissue) properties (physical and mechanical) of the bone. Since QUS is safe, less expensive, faster, simpler and portable compared to the conventional X-Ray based methods of diagnosing osteoporosis, further development of QUS towards taking the advantage of these potential

capabilities is beneficial. However, further development of QUS for bone assessment might not be feasible unless these potential capabilities of QUS become practical. In this regards, the physics of the interaction of ultrasonic waves with cancellous bone structure should be fully understood

To comprehend the physics of ultrasonic propagation in cancellous bone, numerical simulations in addition to experimental methods have been utilized by previous researchers. One of the approaches in numerical simulation of ultrasound propagation in cancellous bone is to explicitly model the heterogeneous, anisotropic and porous medium of cancellous bone. In this approach, the complex fluid-saturated microarchitecture of a piece of cancellous bone is explicitly modeled and the computational medium serves a domain for solving the ultrasonic wave equations. The wave equations are then numerically solved using the finite-difference time-domain (FDTD) method. Since this method includes the explicit geometry of the microarchitecture of cancellous bone, it is referred to as micro-scale modeling.

Although the FDTD has demonstrated its capabilities in micro-scale modeling of ultrasound propagation in cancellous bone, there are still notable discrepancies between the simulated results and experimental measurements. One source of discrepancy is believed to be the concerns with the simulation method, i.e. FDTD. Specifically, the FDTD method uses Cartesian grids to sample the microarchitecture of cancellous bone. Cartesian grids lead to non-smooth staircase sampling of the geometry and subsequent generation of wave artifacts during the simulation. Moreover, the material discontinuity (bone and saturating fluid) and the interfacial interaction at the solid-fluid interface cannot be explicitly satisfied by FDTD schemes. This also adds to the observed discrepancies between the FDTD simulations and experiments. To eliminate these source of discrepancies from the simulation towards more accurate simulated results, the standard Galerkin finite element method (FEM) as an alternative to the FDTD method was proposed in the present thesis.

The organization of the thesis in order to introducing the FEM as an alternative method of simulating QUS for bone assessment is as follows:

In **Chapter 1**, a brief introduction to the demand for more accurate method of numerical simulation of QUS for bone assessment was presented. The hypothesis, objectives and specific aims towards using the FEM as an alternative to the conventional FDTD method for simulating

QUS for bone assessment will be described later in this chapter.

Ultrasound and the concept of QUS for bone assessment are covered in **Chapter 2**. The chapter also includes the derivation of ultrasonic wave equation, closed form solutions of the equations and the finite element formulation of ultrasonic wave propagation in solid and fluid media along with their interaction conditions. Moreover, some concepts such as wave propagation phenomena (reflection, refraction and scattering), ultrasonic energy and intensity, ultrasonic attenuation and ultrasonic beams are explained in this chapter. Having the knowledge of these concepts are necessary to understand the physics of ultrasound propagation in any medium.

The applications of the FEM in this thesis were by utilizing a commercial software package (ABAQUS). Therefore, it was necessary to ascertain the accuracy of the software package for numerical simulation of ultrasound propagation in solids and fluids. In this regard, C**hapter 3** was devoted to investigate the appropriate finite element size leading to acceptable simulation accuracy through comparing finite element simulation results with analytical results.

Chapter 4 commences with a literature review on the different methods of studying the physics of ultrasonic propagation in cancellous bone. It continues with reviewing the micro-scale modeling using the FDTD method and its source of numerical errors. The FEM is then proposed as a method with mitigated source of numerical errors associated with the FDTD method. In this regard, a procedure of creating micro-scale finite element models for ultrasound propagation in cancellous bone is explained in this chapter. To demonstrate that micro-scale modeling using the FEM method is capable of simulating QUS for bone assessment, ultrasound propagation in computational (virtual) samples of human wrist cancellous bone was simulated. The simulated results indicated that the finite element simulations were capable of simulating QUS and the results distinguished between healthy and osteoporotic bone samples. Moreover, the simulated results are compared with the results from other available experimental and simulation studies for quantitative and qualitative evaluation purposes.

Although the capabilities of the micro-scale modeling using the FEM regarding the simulation of QUS for bone assessment were demonstrated in chapter 4, the results were not directly verified using corresponding experimental results. To this end, **Chapter 5** is dedicated to performing a set of QUS experiments and corresponding simulations involving ultrasound

propagation in cancellous bone-mimicking phantoms. The results clearly demonstrated and verified the accuracy of the FEM for simulating QUS.

In the final chapter of the thesis, **Chapter 8**, the achievements, advantages and disadvantages of using the FEM for simulating QUS for bone assessment were presented. The chapter also includes suggested future works based on the proposed finite element models for simulating QUS.

1.1.2 LIPUS for the treatment of OIIRR

Orthodontically inflammatory induced root resorption is a condition where the tooth loses substances from its root. One of the common circumstances in which root resorption occurs is during orthodontic movement (treatment) of teeth. The resorption may lead to in-place instability (mobility) of the tooth and consequently affect the result of a successful orthodontic treatment. So far, there is currently no clinically acceptable treatment method. However, few pioneering studies have hypothesized that low intensity pulsed ultrasound (LIPUS) have stimulatory effect on dental tissue regeneration acting towards the prevention and repair of OIIRR. Although the validity of the hypothesis have been demonstrated by experiments, the mechanisms by which LIPUS stimulates dental tissue repair have not yet been fully explored. Indeed, elucidating and understanding the stimulatory mechanisms have significant roles in the development of the proposed treatment method. It has been recognized that stimulatory effects of LIPUS are non-thermal, dose-dependent and originates from the mechanical stresses (or their mechanical energy) induced by the ultrasound. This implies that investigating the value and distribution of the mechanical stresses on the root surface and their correlation with the amount of dental tissue repair (cementum) may lead to clarification of the stimulatory mechanisms.

In this thesis, the LIPUS-induced mechanical stresses in dental tissues are explored using computer simulation. Due to the geometrical complexity of the material layers of a tooth and its surrounding, the finite element method was utilized. The simulating ultrasound propagation in dental tissues and investigating possible correlations between LIPUS-induced mechanical stresses and the amount of dental tissue regeneration is presented in this thesis as follows:

Chapter 1 contains a brief introduction to OIIRR, its proposed treatment by LIPUS and the significance of investigating the stimulatory mechanisms of the ultrasound for the treatment of OIIRR. The hypothesis and objectives towards using FEM simulations to investigate the

ultrasonic-induced mechanical stress in dental tissues and their correlation with the amount of dental tissue regeneration are indicated later in this chapter.

Chapter 2 contains full description of OIIRR and a literature review on its proposed treatment by LIPUS. Additionally, ultrasonic wave equations and finite element formulations for simulation of ultrasound propagation in solid and fluid media (required for investigating wave propagation in dental tissues) are explained in this chapter.

The investigation of the stimulatory effect of LIPUS-induced mechanical stresses on regeneration of cementum (dental tissue) is presented in **Chapter 6**. In this chapter, the finite element method was utilized to simulate a previously published experiment of ultrasonic wave propagation in the dentoalveolar structure (tooth and its surrounding tissues) of beagle dogs. In this regards, qualitative and quantitative relations between the amount of the regenerated cementum in the experiment and the ultrasonic stresses (and energy) were obtained.

In chapter 6, the propagation of ultrasonic waves in the dentoalveolar structure (tooth and its surrounding tissues) of a beagle dog was simulated. One future work in the direction of this study will be studying the LIPUS-induced stresses in human dental tissues. The main modeling concern with finite element modeling of human dentoalveolar structure is that the structure contains a large portion of cancellous bone. This is in contrast with the dentoalveolar structure of a beagle dog which is mainly composed of cortical bone. In a finite element modeling procedure, cortical bone can be assumed and modeled as a homogeneous and isotropic solid material. On the other hand, cancellous bone is composed of fluid-saturated microstructures and consequently cannot be simply assumed as a homogeneous and isotropic material. As will be demonstrated in chapters 4 and 5, the heterogeneous and anisotropic medium of cancellous bone significantly affects the velocity and energy of ultrasonic waves. Moreover, micro-scale finite element modeling of the large amount of cancellous bone existing in human dentoalveolar structure is not practical (discussed in chapter 4). To propose a solution for considering the material properties of cancellous bone in a finite element model, **Chapter 7** is dedicated to establishing an equivalent material model (EMM). Although homogeneous and isotropic, an EMM for cancellous bone is a material that is intended to affect ultrasonic waves as cancellous bone does.

Finally, **Chapter 8** summarises the achievements of investigating ultrasonic propagation in dentoalveolar structure by finite element simulation towards exploring the stimulatory

mechanisms of LIPUS. Moreover, future works related to the proposed finite element simulations and the equivalent material model are addressed.

1.2 Hypotheses and objectives

Investigating QUS for bone assessment using finite element simulations was based on the following hypothesis and objectives:

Hypothesis: The standard Galerkin finite element method (FEM) can effectively be implemented as an alternative to FDTD method for micro-scale modeling of ultrasound propagation in cancellous bone (Chapter 4 and 5).

Objective 1: To introduce the finite element method and the required modeling procedure as a new approach for micro-scale modeling of ultrasound propagating in cancellous bone (Chapter 4).

- Specific aim 1: Creating a finite element model in micro-scale that can simulate an immersion through-transmission experiment associated with QUS for bone assessment.
- Specific aim 2: Simulating ultrasonic (QUS) parameters of healthy and osteoporotic bones for comparison purposes.

Objective 2: To validate the results of the finite element simulation of ultrasound propagation in micro-scale models using relevant experimental results (Chapter 5).

- Specific aim 1: Performing QUS experiments (immersion through-transmission experiments) on cancellous bone phantoms.
- Specific aim 2: Simulating the QUS experiments by the finite element method and comparing the simulated results with the experimental outcomes (frequency-dependent ultrasonic attenuation) for accuracy validation purposes.

The following hypothesis and objectives were considered for the investigation of stimulatory mechanisms of LIPUS regarding the treatment of OIIRR.

Hypothesis: Known as one of the stimulatory mechanisms that triggers the regeneration of dental cementum, LIPUS-induced mechanical stresses (and energy) can be predicted by finite element simulations. Moreover, correlations between the simulated stresses (and energy) and the

amount of biological regenerated cementum can be observed.

Objective 1: To create a finite element model capable of simulating LIPUS propagation in dentoalveolar structures (Chapter 6).

- Specific aim 1: Performing digital reconstruction of the dentoalveolar structure of a beagle dog for the finite element model.
- Specific aim 2: Validating the finite element results through ultrasonic measurements.

Objective 2: To investigate the possible correlations between mechanical stresses (and energy) and cementum regeneration in order to elucidate the stimulatory mechanisms of LIPUS (Chapter 6).

- Specific aim: Retrieving cementum thickness data from the available histological study on control and LIPUS-treated teeth of beagle dogs.

Chapter 2

Background

2.1 Ultrasound

Acoustic (sound) waves with frequencies beyond the limit of human hearing (20 kHz) are categorized as ultrasound. Ultrasonic waves, unlike electromagnetic waves, need a substantial medium to propagate. This makes a strong connection between ultrasound and its medium of propagation leading to a broad field of applications. Underwater acoustics (SONAR), industrial ultrasound, sonochemistry, non-destructive testing/evaluation (NDT/NDE), ultrasound for material characterization, and medical ultrasound are among the most widely known fields of ultrasound applications.

The "heart" of ultrasonic applications is a transducer. A transducer is a device for generating and sensing ultrasonic waves through electromechanical conversion [1]. The electromechanical conversion, conversion between mechanical force and electrical current in either way, occurs in piezoelectric materials. Lead zirconate (PZT) ceramic and Polyvinylidene fluoride (PVDF) are the most utilized materials in many transducers.

Piezoelectric materials generate electricity when deformed under mechanical stress (direct piezoelectricity) and go under deformations when exposed to an electric field (converse piezoelectricity). Piezoelectricity in a material is a bridge between the mechanical and electrical behaviours of the material. This property is originated from the realignment of the internal dipole (a pair of ions with opposite electric charges in the material) structure in a piezoelectric material under mechanical stress or electric fields. Realignment of dipoles accumulates of different electric charges (positive and negative) on opposite surfaces of the material [2].

A transducer can take the advantage of both converse and direct piezoelectric effect. A transducer generates mechanical vibrations (ultrasound) in its surrounding medium when driven by a voltage. Moreover, a transducer can act as a receiver when it converts the vibrations of its surface (caused by ultrasonic waves in the medium) to voltage.

2.2 Medical application of ultrasound

The application of ultrasound in medicine is divided into two branches: diagnostic and therapeutic fields [3]. Ultrasound imaging (ultrasonography) and quantitative ultrasound for bone assessment are two major instances of diagnostic ultrasound. The application of ultrasound in surgical devices, sport medicine and physiotherapy, chemotherapy, drug delivery, acolysis

system (a system to dissolve clots in occluded blood vessels), lithotripsy (using ultrasonic shock waves to disintegrate kidney stones) and lipolysis falls under therapeutic ultrasound. In the following sections, the instances of diagnostic and therapeutic ultrasound related to this thesis are introduced.

2.2.1 Quantitative ultrasound for bone assessment

Osteoporosis, one of the most common skeletal diseases, is characterized by bone mass reduction and microstructural deterioration leading to negative modification of cortical and cancellous bones. This disease is a systemic disorder caused by biochemical and hormonal processes resulting in an imbalance between the resorption (by osteoblasts) and deposition (by osteoclasts) of new bone tissue. The consequence of osteoporosis is clinically evident in the form of bone fractures of the wrist, spine, and hip, mostly occurring to female subjects over the age of 50 [4]. According to the public health agency of Canada 1.5 million Canadians over 40 years of age have been reported with osteoporosis diagnosis. Osteoporosis affects both men and women; however, women have been reported to suffer from osteoporosis more than men do. Bone fracture due to the disease affects 1 in 6 Canadian women over the age of 50. The overall yearly financial burden imposed on the Canadian healthcare system for treating osteoporosis and the related clinical consequences was over $2.3 billion in 2010 [5–7]. Osteoporosis, known as the "silent disease", has no symptoms until the subject suffers a fracture. Therefore evaluating the risk of osteoporosis before resultant bone fractures is vital. Obviously the early detection of the disease will help the efficiency of the preventive treatments [4,8].

Osteoporosis predominantly occurs at the cancellous bone regions [9]. Known also as trabecular bone, cancellous bone consists of a porous interconnected network of rod- and plate-like structures (trabeculae) in-filled by a fluid-like soft tissue, namely bone marrow (Figure 2.1). This type of bone having a role of shock absorber comprises 20% of the human skeleton. Regions near the joint surfaces of long bones, core of the spine vertebral bones, hip region, ribs, skull and calcaneus consist of cancellous bone.

The risk of osteoporosis is clinically assessed via cancellous bone mineral density (BMD)[1] measurements [9]. Quantitative limits for BMD proposed by the World Health Organization (WHO) have been used since 1994 [10]. The four following non-invasive methods

[1] BMD is a measure of the amount of minerals (mainly calcium and phosphorous) in grams per cubic centimeter of bone.

have been used to perform osteoporosis risk assessment [8,11]:

- Quantitative computed tomography (QCT) that measures bone density in the lumbar region of the vertebral column.
- Single photon absorptiometry (SPA); distal radius, phalanges and calcaneus are the region in focus in this method.
- Dual energy X-ray absorptiometry (DEXA or DXA) known as the gold standard, measures the density in the lower spine and hip regions (Figure 2.2).
- Quantitative ultrasound (QUS) that uses the ultrasonic parameters for bone assessment (Figure 2.2).

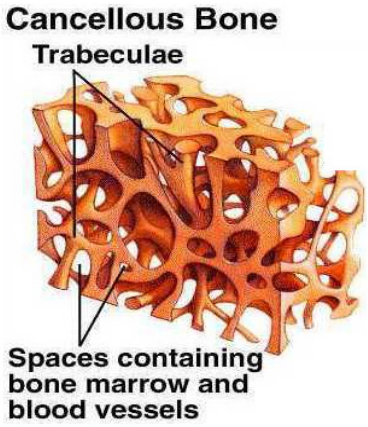

Figure 2.1 Cancellous bone [12]

Figure 2.2 Left: DXA machine, right: QUS devive (Sonost3000) for assessing fracture risk by examining the calcaneus site [13].

The first three methods, QCT, SPA and DXA, are based on the attenuation of ionizing radiation and have been developed and utilized over the last 40 years[2] [11]. However, there are disadvantages accompanying these methods. In terms of systems, DXA and QCT apparatuses are

[2] It was indicated as "in the last 25 years" in [11] published in 1997

bulky, relatively expensive and only available in large general and teaching hospitals. Also the patients are exposed to a level of radiation dose making these methods unsuitable for routine assessments [9]. In addition to their application disadvantages, clinical studies indicate that the BMD measured by these radiation-based methods has not provided sufficient information for reliable diagnoses in all cases. For instance, considerable overlap in BMD measurements of healthy and osteoporotic bones using DXA method was reported [14].

The BMD index describes bone strength, however only 70-75% of the variance in the strength is a function of BMD. Other factors such as bone microstructures and trabecular architecture are also effective in bone strength. The mechanical properties of cancellous bone depend on both the density and trabecular microstructures [9,11]; such that the trabecular microstructures influence the mechanical properties by their micro architecture and material properties i.e. elasticity. Therefore, even if these methods were perfectly accurate in measuring the index, considering only BMD would not be sufficient to assess osteoporosis [15,16].

On the other hand, bone assessment through quantitative ultrasound is nonionizing, less expensive, portable, faster, simpler, and easier to implement. QUS has been developed, documented and clinically used in the past few decades [17]. It has demonstrated to be a strong tool for diagnosis of the disease [11,15,16]. The capability of QUS has been shown through prospective studies predicting the risk of fracture of the proximal femur, the vertebrae and hip [18]. Favorable results have been reported regarding diagnosis and investigating osteoporosis by researchers. These results were encouraging enough to the manufactures to release a great variety of commercial devices for bone assessment by QUS over the past two decades [11,19].

2.2.1.1 Broadband ultrasound parameters and material properties of cancellous bone

A broadband ultrasound refers to a short ultrasonic pressure signal[3] containing a range of desired frequencies. For instance, the following equation represents Gaussian sinusoidal signals used in QUS as instances of broadband ultrasound:

$$P(t) = e^{-\left(\frac{t-\mathrm{D}/2}{a}\right)^2} Cos(2\pi f_0(\mathrm{t} - \mathrm{D}/2)) \qquad (2.1)$$

such that $P(t)$ is the ultrasonic signal as a function of time, $a = \sqrt{2}\sigma$ in which σ is the standard

[3] Ultrasonic signal physically refers to ultrasonic pressure signal. Ultrasonic pressure is converted to voltage when received by a receiving transducer. Therefore, ultrasonic signals (or waves) are usually expressed in their voltage form when measured.

deviation of the Gaussian distribution of the pulse envelop, f_0 is the signal center frequency in and D is equal to the duration of the signal. Figure 2.3 shows an example of an ultrasonic broadband signal and its frequency content (obtained by Fourier transform). The frequency range of 0.1-1 MHz is reported to be the most useful for bone assessment [20]. Frequency bandwidth is also extended to more than 2 MHz in some research studies [17,18].

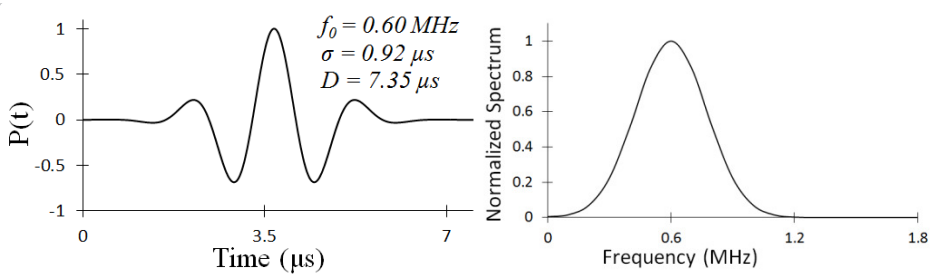

Figure 2.3 An example of a broadband signal and its frequency content.

QUS is based on the fact that ultrasonic waves are affected by the material in which they are propagating. In the case of cancellous bone, material properties of bone (mechanical properties, density and inner architecture) affect ultrasonic waves. The health status of a cancellous bone i.e. healthy or osteoporotic is then directly related to the bone material properties.

In QUS method, the material properties of cancellous bone are sought by transmitting a broadband ultrasonic pressure signal through cancellous bone. The ultrasound transmission can be in-vitro or in-vivo. In an in-vitro transmission, a piece of saw-cut cubic or drilled cylindrical cancellous bone is defatted and the pores are re-saturated with water. Then the specimen is submerged in a water tank and placed between two coaxially located ultrasonic transducers already located in the tank (Figure 2.4a). In this manner, one of the transducers generates a broadband ultrasonic signal and the other one receives the signal after propagation in the specimen [9,15].

On the other hand, a broadband ultrasonic signal is transmitted into a human (or animal) limb in the case of in-vivo QUS. The most common limb in this method is the calcaneus of human heel. Both the coaxially located transducers and the limb (located between the transducers) are submerged in a water bath (immersion coupling method as shown in (Figure 2.4b) or the transducers are directly attached to the limb by ultrasound conductive gel (contact coupling method) [20].

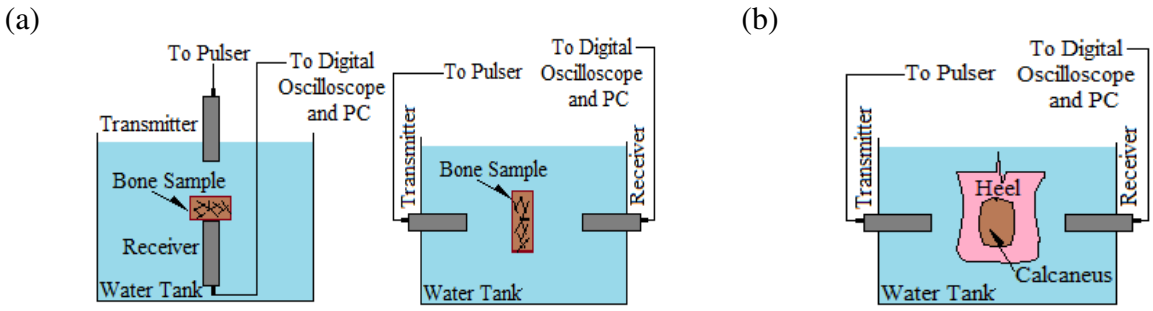

Figure 2.4 (a) Reproduced figures of experimental setups for in-vitro QUS [15,21], (b) reproduced figure of in-vivo QUS setup on calcaneus of human heel [22].

Receiving the broadband signal by the receiving transducer is followed by measuring two common ultrasonic parameters: ultrasound velocity or speed of sound (SOS) and broadband ultrasound attenuation (BUA) [8,18,23]. It is worth mentioning that the ultrasonic parameters (SOS and BUA) depend on both the material and structural (micro-architecture) properties of cancellous bone, whereas, X-ray methods (like DXA) does not reflect information about the structural properties of the bone (fundamentally because X-ray attenuates at atomic level but ultrasound attenuation and speed depend on the bulk material and structural properties) [9]. The ultrasonic parameters and their relation with the material properties of cancellous bone are described as following:

SOS and material properties of cancellous bone:

The application of ultrasound velocity (SOS) for assessment of material properties of bone commenced in 1958 [24]. In this regard, stiffness (Young's modulus), strength and bulk density of cancellous bone are intended to be related to the velocity of a broadband signal (SOS) propagating in the heterogeneous and porous medium of cancellous bone [9,20,25].

Calculating SOS through measurements is performed by dividing the propagation distance by the time delay of the signal. The propagation distance can be regarded as either the specimen thickness or the distance between the transducers in the case of in-vitro QUS. For in-vivo practice of QUS, the propagation distance is considered as the limb thickness (the thickness of heel) [16].

Time delay of the signal is determined by measuring the time of flight (TOF) of different reference points marked on the transmitted signal. The earliest detectable deviation from temporal base-line, the zero-crossing points, maximal peak or other amplitude points [9,25,26] have been used as reference points to calculate TOF (Figure 2.5).

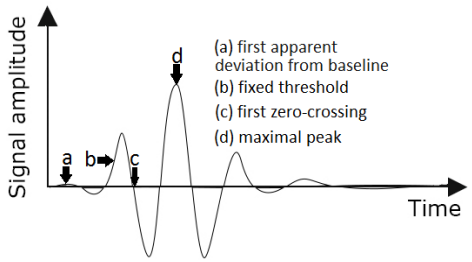

Figure 2.5 Different reference points for measuring TOF

Determining the signal arrival time using different reference points significantly affect the calculated SOS [9]. There are two reasons that can explain the difference in SOS values obtained by using different reference point for calculating TOF. First, the shape of the signal is distorted while propagating into the cancellous bone [9]. Therefore, the time delay between the reference point on the original and the propagated signals may differ leading to dissimilar TOFs. The distortion is due to the medium dispersive property (dependency of wave velocity on its frequency) and the frequency-dependent attenuation of the signal. The second reason is the existence of fast and slow waves in medium affecting the received signal.

The fast and slow waves are two longitudinal waves with different velocities generated while wave propagation in a fluid-saturated porous media. The fast wave makes the solid and the liquid particles vibrate in phase (both phases compress or expand at the same time), whereas the slow wave leads to antiphase vibrations of solid and fluid portions (one phase compresses while the other expands). The origin of those separated waves is the relatively faster and slower waves propagating through the solid and fluid phases [17,23,26,27] . Figure 2.6 depicts the effect of the existence of fast and slow waves on an ultrasonic broadband signal received after propagation in cancellous bone during an in-vitro QUS experiment. The dotted-line signal in the figure shows a typical received signal in the in-vitro experiment (Figure 2.4a) if the bone specimen is omitted and ultrasonic waves are propagating in water between the transducers.

The arrival time of the fast wave is associated with the reference points at the beginning of the signal (like the earliest detectable deviation from base-line and first zero-crossing point). On the other hand, the slow wave arrival time is more related to the reference point in the middle of the signal like the maximal peak. However, in mixed-mode conditions in which the fast and slow waves are not detectably separated the reference points cannot be certainly associated with any of the fast or slow wave (Figure 2.6) [28].

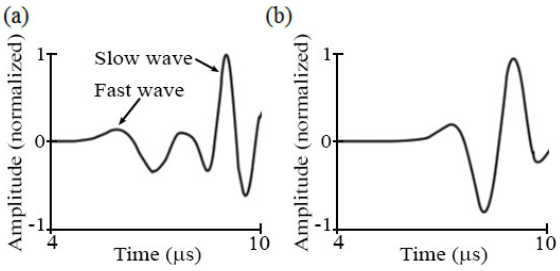

Figure 2.6 (a) Arrivals of fast and slow waves in an ultrasonic broadband signal, (b) overlapping of fast and slow waves in a mixed-mode condition [28] (Figures are reproduced).

BUA and material properties of cancellous bone:

A broadband ultrasonic signal propagating inside cancellous bone weakens due to attenuation. The attenuation of a broadband signal is expressed by the frequency-dependent attenuation coefficient $\alpha(f)$ measured in dB (decibel) for a particular bone [20] .

Generally, the attenuation coefficient is a nonlinear function of frequency content of the transmitted broadband signal (Figure 2.7); however, it can be linearly approximated for a desired frequency bandwidth. According to Langton et al (1984), the slope of the linear regression of the frequency-dependent attenuation over a frequency bandwidth is defined as the broadband ultrasound attenuation [22]. Therefore, BUA is mathematically given by [20]:

$$\alpha(f) = \alpha_0 + BUA \times f \qquad (2.2)$$

where BUA has the unit of dB/MHz provided that f is expressed in MHz. Alternatively, BUA can be normalized by the length of the cancellous bone and denoted by nBUA with the unit of dB/(MHz. cm). Commonly, in-vivo and in-vitro studies report BUA and nBUA respectively [9].

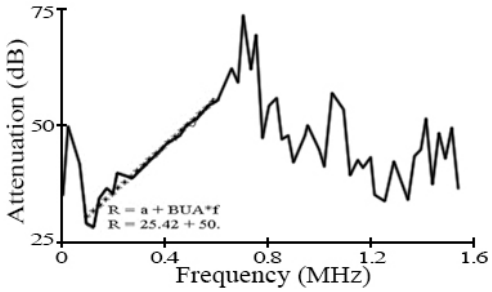

Figure 2.7 Frequency-dependent attenuation coefficient $\alpha(f)$ plotted versus frequencies and the associated BUA [8] (Figure is reproduced).

In bone assessment using QUS, linear dependency of attenuation on frequency in the range of 0.2-1 MHz have been reported by many studies [19]. This range, however, is limited to 0.2-0.6 MHz in clinical practice.

2.2.1.2 In-Vitro and in-vivo studies

The main clinical aims of QUS in bone assessment and osteoporosis diagnosis is to develop a tool for reliable diagnosis of osteoporosis, identification of subjects with high fracture risk and sensitive monitoring of skeletal changes overtime [29]. To achieve these goals, many in-vitro and in-vivo studies have been done over the past 40 years.

A. In-vitro studies

In-vitro QUS study is via experimental approaches devised to find the relationships between ultrasonic parameters and mechanical and physical properties of cancellous bone samples.

Strong positive linear dependencies between SOS and bulk density of cancellous bone samples have been reported [21,30]. Moreover, the relation between SOS and ultimate strength of the bone samples are found to be positively linear [21,25]. However, SOS is found to be linearly correlated (positive slope) with the square root of the Young's modulus of bone samples [31]. Also direct linear relationships between logarithm of SOS and Young's modulus of the bone samples has been reported [32].

The relationship between BUA and bone properties has also been widely investigated since 1984. The relationship between BUA and bone density has been reported to be approximately linear. Generally, positive slopes of BUA (or nBUA) versus bulk density have been reported [20]. However, negative regression slopes and non-linear behavior of BUA as a function of density have also been reported [9,21,30]. These behaviors have been observed for large density ranges; and it is believed that they are caused by the relative role of absorption and scattering in those density ranges [20]. Another determining factor in the BUA-density relation is the signal center frequency. It has been observed that the slope of BUA-density relationship varies with the center frequency of the signals transmitted through the same specimens [19].

BUA has been shown to have the ability of predicting Young's modulus and the maximum strength of cancellous bone. This ability adds to the predictive power of QUS. Strong linear correlations have been found between BUA and ultimate strength of bone. Furthermore, BUA and square root of Young's modulus of cancellous bone are observed to be linearly related with positive slope [20,31,33].

B. In-vivo studies

Through in-vivo studies, detection of osteoporosis, assessment of fracture risk, and skeletal monitoring are intended via measuring ultrasonic parameters (SOS, BUA) at the bones of peripheral regions. Calcaneus, phalanges, tibia, patella and distal radius are the bones that have been assessed using QUS [16,29]. It has been clinically observed (and investigated by in-vitro studies) that osteoporotic bones are associated with less SOS and BUA compared to healthy bones [29]. Figure 2.8 schematically shows general BUA values expected for subjects with and without osteoporosis.

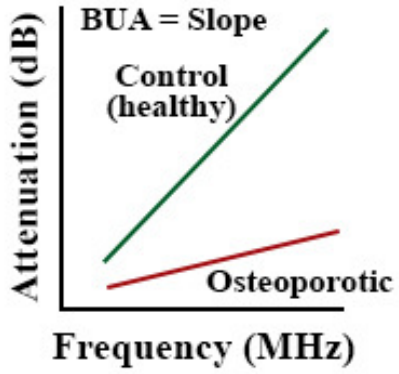

Figure 2.8 The qualitative demonstration of recognition between healthy (control) and osteoporotic bones using BUA [16] (Figure is reproduced).

In clinical practice, in-vivo data of QUS are intended to be correlated with BMD data, fracture risk data, and the disease reports from populations with and without osteoporosis. For the first time, Langton *et al*. showed the relationship between BUA measured at the calcaneus of females with fractured femoral necks and healthy females. Their in-vivo study was performed on 60 female volunteer subjects [22]. The QUS results of their study are illustrated in Figure 2.9.

Correlation of QUS measurements with BMD data depends on the site and method of the BMD measurements in addition to the population under study. It has been reported that the correlation between QUS parameters (SOS, BUA) and BMD is modest and QUS is not a general and direct representative of BMD [20,29]. Reference [29] provides a comprehensive study on correlations between QUS and BMD measurements. Unlike the reported poor correlations for QUS-BMD relationship, significant associations between QUS parameters and osteoporotic fracture risk have been observed. Predictions of osteoporotic fracture risk by QUS can be as reliable as predictions by other bone assessment methods like DXA known as gold standard [18].

In this regard, the privilege of QUS over DXA is that a prediction of fracture risk using QUS does not need any BMD measurement.

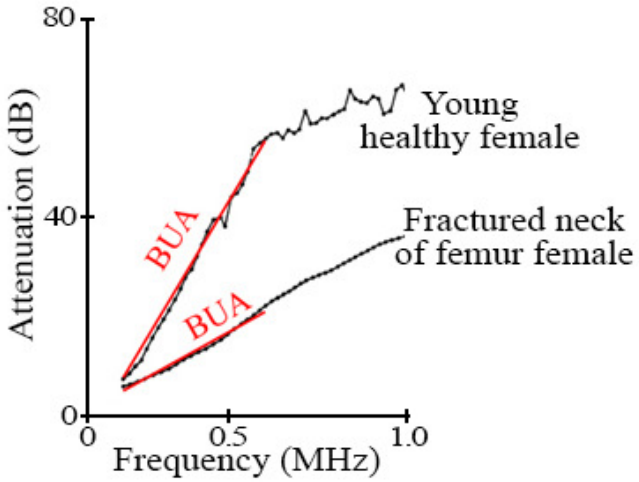

Figure 2.9 The QUS result showing the difference in frequency-dependent attenuation values measured at the calcaneus of two different female populations (healthy and with fractured femoral necks) [22] (Figure is reproduced). Linear relationship between attenuation versus frequency in the clinical range (0.2-0.6MHz) is apparent. Also the results predicted smaller BUA for subjects with osteoporotic in their femoral neck.

2.2.1.3 Commercial QUS Systems and sources of error

The production of commercial QUS systems for bone assessment was initiated in 90s. The first commercial system, Walker Sonix UBA575, was originated from the prototype instrument which was developed based on the initial work of Langton *et al* [22]. Currently there are more than 15 commercial QUS systems which measure SOS or/and BUA at various anatomical sites [9]. Most of the devices measure the parameters at the calcaneus since the calcaneus is about 90% cancellous bone and is well accessible. Additionally, it has been reported that the calcaneus reflects the mechanical environment conditions experienced by proximal femur and spine [20]. Some of those devices measuring the QUS parameters at the calcaneus are listed in Table 2.1.

Table 2.1 QUS systems applying at the calcaneus [9]

system	BUA	SOS	Coupling
Walker Sonic UBA 575+	Y	Bone, TOF	Immersion
Lunar Achilles	Y	TOF	Immersion
McCue CubaClinical	Y	Heel	Contact
Hologic Sahara	Y	Heel	Contact
DMS UBIS3000	Y	Bone, Heel	Immersion
Osteoscan DTU-1	Y	Bone, Heel	Immersion

Most of the commercial QUS devices use the same fundamentals; they usually have two coaxially aligned transducers (transmitter and receiver) to perform the measurements using through-transmission technique (rather than pulse-echo method)[4]. The devices calculate the frequency spectrum of the bone signal and compare it to a pre-recorded reference signal spectrum to obtain BUA. However, differences between the devices result in discrepancies between their measurements and predictions. Some of the differences between the devices are as follow [9,20]:

- The coupling method: The coupling method of a device is the way by which the signal is transmitted from the device to the tissue. To achieve acoustical contact between the transducers and skin, "wet" (immersion) or "dry" (contact) methods or combinations of both are used by the devices. Wet methods use a water bath whereas dry methods take advantage of coupling gels or silicone pads.
- The diameter of transducers.
- Center frequency and frequency bandwidth.
- Method of measuring SOS (definition of SOS).
- The type of transducers: whether they focus the ultrasonic pressure onto a region of bone or they do not have focusing properties.

The QUS devices use the measured BUA and SOS and interpret them using their database to assess the bone condition. Some devices use the combination of BUA and SOS and calculate indices like "stiffness index" or "quantitative ultrasound index" for bone assessment [34]. Due to differences between QUS devices, assessing the same subject's bone on different devices is not recommended [20].

Bone internal changes due to osteoporosis or its treatment is relatively small; therefore, QUS devices must be used with care to monitor those internal variations. Misdiagnosis may happen even if there is a small percentage of error in BUA data. Since very precise measurements of BUA are needed for capturing changes in bone, quality analysis (QA) programs have been designed. Cancellous bone phantoms are provided by most manufacturers for QA

[4] The pulse-echo technique uses a single transducer used for transmitting and receiving ultrasonic pulses. Initially the transducer generates an ultrasonic broadband pulse (signal) which propagates towards the bone sample or limb then the same transducer receives the reflected and scattered waves back from the bone (echo). This technique is used for velocity measurements by some devices, but BUA is still measured by the through-transmission method.

purposes [20].

There are potential sources of error in the QUS parameters measured by the devices. Thickness of the soft tissues might be a source of error for SOS. Values of BUA are mostly affected by errors originated from diffraction, interface loses and phase cancellation. Diffraction may be a source of error in contact method coupling in which the transducer separation varies to accommodate different heel thicknesses (0.6 to 10 dB/MHz). Interface loses are due to the presence of cortical layer varying in thickness over the cancellous bone (up to 20 dB) [20].

In addition to the sources of error, there are factors affecting the precision of measurements, which are: immersion duration of foot in the water bath, water depth, water temperature, presence of detergents and rotations of the foot [16]. The rotation of the foot affects BUA since BUA depends on the structural configuration in the path of the ultrasonic waves.

2.2.1.4 Further studies on QUS for bone assessment

Further studies on QUS for bone assessment are still being performed to make it as a strong tool for diagnosing and monitoring osteoporosis. Some of the study topics on the QUS needed to improve the technique are:

- Assessing the relationship between QUS parameters (single or combined), BMD and mechanical properties of cancellous bone [11].
- Introducing new QUS parameters such as fast and slow waves velocities [23,26], backscattering coefficient [17], and using broader range of frequencies [11].
- Application of bone-mimicking phantoms for better understanding the mechanism involving attenuation [35] and calibration purposes [20].
- Assessment of the sources of error in QUS measurements [11].
- Universally accepted cross-calibration methods for QUS commercial devices and standardizing their measurements [11,20].
- Developing scanning systems for QUS measurements versus single-position systems [8].
- Exploring the physics of ultrasonic propagation in the fluid-saturated medium of cancellous bone by means of Biot's theory [36] and numerical simulations through finite difference methods [37–40].

2.2.2 Treatment of orthodontically-induced inflammatory root resorption by ultrasound

Previous studies have demonstrated stimulatory effect of ultrasound on dental tissue formation towards the treatment of orthodontically induced inflammatory root resorption (OIIRR). This section begins with a brief description of dentoalveolar structure anatomy and OIIRR. Then the section continues to introduce low-intensity pulsed ultrasound and its application for the treatment of OIIRR.

2.2.2.1 Anatomy of a dentoalveolar structure

Dentoalveolar structure refers to a tooth and its surrounding jaw bone. Literally, the word ‘dent’ means tooth and ‘alveolar’ appertains to an alveolus which means a socket or a tooth socket in particular.

To orient a dentoalveolar structure and its components, anatomical directions are needed. Considering the mouth and the jawbone the following anatomical terms are defined (Figure 2.10): distal (toward the back of the mouth), mesial (toward the front of the mouth), lingual (inside and toward the tongue), buccal (outside and toward the cheek). The root can also be divided in three equal parts along its height denoted as coronal, middle and apical levels.

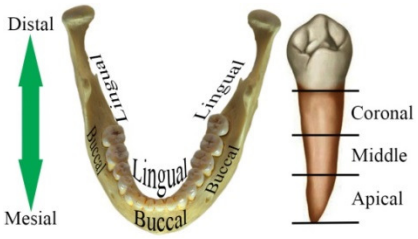

Figure 2.10 Dental anatomical directions [41] (Figure is modified).

A typical dentoalveolar structure majorly consists of jawbone, a tooth and covering tissue on its outside called gingiva (or gum). The tooth is composed of two main parts, the crown and the root (Figure 2.11). The crown, being the exposed part of a tooth, is covered by enamel that is the hardest material in the body. Enamel is brittle since it is almost entirely composed of calcium salts (calcium phosphate). Under enamel, there exists dentin, which is softer than enamel but harder than bone due to its material components i.e. apatite crystals of calcium and phosphate. Dentin continues to form the root while possessing most of the tooth bulk volume. Dentin encapsulates a central pulp cavity or pulp chamber filled with pulp as a mixture of nerves, blood

vessels and connective tissue [42].

The root, being the part of the tooth inside the jawbone, has three layers: dentin filling the core, cementum covering the dentin and the periodontal ligament (or membrane) attaching the cementum to the jawbone. Classified as connective tissue, cementum is a bone-like material that connects the periodontal ligament to the jawbone. The periodontal ligament (PDL) is fibrous connective tissue containing neural and vascular components. PDL supports the tooth in its alveolus and acts as a shock-absorbent material placed between the tooth and jawbone. Additionally, PDL has a remodeling function by continually forming and resorbing cells, a sensory function due to its nerve network, and a nutritive function for its various cells by means of its blood vessels [42].

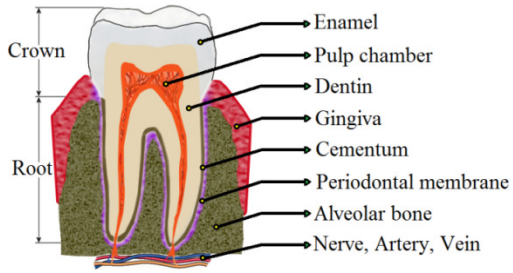

Figure 2.11 Dentoalveolar structure of a typical tooth.

2.2.2.2 Orthodontically-induced inflammatory root resorption (OIIRR)

Being almost the first organs in the human digestive system, teeth play a direct role in maintaining one's quality of life and general health. To properly serve the digestive system, a tooth must withstand occlusal forces. This indicates that a tooth needs to be firmly founded by its root(s) into the alveolar bone (Figure 2.11). Therefore, any damage or trauma to the root adversely influences the functionality of the tooth.

Root resorption, also known as tooth resorption, is one of the incidents leading to root destruction. During the resorption, the tooth loses substances from its cementum and dentin leading to in-place instability (mobility) of the tooth [43–46]. Figure 2.12 depicts severe root resorption that occurred on the roots of the lower and upper central incisors.

One of the circumstances in which root resorption occurs is during orthodontic movement of tooth. The evidence of root resorption due to orthodontic tooth movement has been known since reported in 1927 by Ketcham [46]. This kind of resorption (Figure 2.12), occurred by virtue

of orthodontic treatment, is called orthodontically induced inflammatory root resorption (OIIRR). Undesirably, OIIRR is an inevitable iatrogenic consequence of orthodontic treatment [44–46].

Figure 2.12 severe root resorption occurred on the roots of the lower and upper central incisors (Figure is obtained from Dr. El-Bialy's research laboratory and used with permission).

The mechanism through which the OIIRR occurs has not been completely investigated [47]. One of the hypotheses partly relates the mechanism to the removal of hyalinized zones as follows. Orthodontic forces make the periodontal ligament highly compressed leading to formation of areas of local inflammation and sterile (aseptic) necrosis (histologically called hyalinization). The hyalinized areas of the periodontal ligament begin to be removed by the cells and blood vessels from the adjacent undamaged tissue. Elimination of the hyalinised portions of the ligament also results in the adjacent alveolar bone resorption allowing the tooth to orthodontically move [44,45,47]. However, beside this desirable effect, there is a side effect. It has been hypothesized that the cellular activity associated with the removal of the hyalinized area of the ligament, also damages the external surface of the tooth root [47,48]. The damage appearing as resorption on the external surface of the root has three degrees of severity [47]: (1) Surface or cementum resorption; (2) Deep or dentin resorption; (3) Root shortening or apical root resorption. Unlike cementum resorption which is reversible, dentine and apical root resorption are not reversible or reparable by the body.

It is frequent that patients undergoing orthodontic treatment suffer some unpredictable degree of the resorption [45,48]. Reportedly, clinically important root resorption is observed in 16.5% of patients [45]. In addition, 1-5% of patients are observed to have severe root resorption [45,47,48]. OIIRR affects the outcome of orthodontic treatments when the resultant root resorption is severe. The severity of the OIIRR cannot be detected in patients unless OIIRR happens in a large amount (severe OIIRR). Therefore, intervention during the treatment is

required when OIIRR is detected in a patient. The intervention may include dental splinting when the resorption is so severe that it has caused tooth mobility [43]. The intervention not only affects the treatment but also may embroil orthodontists in malpractice claims [43,49]. To avoid serious intervention and its consequences, OIIRR is to be reduced [43]. The mechanical factors, duration of treatment, nutrition and habits are some of the factors that can be employed to reduce OIIRR [43]. Other than these reductive – or to some extent preventive – methods there is currently no clinically acceptable treatment method [43].

2.2.2.3 Low-intensity pulsed ultrasound (LIPUS)

Utilized as therapeutic ultrasound, LIPUS is composed of repeating bursts of 1-1.5 MHz sinusoidal waves. Figure 2.13 shows the temporal form of typical LIPUS consisting of 200-microsecond bursts of 1.5 MHz sinusoidal pulses repeating at 1 kHz.

LIPUS is characterized as low intensity ultrasound to remove or alleviate the thermal effects of ultrasound on tissues. In this regard, the intensity of LIPUS is limited to values less than 100 mW/cm^2 to remove or alleviate the thermal effects of ultrasound on tissues [50]. The intensity is measured with a power meter and expressed as spatial-average temporal-average intensity (I_{SATA}). The concept of intensity and its measurement in covered in sections 2.5.4 and 2.5.7.

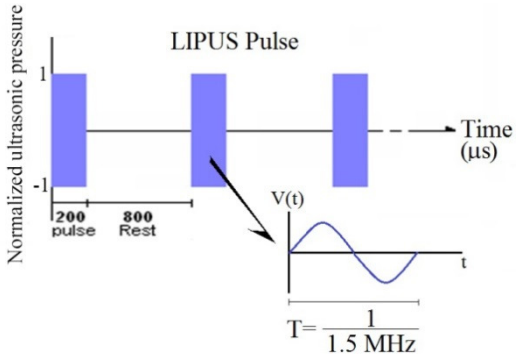

Figure 2.13 Typical pulses by LIPUS

2.2.2.4 Treatment of OIIRR by LIPUS

As previously mentioned, no clinically acceptable treatment method for OIIRR has been proposed yet; however, stimulatory effects of ultrasonic waves on biological response of bone cells have motivated researchers to investigate the effect of ultrasound on dental cells. The application of ultrasound, particularly LIPUS, on fractured bone has been shown to accelerate

fracture healing through enhancing bone formation [51–54]. This enhancing role of ultrasound on bone fracture healing and regeneration is found to be due to ultrasound-induced mechanical stresses rather than possible thermal effects by ultrasound [51]. Therefore, the effect of ultrasound on bone healing and regeneration can be related to Wolff's law which states that bone remodeling through deposition and resorption of bone (by osteoblasts and osteoclasts respectively) are associated with the mechanical stresses acting on bone [54,55].

Motivated by the effect of ultrasound on bone regeneration, researchers have utilized ultrasound towards seeking a therapeutic means of dental tissue repair [51]. Related to OIIRR, the response of cementum and periodontal ligament (PDL) cells to ultrasonic stimulation has been studied. Harle et. al. [56] exposed human PDL cells in cell cultures to 3-MHz continuous-wave ultrasound for 5 minutes. They utilized different intensities of ultrasound as $I_{SATA} = 125, 250, 500 \text{ and } 1000 \text{ mW/cm}^2$. The intensities of ultrasound used in this study indicate high-intensity ultrasound (the intensity limit for low-intensity ultrasound is $I_{SATA} = 100 \text{ mW/cm}^2$). PDL cell growth and proliferation stimulated by the ultrasound were observed in this study; however, the ultrasound intensities did not show notable effect on the cell response. Studies on the stimulatory effect of ultrasound on cementum cells were carried out by Dalla-Bona et. al. [53,54]. They exposed cementoblastic cells (cells that generates cementum) to 1-MHz pulsed ultrasonic waves (200μs sinusoidal pulses repeating at 1KHz) with ultrasonic intensities of $I_{SATA} = 30 \text{ and } 150 \text{ mW/cm}^2$ in one study [53], and ultrasonic intensities of $I_{SATA} = 100, 150 \text{ and } 400 \text{ mW/cm}^2$ in another study [54]. The exposure duration was 15 minutes per day for 6 [53] and 4 days [54]. They found significant cell proliferation in the cell culture when the cells were exposed to the ultrasound with the intensities of $30 \text{ and } 150 \text{ mW/cm}^2$ for 6 days (almost the same increase in the number of cell for both intensities) [53]. Interestingly no significant increase in the number of cells (compared to the number of control cells not being exposed to ultrasound) was observed when the cells were exposed to the intensities of $100, 150 \text{ and } 400 \text{ mW/cm}^2$ for 4 days [54]. However, other biological responses in the form of various cell metabolisms (like increase in calcium content of cells) significantly increased at the intensities of $100 \text{ and } 150 \text{ mW/cm}^2$ during 4-day exposure of the cells to ultrasound; but not for the high intensity of 400 mW/cm^2 [54]. It is worth mentioning that although ultrasound with different intensities may be beneficial to trigger positive biological response in some dental cells (PDL and cementum cells) it may be harmful to dental pulp. It is

reported that ultrasound with intensities above 30 mW/cm^2 may be harmful to dental pulp and may cause pulp fibrosis (thickening and scaring of the tissue) [53].

The above studies can be considered as evidences of the positive effect of ultrasound, particularly LIPUS, on growth, proliferation and metabolism of dental cells. However, they do not explicitly demonstrate the effect of LIPUS on dental cells formation in living tissues (in-vivo situation) and in the circumstances of OIIRR. So far, few studies have investigated the effect of LIPUS on dental cell formation in the condition of OIIRR. Two fundamental and pioneering studies demonstrating and proposing LIPUS for the prevention and treatment of OIIRR are briefly reviewed as follows:

Human study (in-vivo): In a unique pioneering study by El-Bialy et al. [43], the stimulatory effect of LIPUS on minimizing and repairing the resorption in human teeth was demonstrated. To investigate the stimulatory effect, in-vivo experiments were conducted on humans' teeth. Twelve female patients in need of orthodontic treatment were chosen to participate in the study. Each patient had to have their first premolars extracted through the treatment. Therefore, those teeth were designated to receive orthodontic forces and ultrasound. Availability of human teeth needed to be extracted by virtue of orthodontic treatment provided the study the most realistic environment to investigate OIIRR.

For each patient, orthodontic braces were used to exert the orthodontic force on the first premolars. The applied force was intended to provoke OIIRR on the roots of the premolars. During the study, one of the premolars only received orthodontic forces and appointed as control whereas the other one received both orthodontic forces and ultrasound and considered as test.

LIPUS with the frequency of 1.5 MHz and intensity of 30 mW/cm^2 was implemented on the test premolars for 20 minutes per day during the study (four weeks). LIPUS was transmitted into a test tooth by holding the LIPUS transducer on the gingival surface covered by conductive gel (Figure 2.14a).

After 4 weeks the LIPUS treatment was stopped, the orthodontic braces were removed and the first premolars were extracted by a non-traumatic method. The root surface of the premolars was investigated by a scanning electron microscope (SEM). Based on comparing the SEM data of the control and test premolars, a significant decrease in the areas of root resorption was observed in the test premolar. Their study showed that the LIPUS stimulated new cellular

cementum deposition (cementogenesis) on the root surface leading to the main part of the repair of the resorbed areas. Figure 2.14a and b partially demonstrate the root surface of a control and a test tooth; the resorption lacunae on the control root surface is apparent compared with the test root surface.

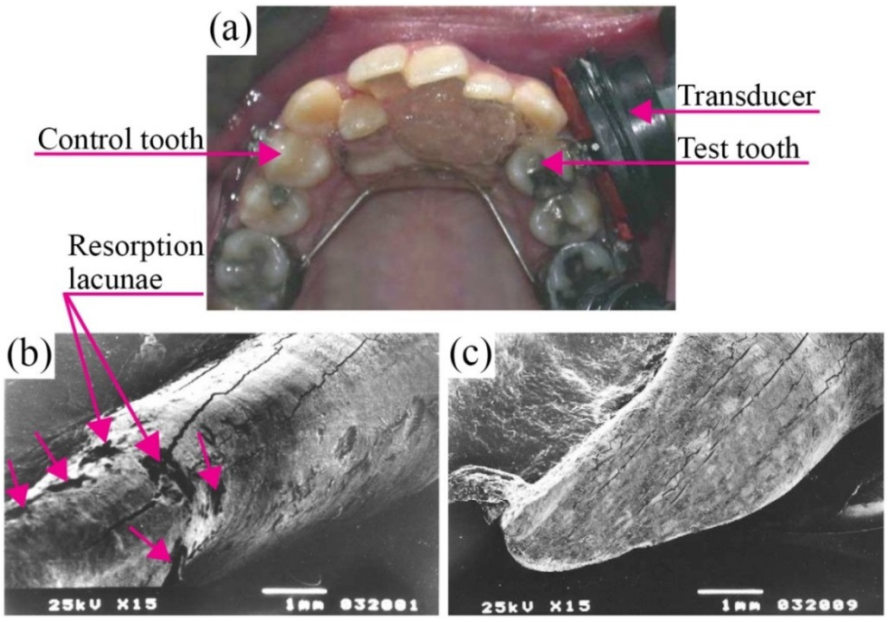

Figure 2.14 (a) Control and test teeth, orthodontic brace and LIPUS transducer in an instance of the human study. (b) SEM of the control root surface. (c) SEM of the test root surface [43] (Figures are used with permission from the author, Dr. El-Bialy).

Animal study (in-vivo): Al-Daghreer et al [57] performed another study in this field on animal subjects (beagle dogs). The same kind of procedure as in the human study by El-Bialy et al. [43] was recruited in the animal study (Figure 2.15a and b). However, to investigate the effects of LIPUS on dental tissues, the animals were euthanized and their mandibles were dissected (Figure 2.15c). The surface of the roots and the thickness of cementum in control and test teeth were investigated through micro-computed tomography scan (μ-CT) and histological study (hematoxylin and eosin staining). Examining the surfaces of the roots exhibited significant reduction in the number and relative volume of the resorbed areas on the test roots. Moreover, histological results demonstrated higher cementum thickness for the test teeth when compared with the control teeth. Figure 2.16 demonstrates an instance of the histological results indicating higher cementum thickness in a test tooth compared with a control one [57]. Being in agreement with the human study, the animal study demonstrated positive therapeutic and preventive effects of LIPUS on OIIRR.

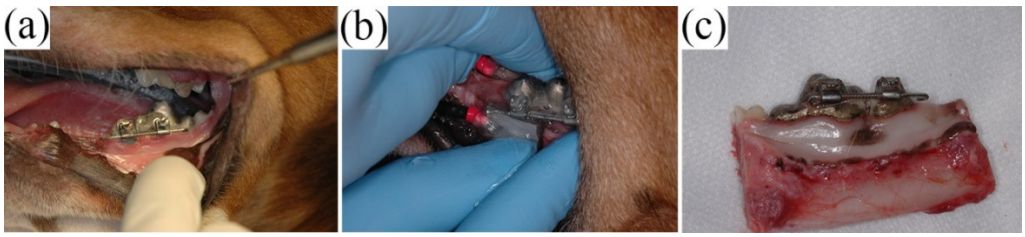

Figure 2.15 Different stages of the animal study. (a) Orthodontic brace applied to the dog's tooth. (b) Application of the ultrasound transducer on the animal's tooth. (c) dissected mandible of the dog for μ-CT and histological study (Figures are obtained from Dr. El-Bialy's research laboratory and used with permission).

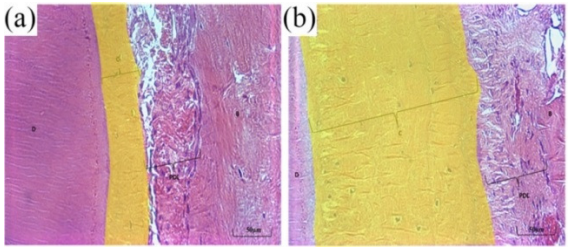

Figure 2.16 An instance of histological study [57] showing the cementum thickness of a control tooth (a) and a test (LIPUS-treated) tooth (b). To better demonstrate the cementum thickness, the area is recolored (yellow) in these images (Figures are used with permission from the author, Dr. El-Bialy).

2.3 Mechanical wave equations

The aim of this thesis is to study two applications of ultrasound i.e. QUS for bone assessment and LIPUS for the treatment of OIIRR. Toward this aim, the mathematical equations governing ultrasound propagation in various media will be solved. In this section, these equations are introduced and discussed.

Ultrasonic waves, sound waves and acoustic waves all refer to one phenomenon, which is mechanical wave or waves. Mechanical waves are mechanical perturbations (disturbance or vibrations) traveling in a substantial medium. Since mechanical waves are inherently localized vibrations of particles in the medium, net transfer of mass (material particles) does not occur in the medium. The speed of the traveling perturbations (wave speed) depends on the material properties of the medium under certain mechanical status and sometimes on the frequency of the traveling waves.

Mechanical waves traveling inside a medium are called body waves and are classified as longitudinal and transverse waves when the medium consists of an isotropic material. Longitudinal waves (also called dilatational, primary or P-waves) exist when the deformations

(relative displacement between two particles) are in the direction of wave propagation. Therefore, compression or/and expansion (volumetric change) occur as the result of longitudinal waves in the medium (Figure 2.17). On the other hand, when the deformations are perpendicular to the direction of propagations, transverse waves (shear, secondary or S-waves) appear (Figure 2.17). Transverse waves create shear deformations in the medium and preserve volumetric changes. Solids and viscous fluids bear both longitudinal and transverse waves whereas only longitudinal waves exist in inviscid (ideal) fluids.

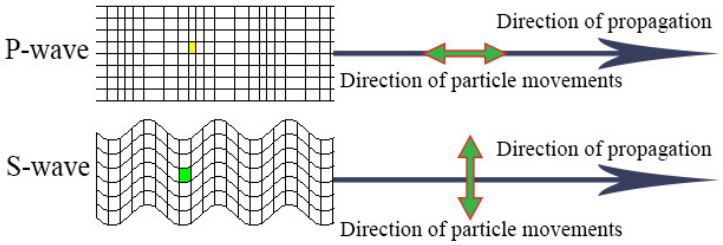

Figure 2.17 P- and S- waves.

On the exterior boundaries of a medium, there exists another type of mechanical waves called surface or boundary-dependent waves. Rayleigh and Love surface waves occur on the surface of a solid medium especially when body waves reach the free surfaces of the medium (Figure 2.18). On the surface of a liquid, gravity surface waves are produced if the surface is disturbed. Bending waves (thin plate Lamb waves) in a plate or a beam, and bar waves (either longitudinal or torsional disturbance traveling along a slender bar) are also classified as boundary-dependent waves.

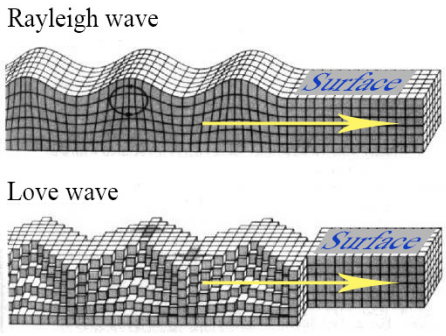

Figure 2.18 Rayleigh and Love surface waves [58].

The propagation of mechanical waves has been studied through well-known wave equations. The wave equations in liquids and solids are reviewed in the next sections to elucidate the assumptions and formulations in the present thesis.

2.3.1 Linear acoustic wave equation in ideal liquids

To derive the acoustic wave equation, the fundamental fluid-mechanical equations being Euler's equation of motion, continuity equation and equation of state are implemented along with infinitesimal-perturbation approximations and linearization of the equations.

Continuity equation: The continuity equation expresses the conservation of mass and has the following Eulerian form:

$$\frac{\partial \rho}{\partial t} + \nabla \cdot (\rho \boldsymbol{v}) = 0 \qquad (2.3)$$

Euler's equation of motion: Consider an ideal fluid[5] from the Eulerian point of view. In this regard, the fluid medium can be assumed to be under a scalar pressure field $p = p(\boldsymbol{x}, t)$. The pressure field ($p \in \mathbb{R}$) is a function of space (Cartesian position vector $\boldsymbol{x} \in \mathbb{R}^3$) and time $t \in \mathbb{R}$. Euler equation of motion is written using the Newton's second law applied on a unit volume (particle or point) of the fluid [2]:

$$\rho \left[\frac{\partial \boldsymbol{v}}{\partial t} + (\boldsymbol{v} \cdot \nabla)\boldsymbol{v}\right] = -\nabla p \qquad (2.4)$$

where $\rho = \rho(\boldsymbol{x}, t), \rho \in \mathbb{R}$ is the density field, $\boldsymbol{v} = \boldsymbol{v}(\boldsymbol{x}, t), \boldsymbol{v} \in \mathbb{R}^3$is the velocity vector field inside the fluid, ∇ is the gradient operator[6] and the dot in $\boldsymbol{v} \cdot \nabla$ denotes the dot product of the vectors. The term $\frac{\partial \boldsymbol{v}}{\partial t}$ is called local acceleration and $(\boldsymbol{v} \cdot \nabla)\boldsymbol{v}$ in known as convective acceleration. Obviously, $\frac{\partial \boldsymbol{v}}{\partial t} + (\boldsymbol{v} \cdot \nabla)\boldsymbol{v}$ expresses the total acceleration of liquid particles.

Equation of state: The relation between the pressure inside a fluid and its density or volume is given by an equation of state.

The pressure inside a liquid can be expressed versus the volumetric change in the liquid per unit volume, which states $p = p(\frac{\Delta V}{V_o})$ such that ΔV is the volumetric change and V_o is the initial volume of the liquid). The bulk modulus (tangential bulk modulus) is defined as the local slope of $p = p(\frac{\Delta V}{V_o})$ curve at any point (Figure 2.19). The slope can be written as differential

[5] Navier-Stokes equations should have been considered if a viscous fluid were considered instead.

[6] $\nabla = \frac{\partial}{\partial x_1}\boldsymbol{e_1} + \frac{\partial}{\partial x_2}\boldsymbol{e_2} + \frac{\partial}{\partial x_3}\boldsymbol{e_3}$, such that e_1, e_2 and e_3 are Cartesian unit vectors along the conventional x- y- and z- directions.

change in pressure divided by the corresponding change in volume or density when the liquid is compressed [59]:

$$\beta := -\frac{dp}{dV/V_o} = \frac{dp}{d\rho/\rho_o} \qquad (2.5)$$

in which dp, dV and $d\rho$ are differential changes in pressure and volume respectively, V_o is the initial volume of the liquid, and β is called adiabatic[7] bulk modulus of the liquid. The bulk modulus is analogous to the modulus of elasticity for solids. However, modulus of elasticity is defined based on one-dimensional variations of strain (change in length per unit length) versus stress.

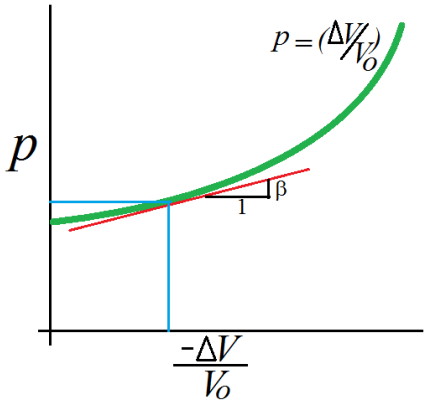

Figure 2.19 Tangential bulk modulus.

Another form of the equation of state can be written in terms of differential change in density ($d\rho$) with respect to differential change in pressure:

$$\kappa := \frac{d\rho/\rho_o}{dp} = \frac{1}{\beta} \qquad (2.6)$$

such that κ is defined as adiabatic compressibility modulus. Since $\rho = \rho(p)$, Eq. 2.6 can be written as:

$$\kappa = \frac{1}{\rho_o}\frac{\partial \rho}{\partial p} \qquad (2.7)$$

Infinitesimal-perturbation approximations: Small-signal or infinitesimal-perturbation approximations are the basic assumptions of linear acoustics. The first approximation is that only infinitesimal strains (deformation) occur in the medium:

[7] It means no heat transfer occurs between the system and its surrounding while the volume of the liquid is being compressed.

$$\frac{\partial u_i}{\partial x_j} \ll 1, \quad i,j = 1,2,3 \tag{2.8}$$

in which u_i is the displacement component (of a liquid particle) in x_i direction in the Cartesian coordinate system. This assumption leads to small volumetric strain indicating small change in the density of the liquid under small perturbation. In other words [2]:

$$\rho = \rho_o + \rho' \text{ and } |\frac{\rho'}{\rho_o}| \ll 1 \tag{2.9}$$

such that ρ_o is the constant density of the unperturbed (stationary) liquid and $\rho' = \rho'(\boldsymbol{x}, t)$ is the small change in the density due to the perturbation.

The second approximation linearizes the density-pressure relationship. If $\rho = \rho(p)$ and $p = p_o + p'$ such that p_o and p' are the unperturbed[8] and perturbed pressure (acoustic pressure) fields respectively, the Taylor series expansion of the density around the unperturbed pressure value is:

$$\rho = \rho_o + \left[\frac{\partial \rho}{\partial p}\right]_{p_o} p' + \frac{1}{2}\left[\frac{\partial^2 \rho}{\partial p^2}\right]_{p_o} (p')^2 + \cdots \tag{2.10}$$

Using Eq. 2.7 results in:

$$\rho' = \kappa \rho_o p' + \frac{1}{2}\left[\frac{\partial^2 \rho}{\partial p^2}\right]_{p_o} (p')^2 + \cdots \tag{2.11}$$

Since the perturbed pressure ρ' is assumed to be small during the perturbation, the higher order terms in the Taylor expansion are neglected; therefore:

$$\rho' \approx \kappa \rho_o p' \tag{2.12}$$

This approximation imposes a magnitude limit on the perturbed pressure (acoustic pressure) as follows:

$$|\kappa p'| \approx |\frac{\rho'}{\rho_o}| \ll 1 \rightarrow |p'| \ll |\frac{1}{\kappa}\ | or\ |p'| \ll \beta \tag{2.13}$$

Later it will be shown that $\beta = \rho_o c_o^2$ in which c_o is the velocity of acoustic waves (speed of sound) in small-signal propagation regime. As an example, small-signal approximations hold if

[8] Unperturbed pressure is assumed to be constant in space and time.

the magnitude of acoustic pressure (p') due to sound waves or ultrasonic waves in water is much less than 1.5MPa.

Linearization of the Euler's equation of motion and continuity equations: The next step towards linear acoustic wave equations is to linearize the Euler's equation of motion and continuity equations. This is achieved through eliminating the non-linear differential terms after substituting Eq. 2.9 into Eq. 2.4 and Eq. 2.3[9] [2]:

$$\frac{\partial \rho'}{\partial t} + \rho_o \nabla \cdot \boldsymbol{v} \approx 0 \tag{2.14}$$

$$\rho_o \frac{\partial \boldsymbol{v}}{\partial t} \approx -\nabla p \tag{2.15}$$

The approximations imply that $(\boldsymbol{v} \cdot \nabla)\boldsymbol{v}$ in Eq. 2.4 and $\boldsymbol{v}.\nabla\rho'$ in Eq. 2.3 are small enough to be neglected. In this regard, neglecting $(\boldsymbol{v} \cdot \nabla)\boldsymbol{v}$ is valid if the order of velocity is smaller than the speed of sound in the medium[10], i.e. $|\boldsymbol{v}| \ll \mathrm{c}_o$. Furthermore, $\boldsymbol{v} \cdot \nabla\rho'$can be neglected if $|\frac{\rho'}{\rho_o}| \ll 1$. It should be noted that the velocity of particles in a liquid is the resultant of acoustic oscillations (due to the perturbation) and flow. The flow velocity is zero in many cases of linear acoustic problems [2].

Assembling the equations: To re-derive the well-known linear acoustic wave equation, it is now enough to substitute Eq. 2.12 into 2.14 and combining the time derivative of the result with Eq. 2.15 to eliminate $\boldsymbol{v}$:

$$\frac{\partial^2 p}{\partial t^2} - \mathrm{c}_o^2 \nabla^2 p = 0 \tag{2.16}$$

where $\nabla^2 = \nabla \cdot \nabla$ and is called Laplacian or Laplace operator and $\mathrm{c}_o^2 = \frac{1}{\kappa \rho_o}$ is the speed of sound in the medium [2]. The constant c_o will be mathematically shown to be the speed of propagation in section 2.4.1.1.

Another form of the linear acoustic wave equations can be derived by taking the time derivative of 2.15 and combining the result with Eq. 2.14 and Eq. 2.12 to eliminate p:

[9] Since $p_o$is constant, $\nabla(p') = \nabla(p)$

[10] proof is available in Appendix A.

$$\frac{\partial^2 \boldsymbol{v}}{\partial t^2} - c_o^2 \nabla(\nabla \cdot \boldsymbol{v}) = \boldsymbol{0} \tag{2.17}$$

If the motion of the liquid is irrotational, i.e. $\nabla \times \boldsymbol{v} = \boldsymbol{0}$ expressing cross multiplication of gradient operator and the velocity field**,** the velocity field can be derived from a scalar potential function as $\boldsymbol{v} = \nabla\Phi$, $\varphi = \Phi(\boldsymbol{x}, t)$. Therefore, Eq. 2.17 becomes [2]:

$$\frac{\partial^2 \Phi}{\partial t^2} - c_o^2 \nabla^2 \Phi = 0 \tag{2.18}$$

2.3.2 Linear elastic waves in solids

Linear elastic wave propagation in solids is formulated based on linear elasticity assuming small (infinitesimal) deformation. In this regard, particles oscillate or vibrate in a small neighbourhood of the unperturbed state. Small deformation assumption allows the formulation to produce the same results if either the Lagrangian or Eulerian description is implemented. For a linearly elastic solid the Cauchy equations of motion (disregarding body forces) in the Cartesian coordinate system are [60]:

$$\begin{aligned}
\rho_o \frac{\partial^2 u_1}{\partial t^2} - \left(\frac{\partial \sigma_{11}}{\partial x_1} + \frac{\partial \sigma_{12}}{\partial x_2} + \frac{\partial \sigma_{13}}{\partial x_3}\right) = 0 \\
\rho_o \frac{\partial^2 u_2}{\partial t^2} - \left(\frac{\partial \sigma_{21}}{\partial x_1} + \frac{\partial \sigma_{22}}{\partial x_2} + \frac{\partial \sigma_{23}}{\partial x_3}\right) = 0 \\
\rho_o \frac{\partial^2 u_3}{\partial t^2} - \left(\frac{\partial \sigma_{31}}{\partial x_1} + \frac{\partial \sigma_{32}}{\partial x_2} + \frac{\partial \sigma_{33}}{\partial x_3}\right) = 0
\end{aligned} \tag{2.19}$$

where $\boldsymbol{u} \in \mathbb{R}^3, \boldsymbol{u} = (u_1, u_2, u_3)$ is the displacement vector field such that $u_i = u_i(\boldsymbol{x}, t), i = 1,2,3$ and $\sigma_{ij}, i, j = 1,2,3$ is an entity of the Cauchy stress tensor. The above equations are based on the following small-deformation assumptions:

$$\begin{aligned}
|\boldsymbol{u}| \ll 1 \\
\left|\frac{\partial u_i}{\partial x_j}\right| \ll 1 \rightarrow \left|\frac{\rho'}{\rho_o}\right| \ll 1 \rightarrow \rho \approx \rho_o \\
\boldsymbol{v} = \frac{\partial \boldsymbol{u}}{\partial t}, \boldsymbol{a} = \frac{\partial^2 \boldsymbol{u}}{\partial t^2}
\end{aligned} \tag{2.20}$$

Linear-elastic stress-strain relationship and small (infinitesimal) strain tensor[11] are [60]:

$$\sigma_{ij} = \lambda\varepsilon_{kk}\delta_{ij} + 2\mu\varepsilon_{ij}$$
$$\varepsilon_{ij} = \frac{1}{2}\left(\frac{\partial u_i}{\partial x_j} + \frac{\partial u_j}{\partial x_i}\right) \quad (2.21)$$

in which λ and μ are the first and second Lame parameters respectively, δ_{ij} is the Kronecker delta, $\varepsilon_{ij}, i, j = 1,2,3$ is an entity of the small strain tensor and $\varepsilon_{kk} = \varepsilon_{11} + \varepsilon_{22} + \varepsilon_{33}$. Therefore, the stress tensor can written in terms of the displacements:

$$\sigma_{ij} = \lambda(\nabla \cdot \boldsymbol{u})\delta_{ij} + \mu\left(\frac{\partial u_i}{\partial x_j} + \frac{\partial u_j}{\partial x_i}\right) \quad (2.22)$$

By substituting Eq. 2.22 into Eq. 2.19 and writing the results as one expression, the linear elastic wave equations are derived:

$$\rho_o \frac{\partial^2 \boldsymbol{u}}{\partial t^2} - (\lambda + \mu)\nabla(\nabla \cdot \boldsymbol{u}) - \mu\nabla^2\boldsymbol{u} = \boldsymbol{0} \quad (2.23)$$

The linear elastic wave equation can be decomposed into two equations expressing longitudinal and transverse waves. According to Helmholtz, a general smooth vector field has both an irrotational (lamellar) and rotational (solenoidal) parts [61]. By the definition, irrotational and rotational vector fields have zero curl and zero divergence respectively. Mathematically, the displacement vector filed can be decomposed as [60]:

$$\boldsymbol{u} = \boldsymbol{u}_L + \boldsymbol{u}_T$$
$$\text{Curl}\ (\boldsymbol{u}_L) \equiv \nabla \times \boldsymbol{u}_L = \boldsymbol{0} \quad (2.24)$$
$$\text{div}\ (\boldsymbol{u}_T) \equiv \nabla \cdot \boldsymbol{u}_T = 0$$

By substituting $\boldsymbol{u} = \boldsymbol{u}_L + \boldsymbol{u}_T$ into Eq. 2.23 and using the Helmholtz decomposition theory, the mechanical wave equation becomes:

$$\rho_o\left(\frac{\partial^2 \boldsymbol{u}_L}{\partial t^2} + \frac{\partial^2 \boldsymbol{u}_T}{\partial t^2}\right) - (\lambda + 2\mu)\nabla^2\boldsymbol{u}_L - \mu\nabla^2\boldsymbol{u}_T = \boldsymbol{0} \quad (2.25)$$

The wave equation for the longitudinal waves appears when the divergence operator is

[11] Small-deformation assumption leaves negligible difference between the Lagrangian and Eulerian stains tensors.

applied[12] on Eq. 2.25:

$$(\frac{\partial^2 \boldsymbol{u}_L}{\partial t^2}) - \mathrm{c}_L^2 \nabla^2 \boldsymbol{u}_L = \mathbf{0} \tag{2.26}$$

such that $\mathrm{c}_L^2 = \frac{(\lambda+2\mu)}{\rho_0}$ and c_L will be shown in section 2.4.1.2 to be the speed of longitudinal waves in the medium [2].

It can be shown that Eq. 2.26 governs longitudinal waves, i.e. waves that only change the volume of the particles in the medium. The fact that Curl $(\boldsymbol{u}_L) \equiv \nabla \times \boldsymbol{u}_L = \mathbf{0}$ everywhere in the medium implies that:

$$\left(\frac{\partial u_{L_1}}{\partial x_3} - \frac{\partial u_{L_3}}{\partial x_1}\right) = \left(\frac{\partial u_{L_2}}{\partial x_1} - \frac{\partial u_{L_1}}{\partial x_2}\right) = \left(\frac{\partial u_{L_3}}{\partial x_2} - \frac{\partial u_{L_2}}{\partial x_3}\right) = 0 \tag{2.27}$$

Additionally, the infinitesimal volumetric strain is ε_V is:

$$\varepsilon_V = \nabla \cdot \boldsymbol{u} = \nabla \cdot (\boldsymbol{u}_L + \boldsymbol{u}_T) = \nabla \cdot \boldsymbol{u}_L \tag{2.28}$$

Using Eq. 2.27 and Eq. 2.28 with Eq. 2.26 and manipulating the result yields:

$$\frac{\partial^2 \varepsilon_V}{\partial t^2} - c_L^2 \nabla^2 \varepsilon_V = 0 \tag{2.29}$$

which clearly demonstrates an equation in terms of volumetric strains.

On the other hand, if the curl operator is applied on Eq. 2.25, transverse waves (waves leading to no volumetric change in particles) equation appears[13]:

$$(\frac{\partial^2 \boldsymbol{u}_T}{\partial t^2}) - \mathrm{c}_T^2 \nabla^2 \boldsymbol{u}_T = \mathbf{0} \tag{2.30}$$

where $\mathrm{c}_T^2 = \frac{\mu}{\rho_o}$ and c_T is the speed of transverse waves (shown in section 2.4.1.2) in the medium [2].

2.3.3 Helmholtz's equation

The waves that harmonically change with time at each point of a medium are called time-harmonic or harmonic waves. An acoustic harmonic wave can be expressed by:

[12] It should be noted that $\nabla \cdot \nabla^2(\,) = \nabla^2[\nabla \cdot (\,)]$
[13] $\nabla \times \nabla^2(\,) = \nabla^2[\nabla \times (\,)]$

$$p(\boldsymbol{x},t) = P(\boldsymbol{x})Cos\big(\omega t - \varphi(\boldsymbol{x})\big), \qquad p(\boldsymbol{x},t), P(\boldsymbol{x}) \in \mathbb{R} \tag{2.31}$$

in which $P(\boldsymbol{x})$ is the spatially changing pressure amplitude, ω denotes the frequency in $\mathrm{rad.\,s^{-1}}$ and $\varphi(\boldsymbol{x})$ is a spatial phase lag. This representation of the harmonic perturbation is often considered as a complex form:

$$p(\boldsymbol{x},t) = \mathrm{Re}\big[P(\boldsymbol{x})e^{i(\omega t - \varphi(\boldsymbol{x}))}\big] = \mathrm{Re}\big[\underline{P}(\boldsymbol{x})e^{i\omega t}\big], \quad \underline{P}(\boldsymbol{x}) \in \mathbb{C} \tag{2.32}$$

where $i^2 = -1$, e is the base of the natural logarithm and $\underline{P}(\boldsymbol{x}) \in \mathbb{C}$ denotes the phasor (here is acoustic pressure phasor)[14]. Since pressure is a physical phenomenon described by a real variable, the real part of the complex description is considered[15].

In the case of linear acoustics, the following simpler representation of a harmonic wave is more practical:

$$\underline{p}(\boldsymbol{x},t) = \underline{P}(\boldsymbol{x})e^{i\omega t}, \quad \underline{p}(\boldsymbol{x},t) \in \mathbb{C} \tag{2.33}$$

However, considering only the real part as the meaningful physical entity (pressure) is still inherent in this form. The complex representation originates from the theorem expressing that the real and imaginary parts of a complex solution are independent real-valued solutions of a linear homogeneous differential equation [62]. This implies that if Eq. 2.33 is a solution to the linear acoustic wave equation (2.16), then the real part is also a solution but with a meaningful physical sense. In this regard, substituting Eq. 2.33 into Eq. 2.16 yields [2]:

$$(k^2 + \nabla^2)\underline{P}(\boldsymbol{x}) = 0 \tag{2.34}$$

where $k = \frac{\omega}{c_o}$ is called the wave number. Eq. 2.34 is known as acoustic Helmholtz's equation describing the steady-state propagation of a harmonic wave inside a fluid. Since Helmholtz's equation is not explicitly time-dependent, it is also referred to as the linear wave equation in the frequency domain. Generally, any of the wave equations, i.e. Eq. 2.26 and Eq. 2.30 can be written in the form of Helmholtz's equation if steady-state harmonic wave propagation is assumed:

$$(k_L^2 + \nabla^2)\underline{\boldsymbol{U}}_L(\boldsymbol{x}) = 0 \tag{2.35}$$

[14] Henceforward, underlining a variable indicates a complex variable.

[15] The imaginary part of the complex representation can also be considered, however the real part is considered the convention.

$$(k_T^2 + \nabla^2)\underline{\boldsymbol{U}}_T(\boldsymbol{x}) = 0$$

in which $k_L = \frac{\omega}{c_L}$ and $k_T = \frac{\omega}{c_T}$.

2.4 Solution methods for the wave equations

In general, there are two methods for solving a partial differential equation (PDE): method leading to closed-form solutions or analytical solutions, and numerical methods. Analytical methods of solution are method of characteristics and general solutions, method of separation of variables, methods of integral transforms, and Green's function method. Numerical methods can be generally divided into finite difference and finite element methods [62].

In the case of linear wave equations, analytical methods provide exact solutions for the equations. However, practical existence of a closed-form solution for the linear wave equations depends on the complexity of the region on which boundary conditions are defined, and the propagation medium. Closed-form solutions are not generally achievable for problems with complex regions of boundary conditions or having a complex shape for the propagation medium, and problems regarding wave propagation in a medium containing material inhomogeneity along with interface conditions. On the other hand, the geometrical shapes of the medium and boundary condition regions do not restrict numerical methods. Moreover, these methods can deal with material inhomogeneity and interface conditions in a propagation medium. The main concerns with numerical methods are that they provide approximate solutions and may become computationally expensive. This implies the significance of analytical solutions as *touchstones* for numerical methods.

In this section, instances of closed-form solutions for wave propagation in semi-infinite media (half space) are demonstrated using d'Alembert method. Although the solutions for basic problems with simple boundary conditions are shown using d'Alembert method, this will help to explain several wave propagation phenomena later. Additionally, the angular spectrum method and the finite element method, which are an analytical and a numerical method respectively, are discussed.

2.4.1 Closed-form solutions by d'Alembert method

The derived linear wave equations in this chapter (2.16, 2.18, 2.23, 2.34, 2.35) are

characterised as a hyperbolic linear homogeneous PDE. If the wave propagation is assumed unidirectional, the wave equations can be solved through d'Alembert method. This method is based on method of characteristics and general solutions for solving PDEs [63]. The d'Alembert solution for the following wave equation with a general scalar wave variable $\mathcal{A}$ and direction variable x

$$\frac{\partial^2 \mathcal{A}}{\partial t^2} - \mathrm{c}_o^2 \frac{\partial^2 \mathcal{A}}{\partial x^2} = 0 \tag{2.36}$$

is:

$$\mathcal{A}(x,t) = F(x - \mathrm{c}_o t) + G(x + \mathrm{c}_o t) \tag{2.37}$$

where F and G are two arbitrary functions that can be determined based on the initial or boundary conditions of the problem. In the next section, it will be shown that $F(x + \mathrm{c}_o t)$ and $G(x + \mathrm{c}_o t)$ correspond to wave forms propagating with the speed of c_o towards the positive and negative x-directions respectively.

2.4.1.1 Plane waves in unbounded acoustic media

Consider the acoustic wave equation (Eq. 2.16) with the following time-varying boundary condition (inhomogeneous boundary condition):

$$\begin{gathered} \frac{\partial^2 p}{\partial t^2} - \mathrm{c}_o^2 \nabla^2 p = 0 \\ p(\boldsymbol{x}, t) = f(t), \qquad \boldsymbol{x} \in \mathrm{S}_\infty \end{gathered} \tag{2.38}$$

where $\boldsymbol{x} \in \mathbb{R}^3$ is a position vector in the global coordinate system defined by the unit normal vectors $\boldsymbol{e}_1$, $\boldsymbol{e}_2$, and $\boldsymbol{e}_3$ and the corresponding components $x_1\boldsymbol{e}_1, x_2\boldsymbol{e}_2$ and $x_3\boldsymbol{e}_3$. $f(t)$ is an arbitrary function defined on an arbitrary infinitely large plane S_∞ with the unit normal $\boldsymbol{n} \in \mathbb{R}^3$ defined in the global coordinate system. A local Cartesian coordinate system is defined by the unit normal vector $\boldsymbol{l}_1$, $\boldsymbol{l}_2$, and $\boldsymbol{l}_3$ and the associated components $\eta_1\boldsymbol{l}_1$, $\eta_1\boldsymbol{l}_2$, and $\eta_1\boldsymbol{l}_3$. Indeed, each unit vector of the local coordinate system can be written as a linear combination of $\boldsymbol{e}_1$, $\boldsymbol{e}_2$, and $\boldsymbol{e}_3$. Without losing generality, the direction of the axis $\eta_1\boldsymbol{l}_1$ is parallel to $\boldsymbol{n}$ and the plane is located at $\eta_1 = 0$. Figure 2.20a demonstrates the state of the problem.

Physically, $f(t)$ represents time-varying acoustic pressure uniformly distributed over a plane region like S_∞. The source of the pressure can be imagined to be due to spatially uniform

vibrations of an infinite-dimension plane located in an unbounded acoustic medium (i.e. liquid).

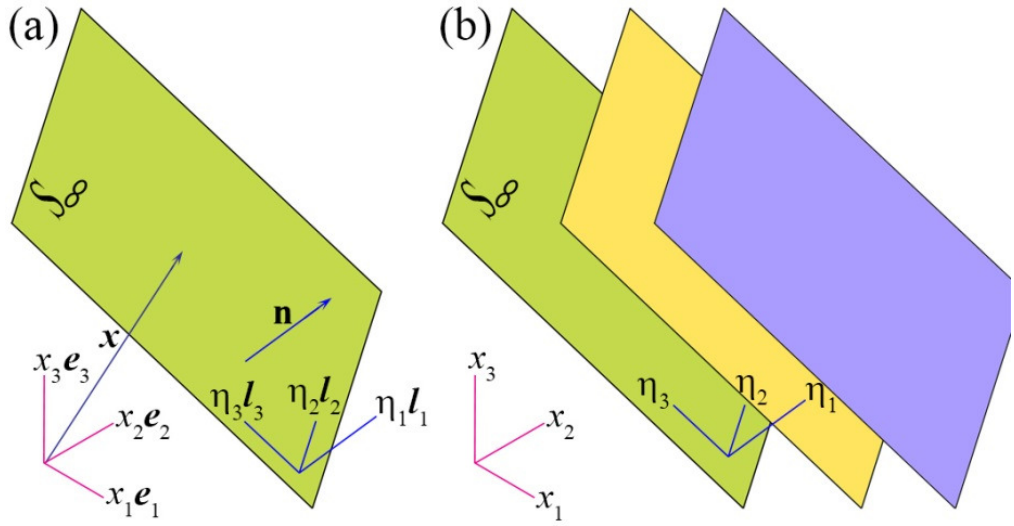

Figure 2.20 (a) Inhomogeneous boundary condition applied on an infinite plane for plane waves, (b) Planes parallel to S_∞.

The uniformity of the time-varying pressure on S_∞ and the infinitely large dimensions of the plane imply that the spatial dependency of a solution must be only on single variable η_1. Therefore, Eq. 2.38 is transformed to the plane local coordinate system and modified by noting the independency of the pressure on η_2 and η_3, i.e.:

$$\frac{\partial^2 p}{\partial t^2} - c_o^2 \frac{\partial^2 p}{\partial \eta_1^2} = 0 \qquad (2.39)$$
$$p(0,t) = f(t)$$

Depending only on η_1 and t, this equation represents the one dimensional linear wave equation with an inhomogeneous boundary condition [63].

If only the half space in front of the vibrating plane is considered, i.e. $\eta_1 \geq 0$, according to d'Alembert method [63] the solution for 2.39 is:

$$p(\eta_1, t) = \begin{cases} f\left(t - \frac{\eta_1}{c_o}\right) & 0 \leq \eta_1 \leq c_o t \\ 0 & \eta_1 > c_o t \end{cases} \qquad (2.40)$$

The physical interpretation of this solution is that a time-varying perturbation ($f\left(t - \frac{\eta_1}{c_o}\right)$) generated at η_o is moving in the positive direction ($+\boldsymbol{n}$) through the space (spatial domain) in

front of the plane ($0 \leq \eta_1$). One may also consider the wave (perturbation) moving in the negative direction ($-\boldsymbol{n}$) through the half space behind the vibrating plane. In this case, using the same method of solution leads to:

$$p(\eta_1, t) = \begin{cases} f\left(t + \dfrac{\eta_1}{\mathrm{c}_o}\right) & -\mathrm{c}_o t \leq \eta_1 \leq \eta_o \\ 0 & \eta_1 < -\mathrm{c}_o t \end{cases} \tag{2.41}$$

Figure 2.21 depicts the propagation of a plane wave form ($\mathrm{c}_o = 1$) in the positive and negative directions at different times[16]. Any function in the form of $f\left(t \pm \frac{\eta_1}{\mathrm{c}_o}\right)$ describing the propagation (movement) of a perturbation in a medium is called a wave function or a waveform.

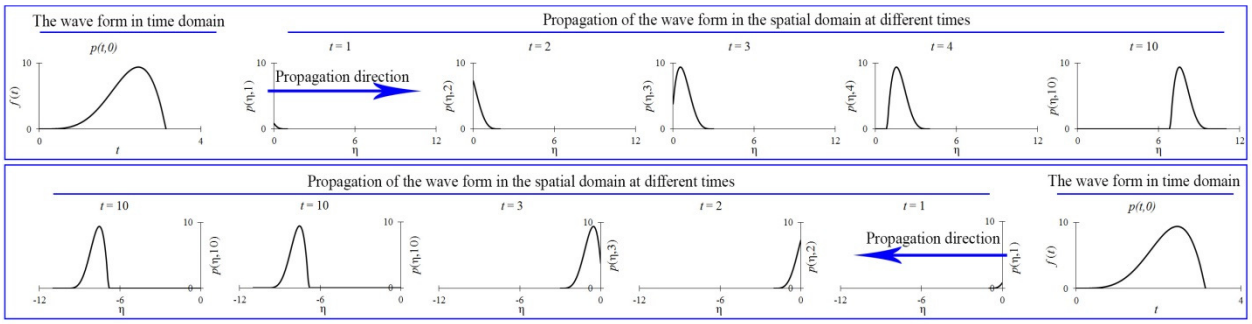

Figure 2.21 Different time stages of the propagation of a waveform in positive and negative directions.

The speed of the propagation of the perturbation can be shown to be c_o. To this end, assume a specific perturbed pressure value at location $\eta_1 = L$ and time t_1 being $p(L, t_1)$. Propagating in the positive direction, the same perturbed pressure value reaches its new location $\eta_1 = L + \Delta\eta_1$ at time $t = t_1 + \Delta t$. Tracking the same perturbation indicates $p(L, t_1) = p(L + \Delta\eta, t_1 + \Delta t)$ or $f\left(t_1 - \frac{L}{\mathrm{c}_o}\right) = f\left(t_1 + \Delta t - \frac{L+\Delta\eta}{\mathrm{c}_o}\right)$. Therefore, $\mathrm{c}_o = \frac{\Delta\eta_1}{\Delta t}$ which expresses the velocity of the propagation [2].

It should be noted that the perturbation cannot propagate faster than c_o. This fact is

[16] The propagation of the perturbation is graphically evaluated using the function transformations. If $y = f(x)$ is a real function ($f: \mathbb{R} \to \mathbb{R}$) and $\{(x, y): x \in \mathbb{R}\}$ is the set of ordered pairs representing the graph of the function in a Cartesian coordinate system (x, y), then the followings hold:

- The graph of $f(x + d)$ is the shifted graph of $f(x)$ by d-unit towards the positive direction ($x > 0$) if $d < 0$ and towards the negative direction if $d > 0$.
- The graph of $f(-x)$ is the reflected graph of $f(x)$ against the vertical axis of the coordinate system.
- The graph of $f(-x + d)$ is the shifted graph of $f(-x)$ by d-unit towards the positive direction ($x > 0$) if $d > 0$ and towards the negative direction if $d < 0$.
- The graph of $f(dx)$ is the graph of $f(x)$ but horizontally shrunk by the factor of $\frac{1}{d}$ if $d > 1$ or horizontally stretched by the factor of $\frac{1}{d}$ if $0 < d < 1$.

explicitly included in the solution by the intervals $0 \leq \eta_1 \leq c_o t$ and $\eta_1 > c_o t$ expressing no perturbation appears in the distance $\eta_1 > c_o t$ from the vibrating plane [63].

The solutions can also be expressed in the global coordinate system. The fact that at a specific time the spatially-uniform pressure $p(\eta_1, t)$ admits a single value on each parallel plane with S_∞ (Figure 2.20b) and $\eta_1 = \boldsymbol{n} \cdot \boldsymbol{x}$ (vector dot product) result in[17]:

$$p(\boldsymbol{x}, t) = \begin{cases} f\left(t - \dfrac{\boldsymbol{n} \cdot \boldsymbol{x}}{c_o}\right) & 0 \leq \boldsymbol{n} \cdot \boldsymbol{x} \leq c_o t \\ 0 & \boldsymbol{n} \cdot \boldsymbol{x} > c_o t \end{cases} \tag{2.42}$$

which is for the waves propagating away from the plane in the direction of the unit vector of the plane. The same procedure can be recruited for the waves propagating away from the plane but in the opposite direction of the unit vector.

Harmonic plane acoustic waves:

Harmonic plane acoustic waves are generated when uniform time-harmonic vibrations or pressure variations (conventionally, Cos function is considered) are defined on an infinite plane. Therefore, if $f(t) = P_o \cos(\omega t), P_o > 0$ in Eq. 2.39, the generated plane pressure waves propagating in the positive direction are expressed by[18]:

$$p(\boldsymbol{x}, t) = \begin{cases} P_o cos(\omega t - \boldsymbol{k} \cdot \boldsymbol{x}) & 0 \leq \boldsymbol{n} \cdot \boldsymbol{x} \leq c_o t \\ 0 & \boldsymbol{n} \cdot \boldsymbol{x} > c_o t \end{cases} \tag{2.43}$$

in which $\boldsymbol{k} = k\boldsymbol{n}$ and $k = \dfrac{\omega}{c_o}$.

To investigate the properties of harmonic waves, assume that the medium is entirely occupied by harmonic waves. This implies that $t \to \infty$ for the intervals in Eq. 2.43. Therefore, the following describes harmonic waves propagating in positive and negative directions respectively [2]:

$$p(\boldsymbol{x}, t) = P_o cos(\omega t - \boldsymbol{k} \cdot \boldsymbol{x}), \textit{ positive direction} \tag{2.44a}$$

$$p(\boldsymbol{x}, t) = P_o cos(\omega t + \boldsymbol{k} \cdot \boldsymbol{x}), \textit{ negative direction} \tag{2.44b}$$

Mathematical operations become simpler if the harmonic wave functions are written in

[17] For simplicity, the plane local coordinate system and the global coordinate system are assumed to share the same origin. i.e. (0,0,0).

[18] A phase lag may also be introduced in the function $f(t)$ as $f(t) = P_o \cos(\omega t + \varphi)$.

the complex form while associating the real part with the physical meaning (pressure):

$$\underline{p}(\boldsymbol{x},t) = P_o e^{i(\omega t - \boldsymbol{k}\cdot\boldsymbol{x})} \tag{2.45a}$$

$$\underline{p}(\boldsymbol{x},t) = P_o e^{i(\omega t + \boldsymbol{k}\cdot\boldsymbol{x})} \tag{2.45b}$$

Considering the above harmonic waves, the solutions or the phasors presented in Helmholtz's equation for plane acoustic waves are:

$$\underline{P}(\boldsymbol{x}) = P_o e^{-i\boldsymbol{k}\cdot\boldsymbol{x}} \tag{2.46a}$$

$$\underline{P}(\boldsymbol{x}) = P_o e^{+i\boldsymbol{k}\cdot\boldsymbol{x}} \tag{2.46b}$$

A harmonic wave propagating in an acoustic medium with a specific speed of sound c_o is characterised by two independent parameters: amplitude $\left|\underline{P}(\boldsymbol{x})\right| = P_o$ and temporal frequency ω (angular frequency). Interchangeably, temporal period T can be used instead of ω. The wave number (spatial frequency) k and the wavelength (spatial period) λ are other parameters which depend on c_o and ω. The definition and relation between these parameters are displayed in Figure 2.22 (propagation along a general axis (like $\eta - axis$) at a specific time t_o is considered).

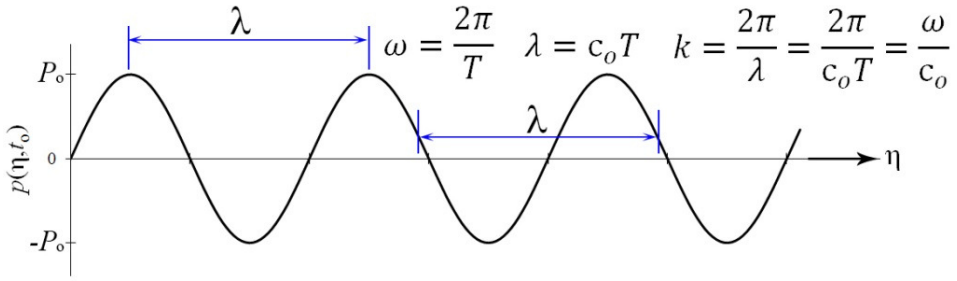

Figure 2.22 Characteristic parameters of a harmonic wave.

2.4.1.2 Plane waves in unbounded solid media

In contrast to linear acoustic wave propagation which is formulated in terms of a scalar pressure field, formulations of elastic waves in solids require a vector field. According to Eq. 2.24, the vector field associated with elastic waves in a solid medium can be decomposed into $\boldsymbol{u} = \boldsymbol{u}_L + \boldsymbol{u}_T$ leading to two separate formulations for longitudinal and transverse waves i.e. Eq. 2.26 and Eq. 2.30.

Solving for longitudinal waves:

A uniformly (spatial) vibrating infinite plane (S_∞) with the configurations described in

section 2.4.1.1 is assumed in an unbounded solid media (Figure 2.23a). Since longitudinal waves are only associated with volumetric changes in the medium, the vibrations of the plane must not generate any transverse waves due to shear displacements. Therefore, considering the local coordinate system of the plane leads to the fact that the vibrations must be restricted to the direction of $\boldsymbol{l}_1$ or the unit normal vector $\boldsymbol{n}$ being parallel to $\boldsymbol{l}_1$. In this regard, the problem is described by:

$$\begin{gathered}\frac{\partial^2 \chi_1}{\partial t^2} - \mathrm{c}_L^2 \frac{\partial^2 \chi_1}{\partial \eta_1^2} = 0 \\ \chi_1(0,t) = f_p(t)\end{gathered} \tag{2.47}$$

where $\chi_1 \in \mathbb{R}$ is the displacement component in the direction of $\boldsymbol{l}_1$ ($\boldsymbol{\chi}_1 = \chi_1 \boldsymbol{l}_1,\ \boldsymbol{\chi}_1 \in \mathbb{R}^3$). The subscript in $f_p(t)$ indicates p-wave. Using the d'Alembert method, a solution for this PDE for propagation in the positive direction ($\boldsymbol{l}_1$ or $+\boldsymbol{n}$) is:

$$\chi_1(\eta_1, t) = \begin{cases} f_p\left(t - \dfrac{\eta_1}{\mathrm{c}_L}\right) & 0 \le \eta_1 \le \mathrm{c}_L t \\ 0 & \eta_1 > \mathrm{c}_L t \end{cases} \tag{2.48}$$

Transforming the solution into the global coordinate system results in:

$$\boldsymbol{u}_L = \chi_1(\boldsymbol{x}, t)\boldsymbol{n} = \begin{cases} f_p\left(t - \dfrac{\boldsymbol{n}\cdot\boldsymbol{x}}{\mathrm{c}_L}\right)\boldsymbol{n} & 0 \le \boldsymbol{n}\cdot\boldsymbol{x} \le \mathrm{c}_L t \\ \boldsymbol{0} & \boldsymbol{n}\cdot\boldsymbol{x} > \mathrm{c}_L t \end{cases} \tag{2.49}$$

Solving for transverse waves:

Any spatially uniform vibration of the infinite plane that is not along the unit normal vector of the plane can be decomposed into two displacement vectors along the in-plane local axes of the plane. As demonstrated in Figure 2.23b, the displacement vectors $\boldsymbol{\chi}_2 = \chi_2 \boldsymbol{l}_2$ and $\boldsymbol{\chi}_3 = \chi_3 \boldsymbol{l}_3$correspond to in-plane vibrations of the plane. Since the vibrations are independent of each other, the problem (in the local coordinate system) leads to the following PDEs with their time-varying boundary condition:

$$\begin{gathered}\frac{\partial^2 \chi_2}{\partial t^2} - \mathrm{c}_T^2 \frac{\partial^2 \chi_2}{\partial \eta_1^2} = 0 \\ \chi_2(0,t) = f_{\mathrm{S}_2}(t)\end{gathered} \tag{2.50a}$$

$$\frac{\partial^2 \chi_3}{\partial t^2} - \mathrm{c}_T^2 \frac{\partial^2 \chi_3}{\partial \eta_1^2} = 0$$
$$\chi_3(0,t) = f_{\mathrm{S}_3}(t) \tag{2.50b}$$

such that $f_{\mathrm{S}_2}(t)$ and $f_{\mathrm{S}_3}(t)$ describes the temporal shear vibrations of the plane. It should be noted that due to the infinite dimensions of the plane, the displacement fields through the half-space only depends on the propagation direction, i.e. $\eta_1 - axis$. Similar to the previous solution procedure, the solution for each of the equations is:

$$\chi_2(\eta_1,t) = \begin{cases} f_{\mathrm{S}_2}\left(t - \dfrac{\eta_1}{\mathrm{c}_T}\right) & 0 \le \eta_1 \le \mathrm{c}_T t \\ 0 & \eta_1 > \mathrm{c}_T t \end{cases} \tag{2.51a}$$

$$\chi_3(\eta_1,t) = \begin{cases} f_{\mathrm{S}_3}\left(t - \dfrac{\eta_1}{\mathrm{c}_T}\right) & 0 \le \eta_1 \le \mathrm{c}_T t \\ 0 & \eta_1 > \mathrm{c}_T t \end{cases} \tag{2.51b}$$

The total displacement field in the medium due to the shear waves is calculated as follows:

$$\boldsymbol{u}_T = \chi_2(\boldsymbol{x},t)\boldsymbol{l}_2 + \chi_3(\boldsymbol{x},t)\boldsymbol{l}_3$$
$$= \begin{cases} f_{\mathrm{S}_2}\left(t - \dfrac{\boldsymbol{n}\cdot\boldsymbol{x}}{\mathrm{c}_T}\right)\boldsymbol{l}_2 + f_{\mathrm{S}_3}\left(t - \dfrac{\boldsymbol{n}\cdot\boldsymbol{x}}{\mathrm{c}_T}\right)\boldsymbol{l}_3 & 0 \le \eta_1 \le \mathrm{c}_T t \\ \boldsymbol{0} & \eta_1 > \mathrm{c}_T t \end{cases} \tag{2.52}$$

Total displacement field:

In a more general case (Figure 2.23c) when the infinite plane vibrates uniformly (spatial) in a specific direction $\boldsymbol{m}$, the boundary condition for Eq. 2.26 and 2.30 considering $\boldsymbol{u} = \boldsymbol{u}_L + \boldsymbol{u}_T$ is $\boldsymbol{u}_o \coloneqq \boldsymbol{u}(0,t) = f(t)\boldsymbol{m}$. Transforming the vibration vector ($\boldsymbol{u}_o$) to the local coordinate system of the plane as described before leads to the independent longitudinal and transverse wave fields. Therefore the total displacement field is:

$$\boldsymbol{u}_T = \boldsymbol{u}_T + \boldsymbol{u}_L = \chi_1(\boldsymbol{x},t)\boldsymbol{n} + \chi_2(\boldsymbol{x},t)\boldsymbol{l}_2 + \chi_3(\boldsymbol{x},t)\boldsymbol{l}_3 \tag{2.53}$$

where each of the unit vectors $\boldsymbol{n}$, $\boldsymbol{l}_2$ and $\boldsymbol{l}_3$ is a linear combination of $\boldsymbol{e}_1$, $\boldsymbol{e}_2$ and $\boldsymbol{e}_3$.

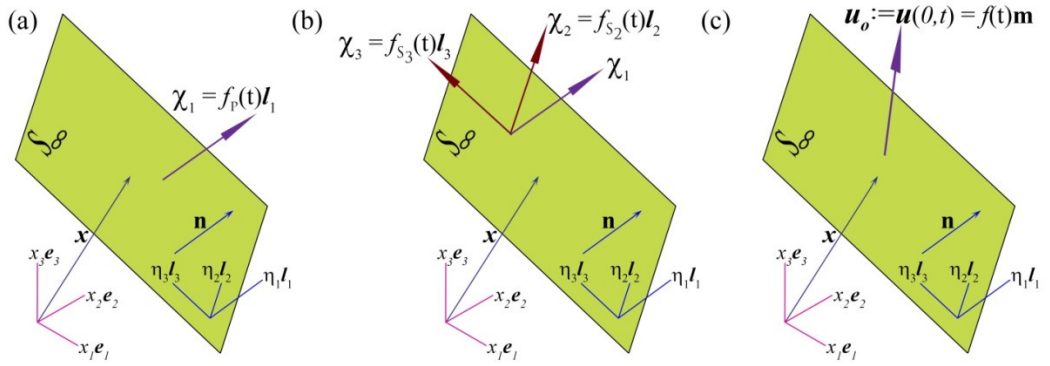

Figure 2.23 (a) spatially uniform vibration of the infinite plane along its normal vector to generate longitudinal waves, (b) spatially uniform vibration of the infinite plane along two perpendicular in-plane directions to generate transverse waves, (c) spatially uniform vibration of the infinite plane in a general direction.

2.4.1.3 Spherical waves in unbounded acoustic media

In some cases, the wave source is located on a curved surface rather than a plane one. Therefore, the boundary conditions of the wave equations should be defined on a curved surface. One of the common curved surfaces is a spherical surface on which a symmetric boundary condition is defined.

Symmetric vibration of a sphere or a spherically symmetric distribution of pressure in an acoustic medium leads to the generation and propagation of longitudinal spherical waves. To study symmetric spherical waves, it is easier to transform the acoustic wave equation (Eq. 2.16) and its boundary condition to spherical coordinate system [63]:

$$\frac{1}{r^2}\frac{\partial}{\partial r}\left(r^2\frac{\partial p}{\partial r}\right) = \frac{1}{c_o^2}\frac{\partial^2 p}{\partial t^2}$$
$$p(r=a) = f(t) \text{ and } r \geq a \qquad (2.54)$$

in which r is the radial distance measured from the origin and a is the radius of the sphere on which the pressure boundary condition is defined. It should be noted that due to the assumed spherical symmetry of the boundary condition, Eq. 2.54 is independent of the angular components in the spherical coordinate system.

If the pressure on the boundary condition is harmonically changing, i.e. $f(t) = P_o cos(\omega t)$, then the closed-form solution for Eq. 2.54 is [64]:

$$p(r,t) = P_o \frac{a}{r} cos(\omega t - k(r-a)), r \geq a \qquad (2.55)$$

Unlike plane waves that maintain their amplitude while propagating, spherical waves decay in amplitude proportionally to $\frac{1}{r}$. Figure 2.24 depicts the spatial decay of amplitudes in typical spherical waves (at a particular time).

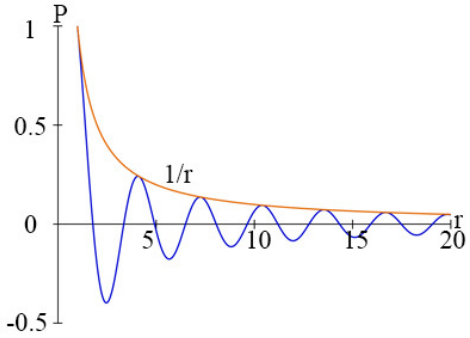

Figure 2.24 Spatial decay of spherical waves at a particular time.

2.4.2 The angular spectrum method

The angular spectrum method (ASM) is a method for solving the Helmholtz equation describing a scalar field of wave propagation in an unbounded half space including any two-dimensional (2D) source distribution of the scalar field. This analytical method is based on integral transform methods for solving PDEs. The main aim of transform methods is to simplify a given PDE and its boundary conditions by reducing the number of independent variable of the PDE. The ASM uses spatial Fourier transforms to simplify the Helmholtz equation to an equivalent ordinary differential equation, which has only one independent variable. In this section, the procedure regarding the ASM for solving a scalar-field Helmholtz equation is explained (the details and proofs of the integral transform methods and the ASM can be found in Refs. [65] and [2]).

Acoustic (ultrasonic) pressure (Eq. 2.16) and velocity potential (Eq. 2.18) are instances of scalar fields. Consider the following problem in the Cartesian coordinate system as depicted by Figure 2.25:

$$\begin{aligned} (k^2 + \nabla^2)\underline{A}(\boldsymbol{x}) &= 0 \\ \underline{A}(x_1, x_2, 0) &= \underline{A}_o(x_1, x_2) \end{aligned} \qquad (2.56)$$

where $\underline{A}$ is the phasor of a scalar field and $\underline{A}_o(x_1, x_2)$ is a known spatial distribution of the scalar

field on the plane $x_3 = 0$. Physically, $\underline{A}_o(x_1, x_2)$ describes the spatial distribution of a plane source of the scalar field. ASM evaluates the spatial distribution of the field on any plane parallel with the source plane ($x_3 = 0$) and located at any distance from the source (Figure 2.25).

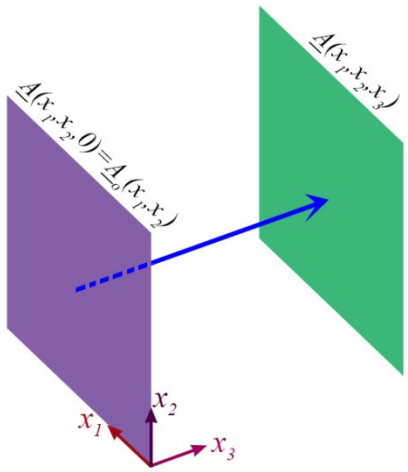

Figure 2.25 ASM and the boundary condition for Helmholtz's equation.

Briefly, the method uses the following steps[19] to calculate the wave field in front of the source plane [2]:

1- The field variable is represented as[20]: $\underline{A}(x_1, x_2 : x_3) \coloneqq \underline{A}(x_1, x_2, x_3)$.

2- The spatial distribution of the wave source located at $x_3 = 0$ is transformed into spatial frequency (k) domain using the 2D Fourier transform:

$$\underline{A}(k_1, k_2 : 0) = \mathcal{F}\left[\underline{A}(x_1, x_2 : 0)\right] \coloneqq \iint_{-\infty}^{+\infty} \underline{A}_o(x_1, x_2)\, e^{-i(k_1 x_1 + k_2 x_2)} dx_1 dx_2 \qquad (2.57)$$

3- A transfer function is utilized to calculate the field on a plane located at x_3 and parallel with the source plane. The transfer function actually propagates the source distribution forward in the spatial frequency domain:

$$\underline{A}(k_1, k_2 : x_3) = \underline{A}(k_1, k_2 : 0)\underline{H}(k_1, k_2 : x_3)$$
$$\underline{H}(k_1, k_2 : x_3) = \begin{cases} e^{-i|k_3|z} & \text{if } k_3^2 > 0 \\ e^{-|k_3|z} & \text{if } k_3^2 < 0 \end{cases} \qquad (2.58)$$

[19] The proof is available in [2].

[20] To discriminate between x_1 and x_2 on which the Fourier transforms are applied and x_3, which is not transformed, the second comma in $\underline{A}(x_1, x_2, x_3)$ is replaced by a separating colon [2].

$$k_3 = -\sqrt{k^2 - (k_1^2 + k_2^2)}$$

4- The inverse Fourier transform is used to transform the calculated field from the spatial frequency domain to spatial domain:

$$\underline{A}(x_1, x_2 : x_3) = \mathcal{F}^{-1}\left[\underline{A}(k_1, k_2 : x_3)\right]$$
$$:= \frac{1}{4\pi^2} \iint_{-\infty}^{+\infty} \underline{A}(k_1, k_2 : x_3)\, e^{i(k_1 x_1 + k_2 x_2)} dk_1 dk_2 \qquad (2.59)$$

The above procedure makes ASM an analytical method when the Fourier transform (and its inverse transform) is numerically evaluated. In this respect, fast Fourier transform (FFT) is utilized to discretely calculate the integral transforms [2].

It can be noted that $\underline{A}_o(x_1 x_2)$ need not to be a continuous distribution although it has to be bounded. This makes the ASM a powerful method when the distribution of the source has finite number of regional discontinuities. For instance, an ultrasonic wave source on any arbitrary plane surface with zero pressure outside the transducer region (**Ω**) on the source plane (Figure 2.26a) is an example of a boundary condition for which the ASM can be used. Multiple ultrasonic sources or ultrasonic transducers with an array of vibrating surfaces (Figure 2.26b) is also a discontinuous wave source that can be used as the boundary condition to solve the linearized wave equation using ASM.

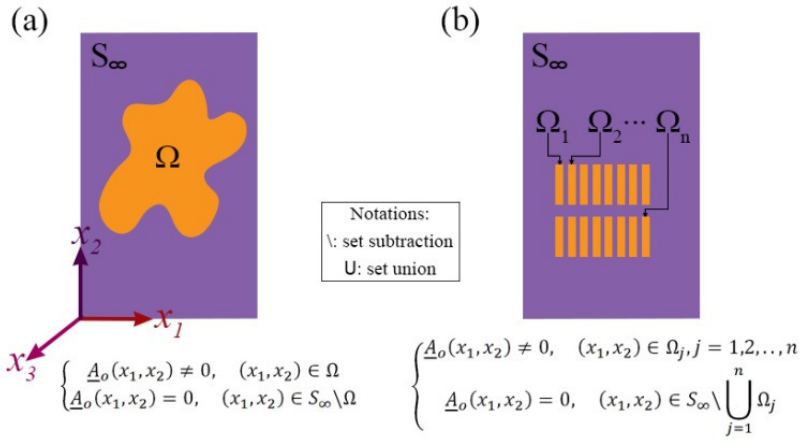

Figure 2.26 (a) A free-form plane scalar field source, (b) multiple wave sources or transducer array.

2.4.3 The finite element method

Closed-form and analytical methods for solving the wave equations are highly restricted

to media with simple geometries and boundary conditions. These methods fail particularly when the propagation medium contain both solid and liquid component interacting with each other. Complicated situation of wave propagation are analyzed through numerical methods such as finite difference or finite element methods. In this section, the formulation of the finite element method (FEM) for solving linear wave propagation in a coupled acoustic-structural medium (a medium with interacting solid and liquid components) is explained.

Time domain:

To derive the finite element formulation for a coupled solid-fluid medium, the fluid part is considered first. Multiplying the linear wave equation in fluids (Eq. 2.16) by an arbitrary smooth variational scalar field $\delta p \in \mathbb{R}$ (also called a test function) and integrating over the entire volume of the fluid Ω_f leads to [66]:

$$\int_{\Omega_\mathrm{f}} \delta p(\ddot{p} - c_o^2 \nabla^2 p) d\Omega_\mathrm{f} = 0$$
$$or \int_{\Omega_\mathrm{f}} (\ddot{p}\delta p - c_o^2 \delta p \nabla . \nabla p) d\Omega_\mathrm{f} = 0 \qquad (2.60)$$

where $\ddot{p} \coloneqq \frac{\partial^2 p}{\partial t^2}$. For the sake of consistency in notations, $\ddot{a} \coloneqq \frac{\partial^2 a}{\partial t^2}$ and $\dot{a} \coloneqq \frac{\partial a}{\partial t}$ are defined for a general field variable (either vector or scalar) 'a'.

Using the vector identity $\nabla \cdot (A\boldsymbol{V}) = A\nabla \cdot \boldsymbol{V} + (\nabla A) \cdot \boldsymbol{V}$ for a scalar valued function A and a vector field $\boldsymbol{V}$, the above equation becomes:

$$\int_{\Omega_\mathrm{f}} (\ddot{p}\delta p + c_o^2(\nabla \delta p \cdot \nabla p) - c_o^2 \nabla \cdot (\delta p \nabla p)) d\Omega_\mathrm{f} = 0 \qquad (2.61)$$

Therefore taking the advantage of the divergence theorem[21] leads to:

$$\int_{\Omega_\mathrm{f}} (\ddot{p}\delta p + c_o^2(\nabla \delta p \cdot \nabla p)) d\Omega_\mathrm{f} + \int_{\partial\Omega_\mathrm{f}} c_o^2 \delta p(\boldsymbol{n}^- \cdot \nabla p) ds = 0 \qquad (2.62)$$

The unit vector $\boldsymbol{n}^-$ is defined as the inward normal vector of the fluid surface[22].

[21] $\int_\Omega \nabla \cdot \boldsymbol{F} d\Omega = \int_{\partial\Omega} \boldsymbol{n} \cdot \boldsymbol{F} ds$, such that Ω is a simple closed volume with bounding surface $\partial\Omega$, $\boldsymbol{n}$ is the outward unit normal vector at each point of $\partial\Omega$ and $\boldsymbol{F}$ is a smooth vector field [78].

The fluid surface $\partial\Omega_{\mathrm{f}}$ is composed of subsurface(s) on which the pressure is explicitly defined S_{fp} and subsurface(s) with unknown pressure value $\partial\Omega_{\mathrm{f}} - S_{\mathrm{fp}}$. Since arbitrary, δp may vanish on S_{fp}. Therefore, Eq. 2.62 becomes:

$$\int_{\Omega_{\mathrm{f}}} (\ddot{p}\delta p + c_o^2(\nabla\delta p \cdot \nabla p))d\Omega_{\mathrm{f}} - \int_{\partial\Omega_{\mathrm{f}} - S_{\mathrm{fp}}} \rho_{\mathrm{f}} c_o^2 \delta p(T) ds = 0 \tag{2.63}$$

in which $T \coloneqq \boldsymbol{n}^- \cdot \frac{\partial \boldsymbol{v}}{\partial t} = \boldsymbol{n}^- \cdot \ddot{\boldsymbol{u}}_{\mathrm{f}}$ is defined using Eq. 2.15. The acceleration of the fluid particles on the surface $\partial\Omega_{\mathrm{f}} - S_{\mathrm{fp}}$ is denoted by $\ddot{\boldsymbol{u}}_{\mathrm{f}}$.

On some surface(s) denoted by S_{ft}, the parameter T may be explicitly determined as $T = T_{\mathrm{ft}}$. This may be utilized to model the oscillation of a rigid body exciting the fluid. In a special case $T_{\mathrm{ft}} = 0$ represents the condition of the fluid surfaces in contact with a rigid body or surface usually called a rigid baffle. On another surface denoted S_{fi}, impedance conditions can be explicitly determined to include radiation boundary condition. A radiation boundary condition has the form $T_{\mathrm{fi}} = -(\frac{1}{a_1}\dot{p} + \frac{1}{a_2}p)$. Absorbing or non-reflecting boundary condition can be implemented by using appropriate values for the parameters a_1 and a_2 [66].

The interaction of fluid with a solid structure at their shared interface (S_{fs}) can also be formulated through acoustic-structural interaction condition [66]. At the fluid-solid interface, the normal displacements of the fluid and solid surfaces must be identical, i.e. $\boldsymbol{n}^- \cdot \boldsymbol{u}_{\mathrm{f}} = \boldsymbol{n}^- \cdot \boldsymbol{u}_{\mathrm{s}}$. However, discontinuity in tangential component of the displacement is allowed if the perfect-slip condition is assumed. Taking the second time derivative of the acoustic-structural condition results in $T_{\mathrm{fs}} = \boldsymbol{n}^- \cdot \ddot{\boldsymbol{u}}_{\mathrm{s}}$.

Expanding Eq. 2.63 by considering the three different possibilities for T and $c_o^2 = \frac{\beta}{\rho_{\mathrm{f}}}$:

$$\begin{aligned}\int_{\Omega_{\mathrm{f}}} (\frac{1}{\beta}\ddot{p}\delta p + \frac{1}{\rho_{\mathrm{f}}}(\nabla\delta p \cdot \nabla p))d\Omega_{\mathrm{f}} - \int_{S_{\mathrm{ft}}} \delta p(T_{\mathrm{ft}}) ds + \int_{S_{\mathrm{fi}}} \delta p \left(\frac{1}{a_1}\dot{p} + \frac{1}{a_2}p\right) ds \\ - \int_{S_{\mathrm{fs}}} \delta p(\boldsymbol{n}^- \cdot \ddot{\boldsymbol{u}}_{\mathrm{s}}) ds = 0\end{aligned} \tag{2.64}$$

[22] In the Ref [66], the inward unit vector $\boldsymbol{n}^- = -\boldsymbol{n}$ is considered instead of the outward unit vector as in the divergence theorem.

This is the weak form[23] of the original differential equation.

To derive the finite element formulation for the solid part coupled with the fluid medium, an arbitrary displacement vector field variation (also called a test function) is multiplied by the equations of motion (Eq. 2.19) through vector dot product. Integrating the result over the solid volume (medium) leads to [60,66]:

$$\int_{\Omega_s} (\rho_s \ddot{\boldsymbol{u}} \cdot \delta \boldsymbol{u} - (\nabla \boldsymbol{\sigma}^{\mathrm{T}}) \cdot \delta \boldsymbol{u}) d\Omega = 0 \tag{2.65}$$

such that $\delta \boldsymbol{u} \in \mathbb{R}^3$ is a variational displacement field, ρ_s is the solid density and $\boldsymbol{\sigma}^{\mathrm{T}}$ is the transpose of the stress tensor. The second term can be written as [66]:

$$\nabla \boldsymbol{\sigma}^{\mathrm{T}} \cdot \delta \boldsymbol{u} = \nabla \cdot (\boldsymbol{\sigma} \delta \boldsymbol{u}) - \sum_{i=1}^{3} \sum_{j=1}^{3} \sigma_{ij} \frac{\partial \delta u_j}{\partial x_i} \tag{2.66}$$

Using the definition of small strain (Eq. 2.21) and substituting Eq. 2.66 in 2.65:

$$\int_{\Omega_s} (\rho_s \ddot{\boldsymbol{u}} \cdot \delta \boldsymbol{u} + \sum_{i=1}^{3} \sum_{j=1}^{3} \sigma_{ij} \delta \varepsilon_{ij}) d\Omega - \int_{\Omega_s} \nabla \cdot (\boldsymbol{\sigma} \delta \boldsymbol{u}) d\Omega = 0 \tag{2.67}$$

The second integral can be written as a surface integral on the solid surface using the divergence theorem, therefore:

$$\int_{\Omega_s} (\rho_s \ddot{\boldsymbol{u}} \cdot \delta \boldsymbol{u} + \sum_{i=1}^{3} \sum_{j=1}^{3} \sigma_{ij} \delta \varepsilon_{ij}) d\Omega - \int_{\partial \Omega_s} \boldsymbol{n} \cdot (\boldsymbol{\sigma} \delta \boldsymbol{u}) ds = 0 \tag{2.68}$$

It should be noted that $\boldsymbol{n} \cdot (\boldsymbol{\sigma} \delta \boldsymbol{u}) = \delta \boldsymbol{u} \cdot \boldsymbol{\sigma}^{\mathrm{T}} \boldsymbol{n} = \delta \boldsymbol{u} \cdot \boldsymbol{t_n}$ such that $\boldsymbol{t_n} \in \mathbb{R}^3$ is the traction vector on a surface with the unit normal vector $\boldsymbol{n}$ [60]. The solid surface can be divided into a free subsurface (S_t) on which the traction vector is known ($\boldsymbol{t_n}$) and a subsurface adjacent to the fluid (S_{fs}). Since the fluid is assumed to be inviscid (no shear forces), the normal component of the traction vector on S_{fs} must be equal to the fluid (acoustic) pressure, i.e. $\boldsymbol{t_n} \cdot \boldsymbol{n} = -p$ (the negative sign is due to the definition of positive pressure). Therefore, Eq. 2.68 becomes [60]:

[23] The equation only needs spatial C^1 continuity (continuous derivatives up to the first order) as opposed to the original PDE demanding C^2 continuity.

$$\int_{\Omega_s}(\rho_s \ddot{\boldsymbol{u}}\cdot\delta\boldsymbol{u}+\sum_{i=1}^{3}\sum_{j=1}^{3}\sigma_{ij}\delta\varepsilon_{ij})d\Omega-\int_{S_t}\delta\boldsymbol{u}\cdot\boldsymbol{t_n}ds+\int_{S_{\mathrm{fs}}}p\delta\boldsymbol{u}\cdot\boldsymbol{n}ds=0 \qquad (2.69)$$

which is the weak form of the equation of motion in solid coupled with fluid.

The final step to derive the finite element formulation for a coupled acoustic-structural problem is to discretize the weak form equations (Eq. 2.64 and Eq. 2.69). To this end, the trial and test functions are spatially approximated using interpolation functions for the acoustic pressure filed (in the fluid) and the displacement field (in the solid) [60]. The Galerkin approach leads to the following approximation:

$$\begin{aligned} p\approx\boldsymbol{HP},\ \delta p\approx\boldsymbol{H}\delta\boldsymbol{P}\\ \boldsymbol{u}\approx\boldsymbol{NU},\ \delta\boldsymbol{u}\approx\boldsymbol{N}\delta\boldsymbol{U}\end{aligned} \qquad (2.70)$$

in which $\boldsymbol{H}\in\mathbb{M}^{1\times\mathrm{M}}$ and $\boldsymbol{N}\in\mathbb{M}^{3\times3\mathrm{N}}$ are a matrices[24] of interpolation functions, $\boldsymbol{P},\delta\boldsymbol{P}\in\mathbb{M}^{\mathrm{M}\times1}$ and $\boldsymbol{U},\delta\boldsymbol{U}\in\mathbb{M}^{3\mathrm{N}\times1}$ denote the nodal pressure and nodal displacements in the discretized fluid and solid media respectively. There are 'M' pressure nodes and 'N' structural nodes in the discretized medium. It should be noted that $\boldsymbol{N}$ needs three rows associated with three independent Cartesian displacement components; consequently, the number of structural degrees of freedom is '3N'.

Substituting the approximations (Eq. 2.70) into Eq. 2.64 and Eq. 2.69 results in the final form of the finite element formulation for the coupled medium:

$$\boldsymbol{M}_{\mathrm{f}}\ddot{\boldsymbol{P}}+\boldsymbol{C}_{\mathrm{fi}}\dot{\boldsymbol{P}}+(\boldsymbol{K}_{\mathrm{f}}+\boldsymbol{K}_{\mathrm{fi}})\boldsymbol{P}-\boldsymbol{S}\ddot{\boldsymbol{u}}-\boldsymbol{F}_{\mathrm{f}}=\boldsymbol{0} \qquad (2.71a)$$

$$\boldsymbol{M}_{\mathrm{s}}\ddot{\boldsymbol{u}}+\boldsymbol{K}_{\mathrm{s}}\boldsymbol{u}+\boldsymbol{S}^{T}\boldsymbol{P}-\boldsymbol{F}_{\mathrm{s}}=\boldsymbol{0} \qquad (2.71b)$$

such that:

$$\begin{aligned}\boldsymbol{M}_{\mathrm{f}}=\int_{\Omega_{\mathrm{f}}}\frac{1}{\beta}\boldsymbol{H}^{\mathrm{T}}\boldsymbol{H}\,d\Omega_{\mathrm{f}}\ ,\ \boldsymbol{C}_{\mathrm{fi}}=\int_{S_{\mathrm{fi}}}\frac{1}{\mathrm{a}_1}\boldsymbol{H}^{\mathrm{T}}\boldsymbol{H}ds\\ \boldsymbol{K}_{\mathrm{f}}=\int_{\Omega_{\mathrm{f}}}\frac{1}{\rho_f}\nabla\mathbf{H}^{\mathrm{T}}\nabla\mathbf{H}\,d\Omega_{\mathrm{f}}\ ,\ \boldsymbol{K}_{\mathrm{fi}}=\int_{S_{\mathrm{fi}}}\frac{1}{\mathrm{a}_2}\boldsymbol{H}^{\mathrm{T}}\boldsymbol{H}ds\end{aligned} \qquad (2.72a)$$

[24] $\mathbb{M}^{a\times b}$ is a matrix space of matrices with *a* rows and *b* columns.

$$\boldsymbol{S} = \int_{S_{\mathrm{fs}}} \boldsymbol{H}^{\mathrm{T}}[\boldsymbol{n}^{-}\boldsymbol{N}]ds \ , \mathbf{F}_{\mathrm{f}} = \int_{S_{\mathrm{ft}}} \boldsymbol{H}^{\mathrm{T}} T_{\mathrm{ft}}\, ds$$

$$\boldsymbol{M}_{\mathrm{s}} = \int_{\Omega_{\mathrm{s}}} \rho_s \boldsymbol{N}^{\mathrm{T}}\boldsymbol{N}\, d\Omega_{\mathrm{s}} \ , \boldsymbol{K}_{\mathrm{s}} = \int_{\Omega_{\mathrm{s}}} \boldsymbol{B}^{\mathrm{T}}\boldsymbol{D}\boldsymbol{B}\, d\Omega_{\mathrm{s}}$$

$$\boldsymbol{F}_{\mathrm{s}} = \int_{\mathrm{S_t}} \boldsymbol{N}^{\mathrm{T}}\boldsymbol{t_n} ds \tag{2.72b}$$

in which $\boldsymbol{n}^{-} \in \mathbb{M}^{1\times 3}$, $\boldsymbol{t_n} \in \mathbb{M}^{3\times 1}$. The matrix $\mathbf{B} \in \mathbb{M}^{6\times 3N}$ is the small strain interpolator containing the spatial derivatives of **N** associated with the row vector representation of the small strain tensor ($\boldsymbol{\varepsilon} = [\varepsilon_{11}, \varepsilon_{22}, \varepsilon_{33}, \varepsilon_{23}, \varepsilon_{31}, \varepsilon_{12}]$). Stress-strain constitutive relation for linear elastic materials is expressed by $\boldsymbol{\sigma} = \mathbf{D}\boldsymbol{\varepsilon}$ such that $\mathbf{D} \in \mathbb{M}^{6\times 6}$.

To solve the coupled equations 2.71a and 2.71b, either an implicit or an explicit temporal discretization scheme can be utilized. The explicit scheme uses the explicit central difference integration rule along with diagonalization of the mass matrix (using a diagonal or lumped mass matrix). This makes the scheme computationally more effective and less expensive than the implicit method for models with large number of degrees of freedom [60].

Frequency domain:

Analysis of wave propagation in the frequency domain is associated with the steady-state propagation of harmonic waves inside a medium. In this case, all the particles in the medium harmonically oscillate with the particular frequency (ω) of the propagating harmonic waves.

Due to the linearity of the wave differential equations, the complex representation of the harmonic oscillation is utilized and the real part is associated with the meaningful physical phenomenon. Accordingly, a typical variable and its time derivatives in Eq. 2.64 and Eq. 2.69 can be replaced with:

$$X(\boldsymbol{x}, t) = \underline{X}(\boldsymbol{x})e^{i\omega t}$$

$$\dot{X}(\boldsymbol{x}, t) = i\omega X \tag{2.73}$$

$$\ddot{X}(\boldsymbol{x}, t) = -\omega^2 X$$

where $\underline{X} \in \mathbb{C}$ is the phasor of the oscillation. Implementing the above equations in Eq. 2.64 and

Eq. 2.69 and using the same Galerkin method for spatial discretization leads to[25] [66]:

$$[-\omega^2 \boldsymbol{M}_{\mathrm{f}} + i\omega \boldsymbol{C}_{\mathrm{fi}} + \boldsymbol{K}_{\mathrm{f}}]\underline{\boldsymbol{P}} + \omega^2 \boldsymbol{S}\underline{\boldsymbol{u}} - \underline{\boldsymbol{F}}_{\mathrm{f}} = \boldsymbol{0} \tag{2.74a}$$

$$[-\omega^2 \boldsymbol{M}_{\mathrm{s}} + \boldsymbol{K}_{\mathrm{s}}]\underline{\boldsymbol{u}} + \boldsymbol{S}^{\mathrm{T}}\underline{\boldsymbol{P}} - \underline{\boldsymbol{F}}_{\mathrm{s}} = \boldsymbol{0} \tag{2.74b}$$

in which the matrices $\boldsymbol{M}_{\mathrm{f}}$, $\boldsymbol{C}_{\mathrm{fi}}$, $\boldsymbol{K}_{\mathrm{f}}$, $\boldsymbol{S}$, $\boldsymbol{M}_{\mathrm{s}}$ and $\boldsymbol{K}_{\mathrm{s}}$ are as previously defined and the completed valued single-column matrices are nodal phasors.

Analyzing the propagation of harmonic waves in a steady-state propagation regime (Eq. 2.74) is referred to as steady-state dynamic analysis. The equations (Eq. 2.74) form two coupled linear complex-valued system of equations that can be solved through Gauss elimination method (direct method) [66].

Time domain vs. frequency domain analyses:

The analysis of wave propagation in time or frequency domains depends on whether the wave transmitted into the medium is in the form of a pulse or long-duration continuous harmonic waves. Although time domain can be used to analyze long-duration continuous waves, it is usually appropriate to perform an analysis when the transient part of particle oscillations is not a concern. Obviously, the duration of continuous waves should be long enough to let all the particles in the medium pass their transient oscillations and reach steady-state harmonic oscillations.

Through a simulation of QUS ultrasound using the FEM, the propagation of a short ultrasonic pulse in a medium (bone or any material subjected to the study) is simulated in time domain. Chapters 4 and 5 of this thesis are based on time-domain simulation of QUS. On the other hand, the finite element simulations of harmonic waves as in chapters 3 and 6 of this thesis were performed using steady-state dynamic analysis in frequency-domain.

2.5 Wave propagation phenomena and definitions

Several phenomena and definitions regarding ultrasonic wave propagation are referred to through this thesis; therefore, they are required to be explained and understood beforehand.

[25] The second term in $(\frac{1}{a_1} i\omega \underline{p} + \frac{1}{a_2}\underline{p})$ is intentionally eliminated leaving $\boldsymbol{K}_{\mathrm{fi}} = \boldsymbol{0}$ according to the reference [66].

2.5.1 Wave interface

Wave interface occurs when two or more waves meet at the same location. In a linear wave propagation regime (described by the linear wave equations), the principle of superposition applies. Therefore, the variables by which the waves are defined (pressure, stress, displacement or potentials) can be superposed on each other at their interfaces. Superposing the waves at an interface may lead to amplifying or weakening the wave variable at the interface. In this regard, constructive and destructive interfaces are defined.

For instance, superposing harmonic waves with the same frequency but out of phase (180°) leads to net reduction in the amplitude of the resultant waves. This is called phase cancellation. A complete phase cancellation occurs for out-of-phase harmonic waves with the same frequency and amplitude.

2.5.2 Wavefront and wave ray

A wavefront is an imaginary surface over which the wave disturbance is uniformly distributed at each time instance [67]. A uniform distribution of wave disturbance indicates the same amplitude and phase over the imaginary surface (wave front) in the case of harmonic waves. The shape of a wavefront depends on the shape of the wave source. A wave ray is an imaginary line (or curve) being perpendicular to the wave fronts and indicating the direction of the propagation.

Plane and spherical waves have plane and spherical wavefronts respectively. Figure 2.27a and b demonstrate wavefronts and rays for harmonic plane and spherical wave. In contrary to plane waves having a unidirectional ray, spherical waves have infinite number of rays indicating propagation in infinite number of directions.

Wavefronts may sometimes change shape[26], become distorted or several wavefronts may foregather to generate a wave front with another shape. For instance, when several sources of spherical waves are horizontally aligned, the resultant wavefronts gradually change their spherical shape to a plane shape as the waves propagate away from the source (Figure 2.27c).

[26] The shape variation of a particular wavefront can be observed if the wavefront is considered at sequential instances of time. In the case of harmonic waves, a wave front can be associated with a particular phase. For instance, a spherical wavefront symmetrically grows as its corresponding spherical waves propagate.

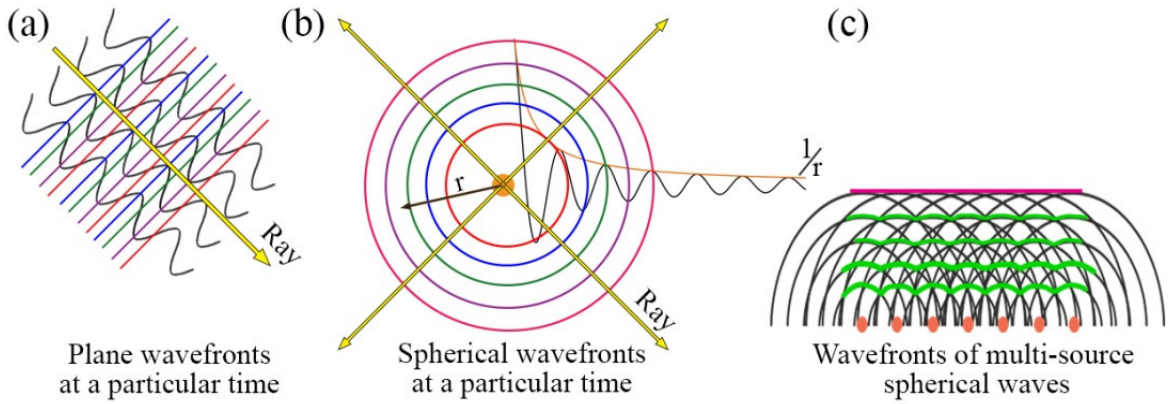

Figure 2.27 (a) and (b) wavefronts and rays for plane and spherical waves, (c) resultant wavefronts of horizontally aligned sources of spherical waves.

2.5.3 Reflection, refraction, mode conversion, and scattering

Reflection, refraction and scattering of waves happen at material interfaces when waves travel from one medium to another. When incident waves reach the material interface between two media, there will be waves reflected back into the first medium and waves transmitted into the second medium [2]. The reflection may occur in a single direction with the same angle as the angle of the incident waves (Figure 2.28a) or several directions (Figure 2.28b) depending on the geometry (global geometry and surface details) of the interface. A single-direction reflection is called specular reflection and multi-direction reflection is categorized as scattering, which is described below. Refraction occurs if the part of the waves transmitted into the second medium (or generated at the interface but in the second medium) has different direction than that of the incident waves (Figure 2.28c).

Scattering is the interaction of waves with an inhomogeneity, also called scatterer, in the medium. Inhomogeneity is a region or object in the medium with properties differing from its surrounding medium. The deformation and whole body movement of a scatterer also contribute to the scattering phenomenon as well [1,2]. When incident waves are scattered by an object, there will be waves propagating in the same direction as the incident waves (forward scattering) and waves propagating backwards from the object (backscatter). Scattering depends on the material properties and geometry of the scatterer as well as the frequency or the wave length of the waves. For a scatterer with a particular shape and size, the magnitude of scattered waves increases with the frequency of the incident waves. Generally, an increase in backscattering or a decrease in forward scattering occur as the wave frequency increases (equivalently as the

wavelength decreases compared with the size of the scatterer) [1,2].

Mode conversion is defined as the generation of one type of wave, either longitudinal or transverse, from another at the material interface. This phenomenon occurs at fluid-solid interfaces when the direction of incident waves are not perpendicular to the interface (Figure 2.28d).

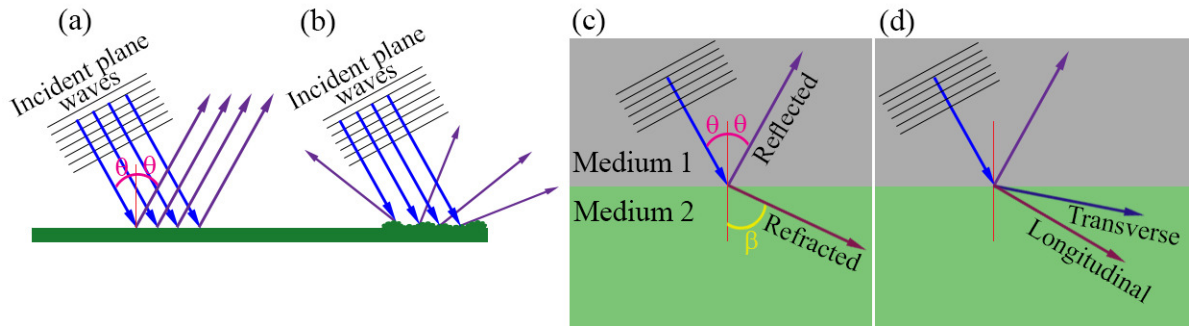

Figure 2.28 (a) Reflection at a surface, (b) scattering at a surface, (c) reflection at a surface and refraction into the second medium, (d) mode conversion into the second medium.

2.5.4 Wave energy and intensity

Wave propagation is associated with kinetic energy due to particles velocities and potential energy due to elastic deformations. The kinetic energy of a small element of volume (dV) locally vibrating with velocity $\boldsymbol{v}$ is [2]:

$$dE_{\mathrm{KE}} = \epsilon_{\mathrm{KE}}(\boldsymbol{x},t)dV$$
$$\epsilon_{\mathrm{KE}}(\boldsymbol{x},t) = \frac{1}{2}\rho_o|\boldsymbol{v}|^2 = \frac{1}{2}\rho_o\boldsymbol{v}\cdot\boldsymbol{v} \qquad (2.75)$$

where $\epsilon_{KE}(\boldsymbol{x},t)$ is called the kinetic energy density expressing energy per unit of volume.

The potential energy associated with elastic deformation of a small volumetric element can be considered as:

$$dE_{\mathrm{PE}} = \epsilon_{\mathrm{PE}}(\boldsymbol{x},t)dV \qquad (2.76)$$

in which $\epsilon_{PE}(\boldsymbol{x},t)$ is the potential elastic energy density which has the following forms for compressible fluid and linear elastic solid media respectively [2,60]:

$$\epsilon_{\mathrm{PE}}(\boldsymbol{x},t) = \frac{p^2}{2\rho_o c_o^2} \qquad (2.77a)$$

$$\epsilon_{\mathrm{PE}}(\boldsymbol{x},t)=\frac{1+\nu}{2\mathrm{E}}(\sigma_{11}^2+\sigma_{22}^2+\sigma_{33}^2+2\sigma_{12}^2+2\sigma_{23}^2+2\sigma_{31}^2)-\frac{\nu}{\mathrm{E}}(\sigma_{11}+\sigma_{22}+\sigma_{33})^2 \tag{2.77b}$$

The constants E and ν are the Young's modulus and Poisson's ratio of the material of the solid medium[27].

Integrating the total energy density, i.e. $\epsilon=\epsilon_{\mathrm{KE}}+\epsilon_{\mathrm{PE}}$, over a volume (V) of the medium leads to the total energy inside the volume:

$$E(t)=E_{\mathrm{KE}}+E_{\mathrm{PE}}=\int_{\mathrm{V}}\epsilon(\boldsymbol{x},t)dV \tag{2.78}$$

The first law of thermodynamic for a system[28] is :

$$\frac{\partial E}{\partial t}=\dot{E}_{in}-\dot{E}_{out}=\dot{W}_{in}-\dot{W}_{out} \tag{2.79}$$

which states that the time rate of increase of the total energy ($\frac{\partial E}{\partial t}$) of the system (a closed volume inside the medium virtually separated from its surrounding) in the absence of heat transfer, is equal to the net time rate of energy addition by work ($\dot{W}_{in}-\dot{W}_{out}$) done on the system [59]. In this regard the flux of energy flowing out of the system will be $-\frac{\partial E}{\partial t}=\dot{E}_{out}-\dot{E}_{in}$.

By using Eq. 2.75, 2.77a and substitution by Eq. 2.7, 2.12 and 2.15, the acoustic energy[29] flux flowing out of a volume is [2]:

$$W(t)=-\frac{\partial E}{\partial t}=\int_{V}(\boldsymbol{v}\cdot\nabla p+p\nabla\cdot\boldsymbol{v})dV=\int_{V}\nabla\cdot(p\boldsymbol{v})dV \tag{2.80}$$

such that $W(t)$ denotes the time rate of energy change and has the unit of power. To demonstrate that Eq. 2.80 reflects the outward energy flux, the integral in converted to a surface integral by the divergence theorem [2]:

[27] $\mathrm{E}=\frac{\mu(3\lambda+2\mu)}{\lambda+\mu}$ and $\nu=\frac{\lambda}{2(\lambda+\mu)}$. Also $\mu=\rho_o\mathrm{c}_T^2$ and $\lambda=\rho_o(\mathrm{c}_L^2-2\mathrm{c}_T^2)$ according to Eq. 2.26 and Eq. 2.30.

[28] Considering a system rather than a control volume indicates the Lagrangian form of equations. However, in small deformation regime Lagrangian and Eulerian forms are identical.

[29] Time-rate of energy change for wave propagation in solid media is discussed in Appendix B.

$$W(t) = \int_{S_V} (p\boldsymbol{v}) \cdot \boldsymbol{n} dS \tag{2.81}$$

in which S_V is the bounding surface of the volume and $\boldsymbol{n}$ is the outward unit vector normal to the surface. The vector $p\boldsymbol{v} \in \mathbb{R}^3$ is defined as instantaneous acoustic intensity ($\mathbf{I}$) with the unit of energy flow per unit area (power/unit area):

$$\mathbf{I}(\boldsymbol{x}, t) = p\boldsymbol{v} \tag{2.82}$$

which expresses energy flux per unit area and in the direction of the velocity.

Energy density and intensity are usually calculated as time-averaged values for acoustic harmonic waves with oscillation period of T:

$$\overline{\epsilon}(\boldsymbol{x}) = \frac{1}{T}\int_0^T \epsilon(\boldsymbol{x}, t) dt \tag{2.83a}$$

$$\overline{\mathbf{I}}(\boldsymbol{x}) = \frac{1}{T}\int_0^T \boldsymbol{I}(\boldsymbol{x}, t) dt \tag{2.83b}$$

For plane harmonic acoustic waves, i.e. $p(x,t) = \mathrm{Re}[P_o e^{i(\omega t - kx)}]$, the time-averaged energy density and time-averaged intensity are [2]:

$$\overline{\epsilon}(x) = \frac{P_o^2}{2\rho_o c_o^2} \tag{2.84a}$$

$$\overline{\boldsymbol{I}}(x) = \frac{P_o^2}{2\rho_o c_o}\boldsymbol{n}, \qquad \text{or} \qquad |\overline{\boldsymbol{I}}(x)| = \overline{I}(x) = \frac{P_o^2}{2\rho_o c_o} \tag{2.84b}$$

The relation between pressure (p) and velocity ($\boldsymbol{v}$) for plane harmonic waves is obtained by Eq. 2.15 (or Eq. 2.14) and discussed in the next section. As a remark, it should be noted that energy (and intensity) is a real valued quantity with physical interpretation; therefore, the real part of the complex representation of harmonic waves should be used in energy calculations.

2.5.5 Impedance, and matching layer

Impedance is a quantity associated with harmonic longitudinal (pressure) waves. As previously demonstrated (Eq. 2.33), harmonic waves can be written using complex variables.

The pressure and velocity fields in a general harmonic wave field are[30]:

$$\underline{p}(\boldsymbol{x},t) = \underline{p}(\boldsymbol{x},\omega)e^{i\omega t} \tag{2.85}$$

$$\underline{\boldsymbol{v}}(\boldsymbol{x},t) = \underline{v}(\boldsymbol{x},\omega)\hat{\boldsymbol{v}}e^{i\omega t} \tag{2.86}$$

such that $\hat{\boldsymbol{v}} = \frac{\underline{\boldsymbol{v}}(\boldsymbol{x},\omega)}{|\underline{\boldsymbol{v}}(\boldsymbol{x},\omega)|}$ is the unit vector specifying the direction of the velocity.

Impedance has three definitions in acoustics. The specific acoustic impedance ($\underline{Z} \in \mathbb{C}$) is defined as:

$$\underline{Z}(\boldsymbol{x},\omega) \coloneqq \frac{\underline{p}(\boldsymbol{x},\omega)}{\underline{v}(\boldsymbol{x},\omega)} \tag{2.87}$$

which has the unit of Rayleigh ($\mathrm{Pa.\,s/m}$) Abbreviated as Rayl (also $1\mathrm{MRayl} = 10^6\mathrm{Rayl}$). Acoustic pressure and particle velocity at a point are not usually in phase leading to a complex variable impedance. Difference in phase happens in the propagation of non-plane waves or when attenuation affects the waves (section 2.5.6).

For a harmonic wave with a particular frequency, combining Eq. 2.82, 2.85, 2.86 and Eq. 2.87 leads to:

$$\begin{aligned}\mathbf{I}(\boldsymbol{x},t) &= \mathrm{Re}\left[\underline{p}(\boldsymbol{x})e^{i\omega t}\right]\mathrm{Re}\left[\frac{\underline{p}(\boldsymbol{x})}{\underline{Z}(\boldsymbol{x})}e^{i\omega t}\hat{\boldsymbol{v}}\right] \\ &= \left[\frac{p^2(\boldsymbol{x})}{Z(\boldsymbol{x})}\cos(\omega t+\varphi)\,cos(\omega t+\psi)\right]\hat{\boldsymbol{v}}\end{aligned} \tag{2.88}$$

such that $p(\boldsymbol{x},\omega) = \left|\underline{p}(\boldsymbol{x})\right|$ and $Z(\boldsymbol{x}) = \left|\underline{Z}(\boldsymbol{x})\right|$. This indicates that:

$$I(\boldsymbol{x},t) \sim \frac{p^2(\boldsymbol{x},t)}{Z(\boldsymbol{x})} \text{ or } \bar{I}(\boldsymbol{x}) \sim \frac{p^2(\boldsymbol{x})}{Z(\boldsymbol{x})} \tag{2.89}$$

in which $I(\boldsymbol{x},t) = |\mathbf{I}(\boldsymbol{x},t)|$. Since any oscillation at a particular spatial location can be written in terms of temporal harmonic terms using Fourier transform, this result (Eq. 2.89) also holds for non-harmonic waves.

If different spatial locations are not to be compared, the following holds at any particular location:

[30] As previously defined, underlining a variable indicates a complex variable.

$$I(\boldsymbol{x},t)\sim p^2(\boldsymbol{x},t) \text{ or } \bar{I}(\boldsymbol{x})\sim p^2(\boldsymbol{x}) \tag{2.90}$$

Acoustic impedance uses the total acoustic force $\underline{F}(\boldsymbol{x},\omega)$ acting on a particular surface and has the following definition (the unit is $\mathrm{N.s/m}$):

$$\underline{Z_a}(\boldsymbol{x},\omega)=\frac{\underline{F}(\boldsymbol{x},\omega)}{\underline{v}(\boldsymbol{x},\omega)} \tag{2.91}$$

The characteristic (acoustic) impedance (Z_o) is defined as the specific acoustic impedance for plane harmonic waves. According to Eq. 2.45, Pressure and velocity can be regarded as $p(x,t)=\underline{P_o}e^{-(i\omega t+kx)}$ and $v(x,t)=\underline{v_o}e^{-(i\omega t+kx)}$ for plane harmonic waves propagating in a general direction x. Phases are assumed for the pressure and velocity by assuming complex values for $\underline{P_o}$ and $\underline{v_o}$. Substituting pressure and velocity terms in Eq. 2.15 and using $\mathrm{c}_o^2=\frac{1}{\kappa\rho_o}$ leads to:

$$Z_o=\frac{\underline{P_o}}{\underline{v_o}}=\frac{P_o e^{i\varphi_1}}{v_o e^{i\varphi_2}}=\mathrm{c}_o\rho_o\in\mathbb{R}\rightarrow\varphi_1=\varphi_2\rightarrow Z_o=\frac{P_o}{v_o}=\mathrm{c}_o\rho_o \tag{2.92}$$

indicating that the pressure and velocity must be in-phase in a plane harmonic waves. Therefore, Eq. 2.89 only depends on $p^2(\boldsymbol{x},t)$ or $p^2(\boldsymbol{x})$.

Being independent of location and frequency, the characteristic impedance only depends on the properties of the material. This parameter is very useful in investigating energy transmission and reflection at material boundaries in a wave propagation medium.

Assume harmonic plane longitudinal waves traveling in a semi-infinite medium are perpendicularly incident on a material discontinuity. The material discontinuity separates two media (Figure 2.29a) having different characteristic impedance properties, i.e. Z_{o1} and Z_{o2}. The continuity of pressure and velocity at the boundary leads to the following coefficients regarding the reflected and transmitted waves at the boundary [2]:

$$R_{\mathrm{A}}=\frac{P_{\mathrm{Re}}}{P_{\mathrm{In}}}=\frac{Z_{o2}-Z_{o1}}{Z_{o2}+Z_{o1}} \tag{2.93a}$$

$$T_A=\frac{P_{\mathrm{Tr}}}{P_{\mathrm{In}}}=1+R_A \tag{2.93b}$$

$$R_{\mathrm{I}} = \frac{\bar{I}_{\mathrm{Re}}}{\bar{I}_{\mathrm{In}}} = \left[\frac{Z_{o2} - Z_{o1}}{Z_{o2} + Z_{o1}}\right]^2 \tag{2.93c}$$

$$T_{\mathrm{I}} = \frac{\bar{I}_{\mathrm{Tr}}}{\bar{I}_{\mathrm{In}}} = 1 - R_{\mathrm{I}} \tag{2.93d}$$

in which R_{A} and T_A are amplitude reflection and transmission coefficients respectively. The reflection and transmission of energy are respectively explained by the time-averaged intensity reflection coefficient (R_{I}) and time-averaged intensity transmission coefficient (T_{I}).

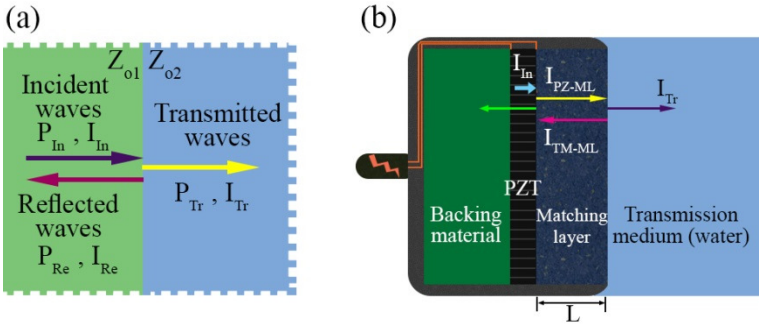

Figure 2.29 (a) Reflection and transmission of plane waves at the boundary of two media, (b) Structure of a PZT transducer including backing material and matching layer.

These coefficients are useful in investigating wave propagation in layered media specially designing ultrasonic transducers. Assume the vibrating material of a transducer to be piezoelectric material Lead zirconate (PZT) ceramic ($Z_o = 29.6$ MRayl) is exposed to either air ($Z_o = 0.000429$ MRayl) or water ($Z_o = 1.5$ MRayl). Therefore, Z_{o1} in Figure 2.29a is associated with PZT and Z_{o2} is associated with air or water. The intensity transmission coefficient for the case of transmission of ultrasonic waves into air and water are 0.00006 and 0.18 respectively. This indicates that almost all of the wave energy is reflected back to the transducer resulting in weak energy transmission. The reflected energy back into the PZT material converts to heat and may cause the transducer to mechanically fail.

To transmit most of the wave energy from PZT material to the medium, a matching layer is located between the PZT and the medium (Figure 2.29b). Additionally, backing material is used to prevent wave reflection back into PZT by damping the reflected energy (Figure 2.29b).

Assume the intensity of harmonic plane waves generate in the PZD material to be I_{In}. At the boundary of the PZT material and the matching layer only a portion of energy is transmitted

into the matching layer, i.e. $I_{\mathrm{PZ-ML}}$. Consequently, some of the energy is transmitted into the transmission medium I_{Tr} and the rest is reflected back ($I_{\mathrm{TM-ML}}$) by the boundary (Figure 2.29b). Full transmission of energy from the transducer to the transmission medium occurs ($\frac{I_{\mathrm{Tr}}}{I_{\mathrm{In}}} = 1$) for a particular impedance and thickness of the matching layer [2]:

$$Z_{oM} = \sqrt{Z_{oPZ} Z_{oTM}}, \qquad L = \frac{\lambda}{4} \tag{2.94}$$

such that Z_{oM}, Z_{oPZ} and Z_{oTM} are the characteristic impedance of the matching layer, PZT material and the transmission medium. The wavelength in the matching layer with thickness L is denoted by λ.

Since the optimum length of its matching layer depends on the frequency of the generated waves, a transducer cannot efficiently transmit waves with an arbitrary large range of frequencies [68]. Therefore, only an effective bandwidth of frequencies is considered. A transducer that is able to transmit a broad range of frequencies (large bandwidth) is called a broadband transducer. The larger the bandwidth the temporally shorter the pulse[31] is generated by the transducer [68].

2.5.6 Attenuation

Attenuation refers to the diminishing of the intensity or the amplitude of waves as they propagate through a medium [2]. The causes of attenuation are geometrical spreading of the waves (geometrical attenuation), wave scattering, energy absorption, and mode conversion.

Geometrical attenuation: when a finite-dimensional source of mechanical waves is exposed to a relatively large medium, the wave energy spreads out into the medium. Spreading of the energy in the medium leads to general decrease in the wave intensity and amplitude as the location gets farther from the source. The wave intensity and amplitude may alternately decrease and increase in distances close to the source (near field) due to constructive wave interfaces, however they eventually decrease in farther distances from the source (far field).

An example of occurrence of geometrical attenuation is the propagation of longitudinal spherical waves. It is obvious that the pressure amplitude ($P_o \frac{a}{r}$) decays as the waves propagate away from the source (Eq. 2.55).

[31] As one of the properties of transformation between time and frequency domains using Fourier transforms.

Wave scattering: the mechanism of wave scattering in wave attenuation is the same as geometrical attenuation, i.e. spreading the wave energy in different directions. However, being not directly dependent on the wave source, scattering occurs due to the existence of inhomogeneous objects (scatterer) or regions in the medium.

Energy absorption: some part of the wave energy may diminish due to the conversion of mechanical energy to other kinds of energy, i.e. heat, light, or chemical energy.

Mode conversion: conversion between wave modes (longitudinal and transverse) creates waves with different directions and velocities leading to wave attenuation.

To measure the attenuation in a material, the intensity of waves is measured and compared before and after propagating through a material specimen. Except the geometrical attenuation that depends on the source, the attenuation due to the rest of mechanisms depends on the properties of the material. Therefore, plane waves[32] (or wave with nearly plane wavefronts) are utilized to eliminate the effect of the geometrical attenuation [2]. An ideal empirical scheme for measuring attenuation is demonstrated in Figure 2.30a. In the ideal circumstances, it is assumed the specimen is surrounded by a medium, called a coupling medium, with zero attenuation. Additionally, the coupling medium and the specimen are perfectly matched indicating that there is no wave reflection at their interfaces[33].

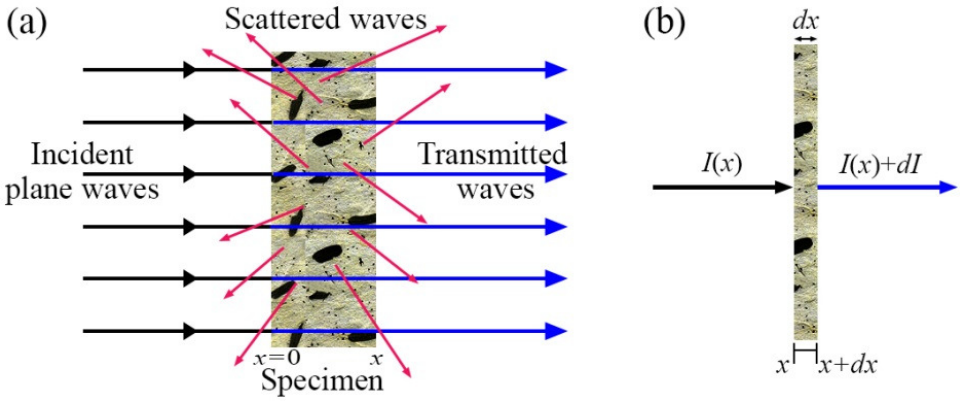

Figure 2.30 (a) An ideal empirical scheme for measuring attenuation, (b) an increment in the thickness of the specimen with a unit cross section area.

Propagation of the incident waves is affected by scattering (reflection, refraction and

[32] Plane longitudinal or transverse waves.

[33] Since the ideal conditions cannot be practically met, ccorrecting coefficients are applied in practice.

mode conversion inside the specimen are also included) and energy absorption through the thickness[34] of the specimen. By considering a thickness increment (dx) of a unit cross section of the specimen, the increment in the wave power or intensity (power per unit area) after propagation in the specimen can be estimated (Figure 2.30b). According to Beer's Law[35], the incremental transmitted intensity (or power) through the specimen is negatively proportional to the incident intensity (or power). Following the Beer's law and taking the time-averaged intensity leads to:

$$d\bar{I} = -\alpha_I \bar{I}(x)dx \Longrightarrow \frac{\bar{I}(x)}{\bar{I}(0)} = e^{-\alpha_I x} \tag{2.95}$$

in which $\bar{I}(0)$ is the time-averaged intensity of the incident waves, $\bar{I}(x)$ denotes the time-averaged intensity of the transmitted waves (Figure 2.30a), and α_I is called intensity attenuation coefficient.

The coefficient α_I can be readily expressed as:

$$\alpha_I = -\frac{1}{x}\ln\left(\frac{\bar{I}(x)}{\bar{I}(0)}\right) \tag{2.96}$$

where α_I is measured in $\mathrm{Np/unit\ length}$ i.e. $\mathrm{Nepper/unit\ length}$.

Substituting the relation between the intensity and the wave amplitude for plane waves, ($\bar{I} \sim P_o^2$) in Eq. 2.96 leads to:

$$\alpha_I = 2\alpha = -2\frac{1}{x}\ln\left(\left|\frac{P_o(x)}{P_o(0)}\right|\right) \tag{2.97}$$

such that $P_o(0)$ and $P_o(x)$ are the amplitudes of the incident and transmitted waves respectively, and $\alpha \coloneqq -\frac{1}{x}\ln\left(\left|\frac{P_o(x)}{P_o(0)}\right|\right)$ is called the amplitude attenuation coefficient ($\mathrm{Np/unit\ length}$).

Alternatively, Eq. 2.95 can be reconsidered in terms of the amplitude attenuation coefficient α as:

[34] It should be noted that the face of the specimen is entirely exposed to incident plane waves. Therefore, the external form of the specimen does not affect the attenuation.

[35] The Beer's law or the Beer–Lambert Law, or the Beer–Lambert–Bouguer Law of attenuation is an equation empirically derived by Pierre Bouguer in 1729, Johann Heinrich Lambert in 1760, and August Beer in 1852. Their independent work led to various forms of the equation.

$$\frac{\bar{I}(x)}{\bar{I}(0)} = e^{-2\alpha x} \tag{2.98}$$

This leads to:

$$-\frac{1}{x}\log_{10}\left(\frac{\bar{I}(x)}{\bar{I}(0)}\right) = 2\alpha\log_{10}(e) = 0.86859\alpha \tag{2.99}$$

According to the definition in the international system of units, the term $\log_{10}\left(\frac{\bar{I}(x)}{\bar{I}(0)}\right)$ is measured in the unit of bel (B). Therefore [2]:

$$1\text{Np} = 0.86859\ \text{B or } 1\text{Np} = 8.6859\ \text{dB} \tag{2.100}$$

It is usual to utilize the amplitude attenuation coefficient in dB/unit length i.e. $\text{decibel/unit length}$ for expressing the attenuation:

$$\alpha = -\frac{10}{x}\log\left(\frac{\bar{I}(x)}{\bar{I}(0)}\right) \tag{2.101}$$

$$\alpha = -\frac{20}{x}\log\left(\left|\frac{P_o(x)}{P_o(0)}\right|\right) \tag{2.102}$$

The attenuation coefficient is found to be significantly dependent on the wave frequency. Generally, higher attenuation is correlated with higher wave frequency.

2.5.7 Ultrasonic beam

Near and far fields:

Ultrasonic waves are generated through the surface vibrations of an ultrasonic transducer. Since the transducer surface has finite dimensions, the generated waves are not simply plane waves. For a finite-dimensional transducer, it can be assumed that each point on the surface generates spherical waves independently. Therefore, the superposition of the spherical wave (Figure 2.27c) forms the wave field and wavefronts in front of the transducer.

A cross section of a typical ultrasonic pressure field by an ideal finite-dimensional transducer generating harmonic waves in an acoustic medium (ideal fluid) is depicted in Figure 2.31a. The ultrasonic pressure field is recognized by the pressure amplitude at each spatial location. The ultrasonic field of a transducer is referred to as ultrasonic beam [1].

An ultrasonic beam is divided into two regions: the near and the far fields. The near field refers to the region close to the transducer in which the profile of the pressure amplitudes[36] across the beam undergo extreme fluctuations (Figure 2.31a). The fluctuations are due to constructive and destructive wave interfaces near the ultrasonic source. On the other hand, the far field is distant from the transducer and the pressure amplitudes across the beam have much less or no fluctuations [2]. Another distinction between the near and the far fields, is that the pressure amplitudes and accordingly the ultrasonic energy are almost distributed over a region (across the beam) that is not greater than the transducer surface (Figure 2.31a). However, the beam gradually diverges in the far field indicating larger regions for the distribution of pressure amplitudes and energy across the beam (Figure 2.31a) [2]. The divergence angle of the beam in the far field for a circular transducer is approximately (Figure 2.31b):

$$\theta = \sin^{-1}(0.6\frac{\lambda}{a}) \tag{2.103}$$

in which λ is the wavelength in the medium and a is the radius of the transducer. The above relation suggests that the beam diverges less with an increase in the wave frequency and the transducer radius.

Investigating the pressure amplitudes[37] on the central axis of the ultrasonic beam ($z-\text{axis}$ as shown in Figure 2.32a) approximately locates the length of the near field. The on-axis ($z-\text{axis}$) pressure amplitudes extremely vary in the near field. However, they start a monotonic change at the boundary of the far field (Figure 2.32b). The monotonic change begins once the last maximum of on-axis pressure amplitudes occurs. The location of the last maximum indicating the length of the near field (measured from the face of the transducer) for a circular transducer is:

$$\mathrm{L_n} = \frac{a^2}{\lambda} \tag{2.104}$$

which indicates that the near field becomes longer with increase in the wave frequency and the transducer radius.

It is worth mentioning that the pressure amplitudes in the far field gradually become proportional to the inverse of the axial distance (Figure 2.32b). This indicates that the pressure

[36] This is also true for ultrasonic intensity.
[37] This is also true for ultrasonic intensity.

field approaches the pressure field of spherical waves in the far field.

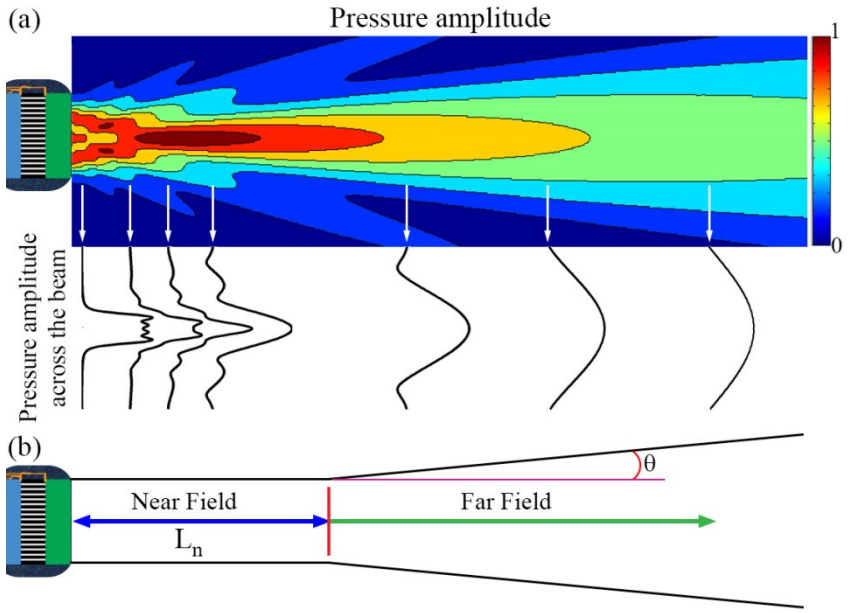

Figure 2.31 (a) A cross section of a typical ultrasonic pressure filed by an ideal transducer generating harmonic waves in an acoustic medium, (b) The length of the near field and the divergence of an ultrasonic beam in the far field.

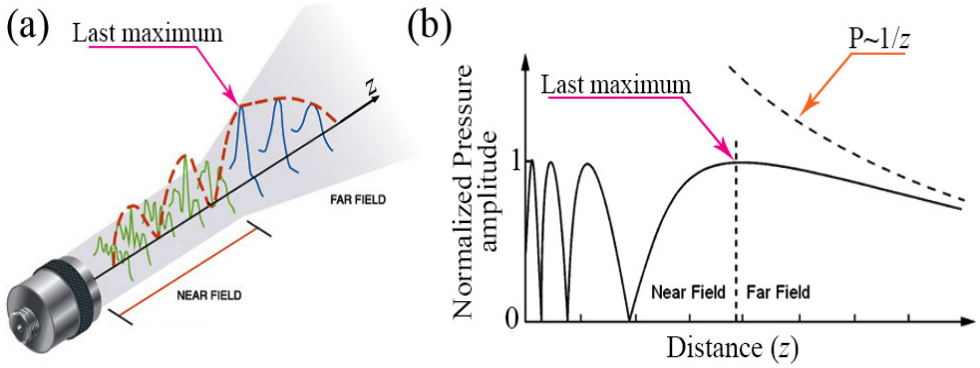

Figure 2.32 (a) Central axis of an ultrasonic beam and on-axis changes pressure amplitudes, (b) On-axis pressure amplitudes, last maximum and monotonic change of the amplitudes in the far filed.

Ultrasonic intensities within an ultrasonic beam:

As previously defined, the local ultrasonic intensity within an ultrasonic field is given by Eq. 2.82, i.e.: $\mathbf{I}(\boldsymbol{x}, t) = p\boldsymbol{v}$. The magnitude of the intensity ($I = |\mathbf{I}|$) varies across and along the beam (Figure 2.33a). This indicates that a localized intensity value generally does not reflect the status of the intensity or the energy within the whole beam. Therefore, some other intensity parameters based on the spatial and temporal distribution of intensity magnitudes are defined [69]:

I_{sp}: The spatial peak intensity is the maximum value of intensity within the beam at a particular time (Figure 2.33).

I_{sa}: The spatial average intensity is the average of the intensity values distributed over a cross section area of the beam (Figure 2.33), i.e. $I_{sa} = \frac{\int_A I(\boldsymbol{x},t)dA}{A}$. Sometimes the cross section area of the transducer is considered rather than the entire beam cross section area (the diameter of a circular transducer is denoted by 'D' in Figure 2.33b). Since most of the wave power in the near field crosses an area not larger than the transducer surface area, I_{sa} is almost the same for any cross section in the near field.

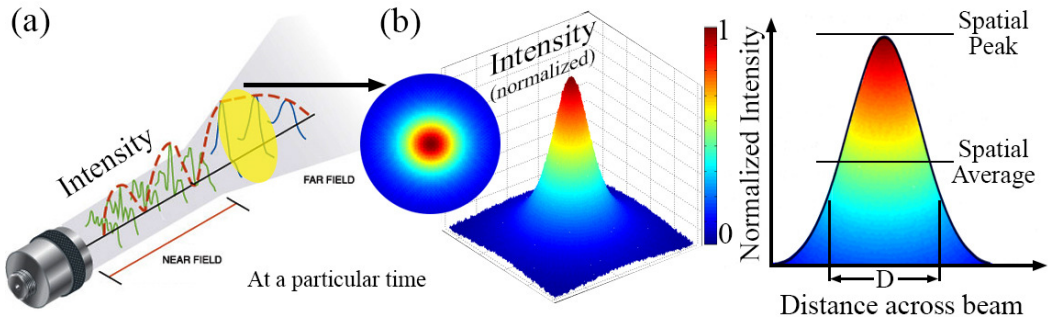

Figure 2.33 (a) Variation of intensity across and along an ultrasonic beam, (b) spatial distribution, the spatial peak and the spatial average of intensity on a beam cross section at a particular time.

I_{TA}: The temporal average intensity is the time-average of the intensity at a particular location within the beam during the period of the ultrasound ($I_{TA} = \frac{\int_T I(\boldsymbol{x},t)dt}{T}$).

I_{PA}: The pulse average intensity is the time-average of the intensity at a particular location within the beam during one pulse of the ultrasound ($I_{PA} = \frac{\int_{t_P} I(\boldsymbol{x},t)dt}{t_P}$). Ultrasound in the form of ultrasonic pulses consists of pulses repeating at a particular period (Figure 2.34). This makes I_{PA} different from I_{TA} for a pulsed ultrasound (Figure 2.34). The relation between the two intensities is: $I_{TA} = \text{duty cycle} \times I_{PA}$ such that $\text{duty cycle} \coloneqq \frac{\text{Pulse duration}}{\text{pulse repetition period}}$.

I_{SPTP}: The spatial peak temporal peak intensity is the maximum value of intensity within the beam during the period of the ultrasound.

I_{SPTA}: The spatial peak temporal average intensity is the temporal average of the intensity at the point in the beam having the maximum intensity.

I_{SATA}: The spatial average temporal average intensity is the spatial average intensity temporally averaged over the period of the ultrasound.

I_{SPPA}: The spatial peak pulse average intensity is the temporal average over one pulse duration (of a pulsed ultrasound) at the point in the beam having the maximum intensity.

I_{SAPA}: The spatial average pulse average intensity is the spatial average intensity temporally averaged over one pulse (of a pulsed ultrasound).

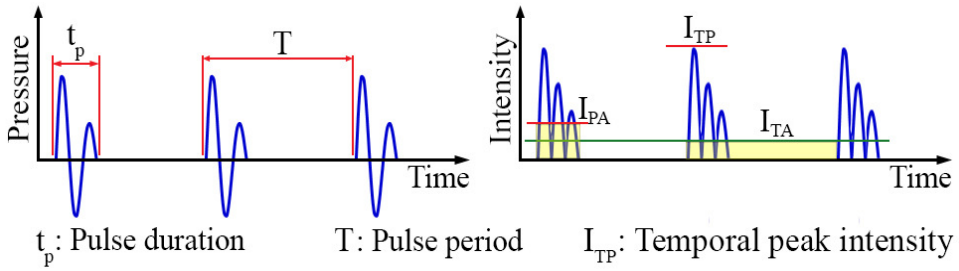

Figure 2.34 Pulse and temporal average intensities.

Other than characterizing ultrasonic beams, the defined intensity parameters are utilized to characterize the acoustic output of ultrasonic transducers operating in a particular fluid (usually water). One of the common methods of characterizing the acoustic output of a transducer is to use I_{SATA}. In this regard, I_{SATA} is measured[38] in water by an ultrasound power meter.

2.5.8 Negative acoustic pressure and cavitation in liquids

Mathematical description of acoustic wave propagation in liquids through the linear wave equations does not restrict the propagation medium (liquid) to experience any deformation or pressure. However, this might be asked that whether tension or absolute negative pressure predicted by the linear wave equation in liquids is physically possible or not. In this section, the possibility of tension in liquids due to acoustic (ultrasonic) wave propagation is explained.

The propagation of acoustic waves in fluids creates regions in which fluid particles are compressed (compression regions) together and regions where the particles are spread apart (rarefaction regions). Although compression indicates compressive forces or positive pressure, rarefaction does not necessarily lead to tension forces or absolute negative pressure. To

[38] Practically, the temporal average of ultrasonic power across the ultrasonic beam measured by an ultrasound power meter is divided by the transducer surface area to obtain I_{SATA}.

investigate the circumstances under which a fluid can undergo and resist negative pressure, different material phases should be considered.

There are three stable phases for materials, i.e. gas, fluid and solid. The state of a material at a particular pressure and temperature depends on the kinetic energy of the particles (molecules or atoms) and the attractive forces between the particles. The attractive forces originate from inter and intra molecular forces.

In contrast to gases, solids and liquids can exist in condense phases due to high attractive forces and low kinetic energy of their molecules. Condense material phases (liquid and solid) can resist tension forces or negative pressure which is accompanied by local density reduction [70]. However, the imagination of tension or absolute negative pressure inside a liquid is weird at first glance. The usual notion is that a liquid will change its phase into vapor if its pressure descends below its saturated vapor pressure (0.1MPa for water) while constant temperature. Therefore, one might infer that there would not be a possibility for negative pressure since a gas cannot resists tension. Indeed gases cannot resist tension (or negative pressure); however, liquids can resist some negative pressure before vaporizing.

Experiments have verified the existence of negative pressure due to stretching liquids. Negative pressure values of -21MPa and -59MPa were respectively observed during acoustic and shock waves propagating in room-temperature water [71]. There are other situations like micro capillary water bridge with reported negative pressure of -160MPa [72], negative pressure of about -0.5MPa in 100-meter tall Californian redwoods for sap transportation [73]. Negative pressure experiments and early historical observations can be found in [73] and [74].

Negative pressure in liquids can be explained through the concept of meta-stability. To clarify the concept, a typical phase diagram of a liquid (like water) is considered here (Figure 2.35). The phase diagram represents the state of a material in a particular pressure and temperature. Barriers on the diagram separate the stable states of the material. For a specific pressure and temperature on a barrier, more than one phase of the material can exist being in equilibrium with each other. A change in the phase of the material occurs when the thermo dynamical conditions (pressure and temperature) of the material cross a barrier on its phase diagram. This phase change is discontinuous in type except for supercritical fluid which is out of the scope of this thesis.

Although in a phase transition the pressure and temperature should necessarily correspond to the new phase, the transition may be temporarily postponed. In other words, the material may still preserve its current phase but in a metastable state [70]. For example, liquid water can be restrained from changing to ice or vapor when supercooled (temperature below 0 ℃ up to -40 ℃) or superheated (temperature above 100 ℃ up to 280 ℃) respectively [70]. The same is true for negative pressure, i.e. a liquid under constant temperature can temporarily be subjected to negative pressure (or pressure less than its saturated vapor pressure) without changing to vapor [70,72].

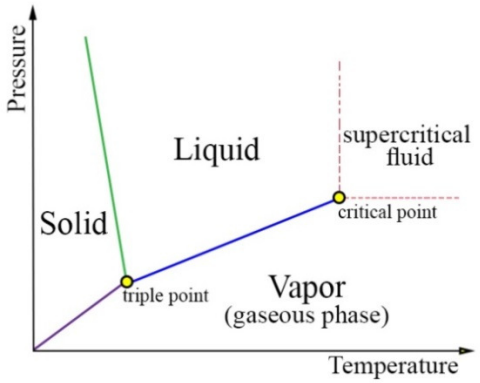

Figure 2.35 A typical phase diagram of water.

Figure 2.36 demonstrates a typical metastable region on the phase diagram. The curve indicating the barrier of the metastable region is called liquid-vapor spinodal. The spinodal curve expresses the ultimate negative pressure that can be resisted by the liquid at a specific temperature. Although the shape of the curve is still debatable for water, the ultimate negative pressure for room-temperature water is predicted to be in the range of -200MPa to -400MPa [73]. The limits of metastable pressure inherently depend on the intermolecular distances. The intermolecular distance becomes larger and mutual intermolecular attraction weakens as pressure decreases. This eventually leads to the instability of the liquid phase towards the vapour phase [75].

A metastable state is practically temporal since a small amount of energy fluctuation due to external disturbance aborts its equilibrium towards the more stable phase. The stability states of a phase can be schematically demonstrated by the mechanical analogy of a ball and multiple valleys (Figure 2.37). This question may arise that where the extra energy from the disturbance is consumed to end the meta-stability and complete the phase transition. This extra energy is spent

to create an interface for the more stable phase in a metastable phase. Scientifically, the formation of local stable phase interfaces is called nucleation. Nucleation may occur on nucleation sites (heterogeneous nucleation) or without preferential location, i.e. randomly (homogeneous nucleation).

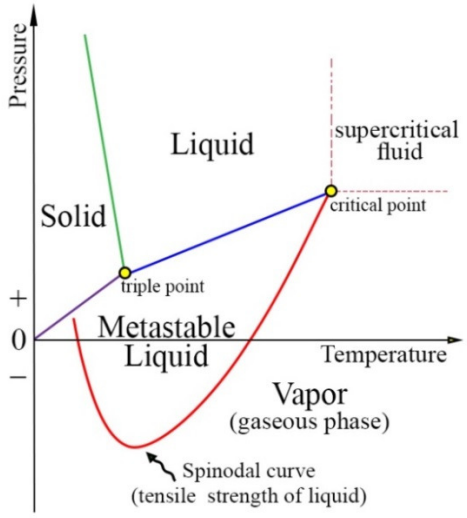

Figure 2.36 A metastable region on the phase diagram.

In the case of negative pressure (or pressure less than saturated vapor pressure) in constant-temperature liquids, nucleation is the formation of vapor bubbles (stable phase) referred to as cavitation [75]. Cavitation is of two types: hydrodynamic cavitation (not in the scope of the thesis) and acoustic cavitation. Acoustic cavitation, especially when ultrasonic waves propagate in water happens if the oscillation amplitude (proportional to ultrasonic intensity) is large enough to break down the cohesive (attractive) forces between water molecules [75]. Additionally, ultrasonic frequency reversely contributes to cavitation, i.e. the lower the frequency the more easily the cavitation occurs for a particular ultrasonic intensity [76].

The pressure at which acoustic cavitation occurs (cavitation pressure) in water is much larger than the theoretical negative pressure (-140MPa). Typical cavitation pressure for water via experiments falls in the range of -26MPa to $+0.1\text{MPa}$ depending on the temperature and puerility of water [75]. The theoretical negative pressure that water can resist without cavitation is merely a threshold for homogeneous nucleation, whereas in real experimental conditions heterogeneous nucleation occurs due to cavitation nuclei. Cavitation nuclei (nucleation sites) are weak locations in the water medium like impurities and dissolved gases [75,77]. Moreover, in an

ultrasonic experiment, cavitation may occur at the substantial surfaces surrounding the water or the ultrasonic transducer surface. Water (or any liquid) attaches to solid materials (surfaces) through molecular adhesive forces. If the tensile force or negative pressure advances the adhesive forces, water loses contact with its adjacent surface leading to creation of voids. This is the inception of cavitation at a surface [75].

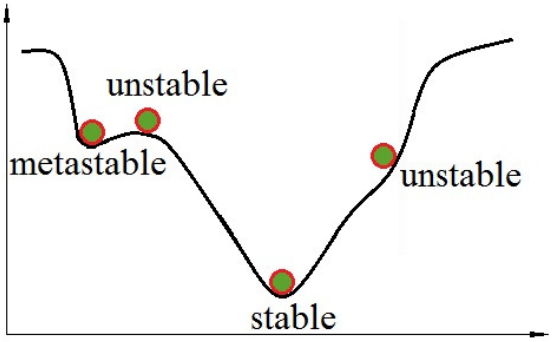

Figure 2.37 Schematic of stability states.

2.6 References

[1] D. Ensminger, L. Bond, Ultrasonics, 3rd ed., 2011.

[2] R.S.C. Cobbold, Foundations of Biomedical Ultrasound, Oxford University Press, 2007.

[3] T.J. Mason, Therapeutic ultrasound an overview, Ultrason. Sonochem. 18 (2011) 847–852.

[4] P. Werner, Knowledge about osteoporosis: assessment, correlates and outcomes., Osteoporos. Int. 16 (2005) 115–27.

[5] Public health agency of Canada, What is the impact of osteoporosis in Canada and what are Canadians doing to maintain healthy bones?, (2010) 1–3.

[6] J.-E. Tarride, R.B. Hopkins, W.D. Leslie, S. Morin, J.D. Adachi, A. Papaioannou, et al., The burden of illness of osteoporosis in Canada, Osteoporos. Int. 23 (2012) 2591–600.

[7] A.M. Cheung, D.S. Feig, M. Kapral, N. Diaz-Granados, S. Dodin, Prevention of osteoporosis and osteoporotic fractures in postmenopausal women: recommendation statement from the Canadian Task Force on Preventive Health Care., C. Can. Med. Assoc. J. 170 (2004) 1665–7.

[8] J.A. Maia, E.T. Costa, J.F.M. Neto, V.L.S.N. Button, Broadband ultrasound attenuation in the calcaneal region: a comparative study of single-position versus scanning systems, IEEE Trans. Ultrason. Ferroelectr. Freq. Control. 55 (2008) 64–73.

[9] C.M. Langton, C.F. Njeh, Acoustic and ultrasonic tissue characterization--assessment of osteoporosis, Proc. Inst. Mech. Eng. Part H J. Eng. Med. 213 (1999) 261–269.

[10] L. Lenchik, Current concept in osteoporosis, Am. Roentgen Ray Soc. (1997) 905–911.

[11] C.C. Glüer, Quantitative Ultrasound Techniques for the Assessment of Osteoporosis : Expert Agreement on Current Status, J. Bone Miner. Res. 12 (1997) 1280–1288.

[12] http://fau.pearlashes.com/anatomy/Chapter%209/Chapter%209.htm, (n.d.).

[13] http://www.medi-shop.gr/en/MedicalDevices/Ultrasound-Bone- Densitometers/Sonost-3000, (n.d.).

[14] S.L. Silverman, Lessons from osteoporosis clinical trials, Alzheimers. Dement. 2 (2006) 155–9.

[15] S. Chaffaï, F. Padilla, G. Berger, P. Laugier, In vitro measurement of the frequency-dependent attenuation in cancellous bone between 0.2 and 2 MHz, J. Acoust. Soc. Am. 108 (2000) 1281–9.

[16] C.F. Njeh, C.M. Boivin, C.M. Langton, The role of ultrasound in the assessment of osteoporosis: a review, Osteoporos. Int. 7 (1997) 7–22.

[17] V. Roberjot, F. Peyrin, G. Berger, P. Laugier, I. Introduction, Frequency dependence of ultrasonic backscattering in cancellous bone: Autocorrelation model and experimental results, 108 (2000) 2403–2411.

[18] C.C. Glüer, R. Eastell, D.M. Reid, D. Felsenberg, C. Roux, R. Barkmann, et al., Association of five quantitative ultrasound devices and bone densitometry with osteoporotic vertebral fractures in a population-based sample: the OPUS Study, J. Bone Miner. Res. 19 (2004) 782–93.

[19] K.A. Wear, Ultrasonic attenuation in human calcaneus from 0.2 to 1.7 MHz, IEEE Trans. Ultrason. Ferroelectr. Freq. Control. 48 (2001) 602–8.

[20] C.M. Langton, C.F. Njeh, The measurement of broadband ultrasonic attenuation in cancellous bone--a review of the science and technology, IEEE Trans. Ultrason. Ferroelectr. Freq. Control. 55 (2008) 1546–54.

[21] B.K. Hoffmeister, S.A. Whitten, J.Y. Rho, Low-megahertz ultrasonic properties of bovine cancellous bone, Bone. 26 (2000) 635–642.

[22] C.M. Langton, S.B. Palmer, R.W. Porter, The measurement of broadband ultrasonic attenuation in cancellous bone, Eng. Med. 8 (1979) 153–159.

[23] B. Lashkari, A. Manbachi, A. Mandelis, R.S.C. Cobbold, Slow and fast ultrasonic wave detection improvement in human trabecular bones using Golay code modulation, J. Acoust. Soc. Am. 132 (2012) EL222–8.

[24] W. Abendschein, G.W. Hyatt, Ultrasonics and selected physical properties of bone, Clin. Orthop. Relat. Res. 69 (1970) 294–301.

[25] C.F. Njeh, R. Hodgskinson, J.D. Currey, C.M. Langton, Orthogonal relationships between ultrasonic velocity and material properties of bovine cancellous bone, Med. Eng. Phys. 18 (1996) 373–81.

[26] C. Zhang, L.H. Le, R. Zheng, D. Ta, E. Lou, Measurements of ultrasonic phase velocities and attenuation of slow waves in cellular aluminum foams as cancellous bone-mimicking phantoms, J. Acoust. Soc. Am. 129 (2011) 3317–26.

[27] L. Cardoso, F. Teboul, L. Sedel, C. Oddou, A. Meunier, In vitro acoustic waves propagation in human and bovine cancellous bone, J. Bone Miner. Res. 18 (2003) 1803–12.

[28] G. Haïat, F. Padilla, F. Peyrin, P. Laugier, Fast wave ultrasonic propagation in trabecular bone: numerical study of the influence of porosity and structural anisotropy, J. Acoust. Soc. Am. 123 (2008) 1694–705.

[29] E.W. Gregg, A.M. Krishka, L.M. Salamone, M.M. Roberts, S.J. Anderson, R.E. Ferrell, et al., The epidemiology of quantitative ultrasound: a review of the relationships with bone mass, osteoporosis and fracture risk, Osteoporos. Int. 7 (1997) 89–99.

[30] L. Serpe, J.-Y. Rho, The nonlinear transition period of broadband ultrasound attenuation as bone density varies, Biomechanics. 29 (1996) 963–966.

[31] M.L. Bouxsein, S.E. Radloff, Quantitative ultrasound of the calcaneus reflects the mechanical properties of calcaneal trabecular bone, J. Bone Miner. Res. 12 (1997) 839–46.

[32] R. Hodgskinson, C.F. Njeh, J.D. Currey, C.M. Langton, The ability of ultrasound velocity to predict the stiffness of cancellous bone in vitro, Bone. 21 (1997) 183–190.

[33] C.M. Langton, C.F. Njeh, R. Hodgskinson, J.D. Currey, Prediction of mechanical properties of the human calcaneus by broadband ultrasonic attenuation., Bone. 18 (1996) 495–503.

[34] E.M. Lewiecki, B. Richmond, P.D. Miller, Uses and misuses of quantitative ultrasonography in managing osteoporosis, Cleve. Clin. J. Med. 73 (2006) 742–749.

[35] K. a Wear, Mechanisms for attenuation in cancellous-bone-mimicking phantoms., IEEE Trans. Ultrason. Ferroelectr. Freq. Control. 55 (2008) 2418–25.

[36] T.J. Haire, C.M. Langton, Biot theory: A review of its application to ultrasound propagation through cancellous bone, Bone. 24 (1999) 291–295.

[37] E. Bossy, F. Padilla, F. Peyrin, P. Laugier, Three-dimensional simulation of ultrasound propagation through trabecular bone structures measured by synchrotron microtomography, Phys. Med. Biol. 50 (2005) 5545–56.

[38] Y. Nagatani, K. Mizuno, T. Saeki, M. Matsukawa, T. Sakaguchi, H. Hosoi, Numerical and experimental study on the wave attenuation in bone--FDTD simulation of ultrasound propagation in cancellous bone, Ultrasonics. 48 (2008) 607–12.

[39] F. Padilla, E. Bossy, G. Haiat, F. Jenson, P. Laugier, Numerical simulation of wave propagation in cancellous bone, Ultrasonics. 44 Suppl 1 (2006) e239–43.

[40] A.S. Aula, J. Töyräs, M.A. Hakulinen, J.S. Jurvelin, Effect of bone marrow on acoustic properties of trabecular bone-3D finite difference modeling study, Ultrasound Med. Biol. 35 (2009) 308–18.

[41] https://commons.wikimedia.org/wiki/File:Human_jawbone_top.jpg, (n.d.).

[42] E.N. Marieb, Essentials of human anatomy and physiology, 6th ed., Addison Wesley Longman, San Francisco, 200AD.

[43] T. El-Bialy, I. El-Shamy, T.M. Graber, Repair of orthodontically induced root resorption by ultrasound in humans, Am. J. Orthod. Dentofac. Orthop. 126 (2004) 186–193.

[44] A.D. King, T. Turk, C. Colak, S. Elekdag-Turk, A.S. Jones, P. Petocz, et al., Physical properties of root cementum: part 21. Extent of root resorption after the application of 2.5° and 15° tips for 4 weeks: a microcomputed tomography study., Am. J. Orthod. Dentofacial Orthop. 140 (2011) e299–305.

[45] N. Bartley, T. Türk, C. Colak, S. Elekdağ-Türk, A. Jones, P. Petocz, et al., Physical properties of root cementum: Part 17. Root resorption after the application of 2.5° and 15° of buccal root torque for 4 weeks: a microcomputed tomography study., Am. J. Orthod. Dentofacial Orthop. 139 (2011) e353–360.

[46] A. Paetyangkul, T. Türk, S. Elekdağ-Türk, A.S. Jones, P. Petocz, L.L. Cheng, et al., Physical properties of root cementum: Part 16. Comparisons of root resorption and resorption craters after the application of light and heavy continuous and controlled orthodontic forces for 4, 8, and 12 weeks., Am. J. Orthod. Dentofacial Orthop. 139 (2011) e279–284.

[47] K. Lopatiene, A. Dumbravaite, Risk factors of root resorption after orthodontic treatment., Stomatol. Balt. Dent. Maxillofac. 10 (2008) 89–95.

[48] V.C.J. Montenegro, A. Jones, P. Petocz, C. Gonzales, M.A. Darendeliler, Physical properties of root cementum: Part 22. Root resorption after the application of light and heavy extrusive orthodontic forces: a microcomputed tomography study., Am. J. Orthod. Dentofacial Orthop. 141 (2012) e1–9.

[49] N. Brezniak, a Wasserstein, Root resorption after orthodontic treatment: Part 2. Literature review., Am. J. Orthod. Dentofacial Orthop. 103 (1993) 138–46.

[50] A. Khanna, R.T.C. Nelmes, N. Gougoulias, N. Maffulli, J. Gray, The effects of LIPUS on soft-tissue healing: A review of literature, Br. Med. Bull. 89 (2009) 169–182.

[51] B. a a Scheven, R.M. Shelton, P.R. Cooper, a D. Walmsley, a J. Smith, Therapeutic ultrasound for dental tissue repair, Med. Hypotheses. 73 (2009) 591–3.

[52] F. Padilla, R. Puts, L. Vico, K. Raum, Stimulation of bone repair with ultrasound: a review of the possible mechanic effects., Ultrasonics. 54 (2014) 1125–1145.

[53] D.A. Dalla-Bona, E. Tanaka, T. Inubushi, H. Oka, A. Ohta, H. Okada, et al., Cementoblast response to low- and high-intensity ultrasound., Arch. Oral Biol. 53 (2008) 318–323.

[54] D.A. Dalla-Bona, E. Tanaka, H. Oka, E. Yamano, N. Kawai, M. Miyauchi, et al., Effects of ultrasound on cementoblast metabolism in vitro., Ultrasound Med. Biol. 32 (2006) 943–948.

[55] T. Inubushi, E. Tanaka, E.B. Rego, J. Ohtani, A. Kawazoe, K. Tanne, et al., Ultrasound stimulation attenuates resorption of tooth root induced by experimental force application., Bone. 53 (2013) 497–506.

[56] J. Harle, V. Salih, F. Mayia, J.C. Knowles, I. Olsen, Effects of ultrasound on the growth and function of bone and periodontal ligament cells in vitro., Ultrasound Med. Biol. 27 (2001) 579–586.

[57] S. Al-Daghreer, M. Doschak, A.J. Sloan, P.W. Major, G. Heo, C. Scurtescu, et al., Effect of low-intensity pulsed ultrasound on orthodontically induced root resorption in beagle dogs., Ultrasound Med. Biol. 40 (2014) 1187–96.

[58] http://www.ukm.my/rahim/Seismic%20Refraction%20Surveying.htm, (n.d.).

[59] B.R. Munson, D.F. Young, T.H. Okiishi, W.W. Huebsch, Fundamentals of fluid mechanics, 6th ed., Wiley, 2009.

[60] S. Adeeb, Introduction to solid mechanics and finite element analysis using Mathematica, Kendall Hunt Publishing, 2012.

[61] H. Bhatia, S. Member, G. Norgard, The Helmholtz-Hodge Decomposition — A Survey, IEEE Trans. Vis. Comput. Graph. 19 (2013) 1–19.

[62] R.K. Nagle, E.B. Saff, A.D. Snider, Fundamentals of differential equations, 6th ed., Pearson, 2011.

[63] Walter Strauss, Partial Differential Equations: An Introduction, illustrate, Wiley, 1992.

[64] U. Ingard, Notes on acoustics, INFINITY SCIENCE PRESS LLC, Hingham, 2008.

[65] K.F. Riley, M.P. Hobson, Essential mathematical methods for the physical sciences, cambridge university press, 2011.

[66] D. Systèmes, Abaqus theory manual, 2012.

[67] D. Halliday, R. Resnick, J. Walker, Fundamentals of physics, 6th ed., Wiley, New York, 2001.

[68] T. a Whittingham, Broadband transducers, Eur. Radiol. 9 (1999) 298–303.

[69] P. Hoskins, K. Martin, Abigail Thrush, Diagnostic Ultrasound: Physics and Equipment, 2nd ed., cambridge university press, New York, 2010.

[70] S. Balibar, F. Caupin, Metastable liquids, J. Phys. Condens. Matter. 15 (2002) S75–S82.

[71] E. Herbert, S. Balibar, F. Caupin, Cavitation pressure in water., Phys. Rev. E. Stat. Nonlin. Soft Matter Phys. 74 (2006) 041603.

[72] M. Nosonovsky, B. Bhushan, Phase behavior of capillary bridges: towards nanoscale water phase diagram, Phys. Chem. Chem. Phys. 10 (2008) 2137–2144.

[73] A.R. Imre, On the existence of negative pressure states, Phys. Status Solidi Basic Res. 244 (2007) 893–899.

[74] G.S. Kell, Early observations of negative pressures in liquids, Am. J. Phys. 51 (1983) 1038.

[75] F. Caupin, E. Herbert, Cavitation in water: a review, Comptes Rendus Phys. 7 (2006) 1000–1017.

[76] J.-L. Capelo-Martínez, Ultrasound in chemistry: analytical applications, Wiley-VCH, 2009.

[77] M. Ashokkumar, The characterization of acoustic cavitation bubbles - An overview, Ultrason. Sonochem. 18 (2011) 864–872.

[78] J. Stewart, Calculus, 6th ed., Nelson education Ltd., Scarborough, 2007.

Chapter 3

Verification of Finite Element Analyses of Wave Propagation by the Angular Spectrum Method

3.1 Abstract

Numerical simulations of instances of ultrasound propagation in fluid and solid media were performed by the finite element method (FEM). The simulation results were compared to the results obtained from the angular spectrum method (ASM). It was shown that the FEM could simulate the wave propagation with an acceptable precision if the nodal distance of the finite elements was chosen to be less than one tenth of the smallest wavelength in the medium. It was also demonstrated that the nodal distance for accurate results was governed by the transverse wavelength when waves propagated in a solid medium.

3.2 Introduction

The finite element method (FEM) is known as one of the effective numerical methods for solving partial differential equations. The FEM, like other numerical methods, plays its unique role when complicated boundary conditions exist in the problem. Analysis of wave propagation in geometrically complicated structure or in non-homogeneous media is a very common situation needing the implementation of numerical methods like the FEM.

The implementation of the FEM for numerically solving the wave equations in this thesis was through the application of a commercial software package, i.e. ABAQUS (ABAQUS 6.10). Although ABAQUS is sophisticated and well-known finite element software, it was important to investigate its reliability for solving the problems in this thesis. The reliability was investigated by estimating the numerical errors generated by the software. In this regard, numerical errors were estimated through solving some problems with the software package and comparing the results with exact solutions.

The finite element analyses of wave propagation problems in this thesis commonly included linear wave propagation in unbounded (or semi unbounded) three-dimensional (3D) media. Considered as basic problems for error estimation purposes, linear wave propagation problems in semi-unbounded (half space) two-dimensional (2D) media were analysed in this chapter. To estimate the numerical errors, the analyses were performed by the finite element method and the results were compared with the exact solutions obtained through the ASM (section 2.4.2) for the same problems. The goals of the finite element analyses in this chapter were to investigate the effect of different finite element nodal distances on the results, the

accuracy of non-reflecting boundary conditions and the reliability of the software.

3.3 Materials and methods

Any numerical method for solving the partial differential equation (PDE) of wave propagation is associated with some numerical errors. The accuracy of the finite element method for wave propagation analysis depends on the spatial and temporal discretization schemes and resolutions. Three common numerical phenomena leading to errors in the finite element analysis of wave propagation are numerical dissipation, numerical dispersion and spurious oscillations. The appearance of these phenomena is due to truncation errors manifested in the discretized form of the wave equations [1].

Numerical dissipation (numerical diffusion or attenuation, or artificial viscosity) introduces undesirable wave attenuation into the solution medium and makes the waves lose their amplitudes while propagating. Numerical dispersion affects the numerical[1] wave velocity leading to difference between the physical and the numerical wave length [2]. Spurious oscillations occur in both time and space such that they have high frequency in time and short wavelength in space.

The semi-discrete[2] form of the standard (classical) Galerkin method for finite element analyses of wave propagation in (homogeneous) solids or fluids leads to the following system of ordinary second-order differential equation[3]:

$$\boldsymbol{M\ddot{\eta} + C\dot{\eta} + K\eta = F} \qquad (3.1)$$

in which $\boldsymbol{M}$, $\boldsymbol{C}$ and $\boldsymbol{K}$ are mass, damping and stiffness matrices, $\boldsymbol{\eta}$ is a vector containing the nodal physical quantity (pressure or displacement) and $\boldsymbol{F}$ is a vector expressing the external assignment of physical quantities or relations on the finite element nodes. Since this method uses approximate integration schemes in time and piecewise linear (or quadratic) interpolation functions in space, its accuracy is highly dependent on the temporal and spatial resolutions (time increments and element size or nodal distances).

Large temporal increments lead to inaccurate results and introducing numerical

[1] Simulated by numerical methods as opposed to the true physical velocity.
[2] This scheme is called semi-discrete since the discretization only contains spatial functions and the time is discretized using the finite difference methods for ordinary differential equations [11,12].
[3] Details are available in 2.4.3.

dispersion and dissipation in the solution. Moreover, explicit integration schemes become numerically unstable for large time increments [1]. On the other hand, the size of the finite elements is highly influential on errors due to numerical dissipation, dispersion and spurious oscillations [1,2]. In a wave propagation analysis using the FEM, deciding for a right nodal distance precedes choosing the temporal increment. The nodal spacing required in order to reasonably resolve (sample) a particular wavelength in the medium is recommended to be smaller than 0.1λ such that λ is the smallest wavelength in the medium [1].

To investigate the effect of nodal distances on the finite element analysis results, the propagation of harmonic waves formulated by the Helmholtz equation was considered. Since the time variable is not explicitly present in the Helmholtz equation, temporal discretization and integration is not needed in the finite element procedure. Therefore, the accuracy of the solutions is merely dependent on the spatial discretization and its resolution (nodal distances).

The steady-state linear propagation of 1-MHz harmonic mechanical waves in unbounded fluid and solid media were investigated through solving the corresponding Helmholtz equation. For simplification purposes, a two-dimensional (2D) medium was assumed for each of the media. The analysis of wave propagation in a 2D medium is valid when the propagation is independent of one of the directions in the Cartesian coordinate system (the *x*-direction here). In this regard, a unit-height (1cm) rectangular wave source (ultrasonic transducer) with an infinite width was assumed in a half-space. Figure 3.1a illustrates the half space (3D) and the 2D medium, i.e. plane 'S', in which the wave propagation was considered. Since the 2D medium was itself a 2D half space, the wave propagation analyses were performed on a finite region (with the dimensions of $\text{w} \times \text{h}$) in the half space (Figure 3.1b).

Solving the Helmholtz equation using the ASM was through following the procedure described in section 2.4.2. The procedure, including the integrations (numerical calculation of the Fourier transform pair), was performed through running a piece of code (Appendix C) written in MATLAB (MathWorks 2012). The finite element procedures including mesh generation, applying boundary conditions, radiation conditions (non-reflecting boundary conditions) and solving the equations (using the direct solver) were performed by the finite element software ABAQUS (ABAQUS 6.10).

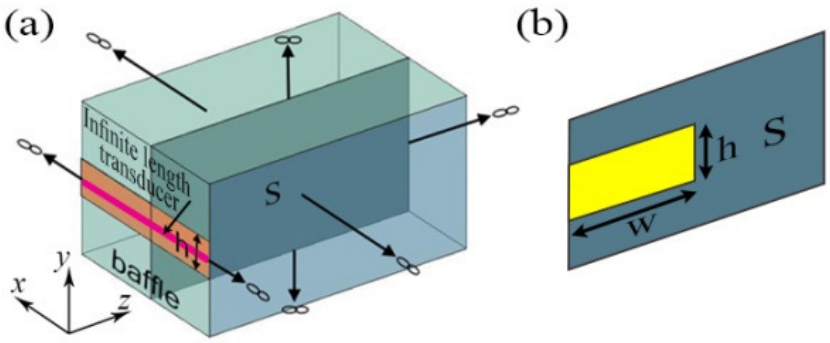

Figure 3.1 Description of 2D propagation medium.

3.3.1 Fluid medium

For the case of fluid medium, the material properties and the dimensions of the medium were chosen as shown in Table 3.1. The dimensions were arbitrarily chosen; however, the material properties of the fluid represented material properties of water and biological soft tissues if their viscous properties were disregarded.

The steady-state linear propagation of pressure waves in the inviscid fluid (Table 3.1) was expressed by the Helemhotz equation (Eq. 2.34):

$$(\nabla^2 + k^2)\underline{P}(\boldsymbol{x}) = 0 \tag{3.2a}$$

subjected to the following boundary condition:

$$\underline{P}(\boldsymbol{x}) = \begin{cases} 1 & \boldsymbol{x} \in \{-0.5 \leq y \leq 0.5, z = 0\} \\ 0 & \boldsymbol{x} \in \{y < -0.5, y > 0.5, z = 0\} \end{cases} \tag{3.2b}$$

in which $\underline{P}(\boldsymbol{x}) \in \mathbb{C}$ is the scalar field of acoustic pressure, $\boldsymbol{x} \in \mathbb{R}^2$ such that $\boldsymbol{x} = (y, z)$ is the Cartesian position vector and k is the wave number. It should be noted that based on the assumed 2D wave propagation, the differential equation is independent of the x-direction (Figure 3.1a). The boundary condition (Eq. 3.2a) defines a source of (harmonic) acoustic pressure with unit amplitude in the half-space. The $z = 0$ plane, which is the half-space barrier, is called a soft baffle (Figure 3.1a). A soft baffle is a plane on which the acoustic pressure (or mechanical stresses) vanishes (becomes zero) except a finite region with non-zero defined pressure (or mechanical stresses).

The exact solution of the 2D Helmholtz equation was obtained by the ASM described in section 2.4.2 (the application of the procedure for the particular problem in this section is available in Appendix C).

The wave propagation analyses using the FEM were based on solving the following discretized form of the Helmholtz equation[4]:

$$[\mathbf{K} - \omega^2\mathbf{M}]\underline{\mathbf{P}}^N = \underline{\mathbf{T}} \qquad (3.3)$$

in which $\underline{\mathbf{P}}^N \in \mathbb{C}^N$ denotes nodal pressure amplitudes associated with N finite element nodes, $\mathbf{M} \in \mathbb{M}^{N\times N}$ is the mass matrix, $\mathbf{K} \in \mathbb{M}^{N\times N}$ is the acoustic stiffness matrix, $\mathbf{T} \in \mathbb{R}^N$ expresses the pressure gradient normal to the boundary of the medium (Neumann boundary condition) and ω is the excitation frequency. Known pressure amplitudes on the boundary of the medium are included in $\underline{\mathbf{P}}^N$. The pressure gradient vector $\mathbf{T}$, applied on the part of the boundary with no prescribed pressure values, is used to define non-reflecting boundary condition.

Table 3.1 Material properties and dimensions of the fluid 2D medium.

Density (kg/m^3)	1000
Bulk Modulus (MPa)	$B = 2250^*$
Wave velocity (m/s)	1500
Wavelength λ (mm)	1.5
Medium dimensions ($w \times h$)	8×5cm

Since it is not practical to completely include the infinite 2D medium in a finite element model (due to infinite dimensions of the medium), the finite element model was bounded by artificial boundaries (Figure 3.2a). The non-reflecting boundary condition was imposed on the artificial boundaries to compensate the effect of the omitted surrounding medium by allowing the impinging wave energy pass through the artificial boundaries (Figure 3.2a). The non-reflecting boundary condition was implemented using appropriate acoustic radiation condition (impedance boundary condition per unit area) [3]:

$$\boldsymbol{n}.\nabla\underline{P}(\boldsymbol{x}) - ik\underline{P}(\boldsymbol{x}) = 0 \text{ such that } \boldsymbol{x} \in \partial\Omega_A \qquad (3.4)$$

in which $\boldsymbol{n}$ is the outward unit normal vector of the artificial exterior boundaries denoted by $\partial\Omega_A$. The impedance boundary condition is embedded in the finite element formulation of 3.3 as described in 2.64.

To discretize the medium using the finite elements, linear triangular acoustic elements having one pressure degree of freedom at each node were used (Figure 3.2b). The nodal distance of the elements was chosen based on 0.1λ, such that λ is the wavelength associated with the 1-MHz harmonic waves presented in the medium (Table 3.1).

[4] Details are available in 2.4.3.

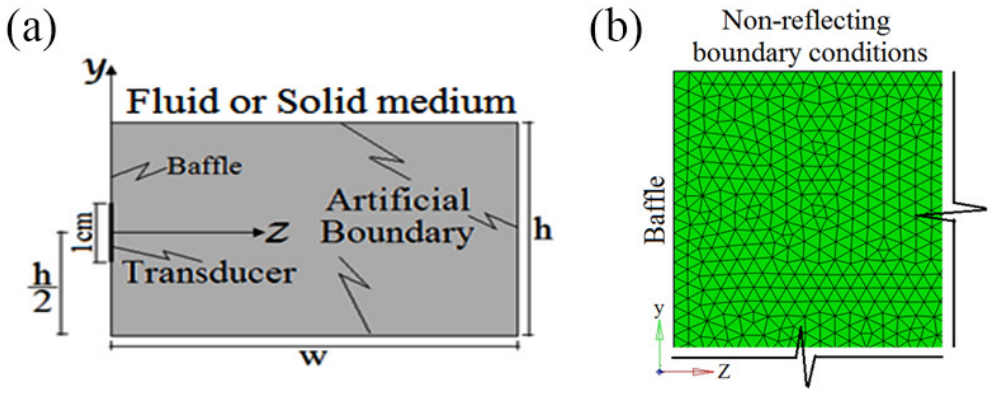

Figure 3.2 (a) Geometry and dimensions of the 2D fluid or solid medium, (b) generated finite element mesh for the fluid medium.

3.3.2 Solid medium

The material properties and the dimensions of the solid medium were chosen as shown in Table 3.2. The dimensions were arbitrary; however, the material properties represented material properties of biological hard tissue of bone without any viscous properties.

The steady propagation of harmonic waves in a non-energy-absorbing 2D solid medium (Table 3.2) was explored based on two independent equations[5] for longitudinal and transverse modes:

$$(\nabla^2 + k_L^2)\underline{\boldsymbol{U}}_L(\boldsymbol{x}) = \mathbf{0} \tag{3.5a}$$

$$(\nabla^2 + k_T^2)\underline{\boldsymbol{U}}_T(\boldsymbol{x}) = \mathbf{0} \tag{3.5b}$$

$$\underline{\boldsymbol{U}} = \underline{\boldsymbol{U}}_L + \underline{\boldsymbol{U}}_T \tag{3.5c}$$

in which $\boldsymbol{x} \in \mathbb{R}^2$ such that $\boldsymbol{x} = (y, z)$, k_L and k_T are the wave numbers for the longitudinal and transverse wave modes respectively, $\underline{\boldsymbol{U}}_L \in \mathbb{C}^2$ and $\underline{\boldsymbol{U}}_T \in \mathbb{C}^2$ are the longitudinal and transverse displacement phasors, and $\underline{\boldsymbol{U}} \in \mathbb{C}^2$ is the total displacement phasor.

Table 3.2 Material properties and dimensions of the solid 2D medium.

Density (kg/m^3)	1600
Modulus of Elasticity (MPa)	$E = 19100$
Poisson's ratio	$\nu = 0.30^*$
Longitudinal wave velocity (m/s) and wavelength λ_L (mm)	4000, 4.00
Transverse wave velocity (m/s) and wavelength λ_T (mm)	2140, 2.14
Medium dimensions ($w \times h$)	8×8cm

[5] Details are available in 2.3.3.

The longitudinal vector displacement field is a lamellar field ($\nabla \times \boldsymbol{u}_L = \mathbf{0}$), therefore, Eq. 3.5a was rewritten in terms of the gradient of a scalar potential function[6]:

$$(\nabla^2 + k_L^2)\varphi_L(\boldsymbol{x}) = 0 \qquad (3.6)$$

such that:

$$\underline{\boldsymbol{U}}_L = -\nabla\varphi_L \qquad (3.7)$$

where $\varphi_L(\boldsymbol{x}) \in \mathbb{C}$ is the longitudinal displacement potential function. In this regard, the problem reduced to finding a scalar field.

In contrary to the longitudinal mode, the transverse mode represents a solenoidal field ($\nabla . \boldsymbol{u}_T = 0$), therefore, it was expressed by a vector potential as[7]:

$$(\nabla^2 + k_T^2)\boldsymbol{\psi}(\boldsymbol{x}) = 0 \text{ such that } \underline{\boldsymbol{U}}_T = -\nabla \times \boldsymbol{\psi} \qquad (3.8)$$

in which $\boldsymbol{\psi}(\boldsymbol{x}) \in \mathbb{C}^3$ is the vector potential of the transverse displacement field. Furthermore, the 2D wave propagation assumption indicated a plane strain condition [4] for the 2D solid medium. In the plane strain condition, the variables describing the propagation are independent of direction associated with the infinite side of the source. Therefore, the vector potential $\boldsymbol{\psi}(\boldsymbol{x})$ became independent of the x-direction in the plane strain condition, i.e. $\frac{\partial}{\partial x} \equiv 0$ which implies:

$$\underline{\boldsymbol{U}}_T = \left(\frac{\partial \psi_y}{\partial z} - \frac{\partial \psi_z}{\partial y}\right)\hat{x} + \left(-\frac{\partial \psi_x}{\partial z}\right)\hat{y} + \left(\frac{\partial \psi_x}{\partial y}\right)\hat{z} \qquad (3.9)$$

such that $\hat{x}, \hat{y}$ and $\hat{z}$ are the unit vectors in Cartesian coordinate system and ψ_x, ψ_y and ψ_z are the components of the vector field $\boldsymbol{\psi}$. The first term in Eq. 3.9 is the displacement in the x-direction which is constant due to the plane strain condition $\frac{\partial \underline{U}_{T_x}}{\partial x} = 0$ ($\underline{\boldsymbol{U}}_{T_x}$ is the component of $\boldsymbol{u}_T$ in x-direction). Therefore, Eq. 3.9 became:

$$\underline{\boldsymbol{U}}_T = \mathrm{C}\hat{x} + \left(-\frac{\partial \psi_x}{\partial z}\right)\hat{y} + \left(\frac{\partial \psi_x}{\partial y}\right)\hat{z} \qquad (3.10)$$

Equation 3.10 expresses that the 2D transverse displacement field is only a function of the scalar variable ψ_x. Additionally, the component of $\underline{\boldsymbol{U}}_T$ in the x-direction is a constant indicating a constant displacement of the whole medium in the x-direction. This has no effect on

[6] Since $\nabla^2[\nabla(\varphi)] = \nabla[\nabla^2(\varphi)]$ such that φ is a scalar field.
[7] Details are available in 2.3.2.

the solution and may be assumed to be zero. Thus, the Helmholtz equation for the transverse wave propagation in the solid 2D medium became:

$$(\nabla^2 + k_T^2)\psi_x(y,z) = 0 \tag{3.11}$$

such that:

$$\underline{\boldsymbol{U}}_T = \left(\underline{U}_{Ty}, \underline{U}_{Tz}\right) = \left(-\frac{\partial \psi_x}{\partial z}, \frac{\partial \psi_x}{\partial y}\right) \tag{3.12}$$

The boundary conditions for Eq. 3.6 and 3.11 were chosen as:

$$\psi_x(y) \text{and } \varphi_L(y) = \begin{cases} 1 & -0.4 \le y \le 0.4 \\ e^{-10^4(y-0.4)^2} & 0.4 < y \le 0.5 \\ e^{-10^4(y+0.4)^2} & -0.5 \le y \le -0.4 \\ 0 & y < -0.5 \end{cases} \tag{3.13}$$

Figure 3.3 demonstrates the plots of the displacement potentials on the boundary $\varphi_L(y)$ and $\psi_x(y)$.

Equation 3.6 and 3.11 with the defined boundary conditions on the baffle were solved through the ASM and the final displacement fields was obtained by numerically evaluating the derivatives within Eq. 3.8 and Eq. 3.12 (The Matlab code is available in Appendix C).

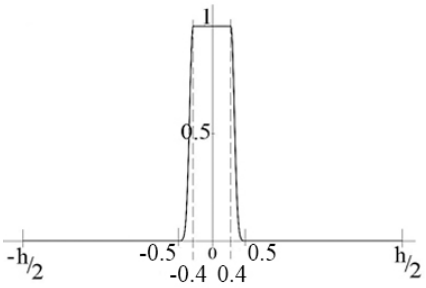

Figure 3.3 The displacement potentials on the baffle region.

The finite element analysis of the wave propagation in the solid medium was based on the discretized form of the Helmholtz equation[8]:

$$[\mathbf{K} - \omega^2 \mathbf{M}]\underline{\boldsymbol{U}}^N = \underline{\mathbf{F}} \tag{3.14}$$

where $\mathbf{M} \in \mathbb{M}^{N\times N}$, $\mathbf{K} \in \mathbb{M}^{N\times N}$ and $\mathbf{F} \in \mathbb{R}^N$ are mass matrix, stiffness matrix and the applied load (or any load-displacement load-velocity relation) vector on a set of nodes. The vector $\underline{\boldsymbol{U}}^N \in \mathbb{C}^N$

[8] Details are available in 2.4.3.

contains the total displacement vector of finite element nodes. The superscript *N* denotes the total number of nodes.

Since the finite element formulation was based on displacements, the wave source was defined as displacement boundary conditions in the finite element analyses. To this end, the displacements in *y*- and *z*-directions were numerically obtained out of the ASM analysis results and imposed on the nodes associated with the wave source (transducer) on the baffle (Figure 3.2a). The displacement boundary condition was obtained through Eq. 3.8 and Eq. 3.10 as:

$$\underline{U}_y = -\left(\frac{\partial \varphi_L}{\partial y} + \frac{\partial \psi_x}{\partial z}\right), \qquad \underline{U}_z = -\frac{\partial \varphi_L}{\partial z} + \frac{\partial \psi_x}{\partial y} \tag{3.15}$$

Figure 3.4 demonstrates the real and imaginary parts of the displacement boundary condition on the baffle.

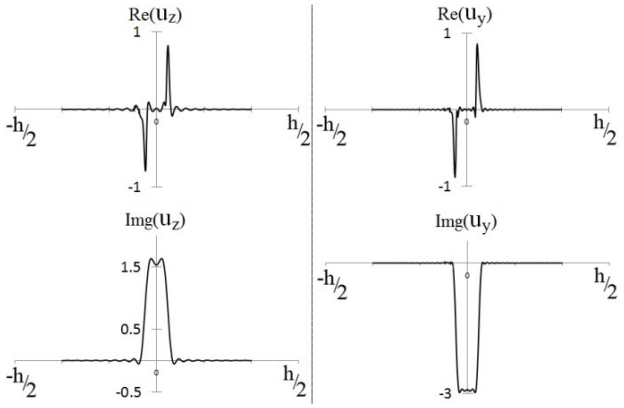

Figure 3.4 The real and imaginary parts of the displacement boundary condition.

To discretize the medium using the finite elements, linear triangular solid elements having three displacement degrees of freedom at each node were used (Figure 3.5a). Three different nodal distances based on $0.1\lambda_L$, $0.1\lambda_T$ and $0.05\lambda_T$ were considered. Such that λ_L and λ_T are the longitudinal and transverse wavelengths associated with the 1-MHz harmonic waves (Table 3.2).

Since a finite region (bounded by artificial boundaries) of the solid 2D half-space was modeled by the finite element method, non-reflecting boundary conditions were imposed on the artificial boundaries. The non-reflecting boundary conditions were based on the following radiation conditions per unit area:

$$\boldsymbol{n}.\nabla\underline{\boldsymbol{U}}(\boldsymbol{x}) - ik_L\underline{\boldsymbol{U}}(\boldsymbol{x}) = 0 \text{ such that } \boldsymbol{x} \in \partial\Omega_A \quad (3.16a)$$

$$\boldsymbol{t}.\nabla\underline{\boldsymbol{U}}(\boldsymbol{x}) - ik_T\underline{\boldsymbol{U}}(\boldsymbol{x}) = 0 \text{ such that } \boldsymbol{x} \in \partial\Omega_A \quad (3.16b)$$

where $\boldsymbol{n}$ and $\boldsymbol{t}$ are respectively the outward unit normal vector and the tangential unit vector of the artificial exterior boundaries denoted by $\partial\Omega_A$. The longitudinal and transverse wave numbers are denoted by k_L and k_T respectively. These radiation boundary conditions were simplified as linear one-dimensional dashpots [5]. Two perpendicular dashpots were used at each finite element node on the boundaries to absorb the impinging longitudinal and transverse waves (Figure 3.5b). The dashpot constants were calculated as [5]:

$$\mathrm{C_n} = A\rho_o \mathrm{c}_L,\ \mathrm{C_t} = A\rho_o \mathrm{c}_T \quad (3.17)$$

such that $\mathrm{C_n}$ and $\mathrm{C_t}$ are the normal and the tangential dashpot constants respectively, 'A' is the area assigned to each dashpot (the area was the nodal spacing on the boundaries since the thickness of the 2D medium was disregarded or assumed to be one unit in the plain strain conditions). The density of the medium is denoted by ρ_o, and c_L and c_T are the longitudinal and transverse wave velocities (Table 3.2). This type of approximate non-reflecting boundary condition applies an external nodal force linearly related to the nodal velocity at each node.

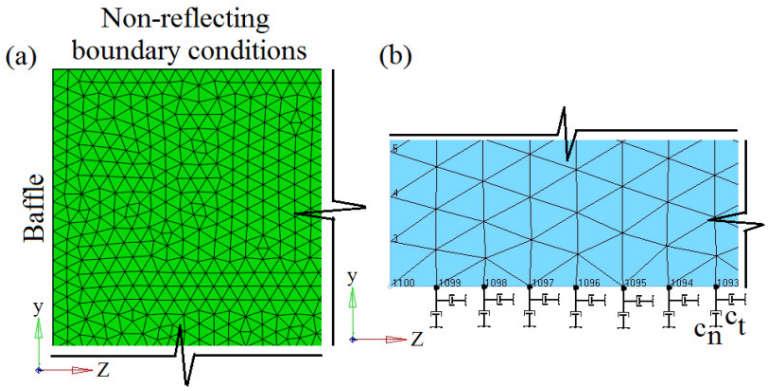

Figure 3.5 (a) discretized solid medium, (b) dashpots utilized to simulate non-reflecting boundary conditions on the artificial boundaries of the solid medium.

3.4 Results and discussion

Figure 3.6 illustrates the spatial distribution of the pressure amplitudes ($|\underline{P}(\boldsymbol{x})|$) in the fluid medium obtained from the exact solution (ASM) and the numerical simulation (FEM). For a better comparison between the solutions, axial pressure amplitudes on the central axis of the medium along the z-axis is plotted in Figure 3.7. Moreover, the variations of the pressure on the

axes parallel to the *y*-axis (denoted by 'lateral pressure') for different distances from the source are demonstrated (Figure 3.8).

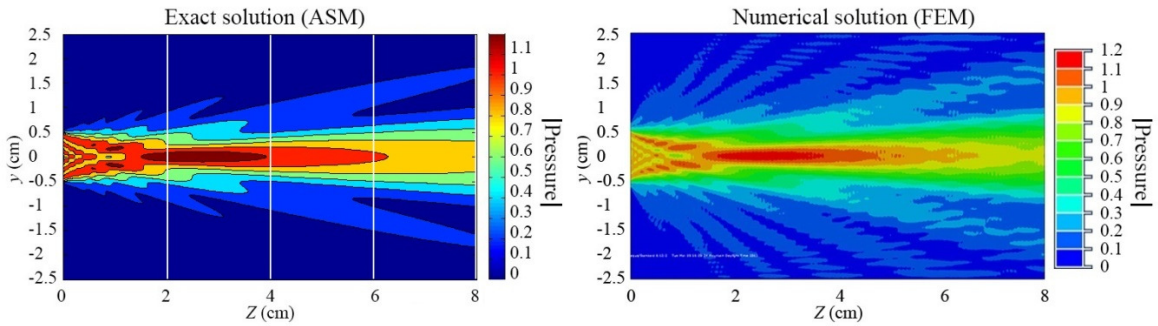

Figure 3.6 Spatial distribution of the pressure magnitude in the fluid medium obtained from the ASM and FEM (The unit of the pressure is arbitrary).

The results indicate close agreement between the numerical solution and the exact solution. This ascertains that the chosen nodal distance (0.1λ or 10 nodes per wavelength) was small enough for the FEM (standard Galerkin method) to produce reasonably accurate results in the case of wave propagation in fluids.

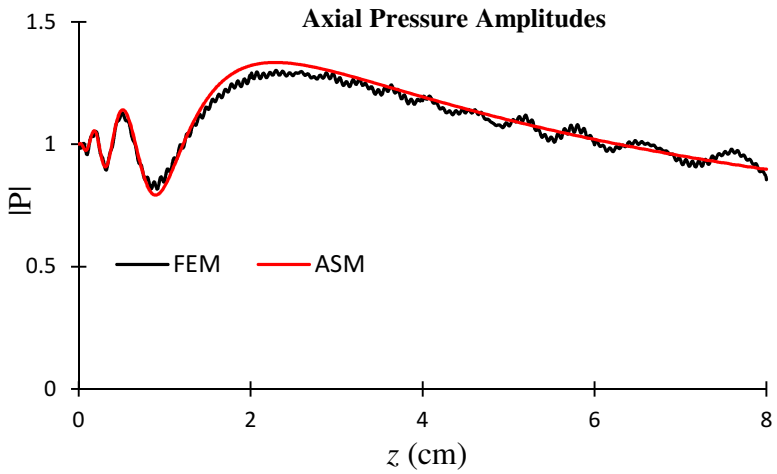

Figure 3.7 Axial pressure amplitudes.

Due to the chosen nodal distance, the effect of numerical dissipation was not observed even for far distances from the source (a distance 8-times larger than the transducer dimension 1cm). However, the numerical solution was polluted by spurious oscillations. The numerical solution of the exterior Helmholtz problem (Helmholtz problem associated with any unbounded medium) using standard Galerkin method has been reported to generate spurious oscillations [6–10].

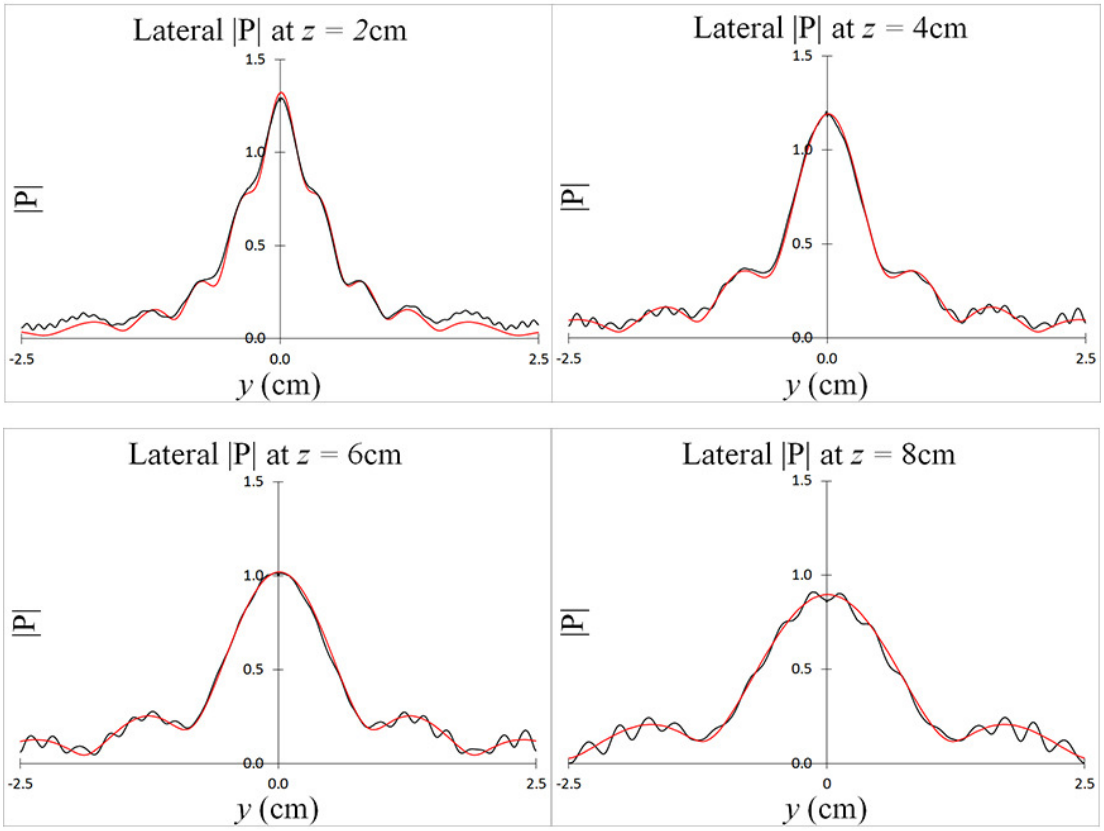

Figure 3.8 Lateral pressure magnitude for different distances from the source

The origin of the spurious oscillations is the deficiency of the standard Galerkin method in expressing the true non-reflecting boundary condition in a discretized space [6–10]. Although using non-linear elements, refining nodal-distances (smaller finite element size), locating the artificial boundaries and the associated non-reflecting boundary conditions farther from the source and changing the geometry of the artificial boundary to circle or semi-circle (sphere and semi-sphere in 3D models) will mitigate the spurious oscillations, the solution (using the Galerkin method)[9] cannot be completely free of the pollution error[10] [9].

The spatial distributions of the components of the displacement field in the solid media obtained by the ASM and the FEM are depicted in Figure 3.9 and Figure 3.10 respectively. The numerical results represent the wave fields for the two different nodal distances chosen based on the transverse and longitudinal wave lengths (λ_L and λ_T). Obviously, the numerical results based on $0.1\lambda_T$ for nodal distances are closer to the exact solution.

[9] Other methods have been proposed to control the spurious oscillations [10].
[10] Except for one-dimensional case [9] .

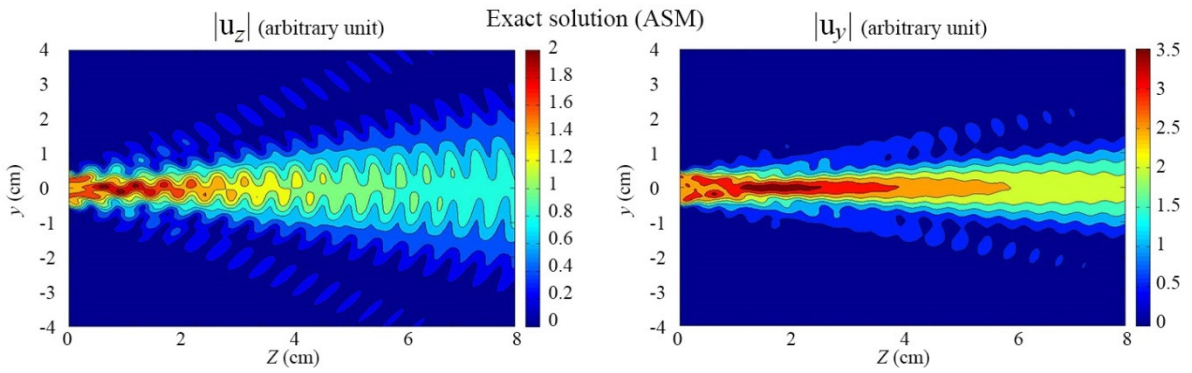

Figure 3.9 Amplitudes of the components of the displacement field obtained by the ASM

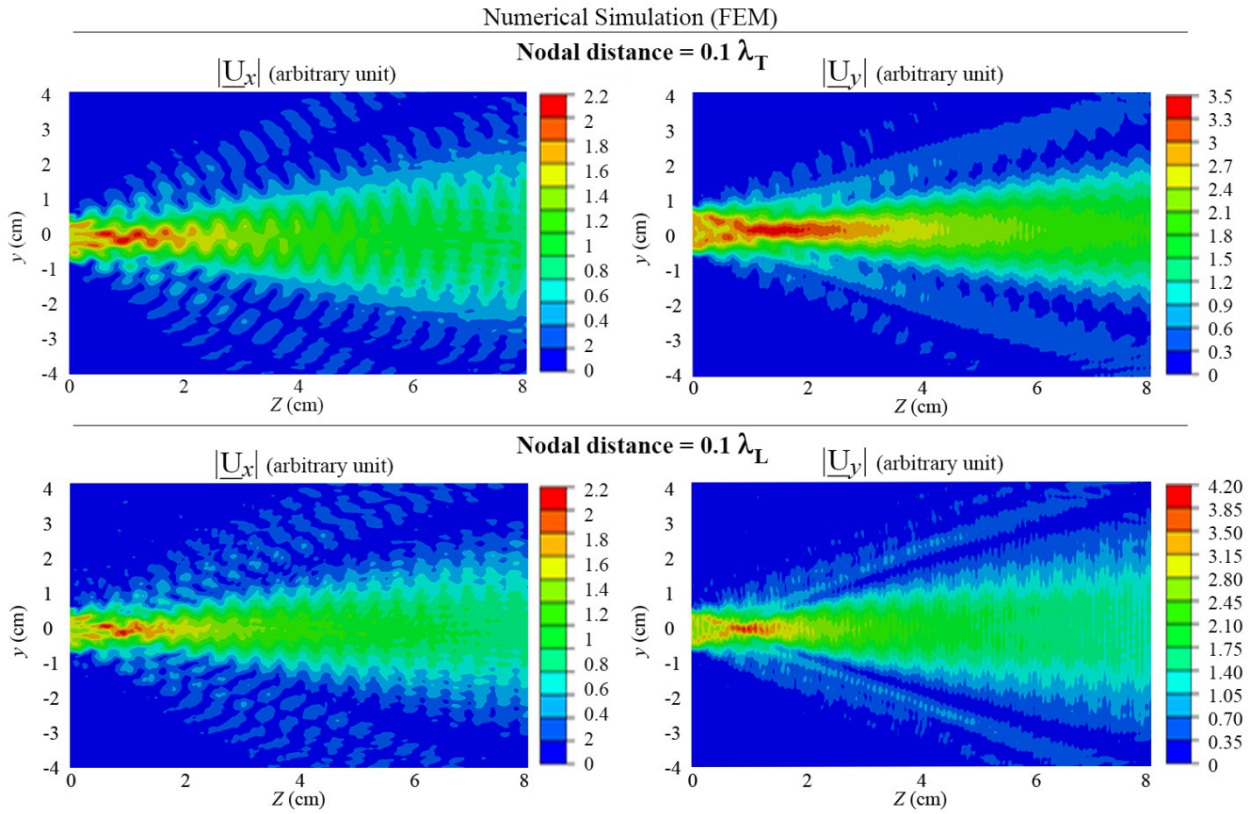

Figure 3.10 Amplitudes of the components of the displacement field obtained by the FEM for two different nodal distances.

The amplitudes of the displacement components on the central axis of the medium (z-axis) obtained from the numerical and exact solutions for different nodal distances are displayed in Figure 3.11 to Figure 3.13. Moreover, Figure 3.14 to Figure 3.16 shows the amplitudes of the displacement components on the lateral axis of the medium at $z = 4\text{cm}$.

The results indicate that choosing the nodal distance of $0.05\lambda_T$ corresponding to 20 nodes per transverse wavelength leads to an accurate finite element solution (maximum relative error

less than 5%). For the larger nodal distance of $0.1\lambda_T$ (10 nodes per transverse wavelength), the numerical solution still has an acceptable accuracy (maximum relative error of 10%) when compared with the ASM solution. However, dissipation and significant spurious oscillations affect the numerical solution when the nodal distance is $0.1\lambda_L$ or approximately equal to $0.2\lambda_T$ (5 nodes per transverse wavelength). In this particular problem, the dissipation associated with $|\underline{U}_y|$ indicates that the nodal distance is too large to adequately resolve the transverse waves. In this case, the maximum relative error is 33%.

Nodal distance = $0.05\lambda_T$

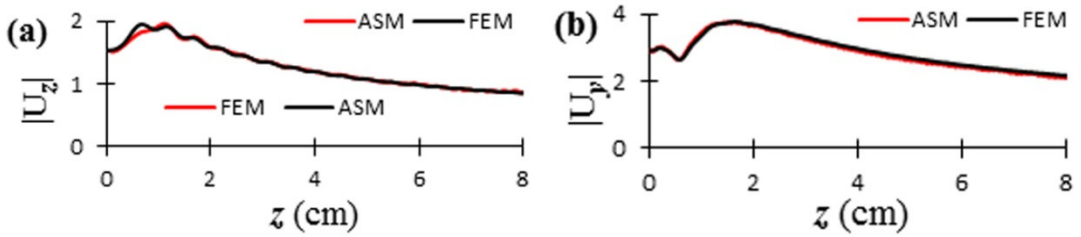

Figure 3.11 Amplitudes of the displacement components on the central axis of the medium (z-axis) obtained from the ASM and the FEM (Nodal distance = $0.05\lambda_T$).

Nodal distance = $0.1\lambda_T$

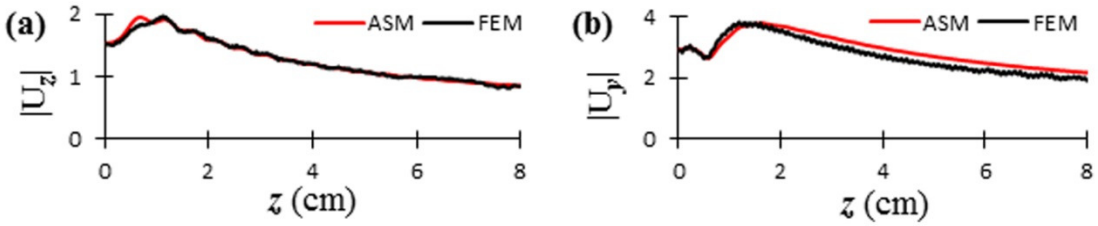

Figure 3.12 Amplitudes of the displacement components on the central axis of the medium (z-axis) obtained from the ASM and the FEM (Nodal distance = $0.1\lambda_T$).

Nodal distance = $0.1\lambda_L$

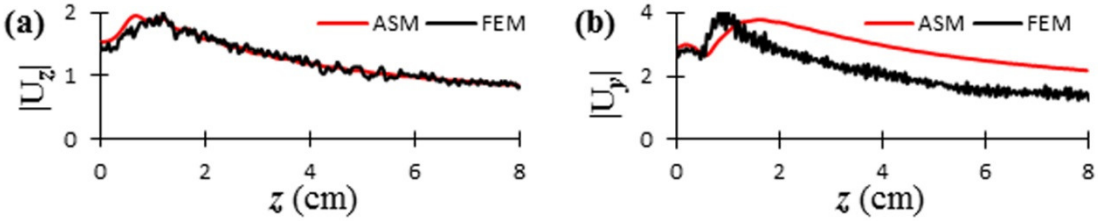

Figure 3.13 Amplitudes of the displacement components on the central axis of the medium (z-axis) obtained from the ASM and the FEM (Nodal distance = $0.1\lambda_L$).

The spurious oscillations, as previously discussed, are due to the discretized form of the non-reflecting boundary conditions in the Galerkin method. Although the spurious oscillation

cannot be avoided in the standard FEM (2D and 3D) [9], using closer nodal distances significantly mitigates the oscillations (as demonstrated by the results).

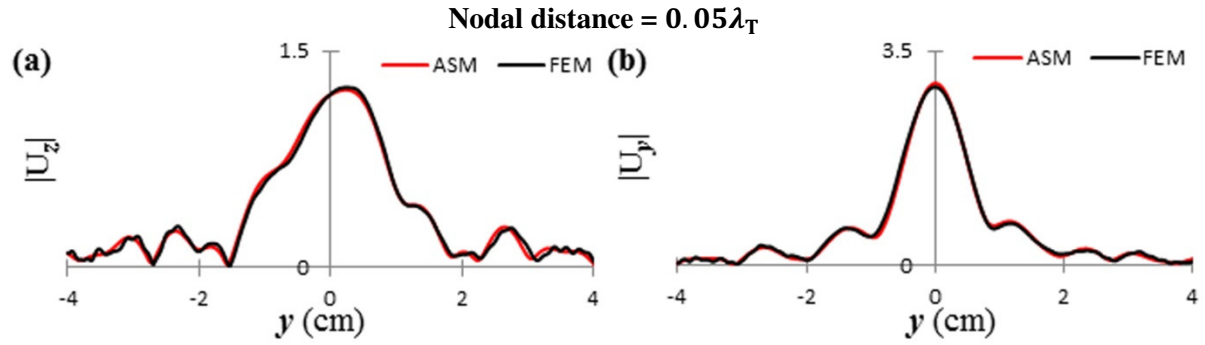

Figure 3.14 Amplitudes of the displacement components on the lateral axis at $z = 4$cm obtained from the ASM and the FEM (Nodal distance = $0.05\lambda_T$).

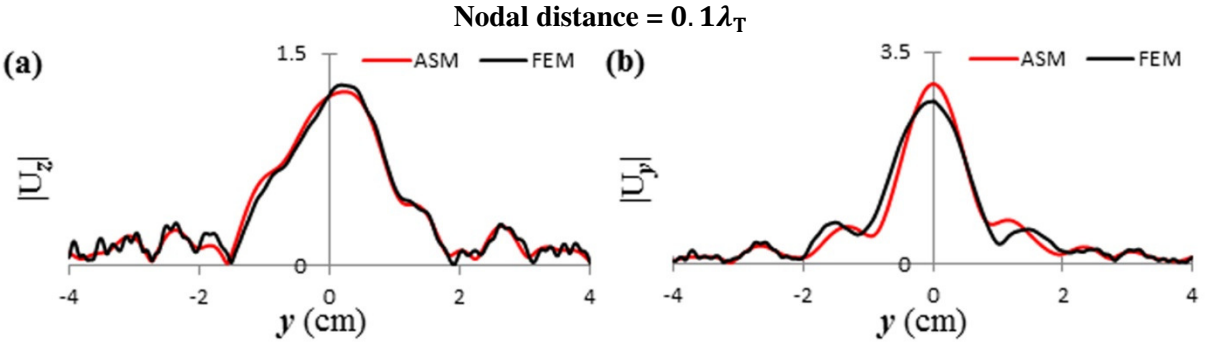

Figure 3.15 Amplitudes of the displacement components on the lateral axis at $z = 4$cm obtained from the ASM and the FEM (Nodal distance = $0.1\lambda_T$).

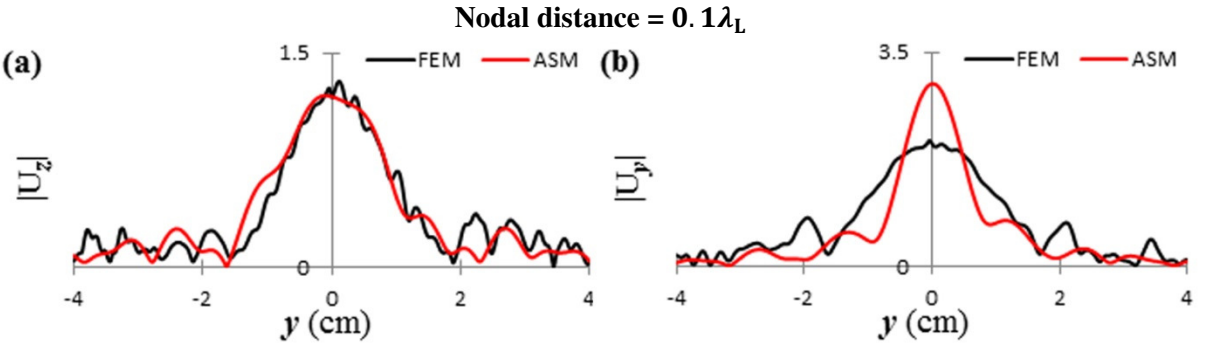

Figure 3.16 Amplitudes of the displacement components on the lateral axis at $z = 4$cm obtained from the ASM and the FEM (Nodal distance = $0.1\lambda_L$).

3.5 Conclusion

Linear steady state wave propagation in fluid and solid media was analyzed using the ASM and the FEM to evaluate the accuracy of the numerical method and the reliability of the software package. The results demonstrate that the accuracy of the numerical method is

significantly dependent on the nodal distance (or the finite element size). It can be concluded that finite element analyses through the standard Galerkin method produce accurate results if the nodal distance is between 0.1λ to 0.05λ (10 to 20 nodes per wavelength). Furthermore, the nodal distance for wave propagation in solid media should be chosen based on the transverse wavelength.

3.6 References

[1] F.J. Seron, F.J. Sanz, M. Kindelan, J.I. Badal, Finite-element method for elastic wave propagation, Commun. Appl. Numer. Methods. 6 (1990) 359–368.

[2] S. Ham, K.J. Bathe, A finite element method enriched for wave propagation problems, Comput. Struct. 94-95 (2012) 1–12.

[3] D. Systèmes, Abaqus theory manual, 2012.

[4] S. Adeeb, Introduction to solid mechanics and finite element analysis using Mathematica, Kendall Hunt Publishing, 2012.

[5] J.P. Wolf, Soil-structure-interaction analysis in time domain, Prentice Hall, 1988.

[6] A. Deraemaeker, I. Babuška, P. Bouillard, Dispersion and pollution of the FEM solution for the Helmholtz equation in one, two and three dimensions, Int. J. Numer. Methods Eng. 46 (1999) 471–499.

[7] R. Lee, A.C. Cangellaris, A study of discretization error in the finite element approximation of wave solutions, IEEE Trans. Antennas Propag. 40 (1992) 542–549.

[8] F. Ihlenburg, I.M. Babuska, Finite element solution of the Helmholtz equation with high wave number Part I : The h-version of the FEM, Comput. Math. Applic. 30 (1995) 9–37.

[9] I.M. Babuska, S. a. Sauter, Is the pollution effect of the FEM avoidable for the Helmholtz equation considering high wave numbers?, SIAM Rev. 42 (2000) 451–484.

[10] I. Babuška, F. Ihlenburg, E.T. Paik, S. a. Sauter, A generalized finite element method for solving the Helmholtz equation in two dimensions with minimal pollution, Comput. Methods Appl. Mech. Eng. 128 (1995) 325–359.

[11] F.Q. Hu, M.Y. Hussaini, P. Rasetarinera, An analysis of the discontinuous Galerkin method for wave propagation problems, J. Comput. Phys. 151 (1999) 921–946.

[12] G.M. Hulbert, T.J.R. Hughes, Space-time finite element methods for second-order hyperbolic equations, Comput. Methods Appl. Mech. Eng. 84 (1990) 327–348.

Chapter 4

The Finite Element Method for Micro-scale Modeling of Ultrasound Propagation in Cancellous Bone

The contents of this chapter have been previously published: B. Vafaeian, M. El-Rich, T. El-Bialy, S. Adeeb, Ultrasonics. 54 (2014) 1663–1676.

4.1 Abstract

Quantitative ultrasound for bone assessment is based on the correlations between ultrasonic parameters and the properties (mechanical and physical) of cancellous bone. To elucidate the correlations, understanding the physics of ultrasound in cancellous bone is demanded. Micro-scale modeling of ultrasound propagation in cancellous bone using the finite-difference time-domain (FDTD) method has been so far utilized as one of the approaches in this regard. However, the FDTD method accompanies two disadvantages: staircase sampling of cancellous bone by finite difference grids leads to generation of wave artifacts at the solid-fluid interface inside the bone; additionally, this method cannot explicitly satisfy the needed perfect-slip conditions at the interface. To overcome these disadvantages, the finite element method (FEM) is proposed in this study. Three-dimensional finite element models of six water-saturated cancellous bone samples with different bone volume were created. The values of speed of sound (SOS) and broadband ultrasound attenuation (BUA) were calculated through the finite element simulations of ultrasound propagation in each sample. Comparing the results with other experimental and simulation studies demonstrated the capabilities of the FEM for micro-scale modeling of ultrasound in water-saturated cancellous bone.

4.2 Introduction

Quantitative ultrasound (QUS) methods have been studied and clinically established for non-invasive assessments of bone status [1,2]. The capabilities of QUS techniques, in the context of osteoporosis, have been shown through prospective studies predicting the risk of fracture of the proximal femur, the vertebrae and hip and favorable results have been reported [3]. The clinical goal of QUS in the fields of bone assessment and osteoporosis diagnosis is to develop a tool for: (1) a reliable diagnosis of osteoporosis, (2) identification of subjects with high fracture risk and (3) sensitive monitoring of skeletal changes overtime [4]. To accomplish this goal, many in-vitro and in-vivo studies have been done over the past 40 years and a great variety of commercial QUS devices for bone assessment has been released over the past two decades [5,6]. However, the method has not yet achieved its ultimate applications especially as reliable diagnosing and monitoring techniques. The capabilities of the QUS methods depend on the interpretations of the QUS parameters i.e. speed of sound (SOS) and broadband ultrasound attenuation (BUA) with respect to bone status. Nevertheless, the interpretations of the

parameters, supposed to unveil the correlation between the estimated parameters and bone status, still lack comprehensiveness [2,7]. The main obstacle to fully reliable interpretations of the measurements is reported to be the insufficient understanding of ultrasonic wave propagation in cancellous bone being a porous, heterogeneous and an anisotropic medium [1,8]. Understanding the physics of wave propagation in cancellous bone is significant since osteoporosis mainly occurs at cancellous bone sites [9].

The physics of ultrasound propagation in cancellous bone has been studied utilizing in-vitro approaches (like the immersion transmission experiments) for more than 40 years to find correlations between ultrasound parameters and physical and mechanical properties of cancellous bone samples [10]. In addition to the experimental methods, theoretical approaches with great potentialities in performing parametric studies have been proposed for exploring the wave propagation in the bone. The theoretical frameworks having been proposed for this purpose during the last two decades are Biot's theory [11–16] stratified or multi-layer models [17–19] scattering model [20], and micro-scale models [1,2,14,21–26].

Micro-scale models of cancellous bone are based on virtual geometries of trabecular networks spatially sampled and served as discrete domains of numerical simulations. The geometry of a trabecular network is either virtually reconstructed by employing micro computed tomography (μ-CT) images [1,2,14,21–26] or through developing geometrical models imitating a trabecular network [27,28]. The micro-scale modeling was proposed as an alternative to the other approaches since they achieved only some moderate success in explaining the physics of the wave propagation [1,21,29]. Accounting for the complex details of micro architectures of cancellous bone saturated with fluid, the micro-scale modeling has been reported to produce evidently more realistic results than that of the other methods [2,14,24]. The capabilities of this method regarding simulating experimentally observed wave propagation phenomena in cancellous bone –like the existence of two compressional waves, linear behaviour of the frequency-dependent attenuation and the correlations between the bone bulk density and the estimated ultrasound parameters– are the evidence for its advantages over the other methods [1,2,21].

Despite the advantages of numerical simulation of ultrasound propagation in cancellous bone using micro-scale modeling, discrepancies between the numerical and experimental results

have been reported [1,2,22,25]. One of the sources of the discrepancies can be reasonably claimed to originate from the numerical method utilized in the micro-scale modeling. Briefly, the micro-scale modeling has employed the finite-difference time-domain method (FDTD) for its numerical approach to solve the linear wave equations governing the ultrasound propagation in the bone. In this approach, FDTD has used a Cartesian grid to spatially discretize the complex and heterogeneous micro-geometry of cancellous bone containing solid and fluid volumes.

A Cartesian grid leads to staircase sampling of the complex bone-fluid boundary (Figure 4.1). Producing a jagged interface, staircase sampling generates unwanted wave artifacts in the solution [30]. The simplest remedy that can mitigate the errors originating from the staircase sampling is using a fine global grid. Evidently, this approach may not be practically and computationally efficient in the case of resolving the geometry of trabecular network. Other alternatives for resolving the sampling issue of boundaries which are not aligned with a Cartesian finite difference grid are local grid refinement [31], quasi-Cartesian grid [32], curvilinear grids [33], contour-path (locally deformed grid) algorithm [34], conformal FDTD techniques [35–40]. Each of these approaches has advantages and limitations for FDTD simulating elastic wave propagation; nonetheless, to the knowledge of the authors, their implementations in the case of wave propagation in trabecular structures have not been reported yet.

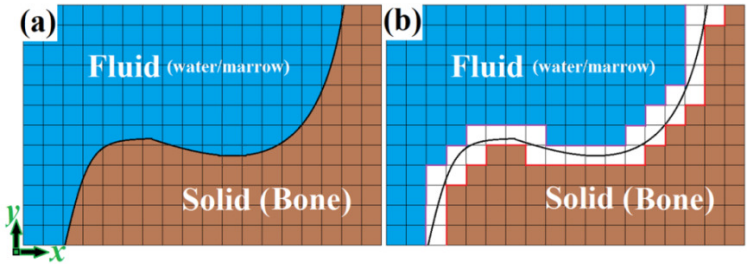

Figure 4.1 FDTD grids for a heterogeneous medium and its boundary sampling.

On the other hand, FDTD method should deal with the material discontinuity and their interfacial interaction at the solid-fluid interface [41]. The appropriate true physical interface condition for the simulations in which the saturating fluid is assumed as water (like in immersion transmission experiment) is perfect-slip[1]. The condition regarded as an acoustic-solid interaction should impose the inter-continuity of normal component of displacement (or velocity) at the

[1] Perfect-slip conditions occur at a solid-fluid interface if there exists (or is assumed) no interfacial friction. Since the saturating fluid inside the computational models was assumed to be non-viscous water, interfacial friction would not emerge at the solid-fluid interface. It should be noted that the dynamic viscosity of water at 25 ºC is about 0.0009 Pa. s which is a relatively small value; therefore, disregarding the viscosity of water in the simulations would not be far from realistic conditions.

interface, the equality of acoustic pressure in the fluid and normal traction in the solid at their shared boundary, and zero shear stresses (tangential component of the traction) at the interface in the solid medium [42]. The acoustic-solid interaction condition can be explicitly or implicitly imposed at the boundary grid points [41,43–45]. The explicit approach to the interfacial condition (also called homogeneous approach) has been generally developed. However its application is restricted to interfaces with simple geometry as horizontal, vertical or inclined line or plane boundaries [41,44]. This approach is impractical to 3-D curve material discontinuity interfaces; especially like the interface separating water/marrow and trabecular structures [41,44,46]. Even it becomes difficult or rather impractical in 2-D cases with curved boundaries since the scheme contains line integrals of the wave field [47] and also the geometry of the boundary must be known as a function of the Cartesian coordinates [41,47].

An alternative approach called the heterogeneous method, implicitly applies the physical acoustic-solid interaction condition at the interface. This method uses effective media parameters for the grid nodes located on the interface [30,42]. Effective media parameters are effective first Lame constant and effective density. These parameters are obtained by spatial averaging or combining the solid and fluid parameters in the vicinity of the interface. The true physical interfacial interaction is not necessarily satisfied by assigning the effective media parameters to the boundary nodes; however, its reliability is assumed [44]. The heterogeneous approach is associated with the first-order velocity-stress finite difference formulation of the wave propagation equation. This formulation is used with staggered grid and reported to be vulnerable to instability when the medium possesses high contrast material discontinuities [48]. The analyses for simulating the application of QUS in bone assessment [1,2,14,21,25–27,49] are mostly based on velocity-stress FDTD formulation on staggered grids; and although not reported, some kind of effective parameters at the fluid-bone interface must have been implemented. Therefore, it is reasonable to blame some part of the observed discrepancy (between simulation and experimental results) on the FDTD approach for the numerical solution of the wave equations in the complex medium.

One approachable remedy that can be claimed to be more efficient –than FDTD– in manipulating the complex geometry, material discontinuity and the acoustic-solid interaction in cancellous bone media is the finite element method (FEM). The FEM, reported to be generally superior to FDTD for elastic wave propagation analyses [50,51], can potentially account for

better geometrical-sampling of any complex geometry [43]. Consequently, it should reduce the possible wave propagation artifacts arising from non-smooth sampling of fluid-bone interface. Regarding the material discontinuity and the interaction, the advantage of FEM over FDTD methods is that the acoustic-solid interaction condition can be explicitly satisfied at the interface [52].

It is worth mentioning that other researchers have already demonstrated that the micro-geometry of a trabecular network can be virtually reconstructed and prepared for static- or harmonic-load finite element analyses [53–56]. The models used either brick (8-node) elements or tetrahedral (4-node) elements to discretize the trabecular micro-geometry. In contrast to brick elements which led to stepwise (staircase) sampling of trabecular micro-geometry, tetrahedral elements generated a linear piecewise smooth approximation of the geometry. The latter even allowed generating a secondary interacting finite element volume-mesh filling the space between trabecular networks [53].

In the case of ultrasound propagation analysis, the FEM has been employed to simulate the wave propagation in a homogeneous micro-geometry of cancellous bone [57]. The simulations employed brick elements and did not consider any saturating fluid between the trabecular networks; hence unable to account for wave attenuation. Furthermore, other studies utilizing FEM to simulate the wave propagation in this field did not explicitly involve the micro-geometry of cancellous bone [7,58].

Although the FEM is theoretically developed enough for elastic wave propagation analysis and commercial software packages capable of considering acoustic-solid interaction are available, micro-scale simulations of ultrasound propagation in fluid-saturated cancellous bone has not yet been elaborated through this method. In this paper, a methodology for micro-scale simulating of ultrasound propagation in fluid-saturated cancellous bone is proposed. The main aims of this study are to demonstrate that the FEM can simulate the phenomena observed in the experiments and to show that the simulations can predict the ultrasonic parameters in healthy and osteoporotic bones. The experimental phenomena such as frequency-dependent attenuation, linear trend of the attenuation in a specific frequency range, dependency of the ultrasound speed on bone density are clear in the simulation results. Additionally, the BUA values for the healthy and osteoporotic bone samples calculated using the simulation results clearly demonstrate

distinguishable differences between the bone samples.

4.3 Materials and methods

In this study, the numerical simulations were associated with a typical immersion transmission experiment for in-vitro bone assessment (Figure 4.2). Located in an acoustically isolated water tank, a transmitting transducer (transmitter) generates an ultrasonic pulse signal and a coaxially situated receiving transducer (receiver) records the signal. A signal emitted by the transmitting transducer is referred to as the transmitted signal. In-vitro QUS bone assessment using this experiments requires two different experimental setups. The first setup is designated to record the propagation of a transmitted signal in the water tank without a bone sample; whereas the second setup includes a bone sample and the recorded signal is hence affected by the sample. The received signals in the former and the later setups are denoted as the reference and the bone signals respectively.

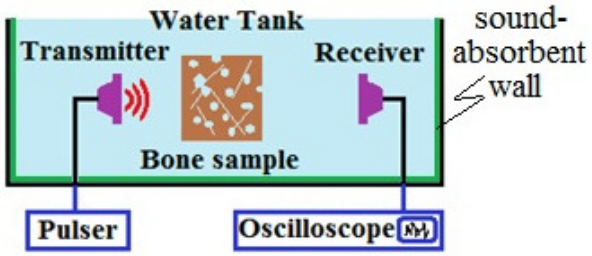

Figure 4.2 Immersion transmission experiment for QUS based bone assessment.

A physical immersion transmission experiment may be carried out with bone samples being defatted and re-saturated with water [2,6,15,26,29]. This replaces the interior bone marrow with water having the same properties as that in the tank. The finite element models in the present study simulated a corresponding experiment containing defatted and re-saturated bone samples.

4.3.1 Devising modeling-schemes for the experiment

Simulating ultrasound propagation based on an immersion transmission experiments was considered as an exterior problem. In an exterior problem, a vibrating structure (here is a water-saturated cancellous bone sample) is surrounded by an infinitely large medium in which presumably no wave reflection happens. In the experiment configuration, the dimensions of the water tank are usually large enough to be assumed as an infinitely large medium during the

measurement time. Practically, a finite element model cannot regard the infinite dimensions of the surrounding medium; therefore, a model of the medium should be restricted to some artificial boundaries on which non-reflecting properties are applied.

To model the QUS experiments by the FEM, the medium of the models was restricted to an artificial boundary bounding the vicinity of a space embedding the transducers[2] (Figure 4.3a and Figure 4.3b). Acoustic infinite elements were mainly chosen to designate a non-reflecting property to the artificial boundary. The infinite elements are different from usual acoustic finite elements in a sense that they radially approximate the surrounding infinite acoustic field by a set of ninth-order polynomials; thereby, they resemble the infinite medium by absorbing waves. Since acoustic infinite elements have their optimum functionality when located on a spherical surface [52], the most desirable surface geometry for the corresponding virtual boundary was spherical. This led to a spherical geometry for the finite element models. However, to introduce more efficiency in the size of the finite element models, the spherical virtual boundary was trimmed to a hemisphere in advance.

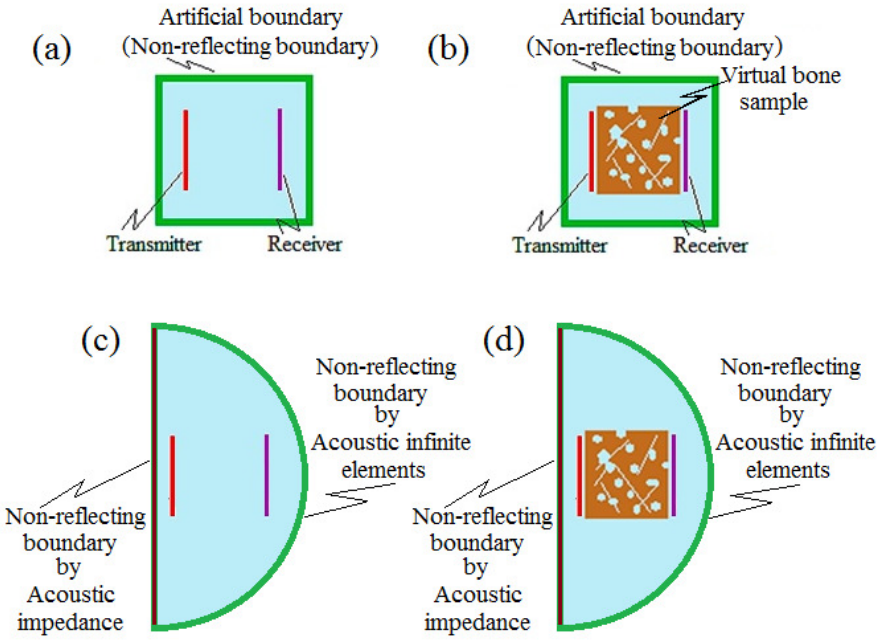

Figure 4.3 (a) The restricted geometry of the model for the experimental setup without bone; (b) The restricted geometry of the model for the experimental setup with bone; (c) The geometry of the model for the experimental setup without bone; (d) The geometry of the model for the experimental setup with bone.

[2] 'Transducer' in the finite element models referred to a numerical transducer defined as specific pressure boundary conditions acting as a transmitter or a set of acoustic nodes at which acoustic pressure was recorded in the case of a receiver.

Being geometrically flat, the back surface of the hemisphere would not lead to the optimal functionality of the acoustic infinite elements[3]. Another alternative to acoustic infinite elements was taking the advantages of acoustic impedance. Acoustic impedance with specific constants imposed on finite element nodes behaves as an approximate wave-absorbing boundary condition at the nodes [52]. Therefore, the non-reflecting property for the back surface was considered using acoustic impedance condition. Figure 4.3c and Figure 4.3d depict the hemispherical geometry of the models resembling the two different experimental setups.

4.3.2 Introducing an ultrasonic pulse

Two different ultrasonic pulse signals were considered in the form of cosine Gaussian functions and expressed by the following equations in time and frequency domains:

$$P(t) := e^{-\left(\frac{t-D/2}{a}\right)^2} Cos(2\pi f_0(\mathrm{t} - \mathrm{D}/2)) \qquad (4.1)$$

$$\mathcal{F}\{\mathrm{P(t)}\} = e^{-\mathrm{D}\pi f j}[1/2\, a\sqrt{\pi}(e^{-\pi^2 a^2 (f-f_0)^2} + e^{-\pi^2 a^2 (f+f_0)^2}) \qquad (4.2a)$$

$$P(f) := |\mathcal{F}\{\mathrm{P(t)}\}| = 1/2\, a\sqrt{\pi}(e^{-\pi^2 a^2 (f-f_0)^2} + e^{-\pi^2 a^2 (f+f_0)^2}) \qquad (4.2b)$$

Such that $P(t)$ is the unit-amplitude[4] ultrasonic pressure on the transmitter surface as a function of time (seconds), $a = \sqrt{2}\sigma$ in which σ is the standard deviation of the Gaussian distribution of the pulse envelop, $\mathrm{D} = 8\sigma$ is the total duration of the signal and f_0 was the signal center frequency in Hertz. In the frequency domain, Eq. 4.2a explicitly expresses the Fourier transform of Eq. 4.1 as a function of frequency f such that $j^2 = -1$ is the imaginary unit. It should be noted that the Fourier transform of the introduced Gaussian signals contains an imaginary part, beside its real part, due to the time-shifting parameter ($\frac{D}{2}$) in time domain. The amplitude of Eq. 4.2a is denoted $P(f)$ and explicitly by given Eq. 4.2b.

Figure 4.4 illustrates the ultrasonic signals and their frequency content (amplitude spectra by Eq. 4.2b) chosen for the analyses. As stated in the figure the center frequency and the

[3] The infinite elements on the hemispherical surface used a reference node located at the sphere center for radial approximation of the infinite medium. If infinite elements had been used on the flat back surface using the same reference node, they would have reflected considerable amount of the waves back into the medium. Additionally, employing another reference node in a distant location corresponding to the infinite elements on the back surface was not possible, since infinite elements with different reference nodes were not to share nodes. This would have been the case for the nodes of the infinite elements situated on the common boundary of the hemisphere and the back surface [52].

[4] The unit of $P(t)$ is arbitrary.

duration of the signals were $f_0 = 0.6MHz$, D = 7.35μs and $f_0 = 0.85MHz$, D = 5.09μs respectively. The first signal ($f_0 = 0.6MHz$, D = 7.35μs) was referred to as the primary signal and the other one was denoted as the secondary signal in the analyses and the results. The secondary signal was introduced in order to investigate the effect of the center frequency and the frequency content of a different signal on the attenuation results.

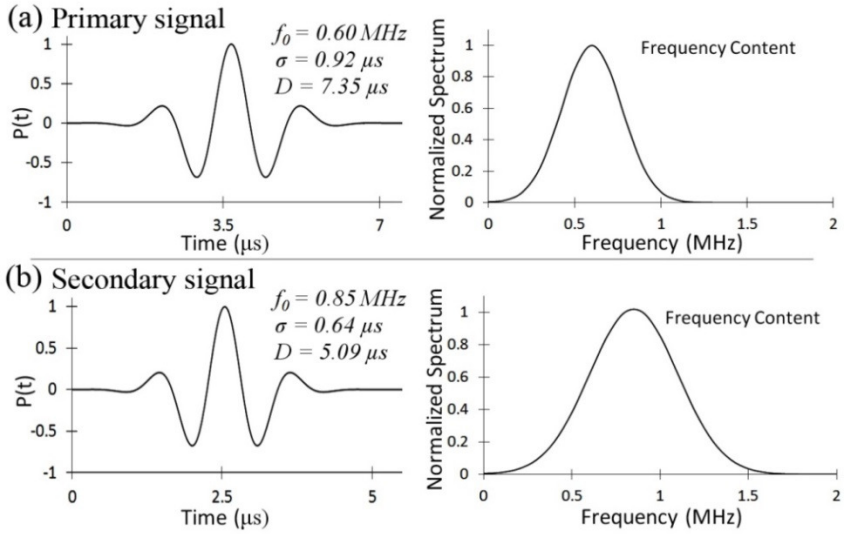

Figure 4.4 Ultrasonic signals in time domain and their frequency contents (amplitude spectra).

The parameters of the signals were chosen in a way that the consequent wavelengths in the finite element models could be resolved by the size of the finite elements with the least possible error. Apparently, the time of the analyses and the needed hardware resources were related to the size and number of the elements, therefore the signal parameters were intuitively optimized to avoid dramatic increase in the number of elements (due to relatively small wavelengths). This suggested that the signals might not associate with a real physical transducer. Nevertheless, the aim of this paper, demonstrating the ability of FEM to simulate ultrasound propagation in trabecular structure, did not require the signals to be associated with real physical transducers, especially when the results were not directly compared with experimental results.

4.3.3 Creating the finite element model for the water-only medium

As previously stated, the propagation of the signal was needed to be initially simulated in the medium without bone i.e. water-only medium, which was assumed to be non-viscous. Linear mechanical wave propagation in a non-viscous fluid was modelled using a linear relationship between fluid excess pressure (acoustic pressure) and its consequent volume change. The

relation is expressed as $p = -B\varepsilon_V$ in which p and B are the acoustic pressure and the fluid bulk modulus respectively (Table 4.1), and ε_V denotes the linear change of fluid volume per unit volume.

The hemispherical geometry of the water-only medium was created and meshed with tetrahedral acoustic elements using a software package called HyperMesh (Figure 4.5). The acoustic elements were associated with acoustic pressure as the only degree of freedom at each of their nodes. The size of the elements inside a virtual cubic volume surrounding the vicinity of transducers and the space between them was $0.1\lambda_w$; such that λ_w was the smallest wave length in the water medium (Table 4.1). Since, only accurate results were needed inside this virtual cube (containing the transmitter and the receiver), the rest of the model being outside this cube up to the hemisphere boundary was meshed with larger elements. This part of the model, with elements gradually increasing in size (from $0.1\lambda_w$ to λ_w), was a means to guide the waves towards the boundary of the hemisphere partially covered by acoustic infinite elements and partially assigned acoustic non-reflecting boundary conditions (acoustic impedance).

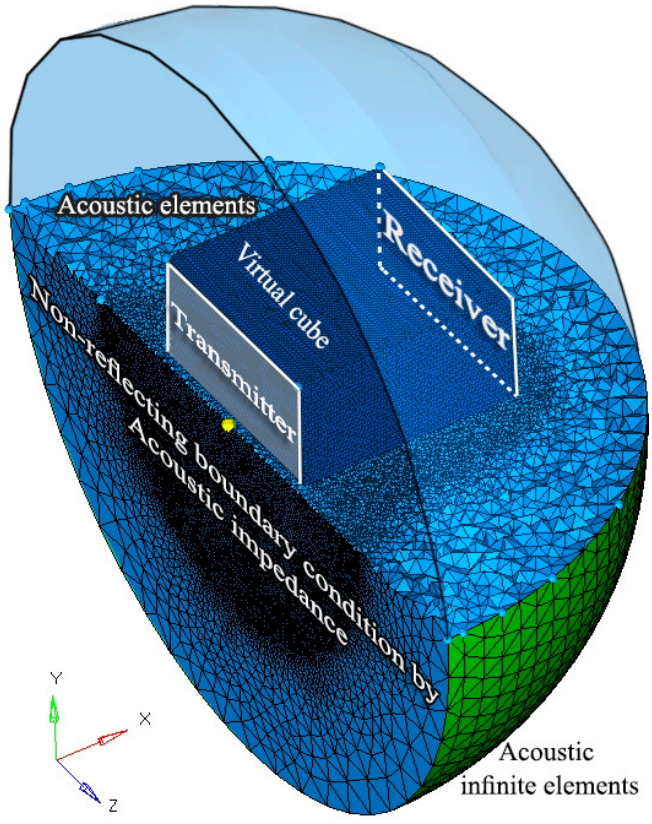

Figure 4.5 The finite element model of the water-only medium (only half of the meshed model is demonstrated).

Totally 7,544,855 elements and 1,270,091 nodes were generated for the finite element model of water medium. The temporal ultrasonic signal was uniformly assigned to the pressure degree of freedom of the finite element nodes aligned on side of the virtual cube indicated as the transmitter in Figure 4.5. The receiver was also a collection of nodes on the other side of the cube located coaxially with the transmitter plane.

Table 4.1 Material properties used in the FEA.

	Bone [1]	Water [1]
Density (kg/m^3)	1850	1000
Constitutive-law constant	$E = 18443^*, \nu = 0.35^*$	$B = 2200^*$
Longitudinal wave velocity (m/s)	4000	1483
Transverse wave velocity (m/s)	1922	0
Smallest wavelength in the material (mm)**	$\lambda_b = 1.6$	$\lambda_w = 1.2$

$*$ E = Modulus of Elasticity (MPa); B = Bulk Modulus (MPa); ν = Poisson's ratio

** Based on the highest frequency i.e. 1.2MHz

4.3.4 Creating the finite element model for the media with bone samples

Micro-computed tomography scan (μ-CT) data of radial bones of four human patients were obtained from Bone Imaging Laboratory at the University of Calgary. An XtremeCT device from Scanco Medical (Switzerland) was utilized to scan $9.02mm$ length of the radial bones at the laboratory. The data were completely anonymous and in the form of DICOM files with nominal isotropic voxel size of 82μm. The patients subjected to μ-CT scan had been diagnosed with three different conditions in their radiuses: osteoporotic, osteopenic and healthy. 3D geometrical representations of the scanned volume of each bone were regenerated out of the μ-CT scan data using "Mimics" (Materialise Mimics 2013.16.0). Figure 6 shows the four reconstructed sets of geometry classified into the 3 different conditions. Cubic geometrical volume ($4 \times 4 \times 4\, mm^3$) in the cancellous portion of the bones' geometry were marked and extracted from different locations of the reconstructed geometry of the radial bones. The virtual[5] cubic bone samples contained the closed geometrical surface of the sampled trabecular structures (Figure 4.6). The geometry data of the virtual trabecular structures confined in the cubic volumes were exported in the form of binary Stereo Lithography (STL) to generate a closed triangular

[5] By virtual, it is intended to discriminate the difference between a real bone sample and the reconstructed geometry of a bone sample by computer.

surface mesh for each of the structures. Due to non-uniformity of the generated STL mesh for the trabecular structures, Geomagic software package (Geomagic Studio 2012.1.0), was employed to enhance the uniformity and the quality of the mesh. At this stage the dimensions of the virtual cubic cancellous bone samples (denoted by a in Figure 4.6) slightly changed (up to 5%) as a result of mesh enhancement. Bone volume to tissue volume (BV/TV) of each virtual sample was calculated considering the variations in the dimensions (Figure 4.6).

Totally six finite element models embracing the virtual bone samples were created by adding the trabecular structures to the finite element model of the water-only medium. Each virtual bone sample was situated in the middle of the virtual cube, hence in the middle of the transducers. This would create a layer of water (acoustic elements) occupying the space between each of the transducers and the trabecular structure in the model. The normal vector of the transmitter surface was perpendicular to the main orientation of the trabecular structure. In other words, the transmitted wave front was perpendicular to the main orientation of the trabecular network or globally perpendicular to the longitudinal direction of the original radial bones.

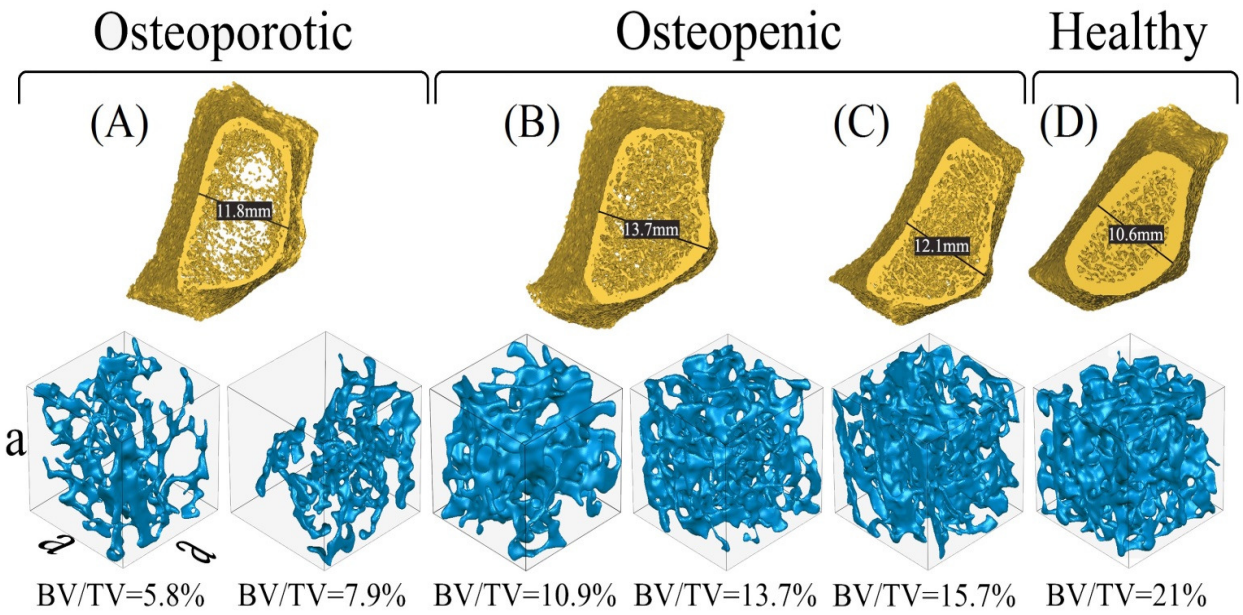

Figure 4.6 Reconstructed geometry of the radial bones and virtual cancellous bone samples.

Tetrahedral solid elements were employed to mesh the bony part of the medium surrounded by acoustic elements. Subsequently, the fluid (non-viscous water) mesh inside the virtual cube was regenerated to conformably surround the embraced trabecular structure geometry. To accurately resolve the waves, the maximum size of the solid elements was

restricted to $0.1\lambda_b$, in which λ_b was the smallest transverse wavelength in the trabecular structures (Table 4.1). However, the size of the elements was also inherently controlled by the geometrical details of the trabecular structures determined by the triangular surface mesh. Figure 4.7 illustrates a typical finite element model including one of the virtual cancellous bone samples. The finite element models of the media with bone samples contained 269,508 to 785,326 solid elements (with 69,463 to 192,882 nodes) and 7,465,000 to 6,939,102 acoustic elements (with 1,196,921 to 1,319,378 nodes) depending on the embraced trabecular structure.

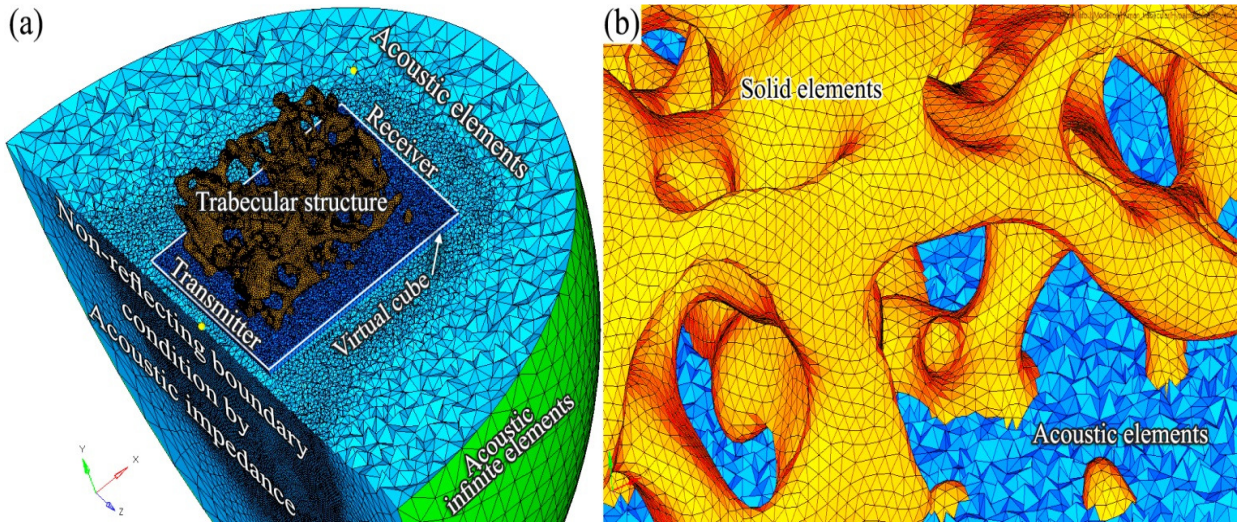

Figure 4.7 (a) The finite element model of a typical virtual calcellous bone sample surrounded by the water medium; (b) A close look at the mesh generated for each of the bone and water media.

The direct sampling consequence of the generated tetrahedral solid mesh was that the outer surface of the elements linearly approximated (sampled) the complex geometry of the trabecular structure. This linear spatial sampling, compared to the staircase sampling by the FDTD, was expected to decrease the wave artifacts at the solid-fluid interface. Moreover, the linear approximation made it possible to later apply an explicit acoustic-solid interaction at the solid-fluid interface.

The advantage of using the FEM was its ability to explicitly satisfy the perfect-slip conditions at the common interface of solid and fluid media (Figure 4.8). At the solid-fluid interface (Ω_{fs}), solid elements having displacement degrees of freedom were exposed to acoustic elements with pressure degree of freedom. The interfacial perfect-slip conditions could be expressed by the following equation, according to its definition [42,52]:

$$\hat{\boldsymbol{n}} \cdot \mathbf{u}_f = \hat{\boldsymbol{n}} \cdot \mathbf{u}_s \quad (4.3a)$$

$$P_{\Omega_{fs}} = \hat{\boldsymbol{n}} \cdot \mathbf{T}_s \quad (4.3b)$$

$$\hat{\boldsymbol{m}} \cdot \mathbf{T}_s = \mathbf{0} \quad (4.3c)$$

where $\hat{\boldsymbol{n}}$ and $\hat{\boldsymbol{m}}$ are the normal and tangential unit vectors of the fluid boundary at the interface (Figure 4.8), $\mathbf{u}_f$ and $\mathbf{u}_s$ are the displacements in fluid and solid media respectively, and $\mathbf{T}_s \in \mathbb{R}^3$is the traction vector on the solid side at Ω_{fs}. In addition, the fluid pressure on Ω_{fs} surface is denoted by $P_{\Omega_{fs}}$. Since the fluid was governed in terms of acoustic pressure, not displacements, the second time derivatives of Eq. 4.3a should be used. Therefore, Eq. 4.3a can take the following form by taking the advantage of the dynamic equilibrium equation in fluids ($\ddot{\mathbf{u}}_f + {}^1/_{\rho_f}\nabla p = 0$, ∇ and ρ_f are the gradient operator and fluid density respectively, $\ddot{\mathbf{u}}_f$ indicates the acceleration of the fluid particles):

$$(-\hat{\boldsymbol{n}} \cdot {}^1/_{\rho_f}\nabla p_{\Omega_{fs}}) = \hat{\boldsymbol{n}} \cdot \ddot{\mathbf{u}}_s \quad (4.4)$$

in which $\ddot{\mathbf{u}}_s$ indicates the second derivative of displacements in solid with respect to time.

The second essential condition was satisfied by exerting the acoustic pressure as an external normal force on the boundary of the solid at Ω_{fs}. Equation 4.3c expressing the zero tangential traction on the solid at the interface was automatically fulfilled since the equation of the fluid was written in terms of pressure; therefore, it did not interact with the solid's equation.

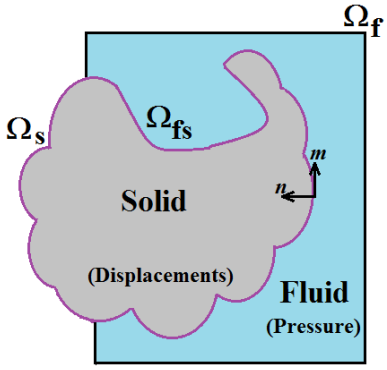

Figure 4.8 A scheme of solid-fluid heterogeneous medium.

4.3.5 Performing finite element analyses

The commercial finite element software ABAQUS (Simulia 6.12) was used to perform time-domain analyses of ultrasound propagation in the finite element models (6 with virtual bone

samples and 1 water-only medium). For simplicity, any energy dissipation mechanisms due to the material properties were disregarded in the simulations (no sort of material damping mechanisms were considered for water and bone materials). Additionally, the simulations did not take the energy dissipation from the solid-fluid internal friction into account. These simplifications indeed caused underestimations in the simulated attenuation values.

The wave propagation simulations including interfacial perfect-slip conditions were based on the following linear differential equations of motion in solid and fluid respectively:

$$(\lambda + \mu)\nabla(\nabla . \boldsymbol{u}_s) + \mu\nabla^2\boldsymbol{u}_s = \rho_s\ddot{\boldsymbol{u}}_s \tag{4.5a}$$

$$\ddot{p} = \frac{B}{\rho_f}\nabla^2 p \tag{4.5b}$$

such that λ, μ are the first and second Lame's parameter, ρ_s is the density of the solid. Double dots (in $\ddot{\boldsymbol{u}}_s$ and $\ddot{p}$) and ∇^2 denote second derivative with respect to time and the Laplacian operator respectively.

The discretization of the equations of motion by the software package was through introducing interpolation functions as:

$$\mathbf{u}_\mathrm{s} \approx \mathbf{N}\mathbf{u}_s^N \tag{4.6a}$$

$$\mathrm{p} \approx \mathbf{H}\mathbf{p}^M \tag{4.6b}$$

in which $\mathbf{u}_s^N$ and $\mathbf{p}^M$ are nodal displacement vector and the vector of nodal pressure value respectively. $\mathbf{N}$ is the interpolation or shape function for the displacements at each solid node and $\mathbf{H}$ is the shape function for the scalar quantity of the pressure. Consequently, the discretized form of the linear mechanical wave equation for solid coupled with the adjacent fluid was derived using a Galerkin method as [52]:

$$\mathbf{M}_s\ddot{\mathbf{u}}_s^N + \mathbf{K}_s\mathbf{u}_s^N + \mathbf{S}^\mathrm{T}\mathbf{p}^M = \mathbf{F}_s \tag{4.7}$$

such that $\mathbf{M}_s$, $\mathbf{K}_s$, $\mathbf{S}$ and $\mathbf{F}_s$ are the mass matrix, the stiffness matrix, acoustic-structure coupling matrix and the load vector of external nodes respectively. Superscript T denotes matrix transpose.

Following the same discretizing method but using a Petrov-Galerkin scheme, the wave equation in the fluid coupled with its adjacent solid took the following discrete form [52]:

$$\mathbf{M}_f \ddot{\mathbf{p}}^M + \mathbf{K}_f \mathbf{p}^M - \mathbf{S}\ddot{\mathbf{u}}_s^N = \mathbf{F}_f \qquad (4.8)$$

where $\mathbf{M}_f$, $\mathbf{K}_f$, $\mathbf{S}$ are the acoustic mass matrix, the acoustic stiffness matrix and acoustic-structure coupling matrix respectively. $\mathbf{F}_f$ is the acoustic pressure load due to existence of acoustic pressure gradient or fluid particles acceleration on parts of the Ω_f at which the pressure values are not explicitly defined. It can be readily noted that, in the case of the models with virtual bone samples, the cause of solid-fluid acoustic coupling appears as the third terms in Eq. 4.7 and Eq. 4.8. The details of the defined matrices in Eq. 4.7 and Eq. 4.8 are available in chapter 2 section 2.4.3.

The time-domain finite element analysis (FEA) of the models was performed using Parallel execution in Abaqus/Explicit. Since the models contained very large number of degree of freedoms, a version of Abaqus installed on one of the clusters (a Linux AMD Istanbul cluster at WestGrid) in Compute-Canada (national platform of supercomputing resources) was utilized. The computation facility provided 48 processors of 2.4 GHz and enough memory (17.5 gigabytes) for the analyses. The FEA contained the transmission of the primary signal into the finite element model of the water-only medium and the models of the media containing the six virtual bone samples. However, the secondary signal, in addition to the water-only media, was only implemented in the models containing the healthy and the osteopenic virtual bone samples with $BV/TV = 10.9\%$ (Figure 4.6).

The direct output of each FEA was in the form of a pressure signal at the finite element nodes located on the receiver surface. To record the computed pressure signals, a temporal sampling frequency of 100MHz was considered. Moreover, the signals were spatially averaged over the receiver surface area at each sampling time[6]; this resembled the average acoustic pressure sensed by an ideal receiver transducer in a typical immersion transmission experiment.

The finite element analyses of the models were based on a weak variational formulation of the equations of motion in the solid and the neighboring fluid media. Furthermore, the explicit interfacial perfect slip conditions introduced in the formulation were theoretically expected to simulate phenomena such as elastic scattering, refraction and mode conversion of the waves [52,59].

[6] A piece of code in Python was written to access the numerical simulation results stored in the database generated by the software (Abaqus) and to perform the averaging over the receiver surface (Appendix D).

4.3.6 Calculating SOS and BUA

4.3.6.1 BUA

Initially, each bone signal was treated with a hamming window in time domain to reduce the leakage effect associated with the Fast Fourier Transform (FFT). Subsequently, the amplitude spectra of the bone and the reference signals were calculated by the FFT. This led to obtaining the normalized frequency-dependent attenuation coefficient for each virtual bone sample as:

$$\alpha_{FEA}(f) = \frac{20}{d}\log(\frac{|A_R|}{|A_B|}) \quad (4.9)$$

in which α_{FEA} (the coefficient obtained through FEA) is given in $^{dB}/_{cm}$ and represents plane wave amplitude attenuation, d is the length of the virtual bone sample in the initial direction of the transmitted signal, $|A_R|$ and $|A_B|$ are respectively the absolute values of the FFT of the reference and bone signals. The frequency-dependent attenuation, $\alpha_{FEA}(f)$, was considered in a frequency bandwidth ranging from 0 to 1.2 MHz.

A linear regression was performed on the attenuation coefficient vs. frequency data over a bandwidth of interest i.e. 0.2–1 MHz. The attenuation values were fitted to the linear model defined by the following equation:

$$\alpha_{model}(f) = \text{nBUA} \times f + \text{c} \quad (4.10)$$

such that nBUA, with the unit of $^{dB}/_{cm.MHz}$, indicates normalized BUA and 'f' is the frequency in MHz. The attenuation index (BUA) was expressed in the normalized form (nBUA) to preserve the consistency with the normalized attenuation coefficients (α_{FEA}).

4.3.6.2 SOS

Estimation of SOS was performed based on recording the time-of-flights (TOF) of two temporal markers on the primary transmitted signal [60]. The markers were considered as the maximal peak and the first zero crossing of the signal. Locating a first-zero-crossing marker on the transmitted signal and retrieving the same marker on the received signals (reference or bone) required a signal-detecting threshold. A threshold range of 5% to 10% of the signal maximal peak was considered for each of the transmitted, reference and bone signals in the simulations.

By recording the TOF of the signal markers, SOS in water-only medium and in virtual

bone samples could be calculated as [61,62]:

$$c_{ref} = \frac{L}{TOF_{ref}} \tag{4.11a}$$

$$\text{SOS} = \frac{L_b}{TOF_b - \frac{L - L_b}{c_{ref}}} \tag{4.11b}$$

where c_{ref}, L and TOF_{ref} are the calculated speed of sound in the water-only medium, the distance between the transducers and the recorded TOF for the signal traveling in the water medium respectively. The speed of sound in a virtual bone sample is denoted by SOS being calculated by knowing the sample thickness L_b and recording the TOF of the signal propagating in the finite element models containing virtual bone samples (TOF_b). It should be noted that L is slightly larger than L_b due to the water layer occupying the space between the transducers and the virtual sample.

4.4 Results and discussion

4.4.1 Transmitting the primary signal

Figure 4.9 shows the primary transmitted and the received (reference) pressure signal $P(t)$ in the medium without bone. The TOF of the two markers, signal's peak and its first zero crossing, are shown by Δt_p and Δt_0 on the figure respectively. Marking the first zero crossing point on the transmitted signal and recognizing the point on the reference signal (received) were based on the defined signal detection criterion (section 4.3.6.2).

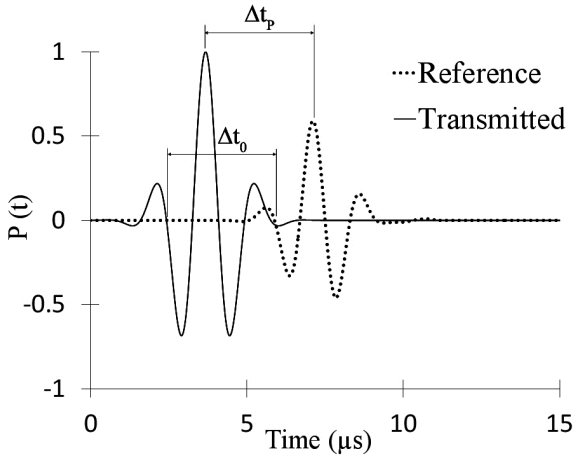

Figure 4.9 Primary transmitted and reference signal (water-only medium).

Recording the TOF of the markers led to obtaining the speed of sound in water (c_{ref}) as $1531\frac{m}{s}$ and $1513\frac{m}{s}$ associated with Δt_p and Δt_0. It can be also noted that the predicted values for c_{ref} differ from its theoretical value i.e. $1483\frac{m}{s}$, such that the maximum error with respect to the theoretical value is 2%. The cause of the differences is due to the fact that different parts of the propagating wave front did not reach to the plane surface of the receiver at the same time (since the wave front was not plane). Consequently, the special averaging over the receiver plane surface did not preserve the relative locations of the markers on the reference signal.

The bone signals along with their amplitude spectra are illustrated in Figure 4.10b to Figure 4.10g. The amplitude spectra calculated by FFT were discrete; however the graphs seem continues due to a close frequency step on the frequency axis.

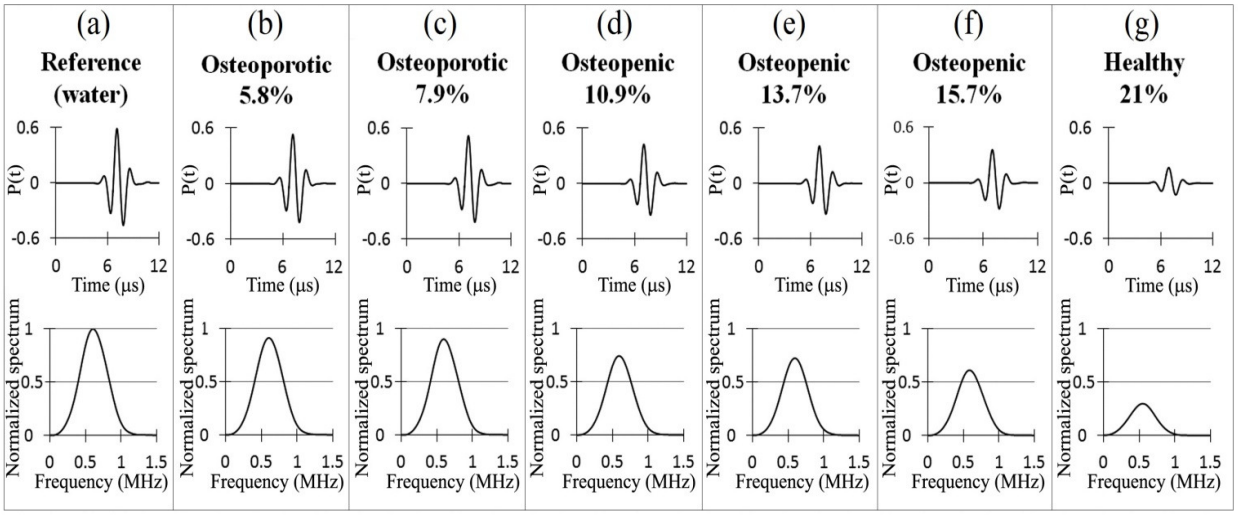

Figure 4.10 (a) The received reference signal in time domain and its amplitude spectrum; (b) to (g) Bone signals and their amplitude spectra.

By taking the advantage of each signal's temporal form, SOS for each water-saturated virtual bone sample was obtained. The predicted SOS values were based on the two predefined markers on the transmitted signal. The maximal peak of each signal was obvious and readily detected, moreover the first zero crossing marker was retrieve based on the signal-detecting criterion for each bone signal. Figure 4.11a illustrates the six received bone signals and the time interval in which the first zero crossing points were detected and retrieved.

The values of SOS were plotted against the ratio BV/TV for each sample and linear regression was employed to linearize the relation between SOS and BV/TV (Figure 4.11b). As

illustrated in Figure 4.11b, SOS had increasing trends with the bone volume ratio and led to a positive correlation with BV/TV regardless of the method of measurement. The trend is reasonable according to this fact that more amount of bone in the medium should generally affect the SOS positively. The same trend is reported in other experimental and numerical studies for the same range of BV/TV [1,14,60,63,64]. Many studies have been carried out to explore the correlation between SOS and bone volume fraction[7]. The correlation factor varies in the range of $0.69 < R < 0.85$ or $0.48 < R^2 < 0.72$ [65–67]. This indicates that the correlation factor of the results presented in this study (R^2=0.85) is in concordance with and the same order of other related studies. Nevertheless, direct comparison of the results should be avoided due to a few data points in this study in addition to different type (and size) of cancellous bone samples employed in other studies.

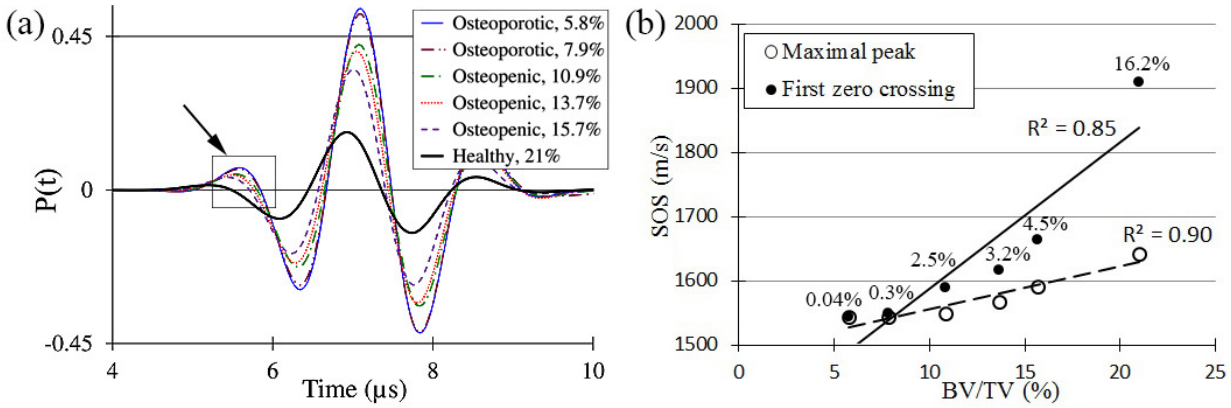

Figure 4.11 (a) Received bone signals and demonstration of the time interval in which the first zero crossing points were detected; (b) Ultrasound velocity in the virtual bone samples (SOS) versus bone volume fraction (BV/TV) and linear regression lines.

It is obvious that the SOS values predicted by the first zero crossing criterion exceeded the values calculated using a marker on the transmitted signal maximal peak. The percentage of difference for each set of values is shown in Figure 4.11b. Interestingly, the difference between the SOS values predicted by the two markers increased with the amount of bone in each trabecular bone model. These observations might indicate the existence of fast and slow waves in the simulations; however in an overlapping appearance in time (mixed mode condition) rather than a distinctly separated form. According to Biot's theory [13,68], fast and slow waves are two

[7] Bone volume fraction (BV/TV), porosity ($1 - BV/TV$) and bone bulk density ($BM/TV, BM = bone\ mass$) are three linearly convertible indices used in the related studies to express the amount of bone material in volumetric samples. These indices can be interchangeably employed.

longitudinal waves with different phase velocities emerging in fluid-saturated porous media as the result of in-phase (for fast wave) and out-of-phase (for slow wave) relative motion of the solid and the fluid phases. These waves have been experimentally shown to be either distinctly separated or overlapped in time when propagating in trabecular bone [8,60,63,64,69–72]. Furthermore, numerical simulations have managed to simulate the propagation of fast and slow waves in 3D virtual bone samples [1,14,21,25,26,28,49]. Nevertheless, the claim in this study should be treated with the following delicate cautions.

Initially, it is significant to state that in an overlapping condition of fast and slow waves, the velocity of each wave cannot easily be obtained by considering the two defined markers on the signals [14]. Therefore, even if the two waves existed in the simulations, the higher SOS values predicted by the first zero crossing criterion should not be designated as fast wave velocity in the present study. The same is true for the other SOS measurement criterion and slow wave velocity. Moreover, fast and slow waves may exist in simulations but appear as a single wave or overlapped waves [1,14,21]. However, additional finite element analyses regarding effective factors on the phenomenon are needed to demonstrate the capabilities of the FEM. Effective factors that may lead to the demonstration of separated fast and slow waves are virtual sample dimensions, bone volume fraction and the relative direction of the transmitted waves with the main orientation of a trabecular network [14,21,28].

Another explanation for the observed differences concentrates on the possible relative change in the shape of the signals. Different markers on a signal obviously predict different TOF values if temporal distances among the values of the signal are not preserved during the propagation or receiving time [73–76]. The following two causes for deformation[8] in the simulated signals are possible:

One source of possible signal shape deformation observed in the received signal is occurrence of phase cancellations due to the spatial averaging of non-plane wave fronts on a plane receiver. This can be relatively small as shown in the case of predicting SOS for the water medium.

The other origin of signal shape deformation that should not be neglected is frequency-dependent attenuation. It is experimentally and theoretically reported that frequency-dependent

[8] Referred to as signal deformation, waveform deformation, signal distortion or signal spreading [73–76]

attenuation may cause signal distortion leading relative change in the location of markers on a signal; particularly the relative location between a zero-crossing marker and the maximal peak marker [73–76]. The difference in SOS values measured using a first zero crossing marker and signal envelope (group velocity) may vary from small percentages to around 25% as the attenuation index nBUA or BUA increases [75,76]. These variations were merely due to the effect of attenuation disregarding any dispersion.

In this study, the relative difference between SOS values predicted by the markers generally increases with nBUA. This observation can be readily viewed by comparing the results in Figure 4.11b and Figure 4.12d. Therefore, the general increase in the difference with respect to nBUA and the order of differences (from 0.04% to 16.2%) are in agreement with other studies [75,76]. However, direct comparisons between the present simulated results and the experiments should be avoided (due the difference in ultrasonic signals, type of bone samples and the saturating fluid, and possible variation between the maximal peak of a signal and the peak of its envelope).

It might be beneficial to mention that simulated signals may experience deformations due to numerical dispersion. However, this effect is assumed to be negligible in the simulations as the finite elements were small enough to sufficiently resolve the waves.

General attenuation of the transmitted signal due to the propagation in each virtual sample becomes apparent when each bone signal (in time or frequency domains) is compared with the reference signal as shown in Figure 4.10. By using the amplitude spectra calculated for the received and bone signals (plotted in Figure 4.10), the frequency-dependent attenuation coefficient, denoted by α_{FEA} in Eq. 4.9, was obtained for each bone sample. Figure 4.12a illustrates α_{FEA} for each of the virtual samples with different status and bone volume fraction value. It can be observed that the attenuation coefficient behaved approximately linear in the frequency range of 0.2–1 MHz and tended to be nonlinear outside of this interval. Although very close linear behaviour was only observable in the frequency range of 0.4–0.8 MHz for all the virtual samples, the chosen bandwidth of interest, i.e. 0.2–1 MHz was considered to preserve the consistency among all the samples. The approximate and almost linear behavior of α_{FEA} respectively in the frequency range of interest (0.2–1 MHz) and 0.4–0.8 MHz is completely in agreement with other experimental and numerical simulation studies [21,29,61,77,78].

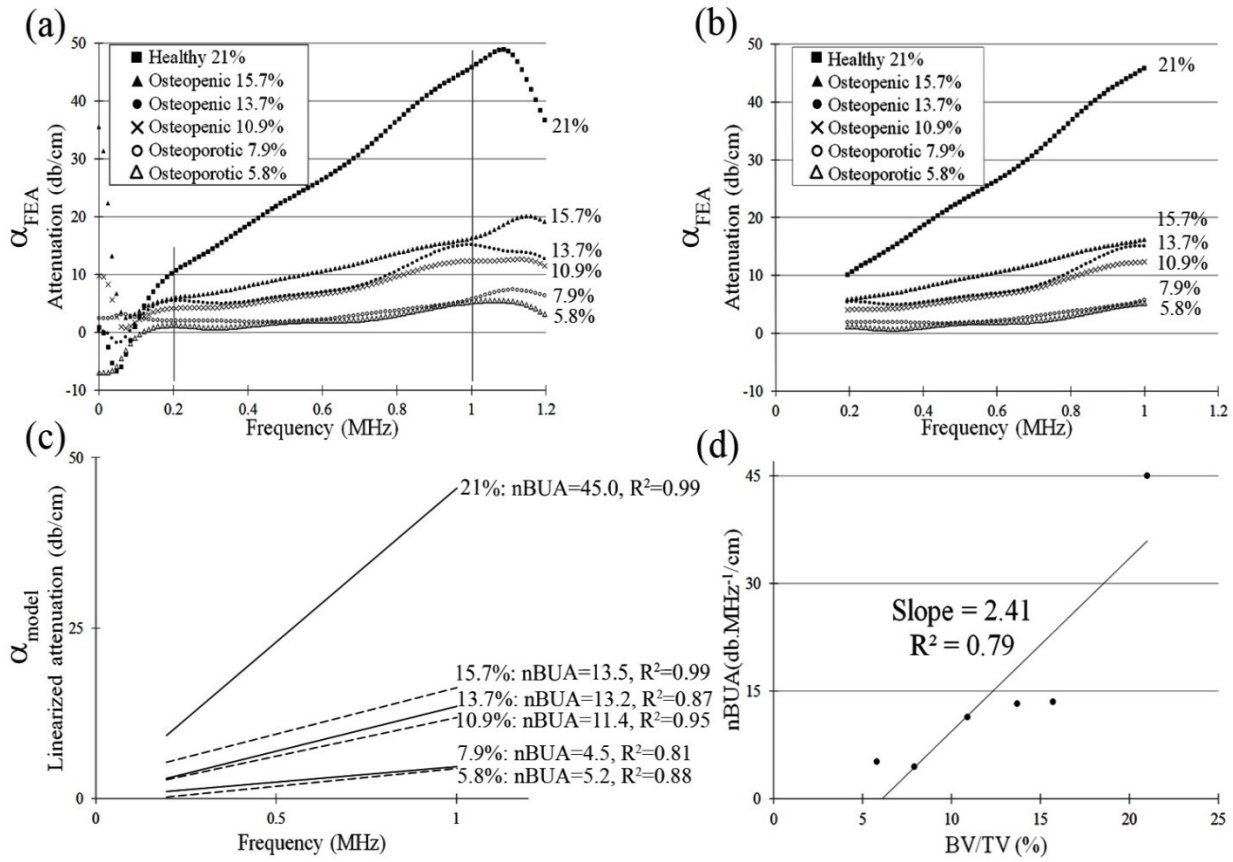

Figure 4.12 (a) Simulated frequency-dependent attenuation (α_{FEA}) graphs for virtual bone samples with different bone volume fraction; (b) Simulated frequency-dependent attenuation graphs restricted to the frequency range of interest; (c) Linearized α_{FEA} by the linear regression model; (d) Simulated nBUA values versus BV/TV of the virtual bone samples along with the associated linear regression line.

It is worth mentioning that the negative attenuation values observed for some samples in the frequency less than 0.1 MHz (Figure 4.12a) does not indicate signal amplification. Based on the definition of the attenuation in this context, the negative attenuation may have the following explanation. Spatial averaging of non-plane pressure waves over a plane surface (receiver) led to phase cancellations (partial or complete). However, different forms of phase cancellation occurred for the reference and bone signals due to the presence of a virtual bone sample and the consequent wave scattering. Therefore, the amplitude spectra of the bone signals may locally possess relatively larger values than that of the reference signal leading to negative attenuation values at some frequencies.

Figure 4.12b and Figure 4.12c respectively plot α_{FEA} and its linear fit, α_{model}, in the frequency range of interest. Positive relationships between the attenuation coefficient and the

bone volume in the virtual samples were observable, i.e. the greater the bone volume fraction was, the larger the attenuation coefficient became. Therefore, as it was expected and also observed in other studies [6,21,25,63], a healthy virtual bone sample was associated with greater ultrasound attenuation when compared with the other non-healthy virtual samples.

The values of nBUA, the slope of the linear model fitted to the simulated values of attenuation (Figure 4.12c), are plotted against the bone volume fraction (BV/TV) of the virtual samples in Figure 4.12d. Although the linear regression of nBUA against BV/TV demonstrated an intermediate correlation ($R^2 = 79\%$), the results (Figure 4.12d) suggested rather a non-linear relation between nBUA and BV/TV. The non-linear relation can be explained by this fact that nBUA must have additional dependency on the microstructure of cancellous bone [77]. Experimental results also reflect that the linear relation between nBUA and BV/TV could occur with a wide range of correlation factor from low ($R = 0.33$) to high values ($R = 0.85$) [9,77,79]. Although, the experimental results are mostly on bovine bone and human calcaneus, if the same bone volume fraction range as in this study is considered, i.e. $5.8\% - 21\%$, the results can be approximately comparable. A linear relation between nBUA and BV/TV for human calcaneus samples can be observed in the experiments performed by R.Hodgskinson *et al* [79]. Another study taking the advantage of both the experimental method and numerical simulations (FDTD for micro-scale modeling) on human calcaneus samples was by E. Bossy *et al* [2]. Their results led to highly correlated linear relationship of nBUA versus BV/TV in the experimental ($R^2 = 0.84$) and the simulation ($R^2 = 0.90$) cases.

In order to demonstrate that the simulation results in this study using the FEM were reasonable and not far from other experimental and simulation results, the linear regression lines of the nBUA versus BV/TV for the current and the results in the latter reference are plotted in Figure 4.13. Identical or very close results must not be expected out of the illustrated comparisons the figure; since the location and type of cancellous bone samples, the signals, and the number of nBUA data (only 6 points in the present study) were not the same in the two studies. In addition, the effect of simulation methods must be considered for the comparison of the simulation results. Nevertheless, it is readily inferable from Figure 4.13 that the FEM simulation results are reasonably in the same order and trend of the other experimental and simulation results.

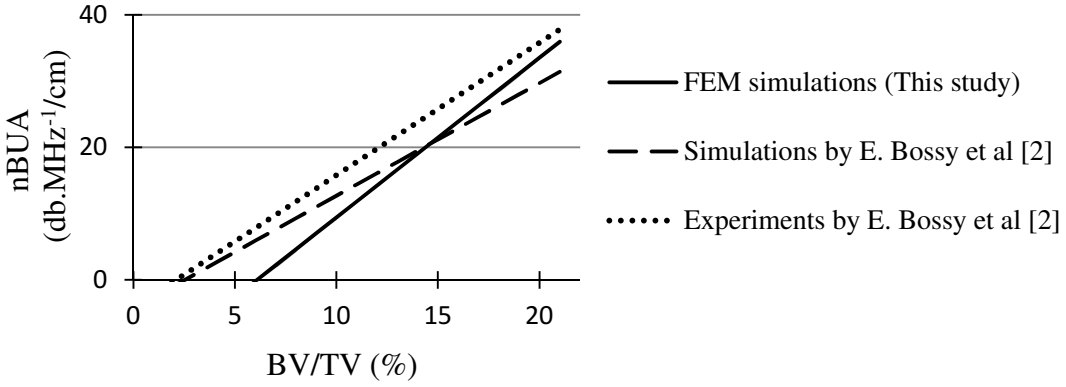

Figure 4.13 Linearized values of nBUA versus BV/TV of the two studies (the present study and the study E. Bossy et al [2] depicted for comparison purposes.

4.4.2 Transmitting the secondary signal

The results for the attenuation coefficient (α_{FEA} in the frequency range of interest) obtained from the transmission of the secondary signal into the models containing the healthy and the selected osteopenic virtual samples are depicted in Figure 4.14. The values of α_{FEA} for the same bone samples but corresponding to the primary signal are also simultaneously plotted for comparison purposes. A maximum relative difference of 18.1% and 17.0% was observed between the simulated values of the coefficient from the two different signals for the healthy and the osteopenic samples respectively.

To explain the emerged difference between the results of the two signals in the frequency range of 0.2–1 MHz, the frequency content of the signals should be considered. According to Eq. 4.2a, the Fourier transform of each signal contains an imaginary part introducing phase lags to the harmonic components of the signals. This imaginary component depends on the time-shifting parameter ($\frac{D}{2}$) having a different value for each of the signals. Therefore, it can be deduced that the signals not only differ in the magnitude of their harmonic components but also possess different phase values for the same-frequency harmonic components. On the other hand, the spatial averaging of a received pressure signal over the receiver surface was associated with phase cancellation. This suggests that each signal might have experienced different form of phase cancellation. Moreover, According to Figure 4.4, the secondary signal contained a wider frequency range up to 1.5 MHz. The frequencies higher than 1.2 MHz were associated with the wavelengths smaller than that being adequately resolved by the size of the finite elements in the

models. This generally causes numerical dissipation leading to gradual numerically-induced variations in the waveform propagating in the medium. Therefore, a part of the difference may be due to the numerical error regarding the spatial discretization.

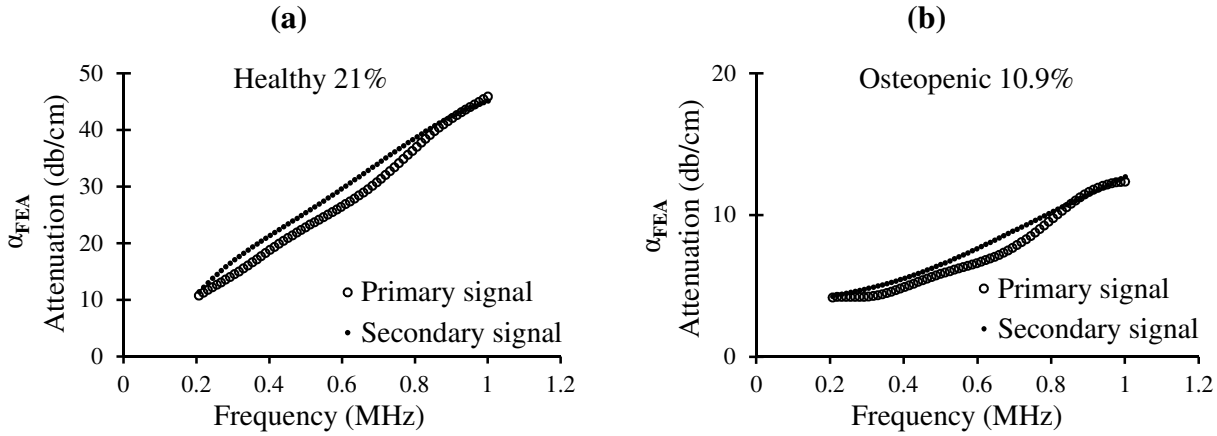

Figure 4.14 Simulated frequency-dependent attenuation (α_{FEA}) graphs for two selected models corresponding to the transmission of the primary and the secondary signals.

The values of nBUA were calculated through performing linear regression on the attenuation data obtained from transmitting the secondary signal into the selected models. Figure 4.15 illustrates the nBUA results corresponding to the two signals. The results indicate 5.6% and 2.7% of difference between the different-signal nBUA results for the healthy and the osteopenic models respectively. The sources of the observed differences may be as explained for α_{FEA}.

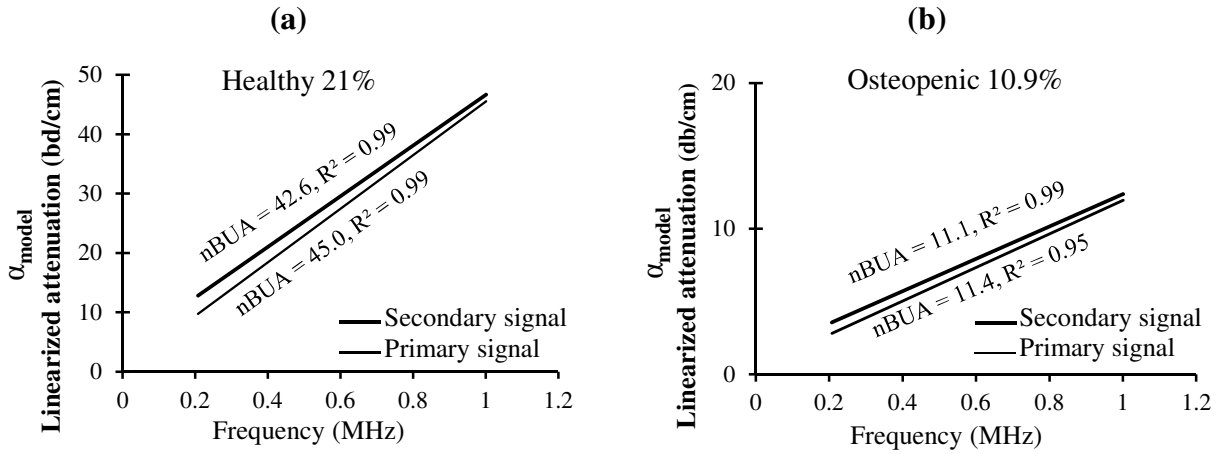

Figure 4.15 Linearized α_{FEA} by the linear regression model and nBUA values for two selected models corresponding to the transmission of the primary and the secondary signals.

4.5 Conclusion

Ultrasound propagation in the heterogeneous and isotropic medium of cancellous bone was simulated using the FEM through a micro-scale modeling approach. For the first time, it was shown that the micro-architecture of cancellous bone saturated by non-viscous water could be virtually reconstructed, meshed and employed by the FEM. Although great efforts were needed for virtually reconstructing the geometry of the trabecular networks and generating the associated finite element mesh, further developments in the needed software packages will mitigate the difficulties in the future.

In this study, the simulation results along with the comparisons with other researchers' results demonstrated that the FEM could be another candidate for simulating ultrasound propagation in fluid-saturated cancellous bone. However, it is apparent that corresponding experimental results are needed to demonstrate the general hypothesis that the time-domain FEM is more accurate than FDTD for the simulations.

4.6 References

[1] F. Padilla, E. Bossy, G. Haiat, F. Jenson, P. Laugier, Numerical simulation of wave propagation in cancellous bone, Ultrasonics. 44 Suppl 1 (2006) e239–43.

[2] E. Bossy, P. Laugier, F. Peyrin, F. Padilla, Attenuation in trabecular bone: A comparison between numerical simulation and experimental results in human femur, J. Acoust. Soc. Am. 122 (2007) 2469–75.

[3] C.C. Glüer, R. Eastell, D.M. Reid, D. Felsenberg, C. Roux, R. Barkmann, et al., Association of five quantitative ultrasound devices and bone densitometry with osteoporotic vertebral fractures in a population-based sample: the OPUS Study, J. Bone Miner. Res. 19 (2004) 782–93.

[4] E.W. Gregg, A.M. Krishka, L.M. Salamone, M.M. Roberts, S.J. Anderson, R.E. Ferrell, et al., Relationships with bone mass , osteoporosis and fracture risk, Osteoporos. Int. 7 (1997) 89–99.

[5] C.C. Glüer, Quantitative Ultrasound Techniques for the Assessment of Osteoporosis : Expert Agreement on Current Status, J. Bone Miner. Res. 12 (1997) 1280–1288.

[6] K.A. Wear, Ultrasonic attenuation in human calcaneus from 0.2 to 1.7 MHz, IEEE Trans. Ultrason. Ferroelectr. Freq. Control. 48 (2001) 602–8.

[7] V. Nguyen, S. Naili, V. Sansalone, Simulation of ultrasonic wave propagation in anisotropic cancellous bone immersed in fluid, Wave Motion. 47 (2010) 117–129.

[8] B. Lashkari, A. Manbachi, A. Mandelis, R.S.C. Cobbold, Slow and fast ultrasonic wave detection improvement in human trabecular bones using Golay code modulation, J. Acoust. Soc. Am. 132 (2012) EL222–8.

[9] C.M. Langton, C.F. Njeh, Acoustic and ultrasonic tissue characterization--assessment of osteoporosis, Proc. Inst. Mech. Eng. Part H J. Eng. Med. 213 (1999) 261–269.

[10] W. Abendschein, G.W. Hyatt, Ultrasonics and selected physical properties of bone, Clin. Orthop. Relat. Res. 69 (1970) 294–301.

[11] M.A. Biot, Theory of propagation of elastic waves in a fluid-saturated porous solid. I. low-frequency range, J. Acoust. Soc. Am. 28 (1956) 168.

[12] M.A. Biot, Theory of propagation of elastic waves in a fluid-saturated porous solid. II. higher frequency range, J. Acoust. Soc. Am. 28 (1956) 179.

[13] T.J. Haire, C.M. Langton, Biot theory: A review of its application to ultrasound propagation through cancellous bone, Bone. 24 (1999) 291–295.

[14] G. Haïat, F. Padilla, F. Peyrin, P. Laugier, Fast wave ultrasonic propagation in trabecular bone: numerical study of the influence of porosity and structural anisotropy, J. Acoust. Soc. Am. 123 (2008) 1694–705.

[15] K. Il Lee, H.-S. Roh, S.W. Yoon, Acoustic wave propagation in bovine cancellous bone: Application of the Modified Biot–Attenborough model, J. Acoust. Soc. Am. 114 (2003) 2284.

[16] M. Kaczmarek, J. Kubik, M. Pakula, Short ultrasonic waves in cancellous bone, Ultrasonics. 40 (2002) 95–100.

[17] W. Lin, Y.-X. Qin, C. Rubin, Ultrasonic wave propagation in trabecular bone predicted by the stratified model, Ann. Biomed. Eng. 29 (2001) 781–790.

[18] E.R. Hughes, T.G. Leighton, G.W. Petley, P.R. White, Ultrasonic propagation in cancellous bone: A new stratified model, Ultrasound Med. Biol. 25 (1999) 811–821.

[19] K.A. Wear, A stratified model to predict dispersion in trabecular bone, IEEE Trans. Ultrason. Ferroelectr. Freq. Control. 48 (2001) 1079–1083.

[20] P.H. Nicholson, R. Strelitzki, R.O. Cleveland, M.L. Bouxsein, Scattering of ultrasound in cancellous bone: predictions from a theoretical model., J. Biomech. 33 (2000) 503–6.

[21] E. Bossy, F. Padilla, F. Peyrin, P. Laugier, Three-dimensional simulation of ultrasound propagation through trabecular bone structures measured by synchrotron microtomography, Phys. Med. Biol. 50 (2005) 5545–56.

[22] Y. Nagatani, K. Mizuno, T. Saeki, M. Matsukawa, T. Sakaguchi, H. Hosoi, Propagation of fast and slow waves in cancellous bone: Comparative study of simulation and experiment, Acoust. Sci. Technol. 30 (2009) 257–264.

[23] G. Luo, J.J. Kaufman, A. Chiabrera, B. Bianco, J.H. Kinney, D. Haupt, et al., Computational methods for ultrasonic bone assessment, Ultrasound Med. Biol. 25 (1999) 823–30.

[24] A.S. Aula, J. Töyräs, M.A. Hakulinen, J.S. Jurvelin, Effect of bone marrow on acoustic properties of trabecular bone-3D finite difference modeling study, Ultrasound Med. Biol. 35 (2009) 308–18.

[25] Y. Nagatani, H. Imaizumi, T. Fukuda, M. Matsukawa, Y. Watanabe, T. Otani, Applicability of finite-difference time-domain method to simulation of wave propagation in cancellous bone, Jpn. J. Appl. Phys. 45 (2006) 7186–7190.

[26] Y. Nagatani, H. Soumiya, T. Saeki, Y. Yaoi, M. Matsukawa, Propagation of ultrasonic longitudinal wave in the cancellous bone covered by the subchondral bone of bovine femur, 2008 IEEE Ultrason. Symp. (2008) 146–149.

[27] A. Hosokawa, Ultrasonic pulse waves in cancellous bone analyzed by finite-difference time-domain methods, Ultrasonics. 44 Suppl 1 (2006) e227–31.

[28] A. Hosokawa, Development of a numerical cancellous bone model for finite-difference time-domain simulations of ultrasound propagation, IEEE Trans. Ultrason. Ferroelectr. Freq. Control. 55 (2008).

[29] S. Chaffaï, F. Padilla, G. Berger, P. Laugier, In vitro measurement of the frequency-dependent attenuation in cancellous bone between 0.2 and 2 MHz, J. Acoust. Soc. Am. 108 (2000) 1281–9.

[30] F. Muir, J. Deltinqert, J. Etqens, D. Nichols, Short note: Modeling elastic fields across irregular boundaries, Geophysics. 57 (1992) 1189–1193.

[31] D.T. Prescott, S.N. V, A mehod for incorporating different sized cells into the finite-difference time-domain analysis technique, IEEE Microw. Guid. Wave Lett. 2 (1992) 434–436.

[32] D. Botteldooren, Acoustical finite-difference time-domain simulation in a quasi-Cartesian grid, Acoust. Soc. Am. 95 (1994) 2313–2319.

[33] D. Appel, N.A. Petersson, A stable finite difference method for the elastic wave equation on complex geometries with free surfaces, Commun. Comput. Phys. 5 (2009) 84–107.

[34] Y. Min, B. Kil, S. Lee, A novel contour-path finite-difference time-domain (CPFDTD) algorithm for modeling objects with curved surfaces, Microw. Opt Technol Lett. 28 (2001) 285–287.

[35] T. Su, Y. Liu, W. Yo, R. Mittra, A conformal mesh-generating technique for the conformal finite-difference time-domain (CFDTD) method, IEEE Antennas Propag. Mag. 46 (2004) 37–49.

[36] S. Dey, R. Mittra, A locally conformal finite-difference time-domain (FDTD) algorithm for modeling three-dimensional perfectly conducting objects, IEEE Microw. Guid. Wave Lett. 7 (1997) 273–275.

[37] W. Yu, S. Member, R. Mittra, L. Fellow, A conformal finite difference time domain technique for modeling curved dielectric surfaces, IEEE Microw. Wirel. Components Lett. 11 (2001) 25–27.

[38] J.B. Schneider, C.L. Wagner, R.J. Kruhlak, Simple conformal methods for finite-difference time-domain modeling of pressure-release surfaces, Acoust. Soc. Am. 104 (1998) 3219–3226.

[39] K.S. Yee, J.S. Chen, A.H. Chang, Conformal finite-difference time-domain (FDTD) with overlapping grids, IEEE Trans. Antennas Propag. 40 (1992) 1068–1075.

[40] J.G. Tolan, J.B. Schneider, Locally conformal method for acoustic finite-difference time-domain modeling of rigid surfaces, J. Acoust. Soc. Am. 114 (2003) 2575.

[41] G. Dahake, S.M. Gracewski, Finite difference predictions of P-SV wave propagation inside submerged solids. I. Liquid-solid interface conditions, Acoust. Soc. Am. 102 (1997) 2125–2137.

[42] R. Van Vossen, J.O.A. Robertsson, C.H. Chapman, Finite difference modeling of wave propagation in a fluid–solid configuration, Geophysics. 67 (2002) 618–624.

[43] S.A. Ralph, A review of finite difference method for seismo-acoustics problems at the seafloor, Rev. Geophys. 26 (1988) 445–458.

[44] R.A. Slawinski, E.S. Krebes, The homogeneous finite-difference formulation of the P-SV-wave equation of motion, Stud. Geophys. Geod. 46 (2002) 731–751.

[45] J. Zahradnik, E. Priolo, Heterogeneous formulation of elastodynamic equations and finite-difference schemes, Geophys. J. Int. 120 (1995) 663–673.

[46] P. Moczo, J.O.A. Robertsson, L. Eisner, The finite difference time domain method for modeling of seismic wave propagatio, Adv. Geophys. 48 (2007) 421–516.

[47] J.S. Sochacki, J.H. George, R.E. Ewing, S.B. Srnlthsont, Interface conditions for acoustic and elastic wave propagation, Geophysics. 56 (1991) 168–181.

[48] E.H. Saenger, N. Gold, S. a. Shapiro, Modeling the propagation of elastic waves using a modified finite-difference grid, Wave Motion. 31 (2000) 77–92.

[49] Y. Nagatani, K. Mizuno, T. Saeki, M. Matsukawa, T. Sakaguchi, H. Hosoi, Numerical and experimental study on the wave attenuation in bone--FDTD simulation of ultrasound propagation in cancellous bone, Ultrasonics. 48 (2008) 607–12.

[50] K.J. Marfurt, Accuracy of finite-difference and finite-element modeling of the scalar and elastic wave equations, Geophysics. 49 (1984) 533–549.

[51] J. Zhang, D.J. Verschuurt, Elastic wave propagation in heterogeneous anisotropic media using the lumped finite-element method, Geophysics. 67 (2002) 625–638.

[52] Abaqus theory manual, Dassault Systèmes, (2012) Section 2.9.

[53] Q.-H. Zhang, G. Tozzi, J. Tong, Micro-mechanical damage of trabecular bone-cement interface under selected loading conditions: a finite element study, Comput. Methods Biomech. Biomed. Engin. 17 (2014) 230–8.

[54] G.L. Niebur, M.J. Feldstein, J.C. Yuen, T.J. Chen, T.M. Keaveny, High-resolution finite element models with tissue strength asymmetry accurately predict failure of trabecular bone, J. 33 (2000) 1575–1583.

[55] T. Adachi, K. Tsubota, Y. Tomita, S.J. Hollister, Trabecular Surface Remodeling Simulation for Cancellous Bone Using Microstructural Voxel Finite Element Models, J. Biomech. Eng. 123 (2001) 403.

[56] R. Hambli, Micro-CT finite element model and experimental validation of trabecular bone damage and fracture, Bone. 56 (2013) 363–74.

[57] L. Goossens, J. Vanderoost, S. Jaecques, S. Boonen, J. D'hooge, W. Lauriks, et al., The correlation between the SOS in trabecular bone and stiffness and density studied by finite-element analysis, IEEE Trans. Ultrason. Ferroelectr. Freq. Control. 55 (2008) 1234–42.

[58] S. Ilic, K. Hackl, R. Gilbert, Application of the multiscale FEM to the modeling of cancellous bone, Biomech. Model. Mechanobiol. 9 (2010) 87–102.

[59] F. Ihlenburg, Finite element analysis of acoustic scattering, Springer-Verlag, New York, 1998.

[60] L. Cardoso, F. Teboul, L. Sedel, C. Oddou, A. Meunier, In vitro acoustic waves propagation in human and bovine cancellous bone, J. Bone Miner. Res. 18 (2003) 1803–12.

[61] C. Zhang, L.H. Le, R. Zheng, D. Ta, E. Lou, Measurements of ultrasonic phase velocities and attenuation of slow waves in cellular aluminum foams as cancellous bone-mimicking phantoms, J. Acoust. Soc. Am. 129 (2011) 3317–26.

[62] P. Rossman, J. Zagzebski, C. Mesina, J. Sorenson, R. Mazess, Comparison of speed of sound and ultrasound attenuation in the os calcis to bone density of the radius , femur and lumbar spine, Clin. Phys. Physiol. Meas. 10 (1989) 353–360.

[63] B.K. Hoffmeister, S.A. Whitten, J.Y. Rho, Low-megahertz ultrasonic properties of bovine cancellous bone, Bone. 26 (2000) 635–642.

[64] T. Otani, Quantitative estimation of bone density and bone quality using acoustic parameters of cancellous bone for fast and slow waves, Jpn. J. Appl. Phys. 44 (2005) 4578–4582.

[65] C.F. Njeh, R. Hodgskinson, J.D. Currey, C.M. Langton, Orthogonal relationships between ultrasonic velocity and material properties of bovine cancellous bone, Med. Eng. Phys. 18 (1996) 373–81.

[66] J.A. Evans, M.B. Tavakoli, Ultrasonic attenuation and velocity in bone, Phys. Med. Biol. 35 (1990) 1387–96.

[67] C.F. Njeh, C.M. Boivin, C.M. Langton, The role of ultrasound in the assessment of osteoporosis: a review, Osteoporos. Int. 7 (1997) 7–22.

[68] T.J. Plona, R.D. Angelo, D.L. Johnson, Velocity and attenuation of fast, shear and slow waves in porous media, in: Ultrason. Symp., 1990: pp. 1233–1239.

[69] K. Mizuno, M. Matsukawa, T. Otani, P. Laugier, F. Padilla, Propagation of two longitudinal waves in human cancellous bone: an in vitro study, J. Acoust. Soc. Am. 125 (2009) 3460–6.

[70] A. Hosokawa, T. Otani, Ultrasonic wave propagation in bovine cancellous bone, J. Acoust. Soc. Am. 101 (1997) 558–62.

[71] K. Mizuno, M. Matsukawa, T. Otani, M. Takada, I. Mano, T. Tsujimoto, Effects of structural anisotropy of cancellous bone on speed of ultrasonic fast waves in the bovine femur, IEEE Trans. Ultrason. Ferroelectr. Freq. Control. 55 (2008) 1480–7.

[72] A. Hosokawa, T. Otani, Acoustic anisotropy in bovine cancellous bone, J. Acoust. Soc. Am. 103 (1998) 2718–22.

[73] M. Ragozzino, Analysis of the error in measurement of ultrasound speed in tissue due to waveform deformation by frequency-dependent attenuation., Ultrasonics. 19 (1981) 135–8.

[74] K.A. Wear, The effects of frequency-dependent attenuation and dispersion on sound speed measurements: applications in human trabecular bone, IEEE Trans. Ultrason. Ferroelectr. Freq. Control. 47 (2000) 265–73.

[75] K.A. Wear, A numerical method to predict the effects of frequency-dependent attenuation and dispersion on speed of sound estimates in cancellous bone, J. Acoust. Soc. Am. 109 (2001) 1213.

[76] G. Haıat, F. Padilla, R.O. Cleveland, P. Laugier, Effects of frequency-dependent attenuation and velocity dispersion on in vitro ultrasound velocity measurements in intact Human Femur Specimens, IEEE Trans. Ultrason. Ferroelectr. Freq. Control. 53 (2006) 39–51.

[77] C.M. Langton, C.F. Njeh, The measurement of broadband ultrasonic attenuation in cancellous bone--a review of the science and technology, IEEE Trans. Ultrason. Ferroelectr. Freq. Control. 55 (2008) 1546–54.

[78] J.A. Maia, E.T. Costa, J.F.M. Neto, V.L.S.N. Button, Broadband ultrasound attenuation in the calcaneal region: a comparative study of single-position versus scanning systems, IEEE Trans. Ultrason. Ferroelectr. Freq. Control. 55 (2008) 64–73.

[79] R. Hodgskinson, C.F. Njeh, M.A. Whitehead, C.M. Langton, The non-linear relationship between BUA and porosity in cancellous bone, Phys. Med. Biol. 41 (1996) 2411–20.

Chapter 5

The Finite Element Method for Micro-scale Modeling of Ultrasound Propagation in Trabecular Structures: A Comparison between the Simulated and Experimental Ultrasonic Attenuation in Aluminum Foams

The contents of this chapter have been submitted for publication: B. Vafaeian, L. H. Le, T. N.H.T. Tran, M. El-Rich, T. El-Bialy, S. Adeeb, Ultrasonics. July 2015.

5.1 Abstract

The application of the standard Galerkin finite element method for simulating broadband ultrasound propagation in water-saturated trabecular bone was already demonstrated in our previous study. However, the accuracy of the results was not verified through experiments. As a complement to our previous work, the accuracy of the finite element method for simulating broadband ultrasound propagation in water-saturated trabecular structure was experimentally investigated in the present study. To this end, micro-scale modeling of broadband ultrasound propagation in water-saturated aluminum foams was performed using the standard Galerkin finite element method. Disregarding the energy absorbing mechanisms (viscous and frictional losses), the simulations represented through-transmission of ultrasonic waves in immersed water-saturated trabecular structures. Corresponding through-transmission experiments were performed to verify the accuracy of the simulated results. The simulated and experimental results were compared with each other through the derived frequency-dependent attenuation coefficients. The maximum and average relative error between the experimental and simulated attenuation coefficients in the frequency range of 0.6–1.4 MHz were 17% and 6% (standard deviation of 4%) respectively. The results strongly suggested that wave scattering and mode conversion were the dominant attenuation mechanisms of ultrasound propagating in aluminum foams. The study further demonstrated the capability of the finite element methods/models to effectively simulate broadband ultrasound propagation in fluid-saturated trabecular structures.

5.2 Introduction

Quantitative ultrasound (QUS) for non-destructive assessment of bone health has been widely employed in research and clinical practice [1–3]. The main objectives of QUS for bone assessment are to diagnose and to monitor osteoporosis [4], which is mainly evident inside cancellous bone [5,6]. The assessment of cancellous bone using QUS is based on potential relationships between the measured ultrasonic parameters (attenuation and velocity) and the physical and mechanical properties of bone [1,2,5–7].

Cancellous bone consists of interconnected micro-architectural network of trabeculae with saturating marrow inside the pores. This structural complexity and heterogeneity of cancellous bone has been a source of difficulty in the exploitation of the interaction mechanisms between ultrasound and cancellous bone. For the past 45 years [8], experimental and theoretical

approaches have been utilized to understand the physics of ultrasound propagation in cancellous bone. However, a comprehensive and unique theoretical framework explaining the physics of the propagation and experimental observations has not yet been established [3,9–13].

So far, theoretical frameworks have been sought through Biot's theory [14–22] , stratified models [23–25], scattering models [26,27], and micro-scale models [3,9,17,28–34]. Among these approaches, only the micro-scale models have the privilege of explicitly accounting for the micro-geometry of the trabecular network inside cancellous bone. Due to this advantage, micro-scale models have manifested more realistic and reliable results than those of the other approaches [3,17,28,29,31,34].

Micro-scale modeling is based on using computational (or virtual) detailed micro-geometries of trabecular structures (including the saturating fluid) and numerically solving the linear elastic (acoustic) wave equations over those computational domains. Two and three dimensional (2D and 3D) computational micro-structure of cancellous bone have been either reconstructed using micro computed tomography (μ-CT) images [3,9,17,28–34] or by developing micro-geometries imitating trabecular networks [35,36]. The numerical method for solving the linear wave equations over the computational domains (fluid-saturated trabecular structures) was mainly based on finite-difference time-domain (FDTD) methods [3,9,17,28–33,35–37]. As an alternative to FDTD, time-domain finite element methods were also employed to simulate ultrasound propagation in trabecular structures [34,38,39]. To the knowledge of the authors, our previous study [34] was the first time-domain finite element simulation that explicitly modeled the 3D micro-geometries of fluid-saturated trabecular structures.

In our previous study [34], the standard Galerkin finite element method (FEM) in time domain was utilized to simulate the propagation of broadband ultrasonic pulses in 3D water-saturated cancellous bone samples. The speed of sound (SOS), frequency-dependent attenuation and broadband ultrasound attenuation (BUA) were simulated by the FEM. Comparing the simulation results with other studies (experimental and simulation) demonstrated that the FEM would be a capable tool for micro-scale modeling of ultrasound propagation in fluid-saturated trabecular structures. Nevertheless, the accuracy of the simulation results was not directly evaluated by corresponding experiments.

The objective of this study was to evaluate the accuracy of the standard Galerkin FEM in

simulating broadband ultrasound propagation in 3D trabecular structures. To this end, the propagation of ultrasound in aluminum foams was investigated by micro-scale finite element simulations and through-transmission experiments. The values of the simulated and experimental ultrasonic attenuation, in the frequency range of 0.6 to 1.4 MHz, were then employed for the evaluation of the simulation results.

5.3 Materials and Methods

5.3.1 Aluminum foams

In this study, ultrasound propagation in water-saturated open-celled aluminum foams were investigated through experiments and simulations. The aluminum foams are made of aluminum alloy 6101 (Table 5.1) for commercial purposes (DUOCEL 6101-aluminum foams, ERG Materials and Aerospace Corporation, Oakland, CA). From a structural perspective, aluminum foams are open-celled structures that are made of networks of interconnected aluminum ligaments (trabeculae) [11]. The structural properties of aluminum foams can be described by two independent parameters: the number of pores (or cells) per inch (PPI) and the nominal aluminum volume fraction (AVF) defined as AV/TV such that AV is the volume of aluminum (solid) material within the total volume, TV, occupied by both the solid and pores. Expressed by a range, the AVF is a statistical population parameter calculated through volumetric measurements on a large number of foam samples. Additionally, actual aluminum volume fraction (AAVF) is defined with the same definition as AVF but for a single sample (piece) of foam with particular dimensions.

Table 5.1 Mechanical properties of the materials in this work.

Aluminum (alloy 6101)[11,40]	
Density, ρ_{al}	2700 kg/m^3
Young's modulus, E	68900 MPa
Poisson's ratio, ν	0.33
Longitudinal wave velocity, c_L	6149 m/s
Transverse wave velocity, c_T	3097 m/s
Saturating water [11,34]	
Density, ρ_w	1000 kg/m^3
Bulk Modulus, β	2200 MPa
Longitudinal wave velocity, c_o	1483 m/s

Other structural parameters that can be dependently defined for the description of aluminum foams are average cell size in millimetres ($CS = 25.4/PPI$), average trabecular

thickness ($\mathrm{TbTh} = \mathrm{CS} \times \mathrm{AVF}$), and average trabecular separation ($\mathrm{TbSp} = (1 - \mathrm{AVF}) \times \mathrm{CS}$) [11].

In the present work, five pre-cut rectangular prisms ($50.8 \times 50.8 \times 12.7\ \mathrm{mm}^3$) of aluminum foams (Figure 5.1a) and their reconstructed μ-CT images were utilized (Figure 5.1b). To obtain μ-CT images of a sample, only part of it denoted as the volume of interest was scanned (Figure 5.1a). The samples had different structural properties as listed in Table 5.2.

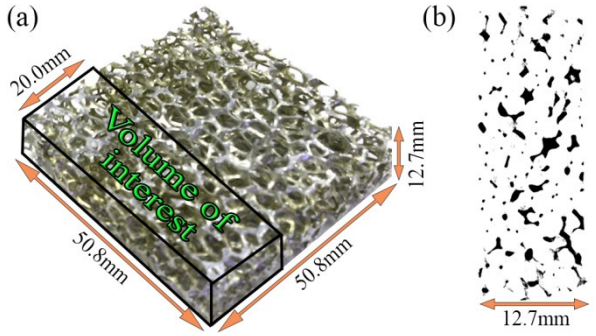

Figure 5.1 (a) A pre-cut aluminum foam sample (PPI:5, AVF:7-8%). (b) Typical reconstructed μ-CT image of an aluminum foam sample (dark and white areas represent aluminum trabeculae and pores respectively).

As indicated by Table 5.2, the first three samples had constant PPI and increasing AVF. For a constant PPI, thinner trabeculae lead to less AVF and larger trabecular separation (this can resemble bone deterioration in osteoporosis). The second three samples, including sample 3, had constant AVF and increasing PPI. For a constant AVF, larger PPI leads to thinner aluminum trabeculae with less separation (Table 5.2).

Table 5.2 Structural properties of the aluminum foam samples.

Sample #	PPI	Nominal AVF (%)	Actual AVF (%)	CS (mm)	TbTh (mm)	TbSp (mm)
1	5	4-5	4.7	5.08	0.23	4.85
2	5	7-8	8.0	5.08	0.38	4.70
3	5	10-12	10.5	5.08	0.56	4.52
4	10	10-12	9.4	2.54	0.24	2.26
5	20	10-12	11.0	1.27	0.14	1.13

5.3.2 Experimental setup

Figure 5.2 illustrates the ultrasonic immersion through-transmission experimental setup. The setup contained a pair of 1.0 MHz (Fractional bandwidth of 47% at -3dB amplitude spectrum) unfocused broadband transducers (Panametrics V303-SU, Waltham, MA) coaxially mounted on two holders. The diameter of the transducers was 12.7 mm and their faces were kept

14.4 mm distant[1] by the holders. To set one of the transducers as a broadband pulse transmitter and the other one as a receiver, an Olympus pulser-receiver device (Olympus 5800, Panametrics, Waltham, MA) excited the transmitter, and a digital oscilloscope (LeCroy WaveSufer 422, Chestnut Ridge, NY), connected to the receiver transducer, received and stored the transmitted signals. The digital oscilloscope sampled the received signals in voltage and at 2 Giga-samples per second at 8-bit resolution.

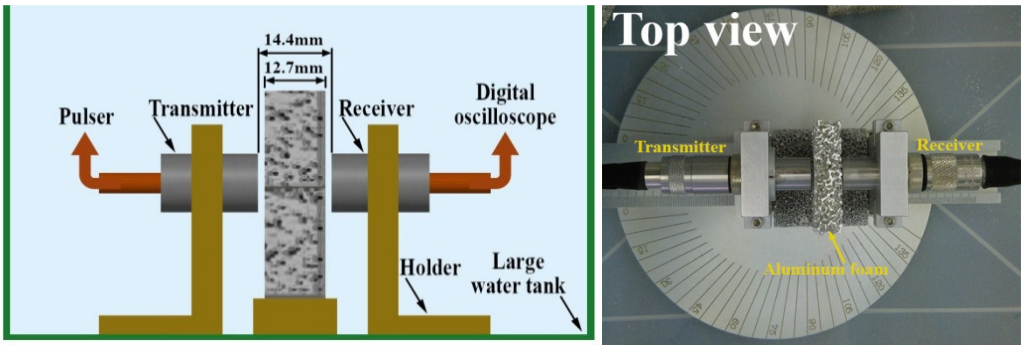

Figure 5.2 Ultrasonic through-transmission experimental setup. The whole setup was immersed in water.

The transducers and holders were first immersed in distilled water inside a large water tank without the foam sample and an ultrasonic broadband pulse was transmitted through water. The received signal in this case was denoted by the reference signal. Then, each aluminum sample, already immersed and shaken underwater to remove air bubbles inside the pores, was located exactly in the middle distance of the transducers. Each sample was placed such that the axis of the transducers was aligned with the thickness dimension (12.7 mm) to set the ultrasonic beam perpendicular to the lager dimensions of the sample, i.e. $50.8 \times 50.8\ \mathrm{mm}^2$ (Figure 5.2). Moreover, the placement of each sample was laterally symmetric with respect to the vertical plane containing the axis of the transducers. The signal received in the presence of a sample was referred to as sample signal.

5.3.3 Finite element simulations

The propagation of ultrasound in fluid-saturated aluminum foam was mathematically formulated based on the linear elastic (acoustic) wave equations and perfect-slip interfacial conditions coupling the fluid and solid media [34]. To solve the equations, the standard Galerkin finite element method in time-domain was implemented. The finite element formulation

[1] The distance between the transducers was chosen to be the smallest practical distance in order to reduce the computational resources need for the simulations.

explicitly considered the interfacial perfect-slip conditions; therefore, the finite element models were expected to simulate phenomena such as elastic scattering, refraction and mode conversion (conversion of longitudinal to transverse waves or vice versa) of the waves [41,42]. However, due to disregarding energy dissipation mechanisms of the material and interfacial properties (Table 5.2), the simulations did not considered energy absorption caused by viscous properties of the materials and the solid-fluid internal friction.

The simulation of ultrasound propagating in aluminum foams, which followed the procedure explained in details in our previous study [34], is described briefly in the following section.

5.3.3.1 Computational aluminum foams

To generate computational aluminum foam samples for the simulations, part of each physical sample ($50.8 \times 20.0 \times 12.7\ \mathrm{mm}^3$) was scanned by a μ-CT device (SkyScan1176, Bruker-microCT, Belgium) at the University of Alberta (Micro-CT facilities were provided by Osteometabolix Pharmaceuticals Inc. Edmonton, Canada). The original pixel size of the reconstructed μ-CT images was increased from 36 μm to 72 μm to facilitate the segmentation procedure. The segmentation and generating the computational geometries of the samples in the form of binary Stereo Lithography (STL) were performed using Mimics software (Materialise Mimics 2014.17.0). To remove the geometrical artifacts originated from the μ-CT images or generated during the segmentation process and to generate uniform STL meshes, the STL data were manipulated using Geomagic software (Geomagic Studio 2014.1.0). Figure 5.3 shows an example of removing geometrical artifacts from parts of the reconstructed geometry (STL) of aluminum foam. The relative volumetric changes due to the manipulations of the STL meshes were less than 1%.

Figure 5.4 depicts the trabecular structures of the physical and the computational samples. The images of the computational samples closely resembled the digital-camera images of the physical samples. It should be noted that the nominal AVF of a physical sample was provided as a range while the actual AVF may have varied depending on the location and size of the sample. However, a particular AVF value for a computational sample was obtainable. The AVF of the computation aluminum samples were calculated and denoted by CAVF (Figure 5.4).

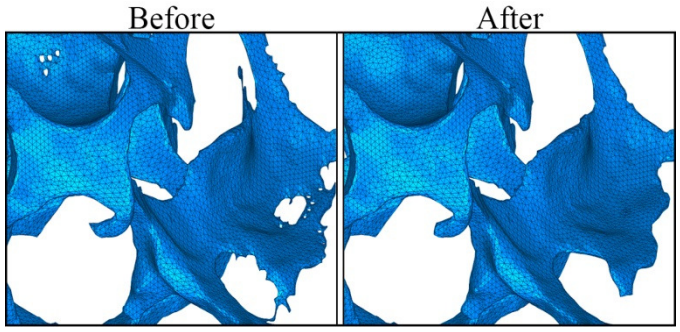

Figure 5.3 Geometrical artifacts removed from parts of the reconstructed geometry of an aluminum foam sample.

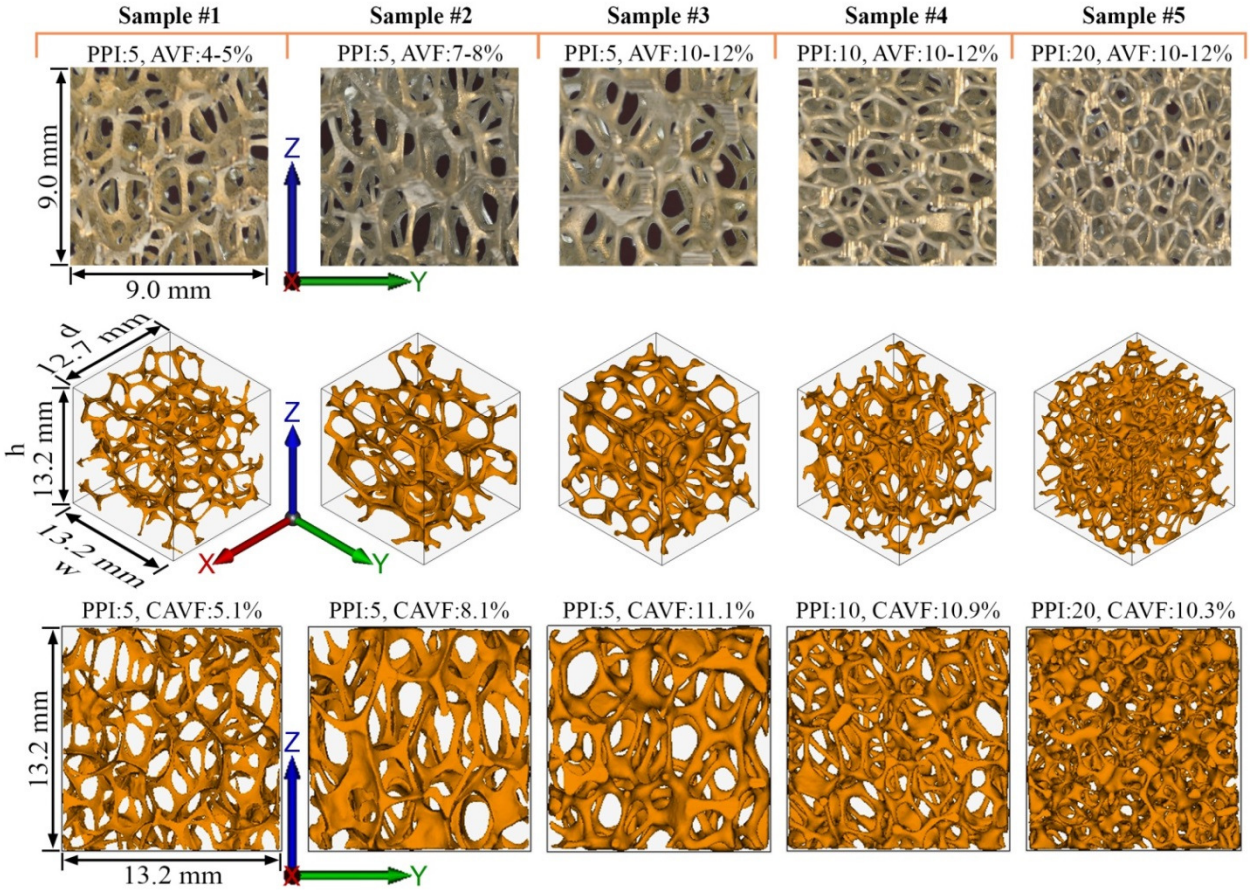

Figure 5.4 Trabecular structures of physical (first row) and computational (second and third rows) samples. The images of the physical samples were obtained using a digital optic camera.

5.3.3.2 Finite element models

During the experiments, it was observed that due to the larger dimensions of the water tank, the reflected waves from the water tank walls and the surface of the water were negligible and received after the main pulse. Therefore, the simulation of the immersion through-

transmission experiments was considered as an exterior problem (where a structure is surrounded by an infinitely large fluid medium [34,41]). In this regards, the finite element model of the physical medium of the experiments was restricted by a hemispherical artificial boundary embracing the transducers (Figure 5.5a). The effect of the exterior water surrounding the hemispherical region was modeled through applying non-reflecting mechanisms (non-reflecting boundary conditions by acoustic impedance and non-reflecting surface by acoustic infinite elements) [34] on the artificial boundary (Figure 5.5a).

Inside the hemispherical volume of the finite element models, a virtual cube containing a volume of $14.4 \times 14.4 \times 14.4\ \mathrm{mm}^3$ between the faces of the transducers was considered (Figure 5.5a). Consequently, this allowed minimizing the required computational hardware resources by recruiting different sizes of the finite elements inside and outside (surrounding water as in Figure 5.5a of the virtual cube [34].

Figure 5.5b and c illustrate the schemes of the finite element models corresponding to the experimental setup without (measurement setup for reference signal) and with a sample. Due to the dimensions of the virtual cube, only a portion of each aluminum sample was present in the model. The portion of the samples chosen for the finite element models had the same thickness but smaller width and height ($13.2 \times 13.2 \times 12.7\ \mathrm{mm}^3$) compared with the original samples used in the experiments. The width and height (13.2×13.2) of the portion were 4% larger than the transducer diameter to bound the simulated ultrasonic beam within the computational trabecular structures. Although portions of the samples having smaller height and width than those of the physical samples were used in the finite element models, the simulations were expected to closely resemble the experiments because the following conditions were satisfied: (1) the thickness of the physical samples was preserved in the models, (2) the diameter and shape of the transducers in the models and experiments were identical, (3) the simulated ultrasonic beam was bounded within the height and width of the computational samples.

It should be mentioned that the transmitter and receiver shown in the schemes (Figure 5.5) were modeled as their computational forms, i.e. collections of finite element nodes with acoustic degree of freedom and located on the regions corresponding to the faces of the physical transducers [34].

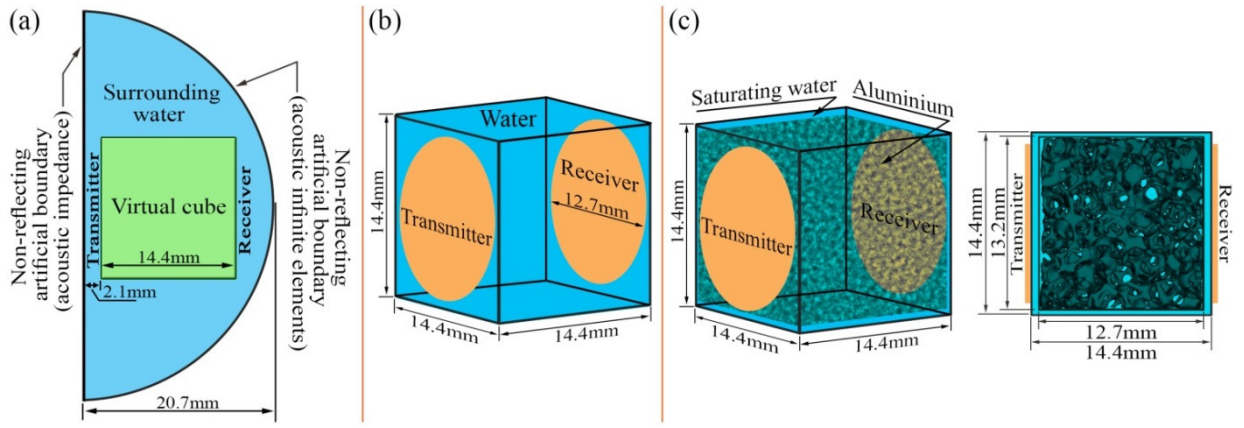

Figure 5.5 (a) Hemispherical artificial boundary, virtual cube and surrounding water. (b), (c) The schemes of the finite element models corresponding to the experimental setup without and with a sample.

The finite element model of the experimental setup without a sample is demonstrated in Figure 5.6. The model, generated with HyperMesh (Altair HyperMesh 2011.11.0, Altair engineering, Troy, MI, USA), contained 28,291,488 linear acoustic tetrahedral elements (4,833,355 acoustic nodes with acoustic-pressure degrees of freedom). The finite element mesh was chosen to resolve the smallest ultrasonic wavelength in the non-viscous water medium. The smallest resolvable wavelength was determined based on the upper limit of the frequency range considered in this study, i.e. 0.6 to 1.4 MHz. Therefore, to simulate accurate ultrasonic pressure inside the virtual cube, the maximum nodal distances of the finite elements inside the cube was equal to $0.1\lambda_{\mathrm{w}}$; such that $\lambda_{\mathrm{w}} = 1.06$ mm was the smallest resolvable wavelength associated with the frequency of 1.4 MHz. The outside of the virtual cube (surrounding water medium) was meshed with larger acoustic elements (up to $1.0\lambda_{\mathrm{w}}$).

To simulate the aluminum signals, the computational samples (Figure 5.4) were utilized and five finite element models were created. Surrounded by acoustic elements (as non-viscous saturating water), each computational sample was meshed by linear solid tetrahedral elements with displacement degrees of freedom. The maximum nodal distances of the solid elements were restricted to $0.1\lambda_{\mathrm{al}}$; in which $\lambda_{\mathrm{al}} = 2.21$ mm was the smallest transverse wavelength associated with the frequency of 1.4 MHz. The maximum number of elements and nodes generated in a finite element model embracing a computational sample was 28,389,785 and 5,121,202 respectively. Figure 5.7 illustrates one of the finite element models including a computational aluminum foam sample.

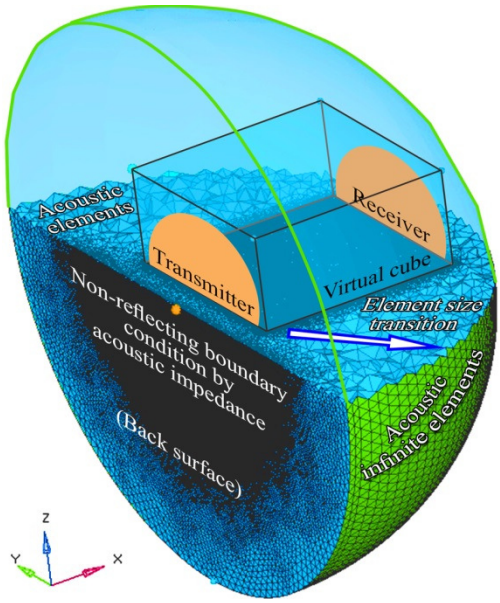

Figure 5.6 The finite element model simulating the reference signal (experimental setup without a sample)

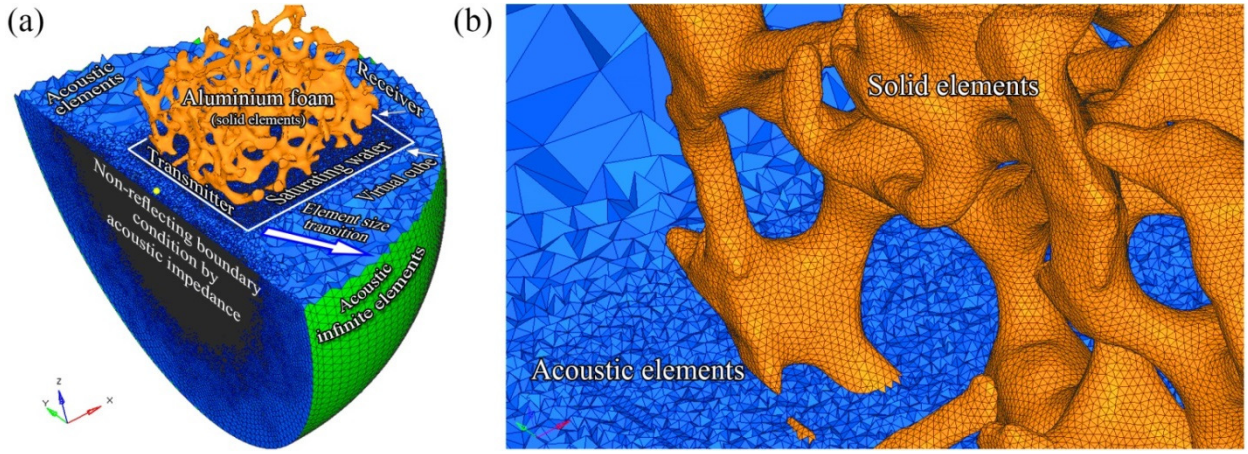

Figure 5.7 (a) The finite element model of a computational aluminum foam sample surrounded by the water (acoustic) medium. (b) A closer view of the mesh generated for each medium.

5.3.3.3 Transmitted ultrasonic pressure

Contrary to a physical transmitter transducer, which converts voltage to ultrasonic pressure, a computational transmitter regionally defines the input values of ultrasonic pressure in the finite element models. To determine a broadband ultrasonic pressure signal for the computational transmitter, the ultrasonic signal generated from the physical transmitter in water was measured by the receiver. To omit high fluctuations from the measurement, the receiver was coaxially located in the far field zone of the transmitter (50 mm away from the transmitter).

Although the signal was measured in the form of voltage, the values were assumed to be directly and uniformly related to ultrasonic pressure. The signal was then normalized by its maximum magnitude and truncated by a rectangular window at -20dB magnitude threshold (Figure 5.8).

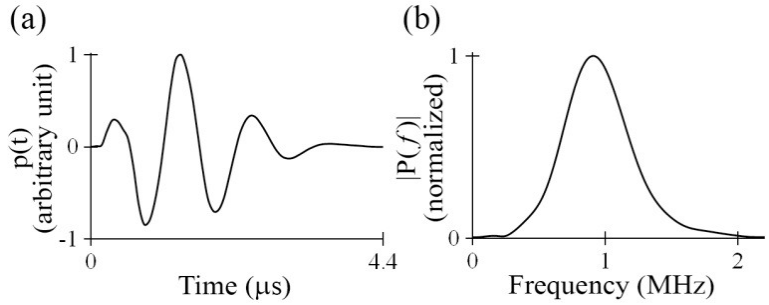

Figure 5.8 Transmitted signal in the simulations: (a) temporal form, (b) amplitude spectrum.

In this study, the experimental and simulated received signals were not intended to be directly compared with each other; but rather the experimental and simulated frequency-dependent attenuation coefficients were compared with each other. Therefore, it was not necessary to obtain the exact values and distribution of the ultrasonic pressure on the surface of the physical transmitter.

5.3.3.4 Time-domain finite element analysis

The propagation of the ultrasonic pressure-pulse in the finite element models was simulated using time-domain finite element analysis (FEA). The analyses were performed using Abaqus/Explicit in the form of parallel execution (48 processors of 2.4 GHz with analysis-required memory of 28 GB) on one of the clusters (a Linux AMD Istanbul cluster at WestGrid) at Compute-Canada (national platform of supercomputing resources). The direct output of each FEA was the simulated ultrasonic pressure signals recorded and spatially averaged over the finite element nodes of the computational receiver. To record the received signals, a temporal sampling frequency of 12.5 MHz was chosen.

5.3.4 Signal processing and simulation-experiment comparisons

Due to unknown voltage-pressure (or vice versa) relation for the physical transducers, direct comparison between the experimental and simulated received signals was not appropriate in this study. Therefore, evaluating the accuracy of the simulations using the experimental results were through calculating and comparing the simulated and experimental frequency-dependent

attenuation coefficients and normalized broadband ultrasonic attenuation (nBUA). The frequency-dependent attenuation coefficients, $\alpha(f)$, in the frequency range[2] of 0.6 to 1.4 MHz were calculated as:

$$\alpha(f) = \frac{20}{\mathrm{d}} \log_{10}\left(\frac{|A_{\mathrm{ref}}|}{|A_{\mathrm{s}}|}\right) \qquad (5.1)$$

in which f denotes the frequency, α in $\mathrm{dB/cm}$ represents amplitude attenuation coefficient, d is the thickness of the samples (1.27 cm), $|A_{\mathrm{ref}}|$ and $|A_{\mathrm{s}}|$ are the values of the amplitude spectra of the reference and sample signals respectively. The amplitude spectra were obtained using the fast Fourier transform (FFT).

To calculate nBUA, a linear regression line was fitted to the attenuation coefficients over the frequency range of interest (0.6–1.4 MHz). In this regard, the following equation expresses nBUA:

$$\alpha_{\mathrm{lin}}(f) = \mathrm{nBUA} \times f + \mathrm{c} \qquad (5.2)$$

such that nBUA has the unit of $\mathrm{dB/cm/MHz}$ and c is the constant of the linear regression.

The above attenuation parameters are dependently calculated based on the amplitude spectra of received ultrasonic signals. On the other hand, in a through-transmission experiment or simulation, a received signal (particularly after traveling in a trabecular structure) consists of a main pulse and preceding and following secondary oscillations. Therefore, it was expected that the secondary oscillations would affect the attenuation parameters. To investigate the effect of the secondary oscillations on the attenuation parameters and their simulation-experiment discrepancies, the received signals were independently truncated to include and exclude the secondary oscillations. Subsequently, two sets of attenuation parameters were calculated.

To truncate the received signals, a rectangular and a Tukey window [43] were independently applied on the temporal forms of the experimental and simulated signals. The rectangular window truncated the signals at $-20\mathrm{dB}$ magnitude (with respect to the peak magnitude) to sufficiently preserve the secondary oscillations. Since the rectangular window led to relatively long-duration signals, the signals were referred to as non-windowed signals. Additionally, a Tukey (Figure 5.9) window was independently applied on the received signals to

[2] Due to weak signal to noise ratio, the amplitude spectra of the received signals were found to be not reliable out of this frequency range.

eliminate the secondary oscillations and preserve the main pulse in the received signals. To this end, the temporal duration of the Tukey window was made identical to the duration of the main pulse[3] (4.4 μs) and the temporal center of the window was pre-shifted to the peak of each received signal. The signals on which the Tukey window was applied were referred to as windowed signals.

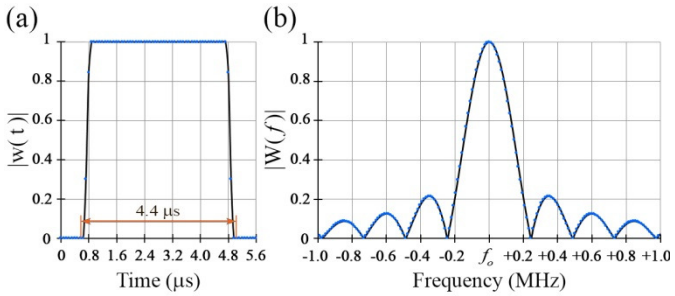

Figure 5.9 (a) Temporal form and (b) amplitude spectrum of the Tukey window.

5.4 Results

Figure 5.10 shows the reference and the sample ultrasonic signals measured by the experiments and simulated by the finite element models. The experimental and the simulated signals were measured and recorded in voltage, $v(t)$, and ultrasonic pressure $p(t)$ respectively. For demonstration purposes, each signal was normalized by the peak value of the related experimental or simulated reference signal. The normalized amplitude spectrum of each signal (normalized by the peak value of the corresponding reference spectrum) is also plotted in the same figure (Figure 5.10).

The experimental and simulated attenuation coefficients in the frequency range of interest, i.e. 0.6–1.4 MHz, are demonstrated in Figure 5.11. The PPI, AVF, AAVF within the parentheses and CAVF corresponding to each sample are also shown in the figure. To quantitatively compare the results, the relative error between the experimental (α_{exp}) and simulated (α_{sim}) attenuation values, $\mathrm{REr} = (\alpha_{exp} - \alpha_{sim})/\alpha_{exp}$, was calculated at each frequency. The maximum relative error (MREr), average relative error (AREr), and standard deviation of relative error values (SDREr), obtained in percentage for each data set are shown in the figure. Moreover, the same error parameters and the average of maximum relative error

[3] The duration of the received signals was estimated based on -20dB magnitude threshold of the reference signals having insignificant secondary oscillations.

values (AMREr), were calculated for all the values (depicted in the box in Figure 5.11). The same trends and the average relative error of 7% with 6% of standard deviation (SD) indicate a strong agreement between the experimental and simulated results.

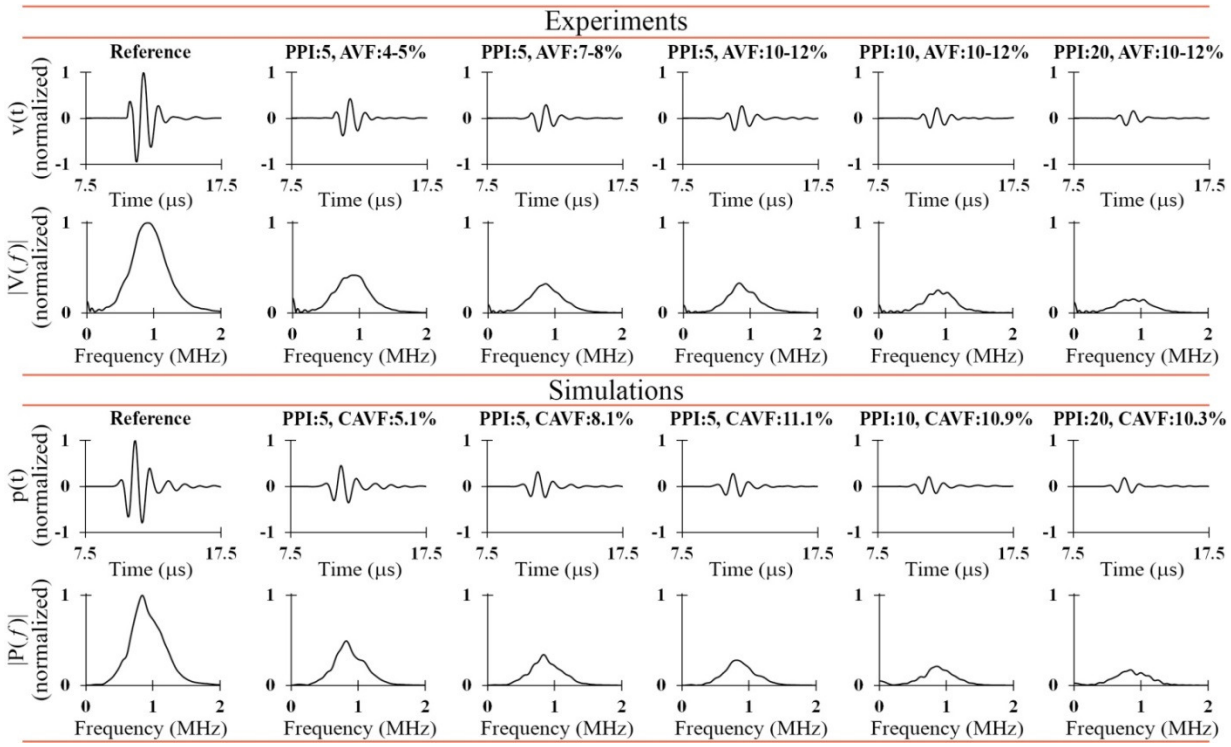

Figure 5.10 The experimental and simulated signals (non-windowed): normalized reference and sample signals (normalized by the peak value of the corresponding reference signal) and their normalized amplitude spectra (normalized by the peak value of the corresponding reference spectrum).

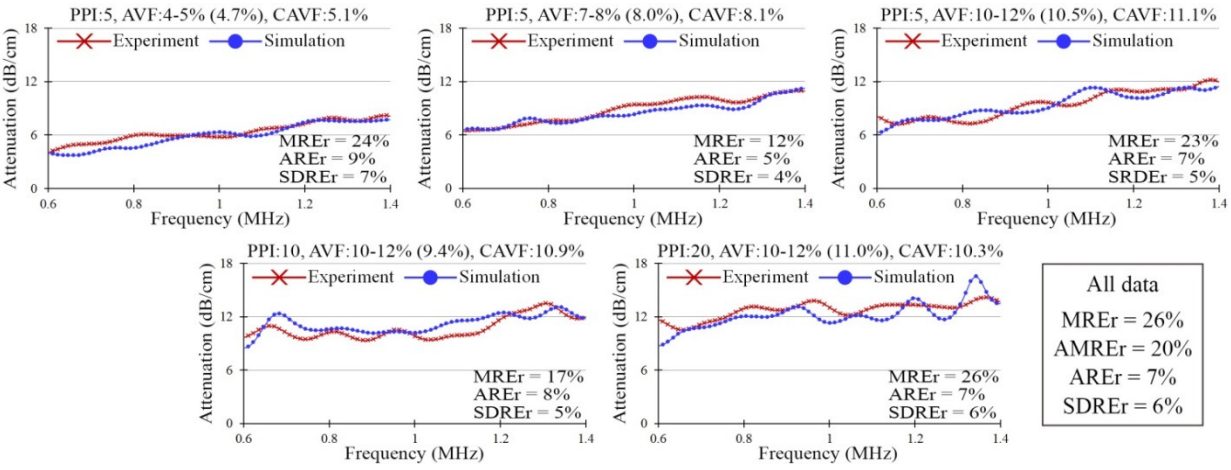

Figure 5.11 Experimental and simulated attenuation coefficients (MREr: maximum relative error, AREr: average relative error, SDREr: standard deviation of relative error, AMREr: average of maximum relative error values).

Figure 5.12a and b show an instance of the direct and consequent effects of the Tukey window on a received experimental signal and its amplitude spectrum respectively. The figures demonstrate that eliminating the secondary oscillations from the received signals also removed the fluctuation in the corresponding amplitude spectrum. The same windowing effects were observed for the signals and their spectra of the other samples.

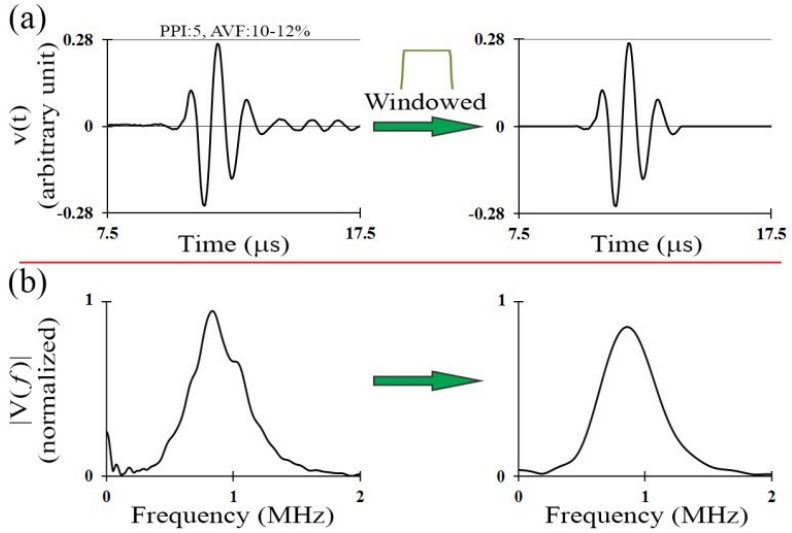

Figure 5.12 (a) Application of the Tukey window on the received signal from sample #3 and (b) the consequent effect on the amplitude spectrum of the signal.

The attenuation coefficients corresponding to the windowed signals are plotted in Figure 5.13. Apparently, eliminating the secondary oscillations from the signals and preserving the main pulse removed the fluctuations in the attenuation plots. Removing the fluctuations led to clear appearance of quasi-linear trends of the frequency-dependent attenuation and reduction of the relative error parameters (Figure 5.13). The simulated attenuation values are in excellent agreement with the experimental values such that the average error and the standard deviation of the error values are 6% and 4% respectively.

To investigate the variation of attenuation relative error with respect to frequency, the values of the relative error for all the samples were averaged at each frequency and plotted (Figure 5.14). Although it seems unclear for the non-windowed signals due to fluctuations in the relative error plot (Figure 5.14a), the decreasing trend of the relative error with frequency is more obvious for the windowed signals (Figure 5.14b).

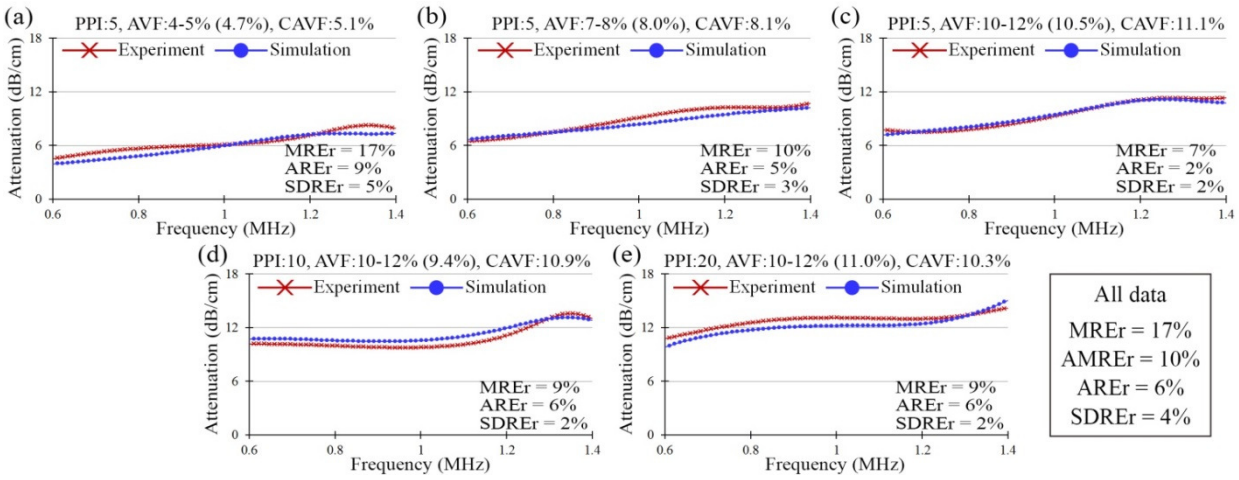

Figure 5.13 Experimental and simulated attenuation coefficients corrsponding to the windowed signals (MREr: maximum relative error, AREr: average relative error, SDREr: standard deviation of relative error, AMREr: average of maximum relative error values).

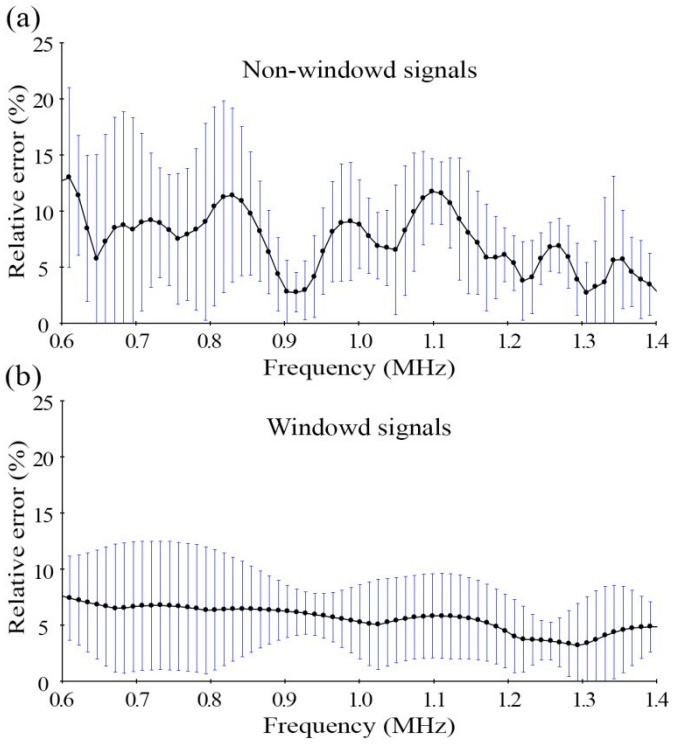

Figure 5.14 Average relative error between the experimental and simulated attenuation coefficients for all the samples regarding the (a) non-windowed signals and (b) windowed signals. The standard deviation at each frequency is shown by an error bar.

Figure 5.15 demonstrates the experimental and simulated values of nBUA as functions of AVF and PPI. The coefficient of determination of the linear fit on each set of attenuation data (R^2) and the relative error (RER) between the experimental and simulated nBUA are included

beside the values in the figure. Comparing the nBUA corresponding to the non-windowed and windowed signals indicated that removing the secondary oscillations generally improved the correlation coefficients (up to 24%) and particularly decreased the relative error for some nBUA values (both underestimation and overestimation of nBUA are observable in the results).

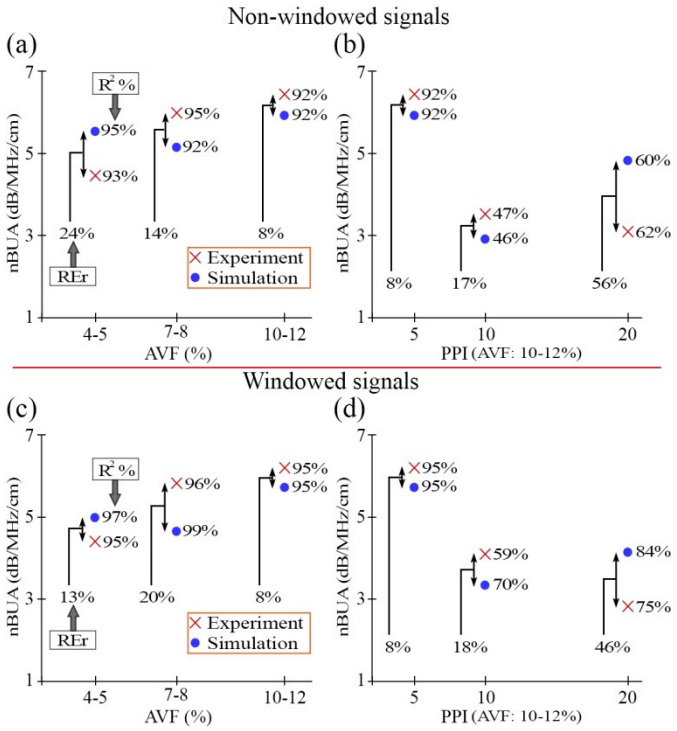

Figure 5.15 Experimental and simulated values of nBUA. R^2: the coefficient of determination of the linear fit on each set of attenuation data, REr: the relative error between the experimental and simulated nBUA.

5.5 Discussion

Computer simulations have been frequently utilized for parametric studies and exploring a variety of wave propagation phenomena in cancellous bone or any trabecular structure. Computer simulations of fluid-saturated trabecular structures in micro-scale have been performed using the FDTD [3,28,32] and the standard Galerkin FEM [34]. Although both methods are inherently powerful for simulating wave propagation, their accuracy and pitfalls should be evaluated and investigated through comparing simulated results with experimental measurements. The accuracy and capabilities of the FDTD method for simulating ultrasound propagation in fluid-saturated cancellous bone have been demonstrated in several publications [3,28,32]; however, to our knowledge, experimental verification of the FEM results in this field

has not yet been reported. In this regard, the present work was performed to evaluate the accuracy of the FEM through experiments.

In this study, the frequency-dependent attenuation of broadband ultrasound propagating in aluminum foams was obtained through experiments and finite element simulations. Prior to comparing the simulated and experimental results with each other, it is appropriate to ascertain the validity of the experimental results. To this end, the experimental results were compared with the results of the study performed by Zhang *et al.* [11]. In that study, they comprehensively investigated the ultrasonic attenuation and structural properties of aluminum foams including the samples in this work. Although different experimental setups were used, the comparison between the results of the two studies indicates strong agreement between the obtained experimental attenuation coefficients (Figure 5.16).

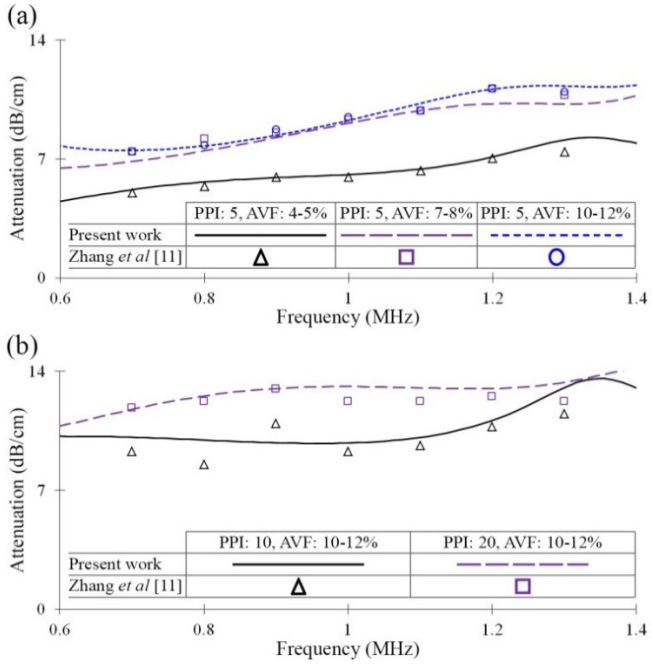

Figure 5.16 Comparison between the experimental attenuation coefficients obtained by Zhang *et al* and the present work (Only a few number of attenuation coefficients were retrieved from the study by Zhang *et al.*).

To evaluate the accuracy of the finite element simulations, the simulated and experimental frequency dependent attenuation coefficients were compared in this work (Figure 5.11 and Figure 5.13). Figure 5.11 shows that both the experimental and simulated attenuation coefficients closely match each other although they experience some fluctuations.

The fluctuations, demonstrated to be induced by the secondary oscillations accompanying the main pulse in the received signals, were effectively removed by the application of the Tukey window on the signals. Exploring the attenuation coefficients after removing their fluctuations (Figure 5.13) reveals better agreement between the simulated and experimental results. Comparing the relative error parameters corresponding to the attenuation coefficients before and after removing the fluctuations (MREr: 26% to 17%, AMREr: 20% to 10%, AREr: 7% to 6%, SDREr: 6% to 4%) shows that the maximum relative error parameters have reduced by 10% while the average relative error has slightly decreased.

Nevertheless, the small average relative error observed in the simulated results (corresponding either to the non-windowed or windowed signals) suggests that the finite element models have effectively simulated the linear wave propagation and the assumed solid-fluid interfacial conditions (perfect-slip conditions). In this regard, wave propagation phenomena such as reflection, scattering and mode conversion are highly expected to be truly simulated.

The ultrasonic attenuation in the aluminum foams are expected to primarily be due to scattering, wave mode conversion and energy absorption mechanisms (material viscosity and frictional loss at solid-fluid interface). Although the simulations neglected the absorption mechanisms in this work, they provided a possibility to explore the relative role of the non-dissipative attenuation mechanisms (scattering and mode conversion) with respect to the total ultrasonic attenuation in the aluminum foams. In this perspective, considering the discrepancies between the simulated and experimental attenuation coefficients suggests that scattering and wave mode conversion are the main sources of attenuation in aluminum foams. If the error is assumed to be entirely due to the absence of the absorption mechanisms in the simulations, it can be deduced that the contribution of scattering in the total attenuation must be approximately 87% (based on $100\% - (\mathrm{AREr} + \mathrm{SDREr})\%$ for attenuation coefficients of non-windowed signals). This is in agreement with other studies suggesting that scattering due to the trabecular network of cancellous bone is the main source of ultrasonic attenuation [3,28,29,32,44].

Investigating the variations of the average relative error of the simulated attenuation coefficients with respect to the frequency values (Figure 5.14) indicated that the relative error values generally decreased as the frequency increased (more obvious in Figure 5.14b). This trend, as also reported by Bossy *et al*. [3], implies that the contribution of scattering in relation

with absorption mechanisms increases with frequency.

In addition to the frequency-dependent attenuation coefficients, nBUA values were obtained to evaluate the accuracy of the finite element simulations for predicting this attenuation parameter. The discrepancies between the experimental and simulated values of nBUA (Figure 5.15) show larger magnitudes of the relative error than what observed between the experimental and simulated attenuation coefficients. The main reason for this observation is that the slope of a linear fit to the attenuation coefficients, i.e. nBUA, may be subjected to large variation over a frequency range for relatively small change in attenuation coefficients. Therefore, any assessment of the simulation accuracy based on nBUA values should be treated with care.

One of the goals of this study was to introduce the FEM as an alternative to the FDTD method that has been prevalent so far for micro-scale simulation of ultrasound propagating in trabecular structure. Therefore, it is of interest to compare the simulation-experiment discrepancies in this work with the discrepancies observed in other studies based on the FDTD method. To this end, the study by Bossy *et al*. [3] on experimental and simulated ultrasonic attenuation in cancellous bone is considered. Their FDTD simulated results predicted the attenuation coefficients with linearly decreasing average relative error from 50% to 30% in the 0.6–1.2 MHz frequency range. Whereas, the average relative error in this study manifests smaller values such that they decrease from 7% to 4% in the same frequency range (Figure 5.14b). The following three explanations may elucidate the difference between the error magnitudes in this study and the work by Bossy *et al*.

First, the simulations in this work utilized the FEM, whereas FDTD was implemented for the simulations through the other study. As discussed in our previous study [34], the FEM is generally superior to the FDTD schemes [45,46], and piece-wise continuous sampling of the solid-fluid interface by finite elements generates less wave artifacts when compared with staircase sampling by a finite difference Cartesian grid [47]. These factors may contribute to smaller relative error observed in our finite element simulations compared with the FDTD simulations in the work of Bossy *et al* [3].

Second, it has been shown that even in the absence of absorption mechanisms a significant part of the attenuation of ultrasound through cancellous bone is due to the wave mode

conversion[4] [29]. Since the wave mode conversion occurs at solid-fluid interface, accurate modeling of the interface condition reduces the error. Although both the FEM in this study and the FDTD method in their study [3] considered perfect-slip conditions at the solid-fluid interface, they completely used different approaches to satisfy the conditions. The interfacial conditions are explicitly included in the finite element formulation of mechanical wave propagation [34], whereas the implicit form of the conditions, through assigning effective material parameters to the boundary nodes, is recruited by the FDTD method [47,48]. The implicit form of the interfacial conditions does not necessarily satisfy the true physical interfacial interaction [49]. In this regard, the FDTD method is not as accurate as the FEM and may generate larger error. However, it should be noted that the magnitude of the error due to deficiencies in the modeling of the interfacial conditions may also depend on the contribution of the wave mode conversion in the total attenuation. It can be shown that the amount of ultrasonic energy that converts to shear wave energy (by wave mode conversion) at the solid-fluid interface in the case of aluminum foam can be much less than that of cancellous bone. To this end, a simple case of longitudinal plane waves (as ultrasonic pressure) incident at a solid-fluid interface under perfect-slip condition was considered (Figure 5.17a). At the interface, part of the power of the incident pressure waves (L_{F_i}) reflects back to the fluid medium (L_{F_r}) and the rest propagates through the solid medium as longitudinal (L_S) and mode-converted shear (T_S) waves (Figure 5.17a). In the case of harmonic plane waves, expressing the ratio of the time-averaged transmitted shear wave energy to the time-averaged total incident energy by its magnitude leads to [50]:

$$T_W^T = \left(\frac{\rho_S \tan\theta_i}{\rho_F \tan\theta_T}\right)\left|\frac{-2(\rho_F/\rho_S)Z_T \sin(2\theta_T)}{Z_L \cos^2(2\theta_T) + Z_T \sin^2(2\theta_T) + Z_F}\right|^2 \qquad (5.3)$$

in which ρ_S and ρ_F are the material density of the solid and fluid media respectively. The angles of the incident plane waves and transmitted mode-converted shear waves with respect to a plane perpendicular to the interface are denoted by θ_i and θ_T (Figure 5.17a). The impedance parameters Z_F, Z_L and Z_T are defined as:

$$Z_F := \frac{c_F \rho_F}{\cos(\theta_i)} \qquad (5.4a)$$

[4] It was shown that disregarding wave mode conversion could reduce nBUA values up to one third [29].

$$Z_L := \frac{c_L \rho_S}{\cos(\theta_L)} \tag{5.4b}$$

$$Z_T := \frac{c_T \rho_S}{\cos(\theta_T)} \tag{5.4c}$$

such that θ_L is the angle of transmitted longitudinal waves into the solid medium, and c_F, c_L and c_T are the speed of pressure waves in the fluid, and the speed of longitudinal and shear waves in the solid.

Based on acoustic Snell's law, the angles of the transmitted longitudinal and shear waves are:

$$\theta_T = \sin^{-1}\left(\frac{c_T}{c_F}\sin(\theta_i)\right) \tag{5.5a}$$

$$\theta_L = \sin^{-1}\left(\frac{c_L}{c_F}\sin(\theta_i)\right) \tag{5.5b}$$

It should be noted that θ_T and θ_L can become complex leading to a complex value for $\left(\frac{\rho_S \tan\theta_i}{\rho_F \tan\theta_T}\right)$ in Eq. 5.3. In this regard, T_W^T is physically zero and mode conversion does not occur.

The percentage of the total incident power transmitted by shear waves into the solid medium as a function of the incident angle (θ_i) was calculated according to Eq. 5.3 and plotted for three homogeneous and isotropic materials (Figure 5.17b): bone, aluminum and nickel. Regarded as a material with higher Young's modulus and density than aluminum, nickel was chosen for comparison purposes. A comparison between the material properties is shown in Figure 5.17c.

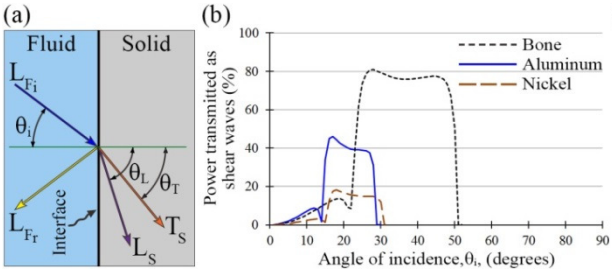

(c)

	Bone	Aluminum	Nickel
Young's modulus (MPa)	18443	68900	200000
Poisson's ratio	0.35	0.33	0.33
Density (kg/cm³)	1850	2700	8890
Wave speed (m/s)			
Longitudinal, c_L	4000	6149	5773
Shear, c_T	1922	3097	2908
Characteristic impedance (MRay)			
Z_L (Longitudinal)	7.4	16.6	51.3
Z_T (Shear)	3.6	8.4	25.8

Figure 5.17 (a) Reflection (L_{F_r}), transmission (L_S, T_S), refraction (θ_L, θ_T) and wave mode conversion at a solid-fluid interface under perfect-slip condition. (b) The percentage of the total incident power transmitted by shear waves into the solid medium as a function of the incident angle for bone, aluminum and nickel materials. (c) Material properties of bone, aluminum and nickel.

As indicated by the plots, bone transmits 40% to 80% of the incident power in the form of shear waves if the incident angle is between 23 and 51 degrees (the rest of the energy is either reflected or transmitted by longitudinal waves). In contrast, aluminum converts around 40% of the incident power into shear waves for the incident angles varying from 15 to 27 degrees. Compared with aluminum, the amount of the transmitted shear wave power is even less for nickel (15%) but in a slightly different range of angles i.e. 17 to 29 degrees. Since part of the attenuation is due to mode conversion and scattering of the mode-converted shear waves inside trabecular structures [29,44], it is expected to observe an increasing trend in attenuation if the material of a trabecular structure is considered to be nickel, aluminum, and bone respectively. Towards showing this expectation, the material properties of bone and nickel were assigned to two of the computational samples and finite element simulations were performed. The simulated attenuation coefficients corresponding to the computational bone, aluminum and nickel trabecular structure are depicted in Figure 5.18. The results show that the bone exhibits the highest ultrasonic attenuation, followed by aluminum then nickel. This is slightly observable in the sample with less solid volume fraction (Figure 5.18a) and clearly apparent for the denser structure (Figure 5.18b). The results suggest the dominant role of mode conversion in the ultrasonic attenuation in bone compared with aluminum or nickel (the same is true for aluminum and nickel). It should be noted that greater impedance mismatch between aluminum and water (characteristic impedance of water is 1.5MRay) compared with bone and water leads to higher amount of wave energy reflected from the aluminum surfaces than that of the bone surfaces; However, the amount of energy that is attenuated through wave mode conversion in bone is more than the amount of energy being attenuated through reflection by aluminum (this also holds for aluminum and nickel foams).

To recapitulate, due to less contribution of wave mode conversion in ultrasonic attenuation in the aluminum foams (also for nickel) compared with cancellous bone, the simulations are less sensitive to modeling-deficiencies of the interfacial conditions. Therefore, it cannot be definitely inferred that the larger relative error observed in the FDTD simulations (i.e. [3]) compared with the FEM simulations has been entirely due to the deficiency of the FDTD method in modeling the interfacial conditions.

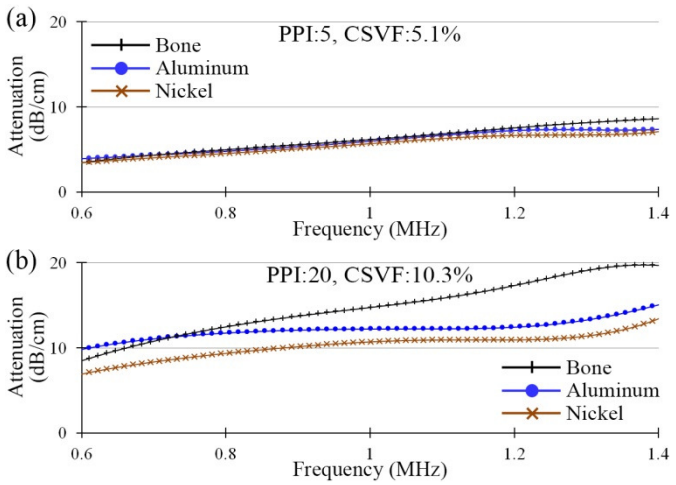

Figure 5.18 The simulated attenuation coefficients corresponding to the computational bone, aluminum and nickel trabecular structure for two foam samples with (CSVF: computational solid volume fraction).

Third, in addition to the scattering mechanism discussed above, the mode-converted shear waves inside the trabecular structures also attenuate through energy absorption mechanisms [44]. The absorption of shear waves in bovine cancellous bone is reported to be as rapid as loss of 98% of the shear wave power for each millimeter of propagation [44]. Therefore, part of the difference observed between the relative error in this study and the other FDTD study ([3]) may be also explained by noting the different amount of the transmitted energy of the mode-converted shear waves in bone and aluminum (Figure 5.17b). In this regard, the absorption of shear waves in aluminum foams are expected to be less dominant than that in cancellous bone. This indicates that regardless of the simulation method and in the absence of absorption mechanisms, simulating ultrasound propagation in aluminum foams may lead to more accurate results than the simulation results of cancellous bone.

Despite the strong agreement observed between the experimental and simulated attenuation coefficients in this study, it is appropriate to address possible sources of discrepancy. Other than the absence of absorption mechanisms of attenuation in the simulations (discussed earlier), the following sources may be considered:

Discrepancy between AAVF and CAVF: in the experiment, the central region of a physical sample located in the path of the ultrasonic could have different AAVF value than the AAVF of the whole sample. Moreover, the CAVF of the corresponding computational sample differed from the AAVF of the physical sample (because the volume of interest (Figure 5.1a) scanned by the μ-CT did not include the middle region of a sample). This source of discrepancy

may explain the apparently higher and lower simulated attenuation coefficients than the experimental values shown in Figure 5.13d and e respectively.

Numerical errors of the simulations: in a numerical wave propagation analysis, part of the errors may appear in the form of numerical dissipation, which introduces numerical attenuation into the results. Being mainly due to insufficient spatial resolution (element size or nodal distance), numerical dissipation increases with the frequency of the waves propagating in the computational medium. In a case of simulating a broadband signal with the finite element method, the finite element mesh with insufficient spatial resolution acts as a low-pass filter [51]. In this work, the maximum nodal distance (element size) was chosen to sufficiently resolve the wave lengths corresponding to the upper limit of the frequency range of interest (1.4 MHz). Therefore, the contribution of numerical dissipation in the experiment-simulation discrepancies must not be significant. As evidence, Figure 5.14 demonstrates that the error is generally decreasing with the frequency; this indicates that the low-pass filtering of the simulated signals by the finite element mesh was insignificant.

Transmitted pressure signal in the simulations: the transmitted signal in the simulations was an ultrasonic pressure signal obtained from the normalized voltage signal measured by the physical receiver located 5 cm away from the physical transmitter. Since the conversion of voltage-pressure is frequency-dependent [52] and the signal was measured some distance away from the surface of the transmitter, the simulation pressure signal did not exactly represent the transmitted pressure signal at the physical transmitter surface. In our previous study [34], it was shown that different broadband signals with different phase content may introduce discrepancies in the attenuation coefficients for the same sample.

Different sources of secondary oscillations: It was shown that part of the discrepancy observed in the results was due to the secondary oscillations. The experimental and simulated secondary oscillations were mainly due to inter-trabecular reflections. However, other sources of secondary oscillations that were different in the experiments than the simulations might have introduced discrepancies in the results. Measurement noise, wave reflections between the close distance of the faces of the physical sample and the transducers, and redundant wave reflection due to the presence of the sample holders could be other experimental causes of the secondary oscillations. On the other hand, the other origin of the secondary oscillations in the simulations

was non-uniformity in the size of elements (especially at the boundary of the virtual cube and the surrounding water where element size transition began) and inevitable imperfectness in non-reflecting properties of the artificial boundaries.

5.6 Conclusions

Through this study, it was demonstrated that the micro-scale finite element models (based on standard Galerkin FEM) could effectively simulate broadband ultrasound propagation in water-saturated aluminum foams. The small average discrepancy (less than 10%) observed between the experimental and simulated results indicated that the main mechanisms of attenuation in water-saturated aluminum foams were scattering and mode conversion. This implies that while disregarding the absorption mechanisms, the models were highly capable of capturing other wave propagation phenomena such as reflection, refraction, scattering and mode conversion.

The simulation error in this study, which utilized the FEM, was notably smaller than the simulation error observed in other studies based on FDTD micro-scale modeling. Part of the error in the FDTD may arise from the deficiency of the method in explicitly modeling the solid-fluid interfacial conditions. However, this is not sufficient to conclude significantly higher dominancy of the FEM over the FDTD. Because the attenuation mechanism in cancellous bone sample used in the studies based on FDTD simulations was shown to be significantly dependent on the absorption mechanism (especially absorption of mode-converted shear waves). Therefore, the accuracy of the FEM over the FDTD method due to the different approaches in modeling the interfacial conditions of different porous material should be further investigated.

5.7 References

[1] C.F. Njeh, C.M. Boivin, C.M. Langton, The role of ultrasound in the assessment of osteoporosis: a review, Osteoporos. Int. 7 (1997) 7–22.

[2] C.M. Langton, C.F. Njeh, The measurement of broadband ultrasonic attenuation in cancellous bone--a review of the science and technology, IEEE Trans. Ultrason. Ferroelectr. Freq. Control. 55 (2008) 1546–54.

[3] E. Bossy, P. Laugier, F. Peyrin, F. Padilla, Attenuation in trabecular bone: A comparison between numerical simulation and experimental results in human femur, J. Acoust. Soc. Am. 122 (2007) 2469–75.

[4] E.W. Gregg, A.M. Krishka, L.M. Salamone, M.M. Roberts, S.J. Anderson, R.E. Ferrell, et al., The epidemiology of quantitative ultrasound: a review of the relationships with bone mass, osteoporosis and fracture risk, Osteoporos. Int. 7 (1997) 89–99.

[5] C.M. Langton, S.B. Palmer, R.W. Porter, The measurement of broadband ultrasonic attenuation in cancellous bone, Eng. Med. 8 (1979) 153–159.

[6] C.M. Langton, C.F. Njeh, Acoustic and ultrasonic tissue characterization--assessment of osteoporosis, Proc. Inst. Mech. Eng. Part H J. Eng. Med. 213 (1999) 261–269.

[7] C.F. Njeh, R. Hodgskinson, J.D. Currey, C.M. Langton, Orthogonal relationships between ultrasonic velocity and material properties of bovine cancellous bone, Med. Eng. Phys. 18 (1996) 373–81.

[8] W. Abendschein, G.W. Hyatt, Ultrasonics and selected physical properties of bone, Clin. Orthop. Relat. Res. 69 (1970) 294–301.

[9] Y. Nagatani, K. Mizuno, T. Saeki, M. Matsukawa, T. Sakaguchi, H. Hosoi, Propagation of fast and slow waves in cancellous bone: Comparative study of simulation and experiment, Acoust. Sci. Technol. 30 (2009) 257–264.

[10] V. Nguyen, S. Naili, V. Sansalone, Simulation of ultrasonic wave propagation in anisotropic cancellous bone immersed in fluid, Wave Motion. 47 (2010) 117–129.

[11] C. Zhang, L.H. Le, R. Zheng, D. Ta, E. Lou, Measurements of ultrasonic phase velocities and attenuation of slow waves in cellular aluminum foams as cancellous bone-mimicking phantoms, J. Acoust. Soc. Am. 129 (2011) 3317–26.

[12] B. Lashkari, A. Manbachi, A. Mandelis, R.S.C. Cobbold, Slow and fast ultrasonic wave detection improvement in human trabecular bones using Golay code modulation, J. Acoust. Soc. Am. 132 (2012) EL222–8.

[13] L.H. Le, C. Zhang, D. Ta, E. Lou, Measurement of tortuosity in aluminum foams using airborne ultrasound, Ultrasonics. 50 (2010) 1–5.

[14] M.A. Biot, Theory of propagation of elastic waves in a fluid-saturated porous solid. I. low-frequency range, J. Acoust. Soc. Am. 28 (1956) 168.

[15] M.A. Biot, Theory of propagation of elastic waves in a fluid-saturated porous solid. II. higher frequency range, J. Acoust. Soc. Am. 28 (1956) 179.

[16] T.J. Haire, C.M. Langton, Biot theory: A review of its application to ultrasound propagation through cancellous bone, Bone. 24 (1999) 291–295.

[17] G. Haïat, F. Padilla, F. Peyrin, P. Laugier, Fast wave ultrasonic propagation in trabecular bone: numerical study of the influence of porosity and structural anisotropy, J. Acoust. Soc. Am. 123 (2008) 1694–705.

[18] K. Il Lee, H.-S. Roh, S.W. Yoon, Acoustic wave propagation in bovine cancellous bone: Application of the Modified Biot–Attenborough model, J. Acoust. Soc. Am. 114 (2003) 2284.

[19] M. Kaczmarek, J. Kubik, M. Pakula, Short ultrasonic waves in cancellous bone, Ultrasonics. 40 (2002) 95–100.

[20] Q. Ji, L.H. Le, L.J. Filipow, S. a. Jackson, Ultrasonic wave propagation in water-saturated aluminum foams, Ultrasonics. 36 (1998) 759–765.

[21] V.-H. Nguyen, S. Naili, V. Sansalone, A closed-form solution for in vitro transient ultrasonic wave propagation in cancellous bone, Mech. Res. Commun. 37 (2010) 377–383.

[22] V.H. Nguyen, S. Naili, Semi-analytical solution of transient plane waves transmitted through a transversely isotropic poroelastic plate immersed in fluid, J. Eng. Math. (2013) 1–14.

[23] W. Lin, Y.-X. Qin, C. Rubin, Ultrasonic wave propagation in trabecular bone predicted by the stratified model, Ann. Biomed. Eng. 29 (2001) 781–790.

[24] K.A. Wear, A stratified model to predict dispersion in trabecular bone, IEEE Trans. Ultrason. Ferroelectr. Freq. Control. 48 (2001) 1079–1083.

[25] E.R. Hughes, T.G. Leighton, G.W. Petley, P.R. White, Ultrasonic propagation in cancellous bone: A new stratified model, Ultrasound Med. Biol. 25 (1999) 811–821.

[26] P.H. Nicholson, R. Strelitzki, R.O. Cleveland, M.L. Bouxsein, Scattering of ultrasound in cancellous bone: predictions from a theoretical model., J. Biomech. 33 (2000) 503–6.

[27] D. Ta, W. Wang, K. Huang, Y. Wang, L.H. Le, Analysis of frequency dependence of ultrasonic backscatter coefficient in cancellous bone., J. Acoust. Soc. Am. 124 (2008) 4083–4090.

[28] F. Padilla, E. Bossy, G. Haiat, F. Jenson, P. Laugier, Numerical simulation of wave propagation in cancellous bone, Ultrasonics. 44 Suppl 1 (2006) e239–43.

[29] E. Bossy, F. Padilla, F. Peyrin, P. Laugier, Three-dimensional simulation of ultrasound propagation through trabecular bone structures measured by synchrotron microtomography, Phys. Med. Biol. 50 (2005) 5545–56.

[30] G. Luo, J.J. Kaufman, A. Chiabrera, B. Bianco, J.H. Kinney, D. Haupt, et al., Computational methods for ultrasonic bone assessment, Ultrasound Med. Biol. 25 (1999) 823–30.

[31] A.S. Aula, J. Töyräs, M.A. Hakulinen, J.S. Jurvelin, Effect of bone marrow on acoustic properties of trabecular bone-3D finite difference modeling study, Ultrasound Med. Biol. 35 (2009) 308–18.

[32] Y. Nagatani, H. Imaizumi, T. Fukuda, M. Matsukawa, Y. Watanabe, T. Otani, Applicability of finite-difference time-domain method to simulation of wave propagation in cancellous bone, Jpn. J. Appl. Phys. 45 (2006) 7186–7190.

[33] Y. Nagatani, H. Soumiya, T. Saeki, Y. Yaoi, M. Matsukawa, Propagation of ultrasonic longitudinal wave in the cancellous bone covered by the subchondral bone of bovine femur, 2008 IEEE Ultrason. Symp. (2008) 146–149.

[34] B. Vafaeian, M. El-Rich, T. El-Bialy, S. Adeeb, The finite element method for micro-scale modeling of ultrasound propagation in cancellous bone, Ultrasonics. 54 (2014) 1663–1676.

[35] A. Hosokawa, Ultrasonic pulse waves in cancellous bone analyzed by finite-difference time-domain methods, Ultrasonics. 44 Suppl 1 (2006) e227–31.

[36] A. Hosokawa, Development of a numerical cancellous bone model for finite-difference time-domain simulations of ultrasound propagation, IEEE Trans. Ultrason. Ferroelectr. Freq. Control. 55 (2008).

[37] A. Hosokawa, Effect of trabecular irregularity on fast and slow wave propagations in cancellous bone, in: Symp. Ultrason. Electron., 2006: pp. 297–298.

[38] L. Goossens, J. Vanderoost, S. Jaecques, S. Boonen, J. D'hooge, W. Lauriks, et al., The correlation between the SOS in trabecular bone and stiffness and density studied by finite-element analysis, IEEE Trans. Ultrason. Ferroelectr. Freq. Control. 55 (2008) 1234–42.

[39] S. Ilic, K. Hackl, R. Gilbert, Application of the multiscale FEM to the modeling of cancellous bone, Biomech. Model. Mechanobiol. 9 (2010) 87–102.

[40] http://www.ergaerospace.com, (n.d.).

[41] Dassault Systèmes, Abaqus theory manual, in: Dassault Systèmes, 2012.

[42] F. Ihlenburg, Finite element analysis of acoustic scattering, Springer-Verlag, New York, 1998.

[43] P. Bloomfield, Fourier analysis of time series: An introduction, Wiley, New York, 2000.

[44] K. Wear, S. Member, Mechanisms for attenuation in cancellous- bone-mimicking phantoms, Wear. 55 (2008) 2418–2425.

[45] K.J. Marfurt, Accuracy of finite-difference and finite-element modeling of the scalar and elastic wave equations, Geophysics. 49 (1984) 533–549.

[46] J. Zhang, D.J. Verschuurt, Elastic wave propagation in heterogeneous anisotropic media using the lumped finite-element method, Geophysics. 67 (2002) 625–638.

[47] F. Muir, J. Deltinqert, J. Etqens, D. Nichols, Short note: Modeling elastic fields across irregular boundaries, Geophysics. 57 (1992) 1189–1193.

[48] R. Van Vossen, J.O.A. Robertsson, C.H. Chapman, Finite difference modeling of wave propagation in a fluid–solid configuration, Geophysics. 67 (2002) 618–624.

[49] R.A. Slawinski, E.S. Krebes, The homogeneous finite-difference formulation of the P-SV-wave equation of motion, Stud. Geophys. Geod. 46 (2002) 731–751.

[50] R.S.C. Cobbold, Foundations of Biomedical Ultrasound, Oxford University Press, 2007.

[51] C. Canada, Analysis of Wave Propagation in Unbounded Media, 1045 (2006) 1037–1045.

[52] A. Hurrell, Voltage to pressure conversion: are you getting `phased' by the problem?, J. Phys. Conf. Ser. 1 (2004) 57–62.

Chapter 6

Simulation of Low Intensity Ultrasound Propagating in a Beagle Dog Dentoalveolar Structure to Investigate the Relations between Ultrasonic Parameters and Cementum Regeneration

The contents of this chapter have been previously published: B. Vafaeian, S. Al-Daghreer, M. El-Rich, S. Adeeb, T. El-Bialy, Ultrasound in Medicine & Biology. Vol. 41, No. 8, pp. 2173–2190, 2015.

6.1 Abstract:

The therapeutic effect of low intensity pulsed ultrasound (LIPUS) on orthodontically induced inflammatory root resorption (OIIRR) is believed to be through LIPUS-induced mechanical signals. However, the stimulatory mechanism triggering dental cell response has not been clearly identified yet. The aim of this study was to evaluate possible relations between the amounts of new cementum regeneration and ultrasonic parameters such as pressure amplitude and time-averaged energy density. We utilized the finite element method to simulate the previously published experiment of ultrasonic wave propagation in the dentoalveolar structure of beagle dogs. Qualitative relations between the thickness of the regenerated cementum in the experiment and the ultrasonic parameters were observed. Our results indicated that the areas of the root surface with greater ultrasonic pressure were associated with higher amounts of cementum regeneration. However, establishing reliable quantitative correlations between the ultrasound parameters and the cementum regeneration requires more experimental data and simulations.

6.2 Introduction

Recognized as a common side effect of orthodontic treatment, orthodontically induced inflammatory root resorption (OIIRR) may affect the outcome of successful orthodontic treatment [1–3]. Reports suggest that 93% of adolescents undergoing orthodontic treatments experience some degree of root resorption [4,5]. However, root resorption becomes a clinical problem when more than one quarter of the tooth root length (1-2mm) is resorbed. This includes moderate to severe (1-3mm) and severe root resorption (>3-5mm) [1,4]. According to prevalence reports, moderate resorption was observed in 15% [5] and 16.5% [6] of cases. Severe root resorption was also found in 10-20% [7], 3-5% [8] and 1-5% [1] of different treatment cases. In severe root resorption, adverse consequences of resorption such as tooth mobility can occur; consequently orthodontists may potentially be subjected to malpractice claims [9].

OIIRR is a pathological process during which destruction and removal of a thin mineralized layer of cementum and dentin occurs depending on the severity of the resorption [8]. The mechanism and etiology of resorption is still not fully understood. However, it is suggested that OIIRR is a multifactorial and inflammatory process related to the cellular activity triggered in response to hyalinised and compressed regions of the periodontal ligament [1,3,4,10,11] . The

process may be reversible through new cementum regeneration if OIIRR only influences the outer layer of cementum. However, the process becomes irreversible when OIIRR affects dentin [1,2,4].

Currently, no clinically applicable methods exist for the prevention or the treatment of OIIRR [3,4]. However, the advantage of low-intensity therapeutic ultrasound as a potential OIIRR prevention/treatment has recently been reported [3,4,9] . Under a specific protocol, El-Bialy et al. (2004) demonstrated that the application of low-intensity pulsed ultrasound (LIPUS) on a human tooth subjected to orthodontic treatment not only minimized the resorption but also led to accelerating the healing of the resorption by reparative cementum. Another in-vivo study on a group of rats who underwent tooth movement experiments indicated that LIPUS significantly reduced the resorption with no effect on tooth movement [4]. Recently, Al-Daghreer et al. (2014) performed an in-vivo animal study involving the application of LIPUS on beagle dogs' teeth subjected to a 4-week period of orthodontic forces and movements. Their results exhibited regeneration of the precementum layer, cementum, and reparative cellular cementum when LIPUS was applied. In addition to the human and animal studies, in-vitro experiments have ascertained the effect of LIPUS on the proliferation and metabolism of cementoblast [12,13] and periodontal ligament cells [14].

The mechanisms regarding the observed biological response of tissues to LIPUS stimulations have not yet been fully elucidated [15,16]. If the cavitation effect (local formation of vapour phase inside a liquid) of LIPUS is ruled out due to its low intensity [16,17], then mechanical stresses, fluid micro-streaming in soft tissues, piezoelectric effects in hard tissues (like bone), and thermal effects are potentially the physical phenomena driving the tissue biological response [15,16,18–20]. The effect of these phenomena on the cellular reactions should be biophysically explored at inter and intra cellular scales to understand the mechanisms behind LIPUS success. In addition, macro-scale modelling through continuum theories may also be informative in determining the effective magnitude of the mechanical signals stimulating the tissue response.

From a macro-scale perspective, investigating the biological effect of LIPUS requires studying acoustic wave propagation through soft tissues by utilizing the continuum assumption for these tissues. In this case, the acoustic stress field, velocity field, intensity field etc. can be

correlated with the tissue-scale biological responses. A clarifying example in this context is *Wolff's Law* [21] when regarded as a tissue-scale phenomenon, i.e. bone deposition and resorption are associated with mechanical stresses acting upon it.

Hypothesizing that acoustic fields are correlated with tissue-scale biological reactions, the aim of this study was to numerically simulate LIPUS propagation in a beagle dog dentoalveolar structure. The simulations were based on utilizing the finite element method to solve the linear mechanical wave propagation in the three dimensional medium of the dentoalveolar structure. The simulated pressure and energy distributions of LIPUS over the root and the periodontal ligament (PDL) surfaces were compared and correlated with the available histological data [3] on the cementum thickness regarding the control and LIPUS treated teeth.

6.3 Materials and methods

In the present study, we intended to simulate LIPUS propagation in a typical dentoalveolar structure of one beagle dog out of the ten subjected to the in-vivo experiment[1] carried out by Al-Daghreer et al. (2014). During the experiment, the mandibular fourth premolars (both left and right) of each dog were orthodontically moved by constant orthodontic forces for 4 weeks. Considered as the LIPUS-treated tooth, one of the premolars was intraorally exposed to LIPUS on its buccal side. In contrast, the other premolar only remained under the constant orthodontic force and was denoted as the control tooth.

The utilized LIPUS (SmileSonica, Inc., Edmonton, AB, Canada) was generated from a square lead zirconate-titanate transducer ($1.2 \times 1.3\ \mathrm{cm}^2$) with the spatial-average temporal-average intensity of $I_{SATA} = 30\ \mathrm{mW/cm}^2$. Each pulse was a 1.5MHz sinusoidal pulse lasting for 200 microseconds and a duty cycle (pulse duration divided by the repetition time between pulses) of 0.2.

6.3.1 Assumptions

Compared to the experimental situation, the configurations of the simulations underwent an idealization and a simplification. The idealization was assuming a uniform pressure distribution on the transducer surface directly transmitted to the gingival corresponding surface.

[1] Under a specific LIPUS exposure protocol, they attempted to investigate the effect of LIPUS on cementum regeneration and prevention of OIIRR in ten beagle dogs.

The simplification estimated the amplitude of the uniformly distributed pressure as:

$$I_{SATA} = (duty\ cycle).I_{SAPA} \approx 0.2\frac{P^2}{2\rho_o c_o} \quad (6.1a)$$

$$duty\ cycle \coloneqq \frac{Pulse\ duration}{pulse\ repetition\ period} \quad (6.1b)$$

where P is the pressure amplitude of a continuous sinusoidal wave, ρ_o and c_o are the density and nominal sound velocity of water (measurement medium) respectively and I_{SAPA}stands for spatial-average pulse-average intensity [22].

Characterized as mechanical waves, the propagation of the LIPUS can be described by the mechanical wave equations. These wave equations are partial differential equations founded on the macro-scale physical laws of continuum mechanical equilibrium while excluding thermal effects, cavitation, biological growth, and age-dependent phenomena. Furthermore, a linearized form of the wave equations (section 2.3.2) based on small signal or infinitesimal deformation were assumed [17,23]. In a linear propagation regime, shock waves and the secondary physical effects of ultrasound propagation such as radiation pressure[2] and acoustic streaming[3] are absent [17].

6.3.2 Geometry and materials of the dentoalveolar models

In the experimental study, the dogs were euthanized and dissected parts of their mandibles were obtained to investigate the root surfaces of the control and LIPUS-treated teeth [3]. Since the dogs were the same age, sex and weight, a dissected part potentially represented a typical dentoalveolar structure of the group. In this study, images from micro-computed tomography scan (μCT) of a dissected part containing a LIPUS-treated forth premolar on the left side and its vicinity (Figure 6.1a) were utilized to generate the geometry of a dentoalveolar structure. Mandibular bone, mandibular cavity, PDL, dentin, pulp chamber and enamel were observable in the μCT images (Figure 6.1b).

To simulate the ultrasound propagation in the dentoalveolar structure of a beagle dog, two modeling approaches were considered: a simple one-dimensional (1D) model and a

[2] Radiation pressure: Part of the total acoustic pressure having relatively smaller magnitude and temporally constant during an ultrasonic pulse.

[3] Acoustic streaming: Bulk movements of a fluid situated in an acoustic field.

comprehensive three-dimensional (3D) one.

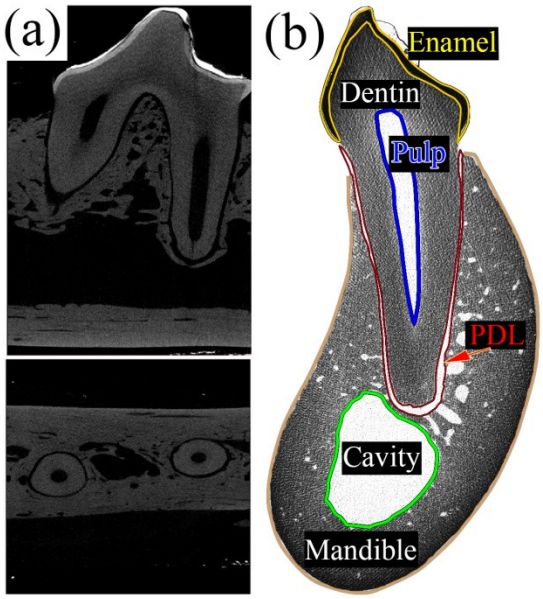

Figure 6.1 (a) Typical μCT images of sagittal and transverse views of the dentoalveolar structure regarding the left premolar. (b) Observable components of the dentoalveolar structure in a typical μCT image.

Simulating ultrasound propagation in a 1D model was a simple but an informative approach to reveal the effect of different material layers on mechanical stress and energy density changes during the propagation. The 1D model for ultrasound propagation was simply a layered 1D medium containing the material layers across the dentoalveolar structure. The thickness of each material layer was digitally measured on a centre line of a frontal section image of the structure (as depicted by line $a - a$ on Figure 6.2).

To generate the 3D geometry out of the μCT images, a segmentation process using the software package Materialise Mimics (2013.16.0, Materialise, Leuven, Belgium) was performed on the images. Inevitable approximation in capturing a continuous region for the mandibular cavity was made through the segmentation (Figure 6.3a and b). Furthermore, while the boundaries for the mandibular bone, mandibular cavity, PDL, dentin, pulp chamber, and enamel were distinct enough in the μCT images, a clear boundary for cementum was not tractable. Therefore, the thin cementum layer was regarded to be part of the dentin with the same material properties [24]. According to some studies [25–27], the average mechanical and physical

properties of cementum, dentin and cortical bone are moderately close (Table 6.1). Consequently, the approximation of combining the cementum and dentin layers was not expected to significantly influence the simulation results.

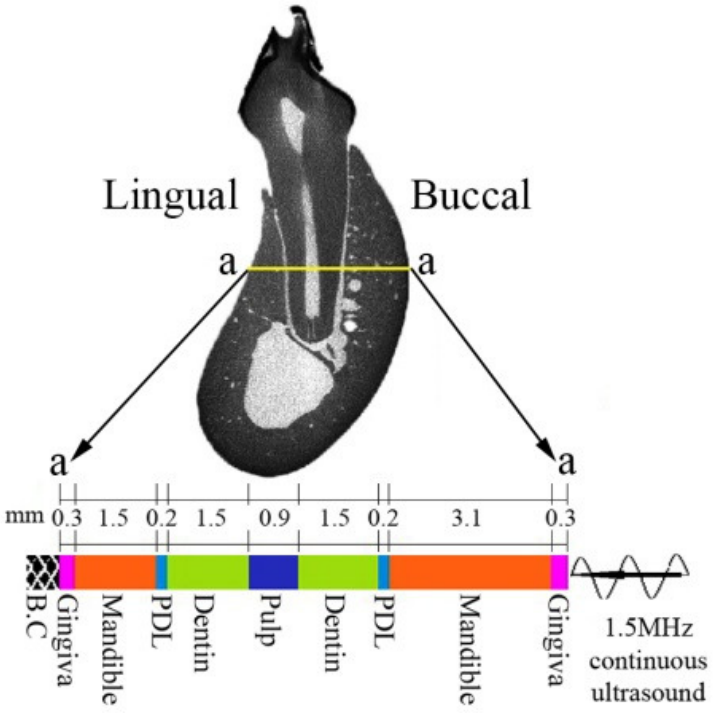

Figure 6.2 One-dimensional layered model of the dentoalveolar structure.

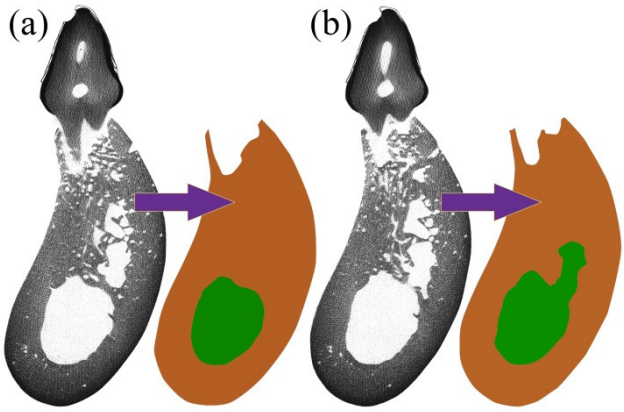

Figure 6.3 Instances of the approximation made in the segmentation of the mandible and the cavity sections.

The outputs of the segmentation procedure (closed surfaces in the form of stereo lithography (STL) data) were processed using Geomagic Studio (2014.1.0, 3D systems, Raleigh, NC, USA) to produce analytical surfaces (non-uniform rational basis splines). By utilizing another computer software package (Altair HyperMesh 2011.11.0, Altair engineering, Troy, MI,

USA), the analytical closed surfaces were converted to volumes. Distinct geometries for the mandibular bone, mandibular cavity content, PDL, dentin with pulp chamber, and enamel were reconstructed through Boolean operations. Afterwards, volumes representing the gingiva and the pulp were created in the finite element meshing process. A uniform-thickness layer of finite elements (0.3 mm) covering the mandible created the gingiva; and the pulp was generated by volumetric finite element filling the pulp chamber.

Table 6.1 Material properties of the dentoalveolar structure components.

Solid materials (hard tissues)				
	Cortical bone[1]	Dentin[2]	Enamel[3]	Cementum[4]
Density (kg/m^3)	1850	2000	2950	2030
Modulus of Elasticity (MPa)	13700	18600	84100	15000
Poisson's ratio	0.30	0.31	0.33	0.31
Longitudinal wave velocity (m/s)	3157	3590	6499	3200
Transverse wave velocity (m/s)	1687	1884	3274	1680
Smallest wavelength in the material (mm)	1.13	1.26	2.18	1.12
Fluid materials (soft tissues)				
	Gingiva[5]	Cavity content (water)	PDL[5]	Pulp[6]
Density (kg/m^3)	1043	1000	1120	1000
Bulk Modulus (MPa)	2542	2200	2914	2465
Longitudinal wave velocity (m/s)	1561	1483	1613	1570
Smallest wavelength in the material (mm)	1.04	0.99	1.08	1.05

[1] [28,29] , [2] [28,30], [3] [31–33], [4] [25–27] ,[5] [34], [6] [35].

To ascertain an acceptable dimensional accuracy, measurements on the 3D geometry and several of its different cross-sections were performed and the results were compared with the dimensions directly measured on μCT images. Figure 6.4a illustrates the virtually reconstructed geometries of the dentoalveolar structure parts.

The material properties for the dentoalveolar components were obtained from a variety of references (Table 6.1). The mandibular bone of the beagle dog was primarily composed of cortical bone although there was a complicated cortical-to-cancellous bone transition towards the PDL. Moreover, the soft tissues (gingiva, PDL, pulp, mandibular cavity content) were approximated as ideal non-viscous fluids. By virtue of this assumption, shear waves were disregarded in the soft tissues.

For simplicity, the material properties did not account for energy dissipation mechanisms (viscous effects) and scattering mechanism (due to material inhomogeneity). This indeed omitted the ultrasound attenuation due to energy absorption and wave scattering.

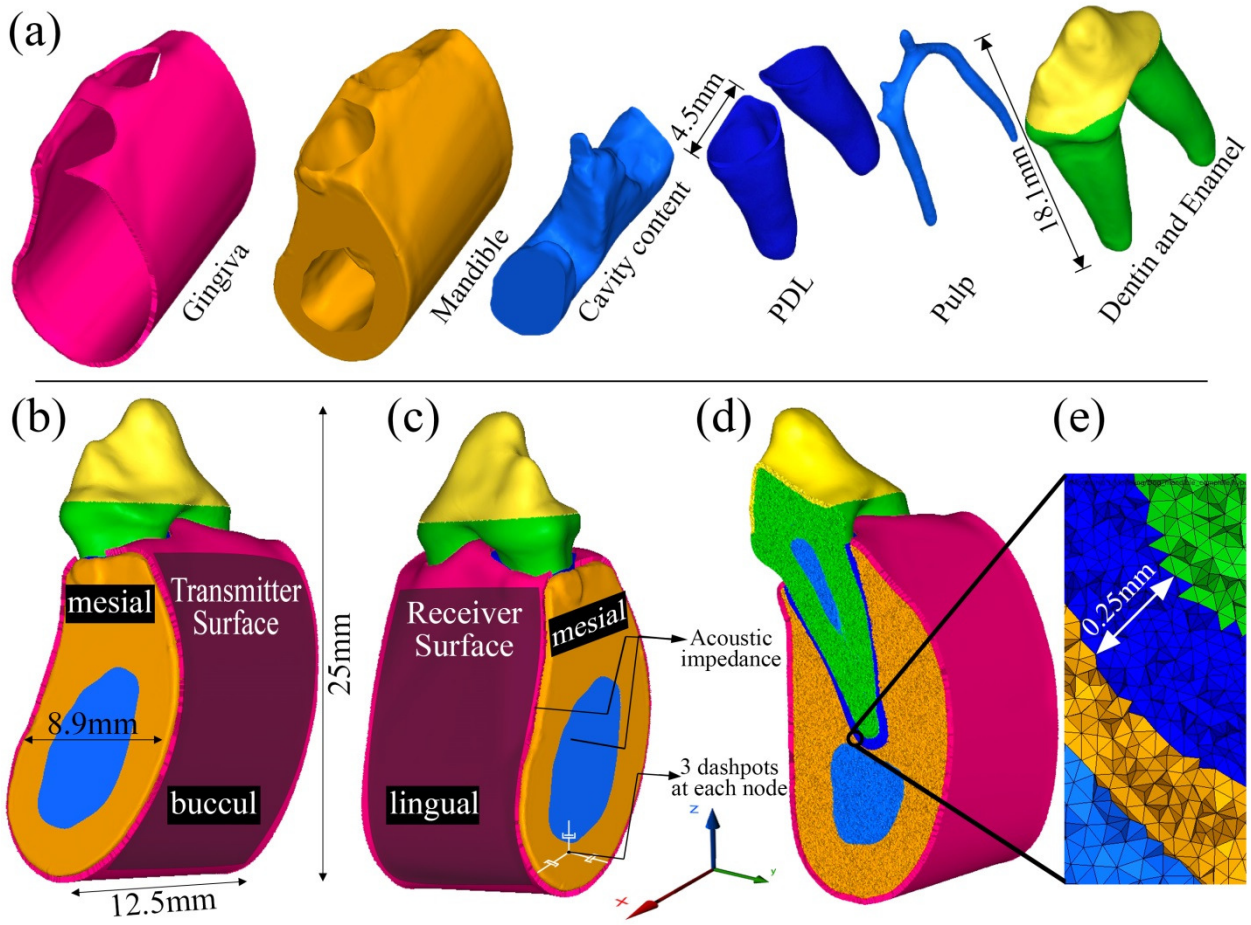

Figure 6.4 (a) The virtually reconstructed geometries of the dentoalveolar structure components regarding the left premolar. (b) The virtual geometry of dentoalveolar structure for finite element analyses, and the region assigned as the transmitter on the buccal side of the mandible. (c) Non-reflecting boundary conditions on the distal side of the mandible (the same was applied on the mesial side), and the region assigned as the receiver on the lingual side of the mandible. (d) A cross-section of the finite element model meshed with tetrahedral elements. (e) A closer view of the generated finite elements.

6.3.3 Numerical simulations and finite element models

The numerical simulations of LIPUS propagating in 1D and 3D models of dentoalveolar structure were performed using the standard finite element method (FEM). Noting the relatively long duration of the LIPUS pulse (200 μs), sound velocity in different layers of the medium (Table 6.1) and the dimensions of the dentoalveolar structure, we assumed a steady state harmonic wave propagation (section 2.3.3 and 2.4.3). In this regard, transient vibrations in the media were ignored.

6.3.3.1 1D model

The 1D model was analyzed based on one-dimensional plane wave propagation; therefore, the displacements and volumetric deformations were unidirectional. Simulating the wave propagation in this medium, the model satisfied the continuity of displacement and pressure at the interfaces of the layers. At the side of the model associated with the buccal side, a unit-amplitude ultrasonic pressure (1.5MHz) was applied (Figure 6.2). The other side was treated with three different conditions being free-end (zero pressure but free to move), fixed-end (zero displacement but non-zero pressure) and non-reflecting boundary conditions (Figure 6.2). The rheological representation for the non-reflecting boundary condition was a linear dashpot with a particular coefficient [36].

The software package ABAQUS (6.12, Dassault Systèmes Simulia Corp., RI, USA,) was utilized for generating a finite element model and simulating LIPUS propagation in the 1D layered medium. The spatial distributions of the steady-state pressure amplitudes and time-averaged total energy density were calculated. The latter is the time-average of the total potential and the kinetic energy per unit volume calculated by (Cobbold 2007):

$$\overline{E_T} = (\overline{E_K + E_P}) = \frac{1}{2}\overline{(\rho_o \dot{u}^2 + \frac{p^2}{\rho_o c_L^2})} \qquad (6.2)$$

such that E_T, E_P and E_K are total, potential and kinetic energy density respectively. The over bar indicates a temporal average over a single period of the continuous waves.

6.3.3.2 3D models

Two 3D models were considered for the simulations. One model included all the dentoalveolar components whereas the other one excluded the PDL. In that model, the cortical bone of the mandible was extended to the boundary of the root. The reason for this approach was due to two facts. Firstly, there is a large variability in the material properties of the PDL reported in the literature [37]. Secondly, assuming the PDL as an ideal fluid restrained transverse waves from reaching to the root surface. Therefore, it was expected that performing a simulation excluding the fluid PDL would reveal some facts about the effect of the PDL on the ultrasound propagation.

The virtual 3D geometry of the dentoalveolar structure with/without PDL served as the

solution domain of the linear wave equations (Figure 6.4b). The solid parts (hard tissues) transmitted longitudinal and transverse waves whereas the fluid parts (soft tissues) only transmitted longitudinal waves. Consequently, a set of coupling equations imposing perfect-slip conditions (section 2.4.3 and Eq. 4.3) at the solid-fluid interfaces were employed (Abaqus theory manual, Dassault Systèmes, 2012; Van Vossen et al., 2002).

In real circumstances, the ultrasound mounted on the gingival surface would propagate and scatter in the entire mandible. However, only the dissected part of the mandible was considered for the simulations. The dissected part was geometrically bounded at its lateral sides (mesial [front] and distal [back] sides) leading to unrealistic wave reflections back into the medium during the simulation. Therefore, the contribution of the excluded parts of the structure had to be reckoned in the simulations to avoid the unwanted wave reflections. To alleviate the unwanted wave reflections, non-reflecting boundary conditions were proposed (Figure 6.4c). For the fluid materials (gingiva and cavity content), the non-reflecting boundary conditions were applied using a proper acoustic impedance boundary condition facilitated by the software (ABAQUS). The non-reflecting boundary conditions applied on the mandible sides (solid materials) had to account for both steady-state longitudinal and transverse waves. An approximate but practical approach was to use a rheological model in a form of linear dashpots [36]. Accordingly, three dashpots corresponding to the global coordinate system were assigned to each finite element node located on the mandible lateral surfaces (Figure 6.4c).

Represented as an acoustic boundary condition, the uniform sinusoidal ultrasonic pressure was buccally applied on the gingival surface. The pressure amplitude ($P = 0.075\text{MPa}$) was obtained from Eq. 6.1 and assigned to the region corresponding to the transmitter surface (Figure 6.4b).

The virtual geometry of the medium was discretized using finite elements (Figure 6.4d and e) generated by the computer software Altair HyperMesh. The size of the elements was chosen based on $\frac{1}{10}\lambda$ where λ was the smallest wavelength in the fluid and solid materials (Table 6.1). Table 6.2 lists the finite element mesh information for each part of the model.

The finite element simulations of ultrasound propagation in the models were performed through solving the discretized form (weak form) of the wave equation. To this end, the direct solver of ABAQUS installed on a large shared memory multiprocessor machine (Edmonton, AB,

Canada) was utilized. The computing facility belonged to WestGrid Compute-Canada supercomputing resources (national platform of supercomputing resources). Due to the large number of the finite elements (or nodes), 1.7 terabytes of memory and 32 processor cores (Intel Xeon E7 CPU family) were recruited during the analysis time (55 hours).

Table 6.2 The finite element mesh information

Component	Linear element type	Degree of freedom	Number of elements	Number of nodes
Gingiva	Prism	Acoustic pressure	663,504	418,950
Mandible	Tetrahedral	Displacements	18,025,713	3,135,218
Cavity content	Tetrahedral	Acoustic pressure	3,386,050	595,594
PDL	Tetrahedral	Acoustic pressure*	1,153,122	230,508
Dentin and Enamel	Tetrahedral	Displacements	5630373	1,001,773
Pulp	Tetrahedral	Acoustic pressure	336,194	63,726
Total			29,194,956	5,431,571

* Displacements when no fluid PDL existed in the model

The outputs of the simulation were regionally focused on the PDL volume, the root surface, and a defined receiver surface area. Acoustic pressure amplitude was the mechanical parameter simulated inside the PDL volume. On the root surface, the pressure amplitude defined as the magnitude of the average normal stress was considered:

$$\left|\overline{P}\right| = |\overline{\sigma}| = \left|\frac{1}{3}(\sigma_{11} + \sigma_{22} + \sigma_{33})\right| \in \mathbb{R} \qquad (6.3)$$

such that σ_{11}, σ_{22} and σ_{33} are the diagonal stresses in the complex stress tensor. The pressure amplitude was obtained by using the norm of a complex number denoted by $|.|$. It should be noted that each component of the complex stress tensor accounts for the amplitude and the phase of that component.

Additionally the time-averaged total energy density for the elements of the root surface was obtained according to (Abaqus theory manual, Dassault Systèmes, 2012):

$$\overline{E_T} = (\overline{E_K + E_P}) = \frac{1}{2}(\rho_o|\dot{u}|^2 + [\frac{1+\nu}{\mathrm{E}}(\sigma_{11}^2 + \sigma_{22}^2 + \sigma_{33}^2 + 2\sigma_{12}^2 + 2\sigma_{23}^2 + 2\sigma_{31}^2) - \frac{\nu}{\mathrm{E}}(\sigma_{11} + \sigma_{22} + \sigma_{33})^2]) \qquad (6.4)$$

in which $|\dot{u}|$ is the magnitude of the velocity vector in the solid medium, ν and E are the Poisson's ratio and the modulus of elasticity respectively, and $\sigma_{ij}, i,j = 1,2,3$ are the components of the stress tensor. The time-averaged total energy density could be regarded as a

comprehensive parameter containing the effect of all the stress components and the kinetic energy.

To record the ultrasonic pressure on the lingual side of the gingiva, a receiver surface was defined on the lingual side. The surface area of the receiver was the same as that of the transmitter. A collection of finite element nodes at which the acoustic pressure was recorded comprised the receiver. The output of the receiver was the spatial average of the acoustic pressure amplitudes distributed over the receiver surface. This amplitude was calculated considering the phase difference at each spatial point of the gingiva.

6.3.4 Cementum thickness from the histological study

To seek relationships between the simulated ultrasonic parameters (pressure amplitude and time-averaged energy density) and regenerated cementum thicknesses, we retrieved the potentially regenerated cementum thickness values from the histological data of the study by Al-Daghreer et al. (2014). Figure 6.5 shows instances of hematoxylin and eosin-stained slides utilized for measuring the cementum thicknesses of the control and LIPUS treated teeth. Ethics approval for the original animal study (Al-Daghreer et al. 2014) was obtained through the animal research ethics committee at the University of Alberta.

In their study, horizontal sections of the roots of premolars at three vertical levels were considered: coronal third, middle third and apical third (Figure 6.6a). The cementum thicknesses in the control (right) and LIPUS-treated (left) premolars were circumferentially measured at several points at each level (Figure 6.6a). To coordinate the circumferential measurements, the circumference of each root (mesial or distal) was divided into four equal-length arcs and each arc was identified according to the dental anatomical orientations (Figure 6.6b and Figure 6.6c). For instance, the abbreviated form ‘BD’ denoted the buccal face of the distal root. Subsequently, the average of the thickness values measured along each arc represented the cementum thickness for the corresponding anatomical face.

To rely on a conservative cementum thickness associated with each anatomical face, the average of cementum thickness values of the ten animals presented in the experiment was considered. Figure 6.7a shows the average cementum thickness of the control and LIPUS-treated teeth on each anatomical face.

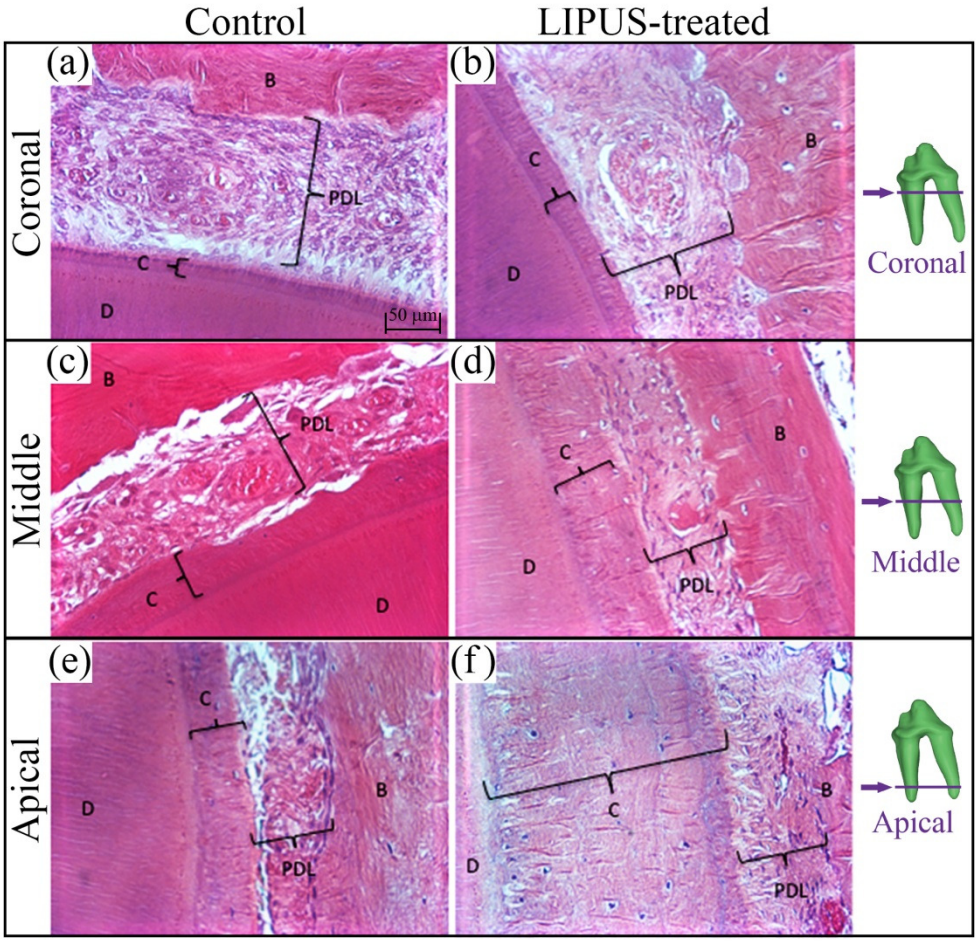

Figure 6.5 Histological sections stained with hematoxylin and Eosin showing the cementum thickness at the three different levels of the root. (40X magnification; C: Cementum, D: Dentin, PDL: Periodontal ligament, B: Alveolar bone). (a) The root surface of the control tooth at the coronal third with thin acellular cementum and compressed PDL. (b) The root surface of the LIPUS-treated tooth at the coronal third with also thin acellular cementum. (c) and (d) The PDL and cementum thicknesses in the middle third of the root for the control and LIPUS-treated sides respectively. Acellular/cellular cementum is thicker in the middle third than that of the coronal third. (e) and (f) The PDL and cementum thicknesses in the apical third of the root for the control and LIPUS sides respectively. Very thick and mainly cellular cementum are observable.

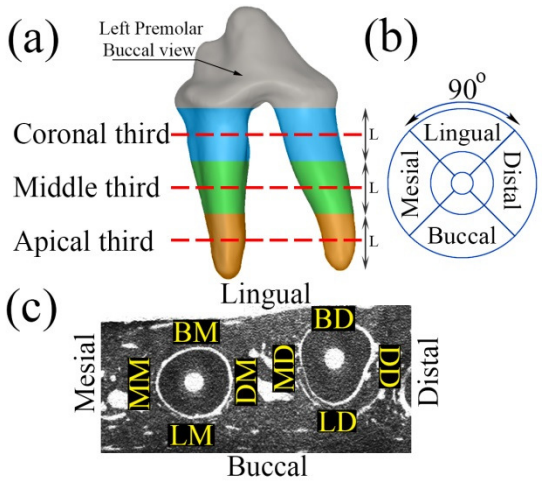

Figure 6.6 (a) Three vertical levels considered on the roots of a premolar. (b) Four equal-length arcs on the root circumferential and the anatomical orientations. (c) Abbreviated anatomical orientations regarding the root surface.

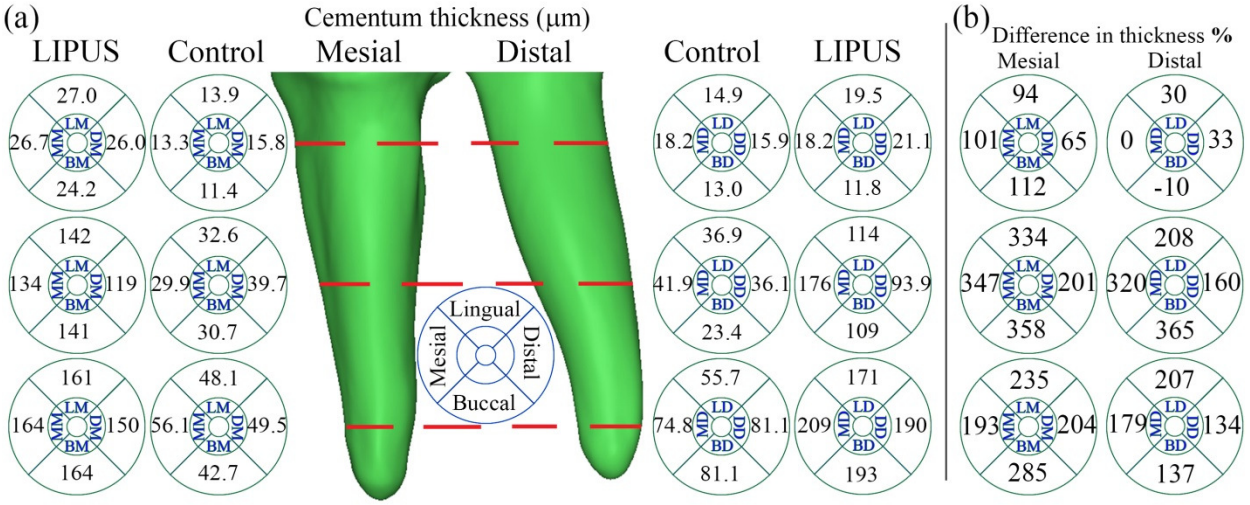

Figure 6.7 (a) Cementum thicknesses (average values regarding ten beagle dogs) on the distal and mesial roots regarding the control and LIPUS-treated teeth. (b) Percentage difference between the cementum thicknesses of the control and the LIPUS-treated teeth.

The values depicted in Figure 6.7b indicate the percentage difference between the cementum thicknesses of the LIPUS-treated and control teeth. The positive difference values observed between the cementum thicknesses were regarded as potentially regenerated cementum. On the other hand, the negative difference between two thickness values (measured on the control and LIPUS-treated teeth) was due to the initial anatomical structure. The regeneration was regarded as potential to denote any initial difference between the thicknesses due to the possible anatomical structure difference. In the present study, possible correlations

between the potentially regenerated cementum values and the simulated ultrasonic parameters were explored.

6.4 Results

6.4.1 1D model

The amplitudes of the harmonically-changing pressure inside the 1D model are depicted in Figure 6.8a. Due to the existence of material layers with different acoustic impedance, wave reflections and standing waves appeared in the medium (1D model). This led to formation of constructive and destructive wave interferences. As it can be observed in Figure 6.8, a unit amplitude sinusoidal ultrasonic pressure resulted in much higher pressure amplitudes in the medium (nearly 10 times larger on the buccal root surface). On the other hand, the pressure amplitude reached zero at the locations where a destructive interface led to wave cancellation. The internal wave reflections eventually reduced the pressure amplitudes toward the other side of the medium (lingual side).

In addition to investigating the pressure amplitudes, time-averaged total energy density ($\overline{E_T}$) was investigated (Figure 6.8b). The spatially constant nature of $\overline{E_T}$ within each layer was due to the propagation of linear plane waves inside the layer [23]. The effect of the dentoalveolar layers on ultrasonic energy reduction is obvious (Figure 6.8b). Due to the internal reflections, a significantly small value of energy reaches to the lingual side. Moreover, because of the small amplitude of pressure and the small amount of energy reaching to the lingual side, the effect of the boundary conditions prescribed on the lingual side appears to be insignificant (Figure 6.8a). The 1D model demonstrated relatively small pressure amplitude (or energy) on the lingual side for fixed or absorbing boundary conditions. The free-end inherently was associated with zero pressure. This observation was verified by the experimental findings of Al-Daghreer et al. (2014), as the pressure amplitude on the lingual side was measured using another transducer. That transducer recorded almost a zero pressure amplitude (also associated with the received energy on the lingual side).

The 1D model predicted very small values of ultrasonic pressure and energy density on the lingual side. This would infer a qualitative correlation with the histological results (Figure 6.7b) showing less potential cementum regeneration on the lingual side. Exceptions

existed for the LD (lingual face of the distal root) at the first and third level.

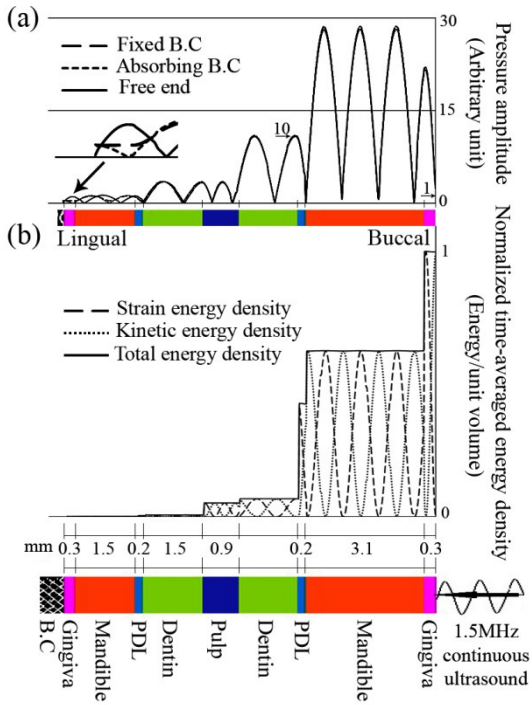

Figure 6.8 (a) Pressure amplitudes and (b) energy density distributions in the 1D model.

6.4.2 3D models

Figure 6.9a and b depict the spatial distribution of pressure amplitudes over the root and PDL outer surfaces. The pressure amplitudes approximately varied from 0.01 to 8 times the applied ultrasonic pressure amplitude (0.075 MPa). However, the regions with pressure amplitudes less than 0.233 MPa associated with 3 times the applied ultrasonic pressure were dominant. The pressure amplitudes were presented with qualitative descriptions (low, moderate, high, very high) for comparison purposes.

The thickness difference considered as the cementum regeneration in percentage for each anatomical face at each level is demonstrated in Figure 6.9a and b. The number inside each rectangle shows the average of the pressure amplitudes at each level over the corresponding anatomical face (Figure 6.9a). The results (Figure 6.9a and b) indicated non-uniform distributions of pressure amplitudes on the surfaces. Assuming that the pressure amplitude is one of the mechanical drivers of regeneration, this would suggest that the non-uniform thickness of the potentially regenerated cementum could be due to the non-uniformity in pressure distribution.

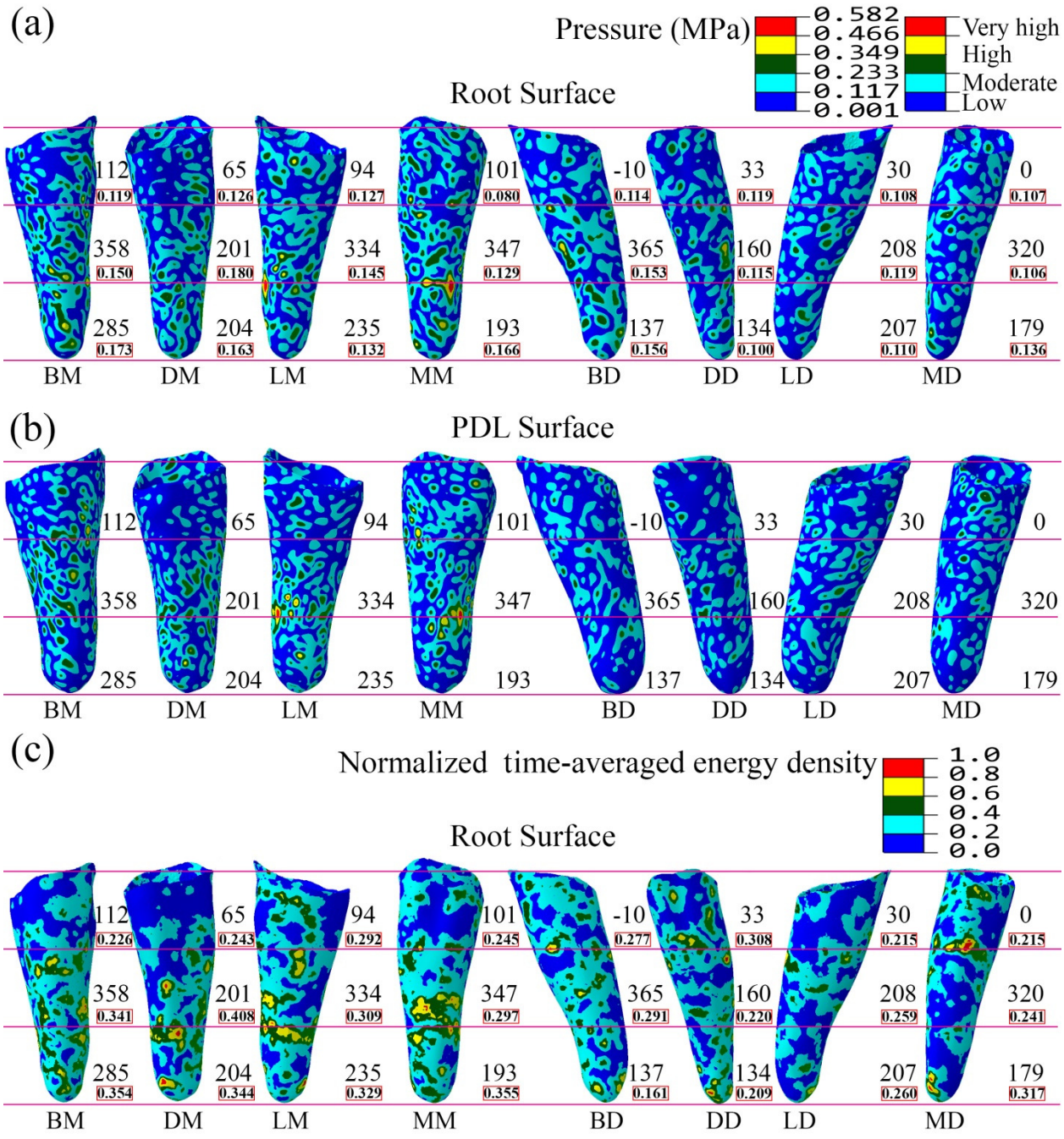

Figure 6.9 (a) and (b) The spatial distributions of pressure amplitudes on the root and on the PDL outer surfaces. (c) Normalized time-averaged energy density distributed over the root surface.

The accumulation of moderate to high pressure amplitudes was observed more at the middle and apical levels of the root and PDL surfaces than the coronal level (Figure 6.9a and b). i.e., the average pressure amplitudes were larger at the middle and apical levels than at the coronal level. This is in agreement with the histological observations indicating that more

potential cementum regeneration occurred at the middle and apical levels of the root surface. However, this qualitative relation did not seem to be proportional and regular.

Moreover, the distal root contained larger areas of low pressure amplitude (dark blue color in Figure 6.9a and b) than those of the mesial root. Exploring the average pressure amplitudes indicated greater pressure amplitudes on the mesial side (some exceptions were observable). To some extent, this indicates conformity to the histological observation that the percentage of regenerated cementum on the distal root was generally less than that of the mesial root.

Investigating and comparing the pressure amplitudes distributed on the buccal and lingual sides (BM-LM and BD-LD) showed an average of 14% pressure amplitude reduction on the lingual side. From the histological point of view, the lingual faces with two exceptions (LD face at the first and the third level) had 20% (on average) less cementum regeneration than those of the buccal side.

The contour plot of the normalized time-averaged total energy density of the ultrasound on the root surface is illustrated in Figure 6.9c. The spatially averaged value of the energy density for each anatomical face is enclosed by a rectangle. Like the pressure amplitudes, the energy density was not uniformly distributed over the root surface. Although a hypothesized relationship between the energy density and the cementum regeneration was initially postulated, no distinct correlation could be concluded.

Figure 6.10 demonstrates the pressure and the energy contours for the model in which the PDL was excluded. The distribution of pressure amplitudes on the different anatomical faces of the root without the PDL is shown in Figure 6.10a. The pressure amplitudes hardly exceeded the moderate values and decreased by 25% on average when compared with the model including the PDL.

Similar to the case with the PDL, higher pressure amplitudes (the moderate values in this case) were observed only on the middle third and the apical third of the root surface where the potential cementum regeneration was higher. In other words, the coronal third having less difference in cementum thicknesses corresponded to the anatomical root face with the lowest pressure amplitudes. The model without the PDL showed an average pressure reduction of 20% (compared to 14% reduction in the case with the PDL) on the lingual faces compared with the average pressure on the buccal faces. This is qualitatively in agreement with less cementum

regenerated at the lingual side.

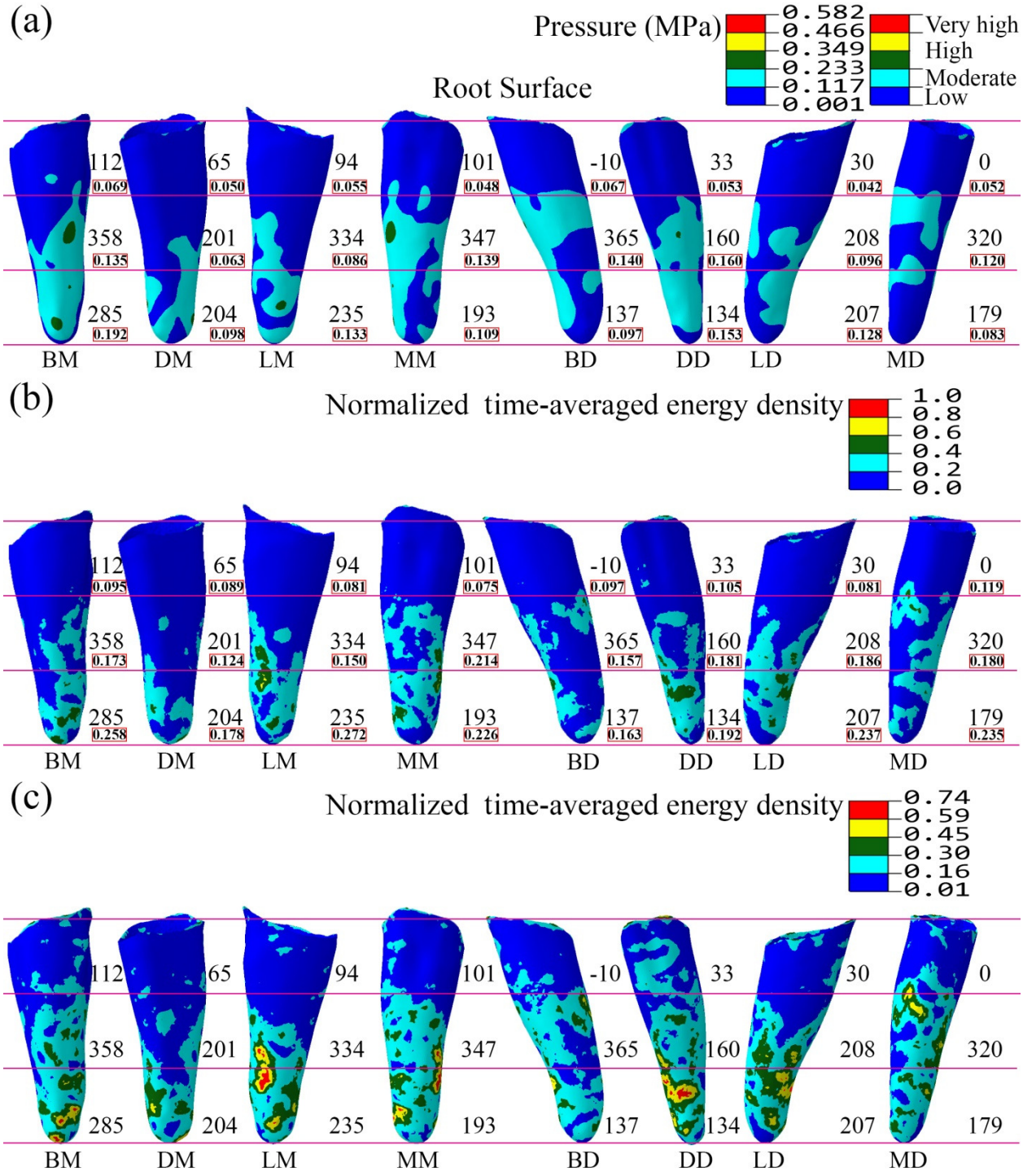

Figure 6.10 (a) The spatial distribution of the pressure amplitudes on the root outer surface simulated via the model without the PDL. (b) Normalized time-averaged energy density distributed over the root surface of the same model (b). (c) A closer look at the distribution of the normalized time-averaged energy density.

The contour plot of the normalized total energy-density distribution on the root surface of the models without the PDL is depicted in Figure 6.10b. The spatially averaged value of the energy density for each anatomical face is enclosed by a rectangle in the figure. For comparison purposes, the average values were also normalized by the maximum value of the total energy-density obtained from the models with the PDL (Figure 6.10c). The model without the PDL predicted less (40% on average) energy density on the root surface compared with the model with the PDL.

According to the results, the coronal third of the root, generally associated with less cementum regeneration, contained less energy density than the middle and apical thirds. However, any correlation between the thickness difference values and the energy density values was not clearly observable.

The distributions of pressure amplitudes on the lingual side of the gingiva for both 3D models are illustrated in Figure 6.11. The spatially averaged value of the pressure amplitudes for both models was 0.0042 MPa when rounded. This value, being 5.6% of the applied ultrasound pressure amplitude, represented the average pressure amplitude that would be recorded by a simulated receiver surface. Receiving much less amplitude of pressure (on the lingual side) than the transmitted one was in agreement with the direct measurements performed by Al-Daghreer et al. (2014) during their experiments.

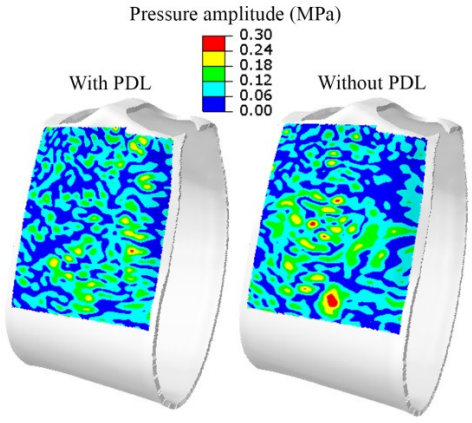

Figure 6.11 The distributions of pressure amplitudes on the simulated receiver surface located on the lingual side of the gingiva.

6.5 Discussion

In this study, simulations of LIPUS propagation in the dentoalveolar structure of a beagle

dog were presented. Simulations were through a simple 1D layered model and two comprehensive 3D models.

The 1D model was able to demonstrate some information about the ultrasound propagation across the buccal-lingual path (Figure 6.8). It predicted the formation of standing waves and the consequent constructive and destructive pressure zones across the medium and between the layers. Interestingly, this model predicted that most of the wave energy could be attenuated due to reflections at the boundaries of the layers (This is called geometrical attenuation due to 1D reflections). Although very simple, the 1D model predicted a general positive qualitative correlation between the ultrasonic parameters and the regenerated cementum thickness across the buccal-lingual path.

The 3D simulations were more informative on the ultrasonic pressure and energy distributions. Due to the complex material properties of the PDL, two finite element models were analysed: namely, the model with the PDL and the model without the PDL.

Comparing the pressure and energy distributions resulting from the two 3D models demonstrates the effect of the PDL on redistributing the ultrasonic parameters on the root surfaces. Excluding the PDL from the model predicted even less pressure amplitudes and energy density compared with the simulation results of the model including the PDL. At first glance, the results of the 3D models seem to contradict those of the 1D model which predicted that the PDL would decrease the ultrasonic parameters. This indicates that the 3D nature of the shape of the PDL, which was ignored in the 1D model, could have a significant role in the propagation of ultrasound around the root.

In order to further explore the effect of the PDL on the ultrasonic parameters, a simplified finite element model of a horizontal rectangular section of the dentoalveolar structure around one of the roots was considered (Figure 6.12a). The root and the PDL sections were approximated as circles. The propagation of the ultrasonic pressure in the two-dimensional (2D) section with and without the PDL (Figure 6.12b and c) was investigated.

Figure 6.13 demonstrates the distributions of the pressure amplitudes and energy density on the root cross-section and its perimeter for the 2D models with and without the PDL. Similar to the 3D simulations, 2D models also predicted higher local and average values of ultrasonic parameters in the model with the PDL (Figure 6.13b). This may be explained by noting the

concave shape of the PDL layer with a particular thickness around the root. The concave PDL layer seems to act as an acoustic lens to create or amplify constructive wave interfaces on the root surface. These results indicate that not only the material properties but also the geometry of the PDL plays a significant role in distributing ultrasonic pressure and energy on the root surface. It may be inferred that if more realistic PDL material properties are utilized in 3D models then the resulting pressure and energy distributions will lie somewhere between the results of the two models in this study.

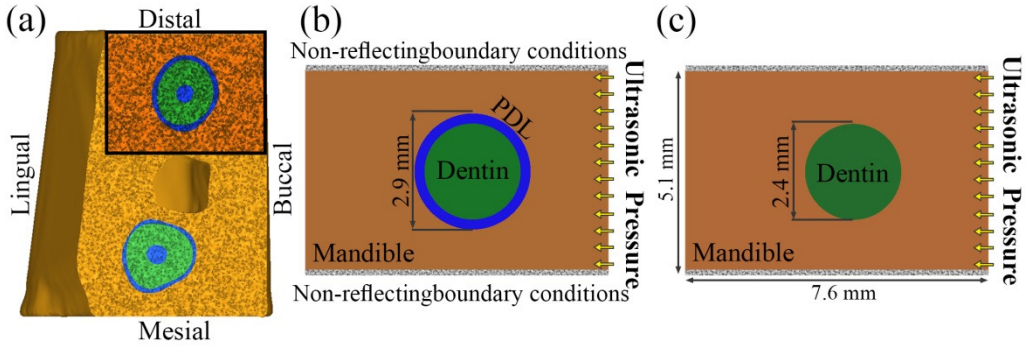

Figure 6.12 (a) Horizontal cross-section of the dentoalveolar structure. (b) The simplified 2D finite element model with the PDL and (c) without the PDL.

We attempted to seek relationships between the simulated distributions of the ultrasonic parameters and the potential cementum regeneration. The 3D simulations (with/without PDL) revealed general qualitative direct relationships. First, non-uniformity was observed in the distributions of the ultrasonic parameters, which is in agreement with the non-uniform experimentally observed regenerated cementum. Second, greater pressure amplitudes (Figure 6.9 and Figure 6.11) and higher energy density (Figure 6.10) in the middle and apical levels predicted by the models were associated with higher amounts of experimentally observed cementum regeneration in those areas.

Quantitative correlations can be demonstrated if the percentage values of the regenerated cementum thicknesses are plotted against the related average pressure amplitudes or average energy density values on the same anatomical face (Figure 6.14). As demonstrated by Figure 6.14, the coefficient of determination (R^2) indicates positive but weak correlations. Interestingly, the correlation in the case of the model without the PDL was higher than that of the model with the PDL. This may suggest that the structural behaviour of the PDL is more towards a solid material (allowing shear waves to pass) than a non-viscous fluid.

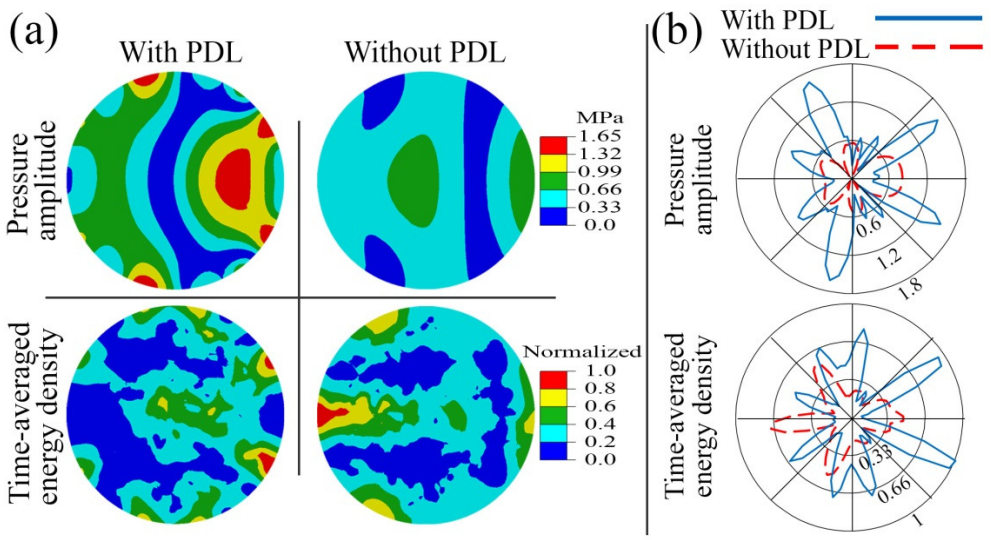

Figure 6.13 The distributions of pressure amplitudes and energy density on (a) the root (dentin) cross-section and (b) its perimeter as the results of the simplified 2D finite element simulations (with/without the PDL).

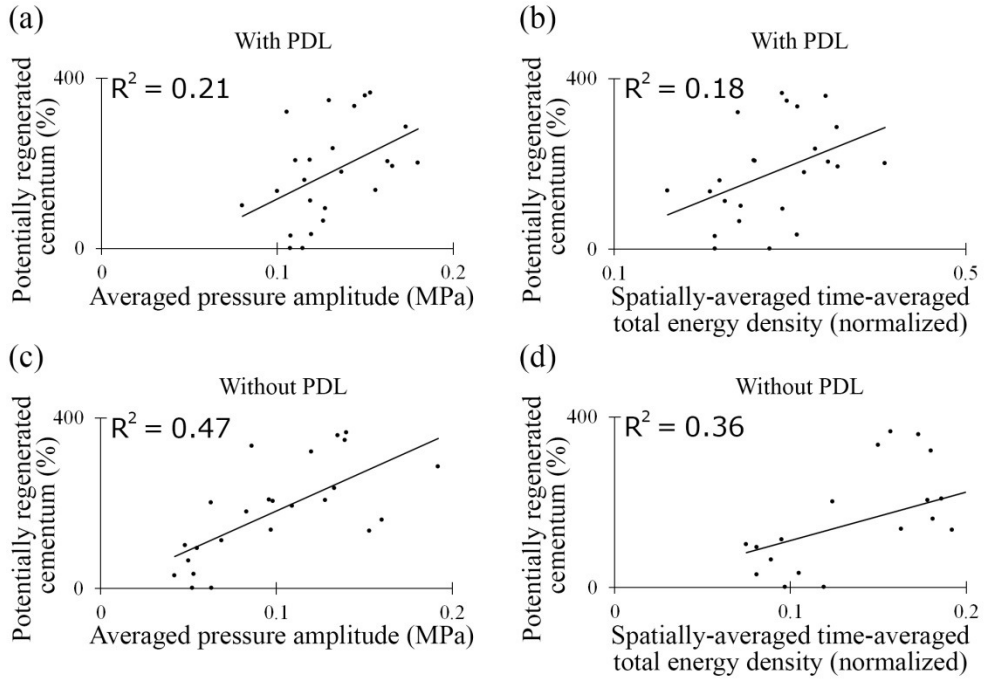

Figure 6.14 Percentage values of potentially regenerated cementum on the LIPUS-treated root against the average pressure amplitudes and spatially-averaged time-averaged total energy density values on the defined anatomical faces; and linearly fitted lines to the values for (a) and (b) the model with the PDL, and (c) and (d) the model without the PDL.

The investigation for corelations in this study is influenced by a number of limitations: (1) It was assumed that possitive difference in cementum thicknesses indicated cementum

regeneration. However, part of the positive difference may have been initially due to the anatomical differences between the dogs' left and right premolars. Since the initial cementum thickness was unknown, the positive difference in the cementum thickness could be only regarded as a potential regeneration. (2) The cementum thicknesses were only measured and available at a few locations on the root (12 locations for each root). (3) Measuring the cementum thicknesses circumferentially at a few locations on each anatomical face and extending the results to the entire anatomical face must have influenced the correlations. (4) Furthermore, it should be noted that the regenerated cementum thicknesses used in this study were the result of a 4-week animal study of LIPUS exposure. The optimum period of exposure to LIPUS for cementum regeneration is not known and therefore the duration of the experiment may also affect the correlations.

In addition to the discussed limitations regarding the experimental data and the histological measurements, the following simulation limitations may also affect the correlations:

Applied ultrasonic pressure. In the experimental case, the pressure did not have a uniform distribution, especially close to the transducer edges. The finite dimensions of the transducer, the coupling gel between the transducer and gingiva, the force exerted by the operator's hand on the transducer held against the dog's gingiva, and the surface geometry of the gingiva can potentially affect the uniformity and amplitude of the pressure. Nevertheless, an approximate uniform pressure amplitude was estimated for the simulations.

Geometrical reconstruction. The geometrical reconstruction did not include minor cavities inside the mandible, cementum, and cortical to cancellous bone transition. These details could have a small effect on the distributions of the ultrasonic parameters; however, they are not expected to globally affect the qualitative outcome of the simulations.

Anisotropic properties of the materials. The cortical bone of the mandible and dentin are generally anisotropic and their mechanical properties depend on the location. However, the materials were assumed isotropic. The effect of anisotropy on the results should be investigated in a separate study.

Energy absorption properties of the materials. The energy absorption properties of the materials were ignored for simplicity. Therefore, overestimation in pressure and energy values is expected. Due to the complexity of the ultrasound propagation inside the dentoalveolar structure,

it is not straight forward to calculate the overestimation. However, a rough approximation based on non-reflecting plane-wave propagation can be obtained for the overestimation. Knowing that the attenuation coefficients of human cortical bone are 39 $\mathrm{db.cm^{-1}}$ and 130 $\mathrm{db.cm^{-1}}$ for a 5 and 10 MHz ultrasound respectively [40] and assuming a power law frequency dependence for the coefficients [23], we can infer the following equation expressing the frequency-dependent attenuation coefficient:

$$\alpha = 2.3f^{1.75} \qquad (6.5)$$

in which f is the ultrasound frequency in MHz. Therefore, the attenuation coefficient for the ultrasound in this study ($f = 1.5$ MHz) can be calculated as $\alpha = 4.7\ \mathrm{db.cm^{-1}}$. If the attenuation in the soft tissues is ignored and the maximum thickness of the cortical bone on the buccal side is assumed to be 0.5 cm, the fraction of the applied pressure amplitude (P_o) on the buccal surface of the root will be[4]:

$$\frac{P}{P_o} = 10^{-(\frac{4.7\times0.5}{20})} \times 100 = 76\% \qquad (6.6)$$

This indicates that the simulated ultrasonic pressure on the buccal side was overestimated by 24%. The same procedure can be repeated to find the percentage of the pressure of the received signal on the lingual surface of the root if the same attenuation coefficient is assumed for the 0.3 mm-dentin (Figure 6.2). Consequently, the ultrasonic pressure amplitude on the lingual face of the root (if attenuation is only due to material absorption) is 65% of the applied pressure amplitude, which indicates 35% of overestimation.

Non-reflecting boundary conditions. Limitations in the available μCT image data and hardware facilities led to a partial modeling of the dentoalveolar structure along with using non-reflecting boundary conditions. The utilized methods for implementing the non-reflecting boundary conditions were based on the propagation of plane waves (unidirectional waves) being orthogonally or tangentially incident on a plane surface (Abaqus theory manual, Dassault Systèmes, 2012; Wolf, 1985). These formulations were used in 3D propagation of non-plane waves occurring in our simulations. While this approximation is not perfect, it is the best practical method to be implemented using the finite element software.

[4] Based on $\frac{\alpha}{\text{distance}} = -20\log(\frac{P}{P_o})$

Nevertheless, the existence of other mechanical mechanisms stimulating the cementum regeneration should not be ignored. Especially considering the radiation pressure of LIPUS, some studies suggested that biological responses arise due to the stimulations by low-frequency alternating ultrasonic radiation pressure rather than the primary pressure alteration of ultrasound [16,41]. Therefore, one might argue that simulation of linear propagation of ultrasound cannot comprehensively explain the ultrasonic pressure-cementum regeneration correlation. However, we were able to demonstrate that the existence of positive correlations between ultrasonic parameters and cementum regeneration in a macro-scale level under the assumption of linear wave propagation regime is possible. We also believe that better correlations are conceivable if more histological data on cementum potential regeneration (or true regenerated cementum thicknesses) become available.

The clinical perspective of this study is that the positive relation between the ultrasonic parameters (especially pressure) and the cementum regeneration supports the clinical results of the effect of LIPUS on cementum regeneration. Furthermore, it was demonstrated that due to inter-layer reflections and scattering, the ultrasonic pressure and energy reduced as the waves traveled from the buccal to the lingual side. From a clinical perspective, this suggests that in order to provide a potent stimulatory effect on the lingual face of a tooth root, another LIPUS transducer may be needed to be applied from the lingual side. Further studies and verification of this hypothesis may be needed.

The verification of the simulation results using ultrasound measuring instruments in the modelled experiment is a difficult task. However, the spatially averaged pressure amplitudes recorded by the simulated receiver surface (Figure 6.11) can be regarded as a means of necessary verification but not sufficient. Our models showed that the average ultrasonic pressure amplitude received on the lingual side was 5.6% of the initial ultrasonic pressure amplitude (applied on the buccal side). This small value, being in agreement with the direct measurements, indicates that most of the wave energy was attenuated due to geometrical attenuation because of ultrasonic beam spreading and wave scattering at the material boundaries of the dentoalveolar components.

6.6 Conclusion

The propagation of therapeutic ultrasound in dentoalveolar structure of a beagle dog was simulated in this study. To our knowledge, our simulations and the 3D finite element modeling

approach for simulating the high frequency ultrasound have not been implemented before. Due to the biological and physical complexities of the problem, some major simplifications were made to allow the problem to conform to the continuum mechanics framework. The simplifications were discussed in detail in order to clarify the simulation limitations. Despite the simplifications, great efforts and huge computational power (software and hardware) were engaged in the finite element modeling and the analyses.

The simulations were capable of revealing some aspects of the ultrasonic pressure and energy density distributions on the root and PDL surfaces. The observed non-uniformity of the distributions may indicate one of the reasons for the non-uniform cementum regeneration. Additionally, we demonstrated that part of the stimulatory effect of ultrasound on cementum regeneration could potentially be correlated with the linear acoustic pressure and energy density fields.

Besides the presented results, this study can be regarded as a motivation towards the macro-scale investigation of the effect of ultrasonic parameters on cementum regeneration. Suggested future studies based on simulation of ultrasonic waves in dentoalveolar structures are the application of two transducers concurrently mounted on the buccal and lingual sides, and utilizing human dentoalveolar structure.

6.7 References

[1] K. Lopatiene, A. Dumbravaite, Risk factors of root resorption after orthodontic treatment., Stomatol. Balt. Dent. Maxillofac. 10 (2008) 89–95.

[2] A.D. King, T. Turk, C. Colak, S. Elekdag-Turk, A.S. Jones, P. Petocz, et al., Physical properties of root cementum: part 21. Extent of root resorption after the application of 2.5° and 15° tips for 4 weeks: a microcomputed tomography study., Am. J. Orthod. Dentofacial Orthop. 140 (2011) e299–305.

[3] S. Al-Daghreer, M. Doschak, A.J. Sloan, P.W. Major, G. Heo, C. Scurtescu, et al., Effect of low-intensity pulsed ultrasound on orthodontically induced root resorption in beagle dogs., Ultrasound Med. Biol. 40 (2014) 1187–96.

[4] T. Inubushi, E. Tanaka, E.B. Rego, J. Ohtani, A. Kawazoe, K. Tanne, et al., Ultrasound stimulation attenuates resorption of tooth root induced by experimental force application., Bone. 53 (2013) 497–506.

[5] J. Kurol, P. Owman-moll, D. Lundgren, Time-related root resorption after application of a controlled continuous orthodontic force, Am. Assoc. Orthod. 96 (1996) 303–310.

[6] L. Linge, B.O. Linge, Patient characteristics and treatment variables associated with apical root resorption during orthodontic treatment, Am. J. Orthod. Dentofac. Orthop. 99 (1991) 35–43.

[7] E. Levander, O. Malmgren, Evaluation of the risk of root resorption during orthodontic treatment: A study of upper incisors., Eur. J. Orthod. 10 (1988) 30–38.

[8] N. Bartley, T. Türk, C. Colak, S. Elekdağ-Türk, A. Jones, P. Petocz, et al., Physical properties of root cementum: Part 17. Root resorption after the application of 2.5° and 15° of buccal root torque for 4 weeks: a microcomputed tomography study., Am. J. Orthod. Dentofacial Orthop. 139 (2011) e353–360.

[9] T. El-Bialy, I. El-Shamy, T.M. Graber, Repair of orthodontically induced root resorption by ultrasound in humans, Am. J. Orthod. Dentofac. Orthop. 126 (2004) 186–193.

[10] A. Paetyangkul, T. Türk, S. Elekdağ-Türk, A.S. Jones, P. Petocz, L.L. Cheng, et al., Physical properties of root cementum: Part 16. Comparisons of root resorption and resorption craters after the application of light and heavy continuous and controlled orthodontic forces for 4, 8, and 12 weeks., Am. J. Orthod. Dentofacial Orthop. 139 (2011) e279–284.

[11] V.C.J. Montenegro, A. Jones, P. Petocz, C. Gonzales, M.A. Darendeliler, Physical properties of root cementum: Part 22. Root resorption after the application of light and heavy extrusive orthodontic forces: a microcomputed tomography study., Am. J. Orthod. Dentofacial Orthop. 141 (2012) e1–9.

[12] D.A. Dalla-Bona, E. Tanaka, T. Inubushi, H. Oka, A. Ohta, H. Okada, et al., Cementoblast response to low- and high-intensity ultrasound., Arch. Oral Biol. 53 (2008) 318–323.

[13] D.A. Dalla-Bona, E. Tanaka, H. Oka, E. Yamano, N. Kawai, M. Miyauchi, et al., Effects of ultrasound on cementoblast metabolism in vitro., Ultrasound Med. Biol. 32 (2006) 943–948.

[14] J. Harle, V. Salih, F. Mayia, J.C. Knowles, I. Olsen, Effects of ultrasound on the growth and function of bone and periodontal ligament cells in vitro., Ultrasound Med. Biol. 27 (2001) 579–586.

[15] E.B. Rego, T. Takata, K. Tanne, E. Tanaka, Current Status of Low Intensity Pulsed Ultrasound for Dental Purposes, Open Dent. J. 6 (2012) 220–225.

[16] F. Padilla, R. Puts, L. Vico, K. Raum, Stimulation of bone repair with ultrasound: a review of the possible mechanic effects., Ultrasonics. 54 (2014) 1125–1145.

[17] V.F. Humphrey, Ultrasound and matter-physical interactions., Prog. Biophys. Mol. Biol. 93 (2007) 195–211.

[18] L.R. Duarte, The stimulation of bone growth by ultrasound., Arch. Orthop. Trauma. Surg. 101 (1983) 153–159.

[19] Y. Khan, C.T. Laurencin, Fracture repair with ultrasound: clinical and cell-based evaluation., J. Bone Jt. Surgery. 90 Suppl 1 (2008) 138–144.

[20] C.L. Romano, D. Romano, N. Logoluso, Low-intensity pulsed ultrasound for the treatment of bone delayed union or nonunion: a review., Ultrasound Med. Biol. 35 (2009) 529–536.

[21] J. Wolff, The law of bone remodelling., 1st ed., Springer-Verlag, 1986.

[22] P. Hoskins, K. Martin, Abigail Thrush, Diagnostic Ultrasound: Physics and Equipment, 2nd ed., cambridge university press, New York, 2010.

[23] R.S.C. Cobbold, Foundations of Biomedical Ultrasound, Oxford University Press, 2007.

[24] K. Tajima, K.-K. Chen, N. Takahashi, N. Noda, Y. Nagamatsu, H. Kakigawa, Three-dimensional finite element modeling from CT images of tooth and its validation., Dent. Mater. J. 28 (2009) 219–26.

[25] S.P. Ho, B. Yu, W. Yun, G.W. Marshall, M.I. Ryder, S.J. Marshall, Structure, chemical composition and mechanical properties of human and rat cementum and its interface with root dentin., Acta Biomater. 5 (2009) 707–18.

[26] A.M. Shaw, D. Student, G.T. Sameshima, L. Angeles, H. V Vu, L. Beach, Mechanical stress generated by orthodontic forces on apical root cementum : a finite element model, Orthod Craniofacial Res. 7 (2004) 98–107.

[27] R. De Santis, L. Ambrosio, L. Nicolais, Mechanical Properties of Tooth Structures, in: Integr. Biomater. Sci., 2002: pp. 589–599.

[28] S. Benazzi, O. Kullmer, I.R. Grosse, G.W. Weber, Using occlusal wear information and finite element analysis to investigate stress distributions in human molars., J. Anat. 219 (2011) 1–14.

[29] S.P. Dodd, J.L. Cunningham, a W. Miles, S. Gheduzzi, V.F. Humphrey, Ultrasonic propagation in cortical bone mimics., Phys. Med. Biol. 51 (2006) 4635–4647.

[30] S.R. Ghorayeb, T. Xue, W. Lord, A finite element study of ultrasonic wave propagation in a tooth phantom., J. Dent. Res. 77 (1998) 39–49.

[31] L.H. He, N. Fujisawa, M. V Swain, Elastic modulus and stress-strain response of human enamel by nano-indentation., Biomaterials. 27 (2006) 4388–4398.

[32] S.M. Weidmann, J.A. Weatherell, M.H. Stella, Variations of enamel density in sections of human teeth., Arch. Oral Biol. 12 (1967) 85–97.

[33] G. Milewski, Numerical and experimental analysis of effort of human tooth hard tissues in terms of proper occlusal loadings., Acta Bioeng. Biomech. 7 (2005).

[34] M.O. Culjat, D. Goldenberg, P. Tewari, R.S. Singh, A review of tissue substitutes for ultrasound imaging., Ultrasound Med. Biol. 36 (2010) 861–873.

[35] S.R. Ghorayeb, E. Maione, V. La Magna, Modeling of ultrasonic wave propagation in teeth using PSpice: a comparison with finite element models., IEEE Trans. Ultrason. Ferroelectr. Freq. Control. 48 (2001) 1124–1131.

[36] J.P. Wolf, Dynamic Soil-Structure Interaction, Prentice Hall, 1985.

[37] J.S. Rees, P.H. Jacobsen, Elastic modulus of the periodontal ligament., Biomaterials. 18 (1997) 995–999.

[38] R. Van Vossen, J.O.A. Robertsson, C.H. Chapman, Finite difference modeling of wave propagation in a fluid–solid configuration, Geophysics. 67 (2002) 618–624.

[39] Dassault Systèmes, Abaqus theory manual, in: Dassault Systèmes, 2012.

[40] R. Lakes, H. sub Yoon, J.L. Katz, Ultrasonic wave propagation and attenuation in wet bone., Biomed. Eng. (NY). 8 (1986) 143–148.

[41] H.M. Argadine, M.E. Bolander, J.F. Greenleaf, Stimulation of proteoglycan synthesis with low-intensity 1 kHz vibration., 2006 IEEE Ultrason. Symp. (2006) 849–851.

Chapter 7

Simplified Equivalent Material Model for Cancellous Bone

7.1 Abstract

The energy of ultrasonic waves propagating in cancellous bone mainly attenuates due to wave scattering by the fluid-saturated complex microstructures (trabeculae) composing the bone. In order to consider the ultrasonic attenuation in a finite element simulation, the geometry of the microstructure and the saturating fluid should be explicitly modeled. However, this is only practical when relatively small volume of cancellous bone (less than $1cm^3$) is present in a finite element simulation. To simulate the ultrasonic attenuation in a large volume of cancellous bone, equivalent material models are proposed in this work. The equivalent material models represent isotropic and homogeneous materials with viscoelastic properties. In this study, it is demonstrated that an equivalent material model can imitate ultrasonic attenuation and velocity in cancellous bone if the density and viscoelastic parameters of an equivalent material model are properly chosen.

7.2 Introduction

In the previous chapter, the propagation of continuous ultrasonic waves in the dentoalveolar structure of a beagle dog was simulated to elucidate the induced ultrasonic pressure on tooth root area. As a future work, it was proposed to simulate the ultrasound propagation in human dentoalveolar structures. In this regard, the same procedure and simulation method can be utilized to simulate ultrasound propagation in a human dentoalveolar structure. However, human mandible is composed of cancellous bone (Figure 7.1) in contrary to dog mandible being made of highly compact cortical bone. Therefore, it is significant to consider ultrasonic attenuation that occurs in cancellous bone due to wave scattering [1,2]. Since scattering in cancellous bone is due to the fluid-saturated microstructures (trabeculae) composing the bone, any computer simulation of ultrasound propagation in the bone should include the complex geometry of the microstructures.

As demonstrated in chapters 4 and 5, creating finite element models of fluid-saturated trabecular structures deals with difficulties for reconstructing the detailed geometry of the inter-connected trabeculae and the saturating fluid. These difficulties make it impractical to model the human mandibular bone as cancellous bone. On the other hand, failing to include the significant ultrasonic attenuation due to wave scattering in cancellous bone may lead to significant overestimation of the induced ultrasonic pressure on the surface of a tooth root. To alleviate this

problem, an equivalent material model (EMM) may be proposed to imitate ultrasonic attenuation inside cancellous bone.

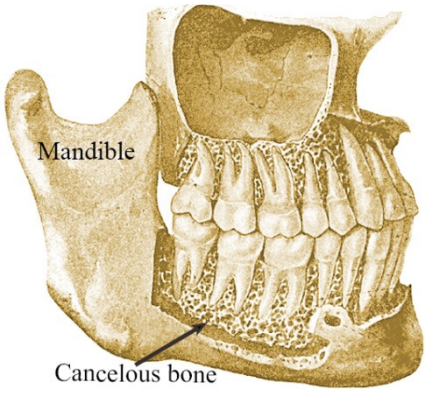

Figure 7.1Human mandible [3].

In this chapter, it is hypothesized that a homogeneous and isotropic material with viscoelastic properties can be proposed as an EMM (Figure 7.2). Considered as a homogeneous material, the attenuation of ultrasonic waves passing through the EMM is not due to scattering; however, the viscous property of the material causes energy dissipation and consequently ultrasonic attenuation. The aim of this chapter is to determine the elastic and viscous properties of the EMM such that it can imitate the attenuation and velocity in cancellous bone. To this end, Kelvin-Voigt (Voigt) and standard linear solid (SLS) viscoelastic material models are considered to expresses the mechanical properties of the EMM. Then, the mechanical and physical parameters of the EMM are determined using the attenuation and velocity data of a cancellous bone sample.

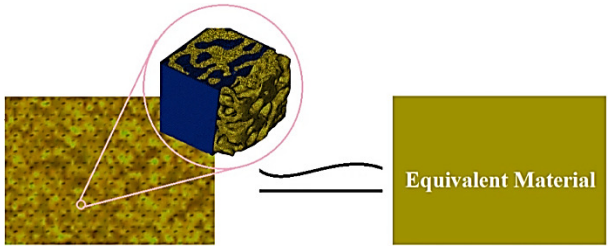

Figure 7.2 Equivalent material model based on a homogeneous and isotropic material with viscoelastic properties.

7.3 Materials and methods

The main roles of an EMM for cancellous bone are imitating the attenuation and velocity in cancellous bone. In this work, the attenuation mechanism in an EMM originates from the

viscous properties of the EMM. In the following sections, Voigt and standard linear solid viscoelastic models are considered for the constitutive law (stress-strain relation) of the EMM. By formulating the simple case of one-dimensional (1D) wave propagation in the EMM and considering the attenuation and velocity data of cancellous bone at particular frequencies, the viscoelastic parameters of the models are determined. The efficiency of the EMM for predicting the velocity and attenuation in cancellous bone is then evaluated at different frequencies.

7.3.1 One-dimensional linear wave propagation in a Voigt solid

The mechanical behaviour of a linear viscoelastic solid can be modeled using Kelvin-Voigt (Voigt) model. The Voigt model expresses the mechanical stress in a material as a linear function of strain and strain rate [4]:

$$\sigma = \mathrm{E}\varepsilon + \eta\dot{\varepsilon} \qquad (7.1)$$

in which E and η are the Young's modulus and viscosity of the material model. The stress, strain and strain rate are denoted by σ, ε and $\dot{\varepsilon} = \frac{\partial \varepsilon}{\partial t}$ respectively. The rheological representation for the Voigt model is a linear spring and dashpot in series leading to a single degree of freedom (DOF) combination (Figure 7.3).

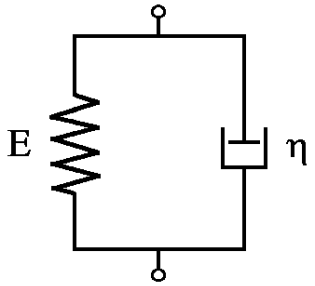

Figure 7.3 Kelvin-Voigt (Voigt) model.

To investigate one-dimensional propagation of ultrasound in a Voigt solid, a 1D solid rod is considered (Figure 7.4). If the displacement field of the rod is denoted by $u = u(x,t)$ and the strains are assumed to be infinitesimal, writing the equation of motion (Newton's second law) based on Voigt model stress-strain relation (7.1) leads to:

$$\mathrm{E}\frac{\partial^2 u}{\partial x^2} + \eta\frac{\partial}{\partial t}\frac{\partial^2 u}{\partial x^2} - \rho_o\frac{\partial^2 u}{\partial t^2} = 0 \qquad (7.2)$$

Figure 7.4 One-dimensional rod.

By assuming steady state harmonic wave propagation in the medium (Section 2.3.3), Eq. 7.2 can be written in the frequency domain:

$$\frac{\partial^2 \underline{u}}{\partial x^2} + \frac{\rho_o \omega^2}{\mathrm{E} + i\omega\eta}\underline{u} = 0 \qquad (7.3)$$

in which $\underline{u}(x) \in \mathbb{C}$ is the displacement phasor. Using the expression for the wave velocity in a linear elastic solid $\mathrm{c_o} = \sqrt{\frac{\mathrm{E}}{\rho_o}}$, and the wave number $\mathrm{k} = \frac{\omega}{\mathrm{c_o}}$ (Fig. 2.22) leads to:

$$\frac{\partial^2 \underline{u}}{\partial x^2} + \underline{\mathrm{k}}\underline{u} = 0 \qquad (7.4)$$

where $\underline{\mathrm{k}} \coloneqq \frac{\mathrm{k}^2}{1+i\omega\mathrm{H}}$ and $\mathrm{H} \coloneqq \frac{\eta}{\mathrm{E}}$.

The general solution of the above differential equation is in the form of $\underline{u}(x) = \underline{\mathrm{A}}e^{\underline{\mathrm{B}}x}$, such that $\underline{\mathrm{A}}, \underline{\mathrm{B}} \in \mathbb{C}$. Therefore, substituting the solution into Eq. 7.4 results in $\underline{\mathrm{B}}^2 = -\underline{\mathrm{k}}$. Expressing the complex variable $\underline{\mathrm{B}}$ in the form of $\underline{\mathrm{B}} = a + bi$ and considering $\underline{\mathrm{B}}^2 = -\underline{\mathrm{k}}$ yield the following nonlinear system of equation:

$$\begin{cases} a^2 - b^2 = -\mathrm{R} \\ 2ab = -\mathrm{I} \end{cases} \qquad (7.5)$$

such that $\mathrm{R} = \frac{\mathrm{k}^2}{1+\omega^2\mathrm{H}^2}$ and $\mathrm{I} = -\frac{\mathrm{k}^2\omega\mathrm{H}}{1+\omega^2\mathrm{H}^2}$ are the real and imaginary parts of $\underline{\mathrm{k}}$ respectively.

Solving the above system of equations leads to:

$$a = \frac{-\mathrm{I}}{2b} \qquad (7.6a)$$

$$b = \pm\sqrt{\frac{\mathrm{R} + \sqrt{\mathrm{R}^2 + \mathrm{I}^2}}{2}} \qquad (7.6b)$$

which becomes:

$$a = \pm\frac{1}{2G}.\frac{\mathrm{k}^2\omega\mathrm{H}}{1+\omega^2\mathrm{H}^2} \tag{7.7a}$$

$$b = \pm\mathrm{G} \tag{7.7b}$$

such that:

$$\mathrm{G} = \sqrt{\frac{\mathrm{R}+\sqrt{\mathrm{R}^2+\mathrm{I}^2}}{2}} = \sqrt{\frac{\mathrm{k}^2}{2(1+\omega^2\mathrm{H}^2)}.[1+(1+\omega^2\mathrm{H}^2)^{\frac{1}{2}}]} \tag{7.8}$$

Thus:

$$\underline{u}(x) = \underline{\mathrm{A}}e^{(a+bi)x} = \underline{\mathrm{A}}e^{ax}e^{bix} \tag{7.9}$$

in which the term $\underline{\mathrm{A}}e^{bix}$ indicates harmonic waves traveling in either the positive or negative x-axis direction if $b = -\mathrm{G}$ or $b = +\mathrm{G}$ respectively (see 2.46). The traveling velocity, according to Eq. 2.46, can be deduced as $\mathrm{c} = \omega/\mathrm{G}$. According to the attenuation coefficient definition[1] in section 2.5.6, e^{ax} causes the waves attenuate while traveling.

Considering the wave propagation in the positive x-axis direction and substituting Eq. 7.7a and Eq. 7.7b into Eq. 7.9 leads to:

$$\underline{u}(x) = \underline{\mathrm{A}}e^{-\underline{\mathrm{K}}x} = \underline{\mathrm{A}}e^{(-\frac{1}{2G}.\frac{\mathrm{k}^2\omega\mathrm{H}}{1+\omega^2\mathrm{H}^2}-\mathrm{G}i)x} \tag{7.10}$$

Recalling $\mathrm{k} = \frac{\omega}{\mathrm{c_o}}$, $\mathrm{c_o} = \sqrt{\frac{\mathrm{E}}{\rho_o}}$ and $\mathrm{H} \coloneqq \frac{\eta}{\mathrm{E}}$ gives the attenuation coefficient for the EMM as:

$$\alpha_{\mathrm{voigt}} = \frac{\omega^2\rho_o\eta\sqrt{2(\mathrm{E}^2+\omega^2\eta^2)}}{2(\mathrm{E}^2+\omega^2\eta^2)\sqrt{\rho_o(\mathrm{E}+\sqrt{\mathrm{E}^2+\omega^2\eta^2})}} \tag{7.11}$$

Equation 7.11 suggests that the attenuation coefficient (in $\mathrm{Np/unit\,length}$ or $\mathrm{dB/unit\,length}$ if multiplied by 8.6859)[2] of ultrasound propagating in a rod with viscoelastic Voigt material depends on the frequency of the waves (ω) and the viscoelastic properties (E, η) of the material model.

[1] According to the definition in Section 2.5.6, the attenuation coefficient based on the decay of wave amplitude between two locations $\mathrm{x_1}$ and $\mathrm{x_2}$ ($\mathrm{x_1} < \mathrm{x_2}$) in the propagation medium is defined by α as appeared in: $\frac{|\bar{\mathrm{u}}(\mathrm{x_2})|}{|\bar{\mathrm{u}}(\mathrm{x_1})|} = \mathrm{e}^{-\alpha(\mathrm{x_2}-\mathrm{x_1})}$.

[2] If $\frac{|\bar{\mathrm{u}}(\mathrm{x_2})|}{|\bar{\mathrm{u}}(\mathrm{x_1})|} = \mathrm{e}^{-\alpha_{\mathrm{Np}}(\mathrm{x_2}-\mathrm{x_1})}$ is defined for measuring the amplitude attenuation in Neper, and $\alpha_{\mathrm{dB}} = \frac{-20}{\mathrm{x_2}-\mathrm{x_1}}\log_{10}(\frac{|\bar{\mathrm{u}}(\mathrm{x_2})|}{|\bar{\mathrm{u}}(\mathrm{x_1})|})$ is defined to measure the amplitude attenuation in decibel (dB), hence the following can be readily inferred: $\alpha_{\mathrm{dB}} = 8.6859\alpha_{\mathrm{Np}}$.

Furthermore, the wave velocity in the Voigt viscoelastic solid can be deduced as $c_{voigt} = \omega/G$ (according to 2.46). Therefore:

$$c_{voigt} = \sqrt{\frac{2(E^2 + \omega^2\eta^2)}{\rho_o(E + \sqrt{E^2 + \omega^2\eta^2})}} \tag{7.12}$$

which indicates that wave velocity in a viscoelastic material not only depends on the viscoelastic properties, but also depends on the frequency of the waves propagating inside the material. The dependency of wave velocity on the wave frequency is called velocity dispersion [5].

7.3.2 One-dimensional linear wave propagation in a standard linear solid

Standard linear solid (SLS) or Zener model [4] is a model predicting linear viscoelastic behaviour of solids. In contrary to Voigt model, it has three rheological component and two degrees of freedom (Figure 7.5).

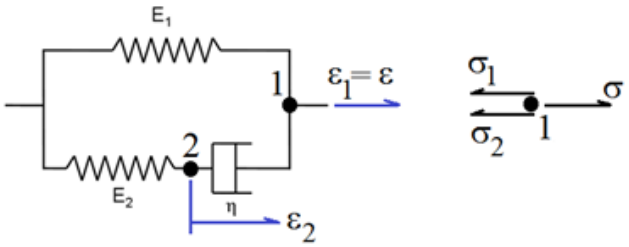

Figure 7.5 Standard linear solid (SLS) and its DOFs.

To find the stress-strain relationship in the SLS, the following equations are used subsequently:

Equilibrium of forces at the first degree of freedom (DOF):

$$\sigma = \sigma_1 + \sigma_2 \tag{7.13}$$

For the spring component (E_1):

$$\sigma_1 = E_1\varepsilon_1 \tag{7.14}$$

At the second DOF:

$$\sigma_2 = E_2\varepsilon_2 \text{ and } \sigma_2 = (\dot{\varepsilon} - \dot{\varepsilon}_2)\eta \rightarrow \sigma_2 = (\dot{\varepsilon} - \frac{\dot{\sigma}_2}{E_2})\eta \tag{7.15}$$

such that $\dot{\sigma}_2 = \frac{\partial \sigma_2}{\partial t}$.

Eq. 7.13 and Eq. 7.14 lead to:

$$\dot{\sigma} = \dot{\sigma}_1 + \dot{\sigma}_2 \rightarrow \dot{\sigma}_2 = \dot{\sigma} - \mathrm{E}_1\dot{\varepsilon}_1 \tag{7.16}$$

Combining the above equations leads to the stress-strain relation in the SLS:

$$\sigma = \mathrm{E}_1\varepsilon + \frac{\eta(\mathrm{E}_1 + \mathrm{E}_2)}{\mathrm{E}_2}\dot{\varepsilon} - \frac{\eta}{\mathrm{E}_2}\dot{\sigma} \tag{7.17}$$

Following the same procedure and assumption of harmonic wave propagation as considered for the Voigt model and taking the time derivative of equation of motion i.e. $\frac{\partial \dot{\sigma}}{\partial x} = \rho_o \frac{\partial^3 u}{\partial t^3}$, leads to the governing equation of 1D wave propagating in a SLS:

$$\mathrm{E}_1 \frac{\partial^2 u}{\partial x^2} + \frac{\eta(\mathrm{E}_1 + \mathrm{E}_2)}{\mathrm{E}_2}\frac{\partial}{\partial t}\frac{\partial^2 u}{\partial x^2} - \rho_o\left(\frac{\eta}{\mathrm{E}_2}\frac{\partial^3 u}{\partial t^3} + \frac{\partial^2 u}{\partial t^2}\right) = 0 \tag{7.18}$$

The above equation can be written in the form of Eq. 7.4 if harmonic wave propagation is considered. In this case:

$$\underline{\mathrm{k}} = \mathrm{R} + \mathrm{I}i \tag{7.19}$$

such that:

$$\mathrm{R} = \frac{\rho_o\omega^2(\eta^2\omega^2(\mathrm{E}_2 + \mathrm{E}_1) + \mathrm{E}_1\mathrm{E}_2^2)}{\mathrm{E}_1^2\mathrm{E}_2^2 + \eta^2\omega^2(\mathrm{E}_1 + \mathrm{E}_2)^2} \tag{7.20a}$$

$$\mathrm{I} = \frac{-\rho_o\eta\omega^3\mathrm{E}_2^2}{\mathrm{E}_1^2\mathrm{E}_2^2 + \eta^2\omega^2(\mathrm{E}_1 + \mathrm{E}_2)^2} \tag{7.19b}$$

Following the same steps according to Eq. 7.5 and Eq. 7.6 leads to obtaining the wave attenuation and velocity as:

$$\alpha_{\mathrm{SLS}} = \tag{7.21}$$

$$\frac{\rho_o\eta\omega\mathrm{E}_2^2}{2(\mathrm{E}_1^2\mathrm{E}_2^2 + \eta^2\omega^2(\mathrm{E}_1 + \mathrm{E}_2)^2)}\sqrt{\frac{2(\mathrm{E}_1^2\mathrm{E}_2^2 + \eta^2\omega^2(\mathrm{E}_1 + \mathrm{E}_2)^2)}{\rho_o((\eta^2\omega^2(\mathrm{E}_2 + \mathrm{E}_1) + \mathrm{E}_1\mathrm{E}_2^2) + \sqrt{(\eta^2\omega^2(\mathrm{E}_1 + \mathrm{E}_2)^2 + \mathrm{E}_1^2\mathrm{E}_2^2)(\eta^2\omega^2 + \mathrm{E}_2^2)})}}$$

Furthermore, the wave velocity is (see Eq. 7.8 and 7.67.9):

$$\mathrm{c}_{\mathrm{SLS}} = \sqrt{\frac{2(\mathrm{E}_1^2\mathrm{E}_2^2 + \eta^2\omega^2(\mathrm{E}_1 + \mathrm{E}_2)^2)}{\rho_o(\eta^2\omega^2(\mathrm{E}_2 + \mathrm{E}_1) + \mathrm{E}_1\mathrm{E}_2^2) + \rho_o\sqrt{(\eta^2\omega^2(\mathrm{E}_1 + \mathrm{E}_2)^2 + \mathrm{E}_1^2\mathrm{E}_2^2)(\eta^2\omega^2 + \mathrm{E}_2^2)}}} \tag{7.22}$$

7.3.3 Obtaining the parameters of Voigt and SLS solids corresponding cancellous bone

For the EMM using either of the viscoelastic models the density and viscoelastic parameters should be determined so that the behaviour of these models simulate a particular behaviour of the cancellous bone. The density of the EMM must be a combination of the density of the materials consisting of cancellous bone i.e. solid bone and saturating fluid. Therefore, the following combination can be assumed for the density of the EMM:

$$\rho_o = \rho_{\mathrm{eq}} \coloneqq \left(\frac{\mathrm{BV}}{\mathrm{TV}}\right)\rho_{\mathrm{solid}} + \left(1 - \frac{\mathrm{BV}}{\mathrm{TV}}\right)\rho_{\mathrm{fluid}} \qquad (7.23)$$

such that $\frac{\mathrm{BV}}{\mathrm{TV}}$ is the ratio of bone volume to total volume of the cancellous bone (bone volume fraction).

To determine the unknown viscoelastic properties (E, η) for the Voigt model, Eq. 7.11 and Eq. 7.12 should be solved as a system of non-linear equations with known values of α and $\mathrm{c}_{\mathrm{voigt}}$. The attenuation and wave velocity parameters are the ultrasonic attenuation and velocity in the cancellous bone. It should be noted that in contrary to ultrasonic attenuation in cancellous bone that is a function of ultrasonic frequency, ultrasonic velocity can be approximately assumed independent of frequency [6]. Therefore, a set of viscoelastic parameters (E, η) would correspond to each frequency. In other words, the EMM based on Voigt model accurately imitates the attenuation and velocity only for a single frequency.

In the case of the EMM based on the SLS viscoelastic model, the model has three parameters (E_1, E_1 and η). Consequently, two known attenuation coefficients at two different frequencies and the ultrasonic velocity in cancellous bone are needed. Using the known ultrasonic parameters in Eq. 7.21 and Eq. 7.22 leads to a system of non-linear equations with three unknowns i.e. the rheological model parameters. The EMM based on the SLS is intended to accurately predict the ultrasonic attenuation in cancellous bone at two different frequencies. Furthermore, it should be noted that the velocity in the EMM based on the SLS (Eq. 7.22) can only be completely satisfied for one of the frequency values.

To evaluate the proposed EMM, the physical properties, the simulated velocity and the simulated attenuation data of one of the cancellous bone samples in chapter 4 are considered. In

that chapter, a broadband signal was used to obtain the wave velocity and attenuation in the cancellous bone sample (section 4.4.1). In this regard, the group velocity of the ultrasonic signal[3] and the frequency-dependent attenuation values depending on the unknown parameters of the EMM are used. Eventually, the coefficients of attenuation and ultrasonic velocity imitated by each EMM are compared with the corresponding values of the cancellous bone sample. This is performed to demonstrate how each EMM can efficiently predict the attenuation in a frequency range.

The selected cancellous bone for this work has bone volume fraction ($\frac{\mathrm{BV}}{\mathrm{TV}}$) of 21% and the ultrasonic group velocity in the sample is 1645 $\mathrm{m/s}$ (see Figure 4.11b); the broadband ultrasonic attenuation in the frequency range of interest is shown in Figure 7.6 (as per Figure 4.12b). To find the viscoelastic parameters for the EMM with Voigt material model, the ultrasonic attenuation at 0.6 MHz is considered (Figure 7.6). The SLS viscoelastic parameters are calculated based on the attenuation values at 0.4 and 0.8 MHz (Figure 7.6).

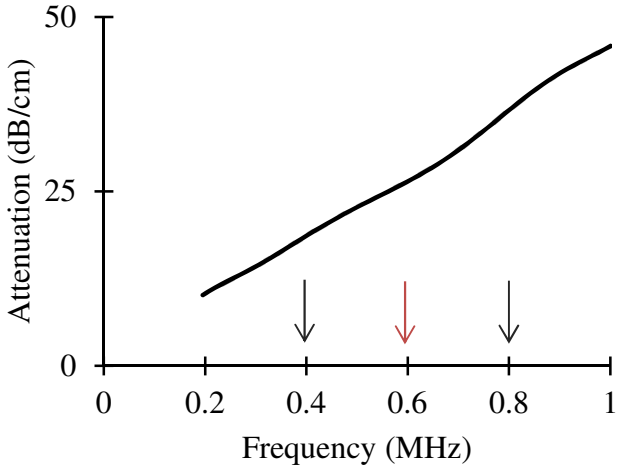

Figure 7.6 Frequency-dependent attenuation of ultrasonic waves propagating in cancellous bone with $\frac{\mathrm{BV}}{\mathrm{TV}} = 21\%$.

7.4 Results and discussion

Considering the ultrasonic attenuation at 0.6 MHz in cancellous bone and solving[4] the nonlinear equations 7.11 and 7.12 leads to the viscoelastic parameters as $\mathrm{E} = 3012\,\mathrm{MPa}$ and

[3] It is closely equal to the propagation distance in the cancellous bone divided by the time of flight of the peak of the transmitted signal (section 4.3.6.2).

[4] Using a trial and error method through writing a piece of code in Matlab.

$\eta = 215 \times 10^{-6}$ MPa. s for the EMM using the Voigt model. Noting the ultrasonic attenuation in cancellous bone at frequencies of 0.4 and 0.8 MHz and solving the equations regarding the EMM with SLS model (equations 7.21 and 7.22) and results in the viscoelastic parameters as $E_1 = 2216$ MPa, $E_2 = 1685$ MPa, and $\eta = 319 \times 10^{-6}$ MPa. s.

The resulting attenuation for each of the two EMM is plotted in Figure 7.7. As it can be observed, the attenuation achieved by each EMM exactly matches the attenuation in cancellous bone at the frequencies used in solving the system of the equations. At other frequencies, the EMM based on the Voigt model predicts the attenuation with a relatively insignificant error between the EMM and the cancellous bone attenuation (less than 10%) in a small frequency range, i.e. 0.55 to 0.65 MHz (Figure 7.7a). On the other hand, the EMM based on SLS model closely predicts the cancellous bone attenuation such that the relative error in the whole frequency range of interest (0.2 to 1.0 MHz) is less than 10% (Figure 7.7b). Comparing the attenuation of the two models indicates that using a viscoelastic model with three rheological parameters can lead to a close curve-fitting between the attenuation obtained by the EMM and that obtained by the cancellous bone. It can be hypothesized that using other viscoelastic models, like the generalized Maxwell-Weichert model [7], having higher number of rheological parts may even be more accurate in predicting ultrasonic attenuation in cancellous bone.

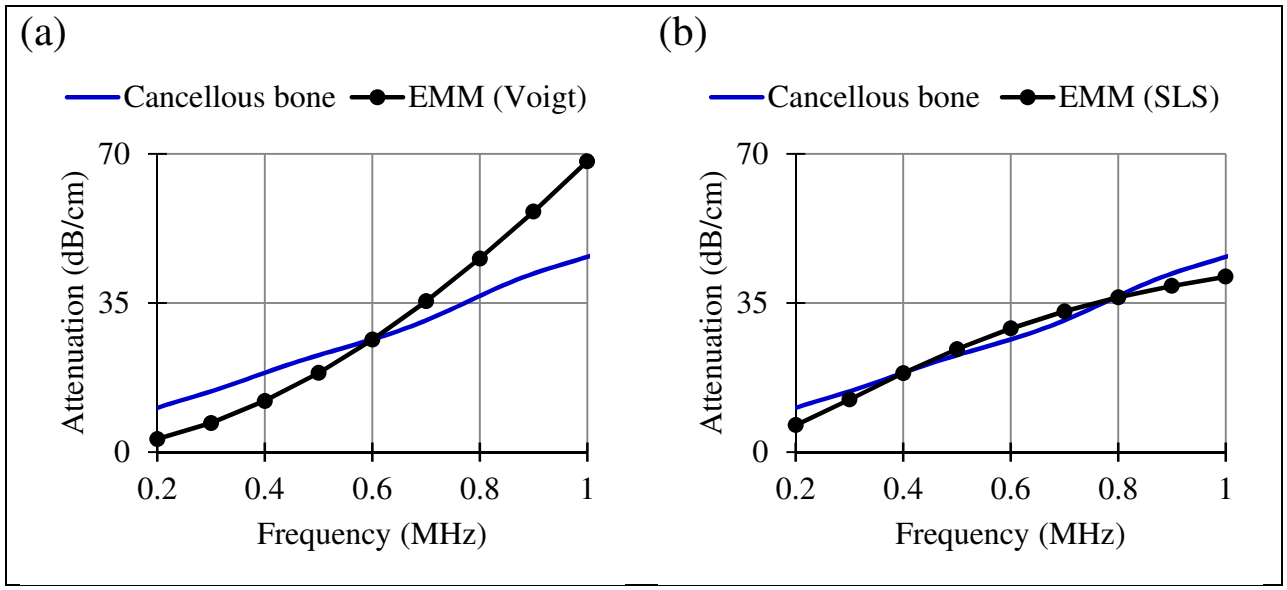

Figure 7.7 Imitated attenuation by each EMM and attenuation in cancellous bone for the frequency range of interest.

As a short note, the generalized Maxwell-Weichert model has the rheological

representation as depicted in Figure 7.9. As it can be observed that the SLS is a simplified instance of this model.

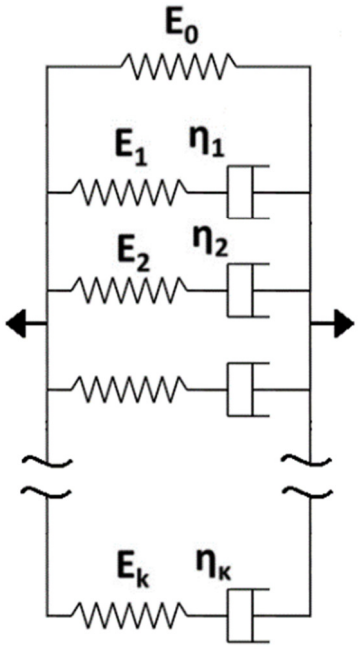

Figure 7.8 The generalized Maxwell-Weichert viscoelastic model [7].

As demonstrated by Eq. 7.12 and Eq. 7.22, the velocity of ultrasound propagating in the EMM is a function of the ultrasonic frequency. Figure 7.9 illustrates the variation of ultrasonic velocity for each EMM and the constant group ultrasonic velocity for the cancellous bone specimen.

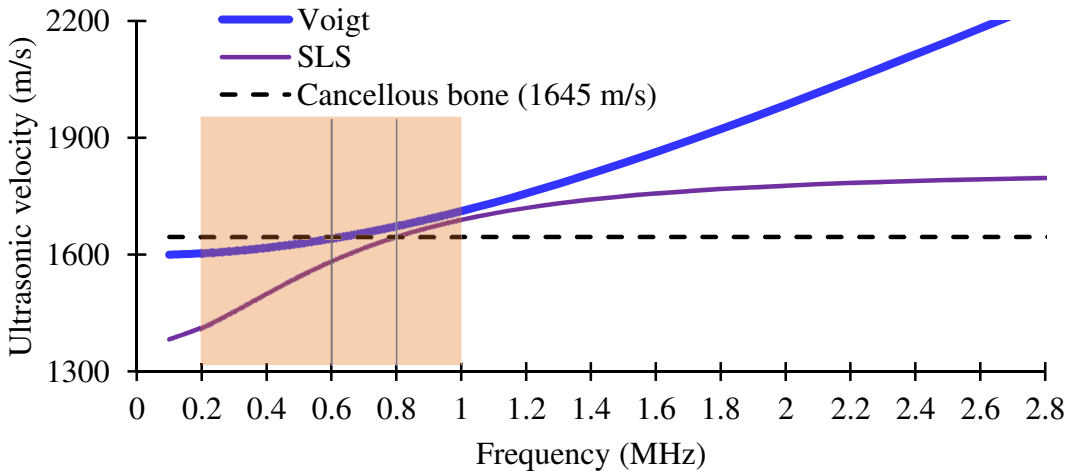

Figure 7.9 Imitated velocity in cancellous bone by the equivalent material models (EMMs) based on Voigt and SLS models.

As shown in Figure 7.9, it is observable that the accuracy of both models in predicting the constant ultrasonic velocity is limited to a small frequency range around 0.6 MHz and 0.8 MHz for the Voigt and SLS models respectively. Notably, both models underestimate the velocity for frequencies less than the frequency of calibration of both models (0.6 MHz and 0.8 MHz for the Voigt and SLS models respectively). For frequencies larger than the calibration frequencies, both models overestimate the velocity. However, the SLS EMM eventually results in almost constant velocity as the frequency increases whereas the Voigt EMM results in increasing velocity values with the frequency. This can be also investigated by noting the limit values of the modeled velocity as the frequency approach infinity (or $\omega \to \infty$) in Eq. 7.12 and Eq. 7.22. Based on experimental observations [6,8,5], the velocity of ultrasound propagating in cancellous bone may slightly (less than 3%) increase with frequency and eventually attains a constant value. Therefore, the qualitative behaviour of the velocity imitated by the SLS EMM is closer to realistic observations.

Exploring the graphs of the velocity predicted by the EMMs implies that using the model with three rheological parameters (i.e. SLS) changes the behaviour of the imitated velocity from an increasing trend to an asymptotic trend. By virtue of this observation, it can be hypothesized that using the general viscoelastic model having more rheological parameters (more than 3 as of the SLS in this work) might lead to closer prediction of velocity by the EMM. Furthermore, it should be noted that using the SLS with three rheological parameters only allows relating the value of the velocity to a single frequency value (frequency values of 0.6 and 0.8 MHz for Voigt and SLS models respectively, as shown in Figure 7.9). However, if a viscoelastic model with more than three rheological parts is used, other velocity values may also be correspondent to other frequencies. Consequently, this can lead to more accurate curve-fitting between the EMM and cancellous bone velocity values.

In this study, only the incorporation of the EMM in 1D wave propagation is investigated. To extend the application of the EMM to 3D wave propagation simulations, the following should be considered. Since the scattering phenomenon is simulated in the EMM models using an energy-absorbing mechanism (viscoelasticity), the total energy of the waves diminishes through a finite element simulation. This is in contrary with the scattering mechanism that merely redistributes the same amount of energy. In this regards, the EMM may lead to overestimation of attenuation; this may notably occur if the outer boundaries of a bounded 3D trabecular medium

are to reflect significant amounts of the scattered wave energy back into the medium.

The EMM that is proposed in this study only accounts for the energy attenuation in 1D pressure or dilatational waves. However, 3D propagation of waves in a bounded medium contains shear or transverse waves that their energy may also be attenuated through some viscoelastic (energy-absorbing) properties. This implies that the shear modulus of an EMM proposed for 3D wave propagation may need some viscoelastic properties. In this regards, the viscoelastic parameters for the shear modulus of the EMM may account for the attenuation of the shear waves inside the solid part of cancellous bone.

7.5 Conclusion and future works

In this work, it is shown that the attenuation due to scattering of ultrasonic waves in cancellous bone can be regarded by means of an EMM having an equivalent density of cancellous bone and deploying a viscoelastic model. In this regard, the proposed EMM may be employed in finite element analysis of ultrasound propagation (single frequency) in human dentoalveolar structures to account for the ultrasonic attenuation due to scattering.

As future works, the following are suggested: 1- Investigating the ultrasonic parameters predicted by an EMM deploying a viscoelastic model with more than three rheological parts and based on the generalized Maxwell-Weichert model. 2- Performing three dimensional finite element analysis of ultrasound propagation in the proposed EMMs and cancellous bone for comparison purposes.

7.6 References

[1] B. Vafaeian, M. El-Rich, T. El-Bialy, S. Adeeb, The finite element method for micro-scale modeling of ultrasound propagation in cancellous bone, Ultrasonics. 54 (2014) 1663–1676.

[2] B. Vafaeian, S. Al-Daghreer, M. El-Rich, S. Adeeb, T. El-Bialy, Simulation of Low-Intensity Ultrasound Propagating in a Beagle Dog Dentoalveolar Structure to Investigate the Relations between Ultrasonic Parameters and Cementum Regeneration, Ultrasound Med. Biol. 41 (2015) 2173–2190.

[3] https://en.wikipedia.org/wiki/Mandibular_canal, (n.d.).

[4] W. Flügge, Viscoelasticity, Springer-Verlag, 1975.

[5] P. Droin, G. Berger, P. Laugier, Velocity dispersion of acoustic waves in cancellous bone., IEEE Trans. Ultrason. Ferroelectr. Freq. Control. 45 (1998) 581–592.

[6] E. Bossy, F. Padilla, F. Peyrin, P. Laugier, Three-dimensional simulation of ultrasound propagation through trabecular bone structures measured by synchrotron microtomography, Phys. Med. Biol. 50 (2005) 5545–56.

[7] D. Gutierrez-Lemini, Engineering Viscoelasticity, Springer, 2014.

[8] C. Zhang, L.H. Le, R. Zheng, D. Ta, E. Lou, Measurements of ultrasonic phase velocities and attenuation of slow waves in cellular aluminum foams as cancellous bone-mimicking phantoms, J. Acoust. Soc. Am. 129 (2011) 3317–26.

Chapter 8

Summary and Conclusions

8.1 Summary

Understanding the physics of ultrasound propagation in diagnostic and therapeutic ultrasound fields is beneficial towards the development of their particular applications. In this study, quantitative ultrasound (QUS) for bone assessment and low-intensity pulsed ultrasound (LIPUS) for the treatment of orthodontically induced inflammatory tooth root resorption (OIIRR) were considered for each category of ultrasound applications (i.e. diagnostic and therapeutic).

8.1.1 The FEM for simulating QUS

QUS for bone assessment is a safe, inexpensive, easy to implement, and portable method compared to X-ray based methods. So far, this method has been successfully utilized to assess osteoporotic fracture risk. However, the ultimate aims of QUS, which are diagnosing osteoporosis and monitoring skeletal changes, have not been achieved yet. The main obstacle hindering the QUS to be utilized as a reliable diagnosing tool is deficient understanding of the physics of ultrasound propagation in cancellous bone. Specially, the relations between structural (micro-architectural) properties of cancellous bone and ultrasonic parameters (defined based on ultrasonic velocity and attenuation) are not fully explored. One approach to study ultrasound propagation in the micro-structure of cancellous bone is using computer simulations. The important perspective of computer simulations is that they can perform a wide range of parametric studies on mechanical, physical and structural properties of cancellous bone. In this regard, the accuracy of computer simulations to precisely capture the wave propagation phenomenon (specially scattering and wave mode conversion) occurring in cancellous bone is crucial.

In this study, QUS for bone assessment was studied through computer simulation of ultrasound propagating in cancellous bone micro-structure. Initially, it was observed that other researches utilized the finite difference time domain (FDTD) method for micro-scale simulation of ultrasound in cancellous bone. To enhance the accuracy of the simulations, the standard Galerkin finite element method (FEM) was proposed as an alternative to the FDTD. In this regard, an appropriate finite element modeling procedure for simulating a QUS experimental scheme including the micro-structure of cancellous bone was devised. Finite element simulation of QUS for diagnosing osteoporotic and healthy samples of human radial cancellous bone was

performed. QUS parameters, i.e. frequency-dependent ultrasonic attenuation, broadband ultrasound attenuation (BUA or nBUA) and speed of sound (SOS) were obtained through the simulations. It was demonstrated that the FEM could simulate reasonable QUS parameters and consequently distinguish between healthy and osteoporotic bones. The accuracy of the FEM was then evaluated through experiments: A set of experiments and the corresponding finite element simulations were performed to evaluate the accuracy of the FEM. To this end, aluminum foams resembling cancellous bone mimicking phantoms were utilized in the experiments and for simulations. Comparing the experimental and simulated results demonstrated highly acceptable accuracy for the FEM. Moreover, the results ascertained that the main source of attenuation in trabecular structures, especially aluminum foams, was scattering mechanisms.

8.1.2 Investigation of ultrasound-induced pressure and energy in dental tissues regarding the treatment of OIIRR

OIIRR is a type of tooth root resorption that occurs during orthodontic treatment and leads to destruction and reduction of cementum and dentin (in the severe case) of the root. So far, the only proposed treatment, which can attain its future clinical practicality, is the application of LIPUS. The stimulatory effect of LIPUS on regeneration of new root cementum has been demonstrated in other researches. This stimulatory effect is believed to be originated from mechanical stresses generated in the dental tissues due to ultrasonic waves. In this study, it was hypothesized that the LIPUS-induced mechanical stresses in the dental tissues and their correlation with cementum regeneration could be obtained through computer simulation of ultrasound propagation in dentoalveolar structure (tooth and its surrounding tissues). In this regard, the FEM was employed to simulate the previously published experiment of ultrasonic wave propagation in the dentoalveolar structure of beagle dogs. Simple one-dimensional and complicated three-dimensional finite element models were created and simplifications and limitations of the models were addressed. Mechanical stresses in the forms of average normal stresses (pressure) on the root surface and acoustic pressure in the periodontal ligament were simulated. Additionally, ultrasonic energy values on the root surface were obtained from the simulated stresses. The simulated results led to qualitative and quantitative relations between the thickness of the regenerated cementum observed in the experiment and the ultrasonic parameters (ultrasonic pressure and energy). Although the results did not lead to strong quantitative

correlations (high coefficient of determination), both of the qualitative and quantitative relations indicated that greater ultrasonic pressure was associated with higher amounts of cementum regeneration. This also implied that the non-uniform thickness of the regenerated cementum might be explained by the observed non-uniform distribution of the simulated ultrasonic parameters. Moreover, it was found that the material layers composing the dentoalveolar structure and the geometrical shape of the periodontal ligaments had a significant effect on ultrasonic attenuation by redistribution of the energy inside the structure.

A beagle dog dentoalveolar structure for the simulation of ultrasonic waves and elucidating the ultrasound-induced mechanical stresses was chosen due to availability of the histological study revealing the cementum thicknesses. To extend the simulations, it will be beneficial to consider the ultrasound propagation in the human dentoalveolar structure. However, a human dentoalveolar structure, unlike the dentoalveolar structure of a beagle dog, contains significant amount of cancellous bone in the jawbone. As demonstrated in this thesis, ultrasound significantly attenuates due to scattering in cancellous bone and the consequent energy loss cannot be neglected. On the other hand, creating computational cancellous bone for a finite element analysis is only practical for relatively small samples of cancellous bone. Therefore, an isotropic and homogeneous equivalent material model (EMM) was proposed in this thesis. The EMM role was to model the scattering attenuation in cancellous bone. It was demonstrated that the EMM could imitate ultrasonic attenuation and velocity in cancellous bone if the density and viscoelastic parameters were properly chosen. Although one-dimensional wave propagation was considered for evaluating the ability of the EMM, it could be inferred that, cancellous bone may be approximated and modeled as an isotropic and homogeneous material in a three-dimensional wave propagation analyses.

8.2 Conclusions and recommendations for future research

8.2.1 The FEM for simulating QUS

Towards employing a more accurate method than the usual FDTD approach for simulating QUS experiments, the standard Galerkin FEM was proposed in this work. Micro-scale finite element models of water-saturated cancellous bone and aluminum foam (bone mimicking phantoms) samples were created to demonstrate the ability of the FEM for simulating ultrasound propagation in trabecular structures.

In the case of finite element simulation of broadband ultrasound propagation in cancellous bone samples, the simulations through the FEM demonstrated their ability towards distinguishing osteoporotic bones from healthy one. Moreover, comparing the simulation results of the present study with the finite difference simulation and experimental results of other researchers indicates that the finite element simulations are able to predict reasonable QUS parameters (attenuation coefficients, nBUA and SOS) for the cancellous bone samples.

To directly validate the accuracy of the finite element simulation, a set of QUS experiments on broadband ultrasound propagation in aluminum foams was performed. The comparison between the results indicated less than 10% difference between the simulation and experimental results. This implies that the FEM can effectively account for linear wave propagation in the solid and the fluid media, the solid-fluid interaction (perfect slip) and phenomena such as wave scattering, reflection and refraction. Moreover, the small discrepancy (10%) suggests that the finite element simulations can accurately model ultrasound propagation in fluid-saturated trabecular structures when the effect of energy-absorbing mechanisms on the attenuation is insignificant.

One of the aims of using the FEM for simulating QUS was to show the superiority of the FEM over the FDTD method. The simulation error (as relative error between simulation and experimental results) in this study appeared notably smaller than the simulation error observed in other studies based on FDTD micro-scale modeling. However, this observation should be treated with care. The FDTD method was used to simulate ultrasonic propagation in cancellous bone whereas the FEM, in this study, incorporated aluminum foams. As demonstrated and discussed in this study, the attenuation of the ultrasound due to absorption of mode-converted shear waves may appear to be greater in cancellous bone than that in aluminum. Therefore, disregarding energy-absorbing mechanisms in simulation of ultrasound propagation in cancellous bone may lead to larger simulation error.

In this research, it was shown that the finite element method could simulate ultrasound propagation in trabecular structures (cancellous bone) with notable level of accuracy. This accurate simulation method and the proposed models have the following possible implementation in further development of the QUS towards becoming a tool for diagnosing and monitoring osteoporosis:

The relation between micro-architectural (structural) properties of cancellous bone and ultrasonic attenuation are still unclear. One approach to elucidate this relation is to utilize physical and computationally-made cancellous bone phantoms with known structural properties. Computer simulations utilizing computationally-made cancellous bone phantoms are powerful for investigating the effect of micro-architecture of cancellous bone on the QUS parameters. The micro-scale simulation method proposed in this study is capable to accurately take the geometry of computationally-made cancellous bone phantoms into account and perform accurate wave propagation analysis.

Manufactural differences between QUS commercial devises lead to significant discrepancies between their measurements and predictions. By utilizing computer simulations, the effect and contributions of each manufactural difference on QUS measurements (SOS, BUA) can be individually determined. For example, the effect of transducer shape, size, centre frequency and bandwidth (different broadband pulse) on the QUS parameters can be considered. This may help to optimize the transducer shape, size, centre frequency and bandwidth among the devices and consequently to standardize the characteristics of commercial devices.

8.2.2 Investigation of ultrasound-induced pressure and energy in dental tissues regarding the treatment of OIIRR

The propagation of therapeutic ultrasound in dentoalveolar structure of a beagle dog was simulated to investigate the hypothesis stating the stimulatory role of LIPUS-induced mechanical stresses on) on the regeneration of new dental cementum.

To perform a finite element simulation of LIPUS propagating in the dentoalveolar structure of a beagle dog, some simplifications were inevitable. The simplifications included assuming linear wave propagation, disregarding the anisotropy and viscosity of the materials, modeling the soft tissues as non-viscous fluids, ignoring small geometrical details inside the dentoalveolar structure, simplifying the transmission mechanisms of the ultrasound into the structure, and assuming steady state conditions for the ultrasonic propagation.

Although simplifications were made, the simulations revealed some aspects of the relation between the simulated ultrasonic parameters (pressure and energy density) and experimentally observed cementum regeneration. The non-uniformity observed in the distributions of the simulated ultrasonic parameters may indicate one of the reasons of the non-

uniform cementum regeneration. Additionally, positive correlations between the simulated ultrasonic parameters and cementum regeneration were observed.

The positive correlations did not show high coefficients of determination ($R^2 = 18{\sim}47\%$). This may be caused by the modeling simplification and/or the limitations of the study. In particular, this indicates that cementum regeneration might have better correlation with the non-linear wave propagation phenomena that were not captured by the linear finite element analyses.

This study is the first of its kind with some moderate success in evaluating the hypothesis on the stimulatory mechanism of the ultrasound regarding the treatment of the OIIRR. Therefore, it can be considered as a motivation in the direction of macro-scale (continuum-scale as opposed to cell-scale) investigation of the effect of ultrasonic parameters on cementum regeneration.

Motivated by this study, implementations of investigating the correlations between ultrasonic induced stresses/energy and cementum regeneration using finite element simulations can be proposed in the form of the following future works:

To induce higher magnitude of ultrasonic stress/energy on root surface, using another transducer on the lingual side of the dentoalveolar structure in addition to the transducer applied on the buccal side may be useful. This can be initially studied using finite element simulations to predict potential cementum regeneration with regard to the observations in this research.

One of the LIPUS characteristic is the ultrasound frequency that may have significant effect on the magnitude and distribution of ultrasonic induced stress/energy on the root. In this regard, an optimal ultrasonic frequency leading to greater magnitudes of the ultrasonic parameters may exist. This can be effectively investigated by simulating ultrasound propagation in a dentoalveolar structure (especially of a beagle dog).

In this research, computer simulations of ultrasound propagation in the dentoalveolar structure of a beagle dog were performed and correlations between the simulated ultrasonic parameters and cementum regeneration were demonstrated. This will be beneficial to extend this study towards the investigation of ultrasound propagation in a human dentoalveolar structure. To this end, a human dentoalveolar structure incorporating the EMM proposed in chapter 7 should be modeled and the cementum regeneration can be predicted based on the observations in this

research.

As previously mentioned (chapter 6), in-vitro studies use cell cultures exposed to ultrasonic waves to stimulate cell metabolism. Finite element simulations can also be beneficial for investigating ultrasonic stress/energy fields related to in-vitro studies on LIPUS-Induced cementum regeneration. In this regard, the ultrasonic pressure distribution inside the cell culture can be obtained and correlated with the growth, changes or proliferation of the cells.

Appendix A.

Condition on fluid particles velocity for neglecting convective terms

Euler's equation of motion (Eq. 2.4) and the Eulerian form of the continuity equation (Eq. 2.3) contain the convective (non-linear) terms $(\boldsymbol{v}\cdot\nabla)\boldsymbol{v}$ and $\boldsymbol{v}\cdot\nabla\rho'$ respectively. However, these terms can be neglected if $(\boldsymbol{v}\cdot\nabla)\boldsymbol{v} \ll \frac{\partial \boldsymbol{v}}{\partial t}$ and $\boldsymbol{v}\cdot\nabla\rho' \ll \rho_o\nabla\cdot\boldsymbol{v}$. It can be prove that the convective term $((\boldsymbol{v}\cdot\nabla)\boldsymbol{v})$ becomes small enough to be neglected if the velocities of the particles have magnitudes much less than the speed of sound in the medium, i.e. $|\boldsymbol{v}| \ll \mathrm{c}_o$. Furthermore, the non-linear term $\boldsymbol{v}\cdot\nabla\rho'$ can be neglected if $\left|\frac{\rho'}{\rho_o}\right| \ll 1$ [1].

To prove the statement, U and Γ are assumed to be the typical magnitudes of velocity and condensation $\frac{\rho'}{\rho_o}$. Moreover, the spatial and temporal derivatives scale the magnitude of a quantity by L^{-1} and τ^{-1} respectively. Summarizing the assumptions gives [2]:

$$|\boldsymbol{v}|\sim U,\ |\frac{\rho'}{\rho_o}|\sim\Gamma$$
$$\frac{\partial}{\partial x_i}\sim\frac{1}{L},\frac{\partial}{\partial x_i}\sim\frac{1}{\tau} \qquad \text{(A.1)}$$

In this regard, the linearized form of the continutiy equation i.e. $\frac{\partial\rho'}{\partial t}+\rho_o\nabla\cdot\boldsymbol{v}=0$ (Eq. 2.14) implies:

$$\frac{\Gamma}{\tau} \sim \frac{U}{L} \qquad (A.2)$$

Also, substituting Eq. 2.12 ($\rho' \approx \kappa \rho_o p'$) into the linearized form of the Euler's equation $\rho_o \frac{\partial \boldsymbol{v}}{\partial t} \approx -\nabla p'$ (Eq. 2.15)[1] and implementing the speed of sound as $c_o^2 = \frac{1}{\kappa \rho_o}$ indicates:

$$\frac{U}{\tau} \sim c_o^2 \frac{\Gamma}{L} \qquad (A.3)$$

Eliminating Γ by combining Eq. A.2 and Eq. A.3 leads to:

$$\frac{L}{\tau} \sim c_o \qquad (A.4)$$

On the other hand $(\boldsymbol{v} \cdot \nabla)\boldsymbol{v} \ll \frac{\partial \boldsymbol{v}}{\partial t}$ holds if:

$$\frac{U^2}{L} \ll \frac{U}{\tau} \qquad (A.5)$$

which indicates the following when Eq. A.4 is considered:

$$U \ll c_o, \text{ i.e. } |\boldsymbol{v}| \ll c_o \qquad (A.6)$$

With same method, $\boldsymbol{v} \cdot \nabla \rho' \ll \rho_o \nabla \cdot \boldsymbol{v}$ holds if:

$$\frac{\Gamma U}{L} \ll \frac{U}{L} \qquad (A.7)$$

which indicates:

$$\Gamma \ll 1, \text{ i.e } \frac{\rho'}{\rho_o} \ll 1 \qquad (A.7)$$

[1] $p = p_o + p'$

Appendix B

Time-rate of energy change for wave propagation in solid media

According to the first law of thermodynamics in the absence of heat transfer, the time rare of increase of total energy of a system is equal to the net time rare of work done on the system (or net time rate of energy addition transferred into the system by work) [3]:

$$\frac{\partial E}{\partial t} = \dot{E}_{in} - \dot{E}_{out} = \dot{W}_{in} - \dot{W}_{out} \tag{2.80}$$

To calculate the time rate of energy change for wave propagation in a solid medium, the system is assumed to be a closed volume inside the solid (Figure B.1).

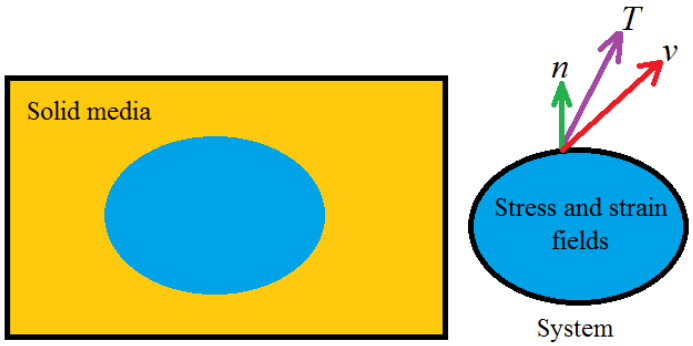

Figure B.1 A system inside a solid media

The net time rate of work done on the system is through the time rate of work (power) of the traction force on the boundary of the system, i.e:

$$\dot{W}_{in} - \dot{W}_{in} = \int_{\partial S} \boldsymbol{T} \cdot \boldsymbol{v} dS \qquad (B.1)$$

in which $\boldsymbol{T}dS$ and $\boldsymbol{v}$ are the traction vector and velocity vectors at a point on the boundary (∂S) of the system. Expressing the traction in terms of the stress tensor gives [4]:

$$\int_{\partial S} \boldsymbol{T} \cdot \boldsymbol{v} dS = \int_{\partial S} [\boldsymbol{\sigma}^{\mathrm{T}} \boldsymbol{n}] \cdot \boldsymbol{v} dS = \int_{\partial S} [\boldsymbol{\sigma v}] \cdot \boldsymbol{n} dS \qquad (B.2)$$

such that $\boldsymbol{n}$ is the unit normal vector of the differential surface**.**

Considering Eq. 2.79 leads to:

$$\dot{E}_{out} - \dot{E}_{in} = \int_{\partial S} -[\boldsymbol{\sigma v}] \cdot \boldsymbol{n} dS \qquad (B.3)$$

where the term $-[\boldsymbol{\sigma v}]$ indicates the time rate of total energy flow out of the system per unit area which is regarded as the wave intensity according to the definition, i.e. energy flux per unit area.

In the case of scalar pressure filed, the vector $-[\boldsymbol{\sigma v}]$ reduces to Eq. 2.82 assuming negative stress to as positive pressure.

The intensity vector $\mathbf{I} = -[\boldsymbol{\sigma v}]$ is sometimes written in the index notation form as $I_i = -\sigma_{ij} v_j$**.**

Appendix C

Matlab codes for utilizing ASM

Fluid medium

```
% initial properties of field and transducer
c=000;          % speed of sound
rho=0000;       % density

fc=000e6;    % source center frequency (fo if monocrome)
a=000;    % transduce radius or length(if square), m
Po=1;      % peak pressure at source

% Derived parameters
lambda=c/fc;    % wavelength of center frequency
wc=2*pi*fc;     % center radial frequency
k=2*pi/lambda;  % wave number of center frequency

% Model parameters
Times_Nyquist_Rate=4;           % Sampling parameter
ky_max=Times_Nyquist_Rate.*k;   % maximum spatial frequency for
sampling
                                %(the resolution of wavelength to be
resolved is lambda/2)

y_obs_max=0.5;    % spatial domain extent
Ty=2*y_obs_max;       % it should be at least the width of the
transducer + y_obs_max

% generating a spetial domain and a spatial frequency domain gridding

dky=pi/Ty;
% the number of intervals from the origin to Tx (in x-y space) or from
the
% origin to kx_max (in k-space)
```

```
Ny=ceil(ky_max/dky);

ky_max=Ny*dky;
dy=pi/ky_max;
Ty=Ny*dy;
y=(-Ny:Ny-1)*dy;
Ky=(-Ny:Ny-1)*dky;
MMy=length(y);

squar_transducer=(-a/2<y & y<a/2);
Po_y=Po.*squar_transducer;

So=fft(Po_y);
So=fftshift(So);        % to mach the k-CS generated by 2FFT with the
one used in H(kx,ky)

N=2000
pz_y=zeros(N,MMy);
z_max_obs=18e-2;

for m=1:N
z_obs=m*z_max_obs/N;     % z-distance of observation plane from the CS
origi
% Sample H (transfer function on k-plane in a discrete form)

H=exp(-1.*(sign(k^2-(Ky.^2))).*(j*z_obs*sqrt(k^2-(Ky.^2))));

% do the propagation from (0,0,0) to dz via the transfer function H
S_z=So.*H;

pz_y(m,:)=abs(ifft(fftshift(S_z)));
end

NMH=0.05/dy;
core=pz_y(:,ceil(MMy/2-NMH/2):ceil(MMy/2+NMH/2));
core=core';
%plotting
[sy sx]=size(core);
x_axis = linspace(1,z_max_obs*100,sx);
y_axis = linspace(-2.5,2.5,sy);
contourf(x_axis,y_axis,core);
xlabel('X (cm)');
ylabel('Y (cm)');
```

Solid medium

```
clear all;
%-------------------------------------------------------------------%
%            Initializing field and transducer variables
%
```

```
%-------------------------------------------------------------------------%
% Material Properties
Em=1.91e10;
nu=0.3;
rho=1600;              % density

% Transducer Properties
fc=1e6;                % source center frequency (fo if monocrome)
a=0.01;                % transduce length, m
phi_0_mag=0.001;       % potential function amplitude

% Derived parameters
G=Em/(2+2*nu);                                  % Shear modulus
cL=sqrt(Em*(1-nu)/(rho*(1+nu)*(1-2*nu)));   % longitudinal velocity
cT=sqrt(G/rho);                                 % Transverse speed of
sound

lambda_L=cL/fc;               % longitudinal wavelength of center
frequency
lambda_T=cT/fc;               % Transverse wavelength of center
frequency
wc=2*pi*fc;                   % center radial frequency
kL=2*pi/lambda_L;             % longitudinal wave number
kT=2*pi/lambda_T;             % transverse wave number

k=min(kL,kT);

%-------------------------------------------------------------------------%
%            Discretization of spatial and frequency domains
%
%-------------------------------------------------------------------------%
Times_Nyquist_Rate=4;          %  Sampling parameter
ky_max=Times_Nyquist_Rate.*k;  %  maximum spatial frequency for
sampling
                               % (the resolution of wavelength to be
                               % resolved is lambda/2)

y_obs_max=0.8;                  % spatial domain extent

Ty=2*y_obs_max;        % it should be at least the width of the
transducer
                       % + y_obs_max

% generating a spetial domain and a spatial frequency domain gridding
dky=pi/Ty;

%  the number of intervals from the origin to Tx (in spatial domain)
or
% from the origin to kx_max (in k-space)

Ny=ceil(ky_max/dky);
ky_max=Ny*dky;
```

```
dy=pi/ky_max;

Ty=Ny*dy;
y=(-Ny:Ny-1)*dy;
Ky=(-Ny:Ny-1)*dky;

MMy=length(y);

%-------------------------------------------------------------------%
%            Generating the displacement potential functions
%
%-------------------------------------------------------------------%

% the same function is generated for the longitudinal & transverse
waves
TX=rect_apdze(a,y,dy);  % Transducer appodization
phi_0=phi_0_mag*TX;     % defining the potential function on the
transducer

So=fft(phi_0);
So=fftshift(So); % to mach the k-CS generated by 2FFT with the one
used
                 % in H(kx,ky) and kz

kz_L=-sqrt(kL^2-(Ky.^2));
kz_T=-sqrt(kT^2-(Ky.^2));
N=200;                    % number of divisions in Z-direction
phi_z_y=zeros(MMy,N);
z_max_obs=8e-2;

%-------------------------------------------------------------------%
%                    Defining displacement vectors
%
%-------------------------------------------------------------------%
Uz_L=zeros(MMy,N);
Uy_L=zeros(MMy,N);

Uy_T=zeros(MMy,N);
Uz_T=zeros(MMy,N);
%-------------------------------------------------------------------%
% Calculating phi and displacement vectors as a function of Z (and y)
%
%-------------------------------------------------------------------%
for m=1:N
z_obs=(m-1)*z_max_obs/N; % z-distance of observation point from CS
(0,0)

% NOTE: the lateral center axis of the medium is when m=N/2+1

% Sample H (transfer function on k-plane in a discrete form)
HL=exp(-1.*(sign(kL^2-(Ky.^2))).*(j*z_obs*sqrt(kL^2-(Ky.^2))));
HT=exp(-1.*(sign(kT^2-(Ky.^2))).*(j*z_obs*sqrt(kT^2-(Ky.^2))));
```

```
% do the propagation from (0,0,0) to dz via the transfer function H
S_z_L=So.*HL;
S_z_T=So.*HT;
phi_L=fftshift(S_z_L);
phi_L=ifft(phi_L);
phi_zy_L(:,m)=phi_L';
phi_T=fftshift(S_z_T);
phi_T=ifft(phi_T);
phi_zy_T(:,m)=phi_T';
% calculating Uz_L and Uy_T
S_Uz_L=-j*(kz_L).*S_z_L;
S_Uz_L=fftshift(S_Uz_L); %  organize the values to the same befor
doing the
                         % fftshift so that matlab can exactly obtain
the
                         % function before fft
U_zL=ifft(S_Uz_L);
Uz_L(:,m)=(U_zL');
S_Uy_T=j*(kz_T).*S_z_T;
S_Uy_T=fftshift(S_Uy_T); %  organize the values to the same befor
doing the
                         % fftshift so that matlab can exactly obtain
the
                         % function before fft
U_yT=ifft(S_Uy_T);
Uy_T(:,m)=(U_yT');

end

% calculating Uy_L and Uz_T through the derivatives of phi
for i=1:N
   Uy_L(1:MMy-1,i)=-diff(phi_zy_L(:,i))/(dy);
end

for i=1:N
   Uz_T(1:MMy-1,i)=-diff(phi_zy_T(:,i))/(dy);
end
%-------------------------------------------------------------------%
%              Calculatingthe total displacement vector field
%
%-------------------------------------------------------------------%
Uz=Uz_L+Uz_T;
Uy=Uy_L+Uy_T;

Uz_mag=abs(Uz);
Uy_mag=abs(Uy);
%-------------------------------------------------------------------%
%                             preparing plots
%
%-------------------------------------------------------------------%
NMH=(8e-2)/dy;  %  8e-2 is the lateral width of the medium to be
```

```
considered
                % for plots

core_TX=TX(ceil(MMy/2-NMH/2):ceil(MMy/2+NMH/2));

core_Uy_mag=Uy_mag(ceil(MMy/2-NMH/2):ceil(MMy/2+NMH/2),:);

core_Uz_mag=Uz_mag(ceil(MMy/2-NMH/2):ceil(MMy/2+NMH/2),:);

%plotting
[sy sx]=size(core_Uy_mag);

x_axis = linspace(1,z_max_obs*100,sx);
y_axis = linspace((-NMH/2*dy)*100,(NMH/2*dy)*100,sy);
xlabel('X (cm)');
ylabel('Z (cm)');

figure(1);contourf(x_axis,y_axis,core_Uy_mag);
figure(2);contourf(x_axis,y_axis,core_Uz_mag);
figure(3);plot(core_TX);

% ------------------------------------------------------------------%
%      Preparing U for the FE model input (Boundary conditions)
%
% ------------------------------------------------------------------%
N_nodes=801;    % number of total FE nodes on the loaded side of the
medium
FE_M_width=0.08;% the width og the FE model on which there is N_nodes
dy_FE=1e-4;     % dy of the width of the FE model
Uz_aba_tmp=Uz(ceil(MMy/2-
1/2*FE_M_width/dy):ceil(MMy/2+1/2*FE_M_width/dy));
Uy_aba_tmp=Uy(ceil(MMy/2-
1/2*FE_M_width/dy):ceil(MMy/2+1/2*FE_M_width/dy));
Ux_aba_real_tmp=real(Uz_aba_tmp'); % X-Y is used in FE model insted of
Y-Z
Ux_aba_imag_tmp=imag(Uz_aba_tmp');
Uy_aba_real_tmp=real(Uy_aba_tmp');
Uy_aba_imag_tmp=imag(Uy_aba_tmp');
% interpolating data to match the values for dy of the FE model
% y's are only for interpolation purposes (dummy y's)
y_initial=(0:dy:(length(Uz_aba_tmp)-1)*dy)';
y_FE_model=(0:dy_FE:FE_M_width)';

%{
if length(y_FE_model~N_nodes)
    disp( warning: N_nodes not equal to y_FE_model points);
end
%}

% interpolating U values to match the FE model nodal distance. values
are
% associated with the N_nodes
```

```
Ux_aba_real=interp1(y_initial,Ux_aba_real_tmp,y_FE_model);
Ux_aba_imag=interp1(y_initial,Ux_aba_imag_tmp,y_FE_model);
Uy_aba_real=interp1(y_initial,Uy_aba_real_tmp,y_FE_model);
Uy_aba_imag=interp1(y_initial,Uy_aba_imag_tmp,y_FE_model);

%{
 values in Uz or Uy arrays (from the 1st element to the last) are
 associated with the bottom of the medium to the top, assigning the
values
 to the FE model nodes must be done with care dippending of the order
of
 the FE model node numbering.
%}
clear Uz_aba_tmp Uy_aba_tmp Ux_aba_real_tmp Ux_aba_imag_tmp
Uy_aba_real_tmp     Uy_aba_imag_tmp;
```

```
function transducer=rect_apdze (a,y,dy)

LY=length(y);
N_cntr=round(LY/2);
trans_unifrm=ones(1,LY);  %defining a uniform transducer on Y-plane
transducer=trans_unifrm;
L_rect=0.8*a/2;
smth_st=0.0001;                          %1/smoothening strength
N_smth_p=round(N_cntr+(L_rect/dy));      %N smooth positive side
N_smth_n=round(N_cntr-(L_rect/dy));      %N smooth negative side
% applying the appodization
transducer(N_smth_p:LY)=trans_unifrm(N_smth_p:LY).*exp(-
1/(smth_st*a)*(y(N_smth_p:LY)-y(N_smth_p)).^2);
transducer(1:N_smth_n)=trans_unifrm(1:N_smth_n).*exp(-1/(smth_st*a)*(-
y(1:N_smth_n)+y(N_smth_n)).^2);
%plot(transducer);
```

Appendix D

Python codes to retrieve numerical simulation results stored in ABAQUS database and to perform the mathematical operation.

A piece of code in Python to access the numerical simulation results stored in ABAQUS database and to perform the averaging over the receiver surface (Chapter 4 and 5).

```
## Data from explicit analysis should be Double precission
# ----------------
## upgrading the ODB
# abaqus upgrade -odb my_odb_name.odb
# Job identifier           : my_ODB_new_name.odb
## runnig scripts :abaqus python script_filename.py


from odbAccess import *
from abaqusConstants import *

#------setting input and output----------------#
odbname=raw_input('enter odb name: ')
odb = openOdb(path=odbname)

outputfile=raw_input('enter output file name: ')
myOutputFile = open(outputfile,'w+')

print '-------------------------------------------'

# use command: type() to get the type of a variable

#------printing odb information-----#
```

```
# the command odb.rootAssembly.instances.keys() teturn a sequence
containing the name of
# the part instances, by refering to the sequence id we can obtain the
name of the part instance we want

for myinstanceName in odb.rootAssembly.instances.keys():
  print 'parts in the model are %s  \n'%myinstanceName


print 'steps in the Odb are\n'
stepID=0
for stepName in odb.steps.keys():
  print 'stepID: %d  step name: %s\n'%(stepID,stepName)
  stepID=stepID+1

firststepname=odb.steps.keys()[0]
myframe=odb.steps[firststepname].frames[0]
for fieldName in myframe.fieldOutputs.keys():
    print 'available field outputs are  %s\n'%fieldName

for stepname in odb.steps.keys():
     print 'step: %s time period is %1.4e
sec\n'%(stepname,odb.steps[stepname].timePeriod)

for Nodesets in odb.rootAssembly.nodeSets.keys():
     print 'available node sets are  %s\n'%Nodesets


#------defining the node set containing the results-----#
#TargetNodeSet=raw_input('define the result node set: ')


#------ defining the target step ----#
stepIDchar=raw_input('\ndefine the target stepID: ')
stepID=int(stepIDchar)
Targetstep=odb.steps.keys()[stepID]

lastframeID=odb.steps[Targetstep].frames[-1].frameId
totalavilframes=len(odb.steps[Targetstep].frames)

print "last frameID is %d \n"%(lastframeID)
print "total available number of frames is %d \n"%(totalavilframes)

#----------definig an initial time; the value of the initial time will
be added to all time increment
#values in the target step; it's good to add step-1 time durarion to
step-2 time increment values
#so the times of the values(step-2) come exactly after step-1, insted
of starting from zero
initialtime_char=raw_input('\ndefine  initial  time  if  applicable  or
press 0: ')
```

```
initialtime=float(initialtime_char)

anykey=raw_input('\npress any key: ')

#---------------- Averaging the POR pressure over a specificnode set
##------------ Setting the current frame -------------------------##
#frameId is counted from 0, while the number of frames will be frameID
+ 1
for currentFramenum in range(0,totalavilframes):
 print '\ncurrent frame number is ',currentFramenum


###-- Getting the time associated with the current frame --###
# currentTime=frametime+initialtime
 currentTime=odb.steps[Targetstep].frames[currentFramenum].frameValue
 currentTime=currentTime+initialtime
 print 'current frame time is %1.4e sec'%currentTime

##------------- Getting the field (POR) for a region (node set 'RSLT)

###-- crating an odbSet object using the predefined node set
TargetNodeSet --###
 #resultset = odb.rootAssembly.nodeSets[TargetNodeSet]
###-- creating a fieldoutput object for a specific frame --###
 # odb.stepd.values()[x] --> x refers to the order of steps as 0:step-
1, 1:step-2 and so on
 Porfield                                                          =
odb.steps.values()[stepID].frames[currentFramenum].fieldOutputs['POR']

# Try: print Porfield

###-- Limiting the field (Porfield) to a specific region --###
 #subporfield = Porfield.getSubset(region=resultset)

# try below: it prints the dataDouble (attribute) part of values
(information) of the second node saved in subporfield object
# print subporfield.values[2].dataDouble
# try below: it prints the lenght of the vector (arrey) in which the
data are stored, it equals the number of nodes in the nodeset
# print len(subporfield.values)

##-------------- Averaging the POR over all the nodes in the nodeset
RSLT for a specific frame: frames(i)--------##

 sum = 0

 for val in Porfield.values:
 #for val in subporfield.values:
  sum = sum + val.dataDouble

 ave = sum / len(Porfield.values)
 #ave = sum / len(subporfield.values)
```

```
 print 'the average over nodes is  %1.5e'% (ave)

##-----------------outputing the average (ave) into a file----------##
 strcurrentTime=str(currentTime)
 strave=str(ave)
 myOutputFile.write('%s\t\t%s\n'%(strcurrentTime,strave))

print '\nthe number of nodes in the nodeset was
',len(Porfield.values)

odb.close()
```

References

[1] R.S.C. Cobbold, Foundations of Biomedical Ultrasound, Oxford University Press, 2007.

[2] C.C. Lin, L.A. Segel, Mathematics applied to deterministic problems in the natural sciences, Society for industrial and applied mathematics, 1988.

[3] B.R. Munson, D.F. Young, T.H. Okiishi, W.W. Huebsch, Fundamentals of fluid mechanics, 6th ed., Wiley, 2009.

[4] S. Adeeb, Introduction to solid mechanics and finite element analysis using Mathematica, Kendall Hunt Publishing, 2012.